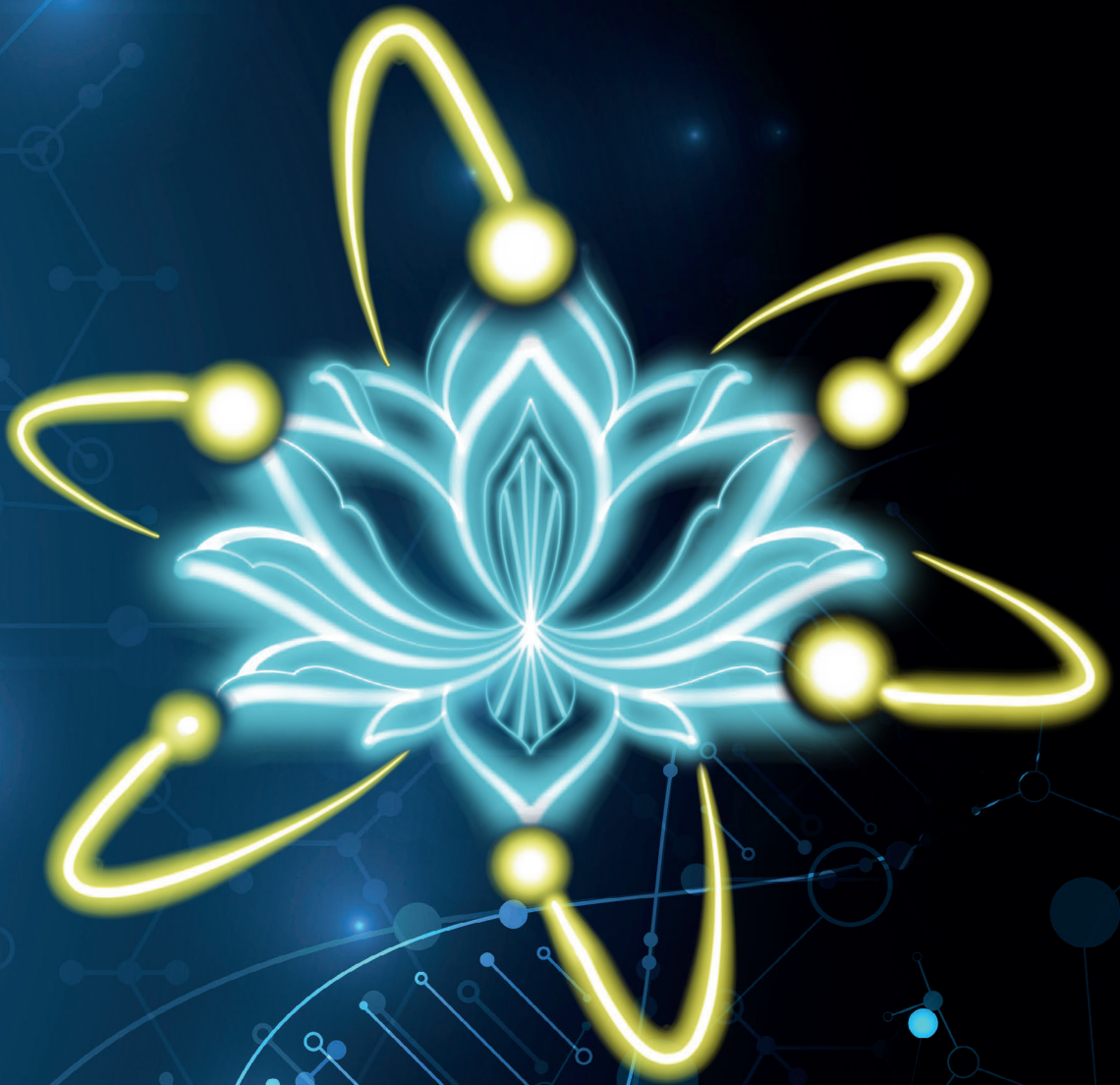


# New PET technologies

performance, image quality, and clinical implications



Joyce van Sluis



# **New PET technologies**

performance, image quality, and clinical implications

Joyce van Sluis

## **Colophon**

New PET technologies - performance, image quality, and clinical implications  
Joyce van Sluis

Cover design: Tim Hardenberg, Tim Hardenberg Tattoos  
and Adobe royalty free stock illustrations  
compiled by Joyce van Sluis

Layout and design: Joyce van Sluis

Printing: Ridderprint | [www.ridderprint.nl](http://www.ridderprint.nl)

ISBN: 978-90-832523-2-2 (hardcopy)  
978-90-832523-3-9 (ebook)

Dissertation of the University of Groningen, Groningen, the Netherlands

Copyright © 2022 Joyce van Sluis

All rights reserved. No part of this thesis may be reproduced, stored, or transmitted in any way or by any means without the prior permission of the author, or when applicable, of the publishers of the scientific papers.

Printing of this thesis was financially supported by the University of Groningen, Graduate School of Medical Sciences.



university of  
 groningen

# **New PET technologies**

performance, image quality, and clinical implications

## **PhD thesis**

to obtain the degree of PhD at the  
 University of Groningen  
 on the authority of the  
 Rector Magnificus Prof. C. Wijmenga  
 and in accordance with  
 the decision by the College of Deans.

This thesis will be defended in public on

Wednesday 7 December 2022 at 14:30 hours

by

**Joyce van Sluis**

born on 5 June 1990  
 in Groningen

**Supervisor**

Prof. R. Boellaard

**Co-supervisors**

Dr. W. Noordzij

Dr. A.H. Brouwers

**Assessment committee**

Prof. J. Pruim

Prof. J.M. Zijlstra

Prof. H.W.A.M. de Jong

**Paranymphs**

Sabine L. Collette

Ananthi Somasundaram



# Contents

---

<b>Chapter 1</b>	General introduction	<b>10</b>
<b>Chapter 2</b>	Digital PET systems <i>Book chapter in Encyclopaedia of Nuclear Medicine. Volume 1. Basic concepts, radiopharmacy, and instrumentation. Elsevier. 2022;408-415.</i>	<b>28</b>
<b>Chapter 3</b>	Performance characteristics of the digital Biograph Vision PET/CT system <i>J Nucl Med. 2019;60:1031-1036.</i>	<b>44</b>
<b>Chapter 4</b>	Image quality and semiquantitative measurements of the Siemens Biograph Vision PET/CT: initial experiences and comparison with Siemens Biograph mCT PET/CT <i>J Nucl Med. 2020;61:129-135.</i>	<b>68</b>
<b>Chapter 5</b>	Image quality and activity optimization in oncological $^{18}\text{F}$ -FDG PET using the digital Biograph Vision PET/CT <i>J Nucl Med. 2020;61:764-771.</i>	<b>90</b>
<b>Chapter 6</b>	Optimization of scan duration and image quality in oncological $^{89}\text{Zr}$ immunPET imaging using the Biograph Vision PET/CT <i>Manuscript in preparation.</i>	<b>110</b>

---

<b>134</b>	First-time imaging of $^{89}\text{Zr}$ -trastuzumab in breast cancer using a long axial field-of-view PET/CT scanner <i>Eur J Nucl Med Mol Imaging. 2022;49:3593–3595.</i>	<b>Chapter 7</b>
<b>140</b>	EARL compliance and imaging optimization on the Biograph Vision Quadra PET/CT using phantom and clinical data <i>Eur J Nucl Med Mol Imaging. 2022; Epub ahead of print.</i>	<b>Chapter 8</b>
<b>158</b>	Use of population input functions for reduced scan duration whole body Patlak $^{18}\text{F}$ -FDG PET imaging <i>EJNMMI Phys. 2021;8:11.</i>	<b>Chapter 9</b>
<b>170</b>	Shortened duration whole body $^{18}\text{F}$ -FDG PET Patlak imaging on the Biograph Vision Quadra PET/CT using a population-averaged input function <i>Accepted for publication in EJNMMI Phys.</i>	<b>Chapter 10</b>
<b>190</b>	Future perspectives and concluding remarks	<b>Chapter 11</b>
<b>206</b>	Summary	<b>Chapter 12</b>
<b>216</b>	Nederlandse samenvatting	<b>Chapter 13</b>
<b>228</b>	List of publications Dankwoord Curriculum Vitae	<b>Appendices</b>



*To mom and dad*



# Chapter 1

---

## General introduction

Adapted from:

*Book chapter 'Digital PET systems' in Encyclopaedia of Nuclear Medicine, Volume 1. Basic concepts, radiopharmacy, and instrumentation. Elsevier. 2022;408-415.*



## **PET principles**

Positron Emission Tomography (PET) is the most specific and sensitive imaging modality for visualizing and measuring human physiology *in vivo* (1). This nuclear medicine imaging modality is based on the intravenous injection of radiotracers labeled with a positron-emitting radionuclide (2). When a positron-emitting radionuclide decays in the body, interaction of the positron with an electron results in an annihilation event emitting two 511 keV annihilation photons in nearly 180-degree opposite directions. The simultaneous emission of these photons sent towards detector rings surrounding the patient form the basis of the detection and localization of positron emitters via a mechanism called coincidence detection (4,5). This process allows localization of the annihilation event to somewhere on the line of response (LOR) connecting the detectors on either side of the detector ring. Typically, approximately  $10^7$  to  $10^8$  coincidence events are collected by the detectors which are used to reconstruct a PET image reflecting the distribution of the radionuclide in the body (2).

### **$^{18}\text{F}$ -FDG PET**

The most commonly used PET tracer is the glucose analogue  $^{18}\text{F}$ -2-fluoro-2-deoxy-D-glucose ( $^{18}\text{F}$ -FDG) and is based on the principle that  $^{18}\text{F}$ -FDG accumulation in tissue is proportional to the amount of glucose utilization (4,5). The research described in this thesis primarily focused on PET using  $^{18}\text{F}$ -FDG which contains  $^{18}\text{F}$ , a cyclotron-produced positron-emitting radioisotope of fluorine.  $^{18}\text{F}$ -FDG has a short half-life of 109.7 min and the low positron energy (640 keV) results in short tissue range which is translated into relatively low radiation dose and high resolution (6). Various molecular tracers can be labeled with  $^{18}\text{F}$  and imaged within a few hours, typically <3 h, after injection. Many cancers demonstrate increased consumption of glucose, which is, in part, related to over-expression of the GLUT-1 glucose transporters and increased hexokinase activity. Once inside the cell,  $^{18}\text{F}$ -FDG is phosphorylated by hexokinase into  $^{18}\text{F}$ -FDG-6-phosphate, which, unlike glucose, because of chemical differences cannot be further metabolized ensuring metabolic trapping (6). For clinical use, static images are most frequently acquired at approximately 60 min post  $^{18}\text{F}$ -FDG radiotracer injection. In oncology,  $^{18}\text{F}$ -FDG PET has become part of the daily clinical routine including initial diagnosis, staging, prognosis, radiation therapy planning, and monitoring response to treatment (7-10).

### **$^{89}\text{Zr}$ immunoPET**

Zirconium-89 ( $^{89}\text{Zr}$ ) is also a cyclotron produced positron-emitting radioisotope.  $^{89}\text{Zr}$  decays with a half-life of 78.4 hours, first via positron emission and electron capture to the meta-stable yttrium-89m ( $^{89\text{m}}\text{Y}$ ), with a half-life of 15.7 s, which

subsequently decays via gamma ray emission (909 keV) to the stable  $^{89}\text{Y}$  (11,12).  $^{89}\text{Zr}$  labeled monoclonal antibodies (mAb) are another type of tracers used in the research described in this thesis. Numerous advantages of  $^{89}\text{Zr}$  such as the long half-life of 78.4 hours, matching the pharmacokinetic behavior of antibodies, and good *in vivo* stability, make it a suitable candidate for labeling of mAb (13).  $^{89}\text{Zr}$  immunoPET provides whole body information on (tumor) target expression (14). The low positron abundance of  $^{89}\text{Zr}$  (23%, as opposed to  $^{18}\text{F}$  with an abundance of 96%) (13) causes PET images acquired on conventional PET/CT systems to have a low signal to noise ratio (SNR). In addition, the long physical half-life limits the amount of radiotracer activity that can be administered to patients in order to keep radiation exposure within acceptable limits (15). Hence, to obtain sufficient count statistics on conventional PET/CT systems for adequate image quality, long scan durations are required, especially at later scan time-points.

### ToF application

Use of time-of-flight (ToF) information can increase the accuracy of localizing the annihilation event along the LOR. The emission distance ( $d$ ) along this LOR can be calculated using Eq. 1:

$$d = c * (t_1 - t_2)/2 \quad \text{Eq. 1}$$

Here,  $c$  represents the speed of light and  $t_1$  and  $t_2$  are the times the coincidence photons are captured by the opposing detectors. In non-ToF PET, the PET system is not capable of measuring the difference in arrival time ( $t_2 - t_1$ ) of the photons precisely enough to determine the location of the annihilation event along the LOR (16,17). Consequently, the probability of the annihilation event along the full length of the LOR is assumed to be uniform over the length of the LOR. Therefore, information from different events is forward- and backward-projected during (iterative) image reconstruction over the entire length of the LOR resulting in slower reconstruction convergence and increased noise levels (or worse SNR) as compared when ToF information would be available during reconstruction, as detailed later. Around the year 2005, improved system characteristics and electronics optimized for ToF imaging, e.g., use of lutetium oxyorthosilicate (LSO) or lutetium-yttrium oxyorthosilicate (LYSO) scintillation crystals with high count rate capabilities and photomultiplier tubes (PMTs) with good timing performance, allowed the first commercial introduction of ToF-PET. Application of ToF in PET image reconstruction allows localization of the annihilation event within a small region of the object along the LOR, i.e., several cm. The system coincidence timing resolution ( $\Delta t$ ) determines the uncertainty in corresponding spatial localization ( $\Delta x$ ) according to Eq. 2:

$$\Delta x = c * \Delta t / 2 \quad \text{Eq. 2}$$

Here,  $c$  represents the speed of light.

During reconstruction with ToF, due to a smaller spatial uncertainty, noise from different annihilation events is now forward- and backward-projected over a reduced number of image voxels leading to improved SNR, as well as a faster image reconstruction convergence (18). A reduction of noise can be equated with an increase in sensitivity, the effective sensitivity gain, which can be calculated using Eq. 3, the modified Budinger's equation (19):

$$ToFgain = \frac{1}{1.47} \frac{D}{c/2\Delta t} \quad \text{Eq. 3}$$

Here,  $D$  is the transverse diameter of the average human abdomen in cm. Eq. 3 can be simplified to Eq. 4:

$$ToFgain = constant * D/\Delta t \quad \text{Eq. 4}$$

The *constant* can then be calculated using Eq. 5:

$$constant = \frac{2/(1.47 * c)}{1 \text{ ps}} = 45.38 \quad \text{Eq. 5}$$

When taking 30 cm as the average human abdominal transverse diameter, *ToFgain* can be calculated using Eq. 6:

$$ToFgain = 45.38 * 30/\Delta t \quad \text{Eq. 6}$$

The effective sensitivity can subsequently be calculated according to Eq.7:

$$Sens_{eff} = Sens * ToFgain \quad \text{Eq. 7}$$

These metrics provide an indication that ToF gain increases with improved coincidence timing resolution, but also with increasing patient size (20). As conventional PET image quality deteriorates considerably with increasing patient size because of increased attenuation causing both loss of true counts and increase of scattered counts, improved image quality with ToF application due to improved SNR and effective sensitivity gain is a powerful tool right where it is needed most (17,20).

## Digital PET

Over the last decades, the main development in PET detector design has been the adoption of solid-state technology (18). Conventional PMTs have been replaced by solid-state read-out devices in recently introduced commercially available PET/CT systems. This detector technology has the advantage of being compact, but its insensitivity to a magnetic field makes it well-suited for PET coupled with Magnetic Resonance Imaging as well. The first clinical PET/MRI systems manufactured by Siemens (Siemens Healthineers, Knoxville, TN, USA) were equipped with avalanche photodiodes (APDs). More recently, further development of APDs resulted in the introduction of silicon-photomultipliers (SiPMs) which are implemented also in the latest clinical PET/CT systems.

An APD is formed by a silicon p-n junction creating a depletion region free of mobile charge carriers. When a 511-keV photon is absorbed in a light-sensitive layer, silicon, an electron-hole pair is created (photo-electric effect). When applying a reverse bias to the photodiode, an electric field will be created across the depletion region causing these charge carriers to be accelerated towards the anode (holes), or cathode (electrons). This way, an absorbed photon will result in a net flow of current in a reverse biased APD.

The applied electric field causes acceleration of electrons which in turn produce a secondary ionization, or avalanche, resulting in amplification of the electric signal. However, this gain is not as high as with conventional PMTs. The slow rise time of the signal makes APDs unsuitable for implementation of ToF PET. In ToF PET, as described above, the difference in the arrival times of the two photons on both detectors is measured with high precision, which helps localize the point of annihilation (with a certain probability) along the line of response (21). However, when the applied reverse-bias voltage is increased sufficiently (approaching the breakdown voltage) a created charge carrier will be accelerated to such an extent that it carries sufficient kinetic energy to create secondary charge pairs; this process is referred to as impact ionization. Accordingly, a single absorbed photon can trigger a self-perpetuating ionization cascade spreading through the silicon volume subjected to the electric field. Breakdown of the silicon occurs making it conductive, effectively amplifying the original electron-hole pair into a macroscopic current flow. This is called Geiger discharge; the APD operates in Geiger mode. Then, a single incoming light photon produces a large signal and the device is referred to as a single-photon avalanche diode (SPAD) of very compact size (10-100  $\mu\text{m}$ ) (22,23). Once a current is running it should be stopped or 'quenched'. Passive quenching is achieved through using a series of resistors which limit the current drawn by the diode during breakdown. This

lowers the reverse voltage seen by the diode to a value below its breakdown voltage. The diode is then available to detect subsequent photons. Through this mechanism, a single SPAD functions as a photon-triggered switch, in either 'on' or 'off' state, resulting in a binary output. Proportional information regarding the photon flux is not available. This lack of proportionality is overcome in the SiPM. An SiPM is comprised of an array of (between 100 and 10,000) SPADs which are read-out in parallel producing an electric signal proportional to the number of detected 511-keV photons in a small detector area (cell). The gain and detection efficiency are comparable to conventional PMTs while using a smaller operating voltage and running at a higher speed. An array of SiPMs can be used instead of the conventional array of PMTs (18).

Currently, there are three different commercially available 'digital' PET/CTs available which are equipped with SiPM-based PET detectors: the Siemens Biograph Vision PET/CT (Siemens Healthineers), the Philips Vereos PET/CT (Philips Healthcare), the GE Discovery MI PET/CT (General Electric Healthcare).

Two different types of SiPM-based PET detectors are currently implemented in the abovementioned three systems. On the one hand there are so called analog SiPM-based detectors and on the other hand digital SiPM-based detectors or Digital Photon Counters (DPC). The analog design incorporates the connection of multiple SiPM arrays together to sum the signals from each SiPM for a summed output (as implemented in the Biograph Vision and the GE Discovery MI PET/CT). The digital approach considers each SiPM separately to achieve a single readout for each SiPM (as used in the Philips Vereos PET/CT) (22).

### **Benefits of digital PET**

The first generation ToF PET/CT systems achieved a system sensitivity of 5-10 kcps/MBq with a timing resolution of 450-600 picoseconds (ps). The sensitivity is largely dependent on the length of the axial field-of-view (FOV), ranging from 16-21 cm. The system spatial resolution of 4 to 5 mm was mostly determined by the use of PMT in combination with somewhat larger detector or crystal element, but also linked to the available sensitivity and acceptable clinical scan durations. For improved spatial resolution, a substantial increase in sensitivity (i.e., count statistics) would have been required to maintain similar noise levels (24).

With the introduction of digital PET/CT systems, ToF improved to a range of 210-400 ps because of implementation of SiPMs with superior coincidence timing compared with PMTs, and an increased sensitivity of up to 20 kcps/MBq due to a longer axial FOV was achieved (18,24). Because of the compact size of SiPM-based detector

elements, crystals of less than 4x4 mm in cross section could be used allowing improved spatial resolution. The improved physical performance characteristics translated to a more sensitive and efficient use of digital PET systems in clinics.

The increased spatial resolution, providing higher measured contrast, combined with a higher sensitivity and improved ToF result in better noise properties. Consequently, improved imaging capabilities of digital PET systems can be used to obtain comparable image quality with a factor 3 shorter scan time (or reduced radiotracer activity) (24,25). Alternatively, improved imaging performance can be used to obtain images with better image quality which may lead to improved clinical diagnostic capabilities, especially for detecting small (tumor) lesions.

## LAFOV PET

The latest development in PET/CT system design has been the introduction of the 'total body' PET system, i.e., long axial FOV (LAFOV) PET system, which holds promising opportunities for future research and patient care. Also equipped with SiPM-based detectors, these systems surround the patient with many more detectors in the axial FOV direction which comes with two major improvements (26):

1. Longer axial extent of the FOV resulting in higher detection efficiency as more photon pairs are captured.
2. One bed position covers a much larger proportion of the patient, thus the same time frame can cover more anatomy.

Three LAFOV systems have so far been introduced. These are the PennPET Explorer (University of Pennsylvania) (27,28) with a 64-cm-long axial FOV, the uEXPLORER (United Imaging Healthcare) (29) which has a 194-cm-long axial FOV, and the Siemens Biograph Vision Quadra PET/CT (Siemens Healthineers) (30) with a 106-cm-long axial FOV.

The substantially increased sensitivity of LAFOV PET systems will allow an even larger reduction in scan time and/or amount of radiotracer administration with respect to digital PET systems, but these systems come with many other opportunities yet to be explored (31,32).

## Quantification

### SUV

Acquired PET images can be interpreted visually, e.g., for staging, or semi-quantitatively, e.g. to determine treatment-response, which requires standardized and harmonized imaging procedures, especially in a multicenter setting (33). The semi-quantitative standardized uptake value (SUV) of  $^{18}\text{F}$ -FDG, derived from static images obtained at 60 minutes postinjection (p.i.), is most commonly used as a

surrogate of metabolic activity for tumor uptake quantification (5,34). To quantify treatment response, patients are classified into response categories based on the relative SUV measurement change; response categories include complete response, partial response, stable disease, and progressive disease. Subsequently, clinical treatment decisions and a prediction of clinical outcome can be guided by these response classifications (35).

When procedure guidelines for standardized tumor imaging such as the European Association of Nuclear Medicine (EANM) procedure guidelines with standardized protocols regarding patient preparation, PET image acquisition, reconstruction settings, and analysis methods are followed, repeatable and reproducible PET acquisition is facilitated (4,34). Subsequently, PET images can be converted reliably to SUV (for most clinical cases) normalizing the radioactive activity concentration as visualized in the image by body weight and amount of injected tracer dose according to Eq. 8:

$$SUV_{BW} = \frac{c_t[kBq/mL]}{Dose[MBq]/weight[kg]} \quad Eq. 8$$

Here,  $SUV_{BW}$  represents the calculated SUV corrected for bodyweight,  $c_t$  is the measured concentration of the tracer in tissue, and the denominator contains the injected dose in MBq and the subject's weight in kg. Herein, bodyweight can sometimes be replaced by body surface area, lean body mass (SUL), or BMI. Using SUV as a metric of relative tissue uptake normalized to the average radioactivity concentration in the body facilitates longitudinal intrapatient- as well as interpatient comparisons (36).

SUV and other PET image biomarkers can be obtained after segmenting a volume of interest (VOI), in tumor lesions or background tissue. Three most commonly derived SUV are  $SUV_{max}$ ,  $SUV_{peak}$ , and  $SUV_{mean}$ .  $SUV_{max}$  represents the highest uptake of a single voxel in the VOI.  $SUV_{peak}$  represents the highest average uptake in a 1 mL area in the defined VOI and  $SUV_{mean}$  is simply the VOI's average SUV (35). Because  $SUV_{max}$  is a single voxel value, it is adversely affected by noise (37,38) leading to quantitative uncertainty. As  $SUV_{peak}$  represents the average SUV in a small fixed-size VOI centered on the highest-uptake part of the total segmented (tumor lesion) VOI, it has been suggested as a more robust alternative (33). However, both  $SUV_{max}$  and  $SUV_{peak}$  are less observer dependent than  $SUV_{mean}$ .  $SUV_{mean}$  requires reproducible segmentations because it depends on the total VOI, i.e., it depends on the observers' manual or semi-automated VOI definition.

Standard PET-based segmentation methods to define tumor VOIs and derive PET

---

image biomarkers, such as SUV, include manual segmentation or semi-automated segmentation. Where manual segmentations can be labor- and time-intensive, and prone to both intra- and interobserver variability, a single widely available and accepted semi-automated method is currently lacking. The EANM Research Limited (EARL) guidelines (34) recommend segmentations based on fixed SUV VOI thresholds of 2.5 or 4.0 g/mL, 41% or 50% of the lesion's  $SUV_{max}$ , and 50% of the lesion's  $SUV_{peak}$  adjusted for background uptake (39-41).

### Patlak

Simplicity and use of an easy static imaging procedure are two of the most important benefits of using SUV, however, measurements are also vulnerable to unwanted variability (37,42). Following standardization methods, such as the EANM procedure guidelines for tumor imaging, can mitigate SUV variability to a great extent (34,43,44). However, these standardization methods are not able to account for changes in plasma kinetics, due to e.g., treatment, or distinguish between specific and nonspecific uptake possibly causing a dissociation between inaccurate SUV measurements and actual tumor metabolic activity (45-48). In contrast, dynamic whole body  $^{18}F$ -FDG PET imaging is able to include this information as it allows spatiotemporal activity concentration measurement, providing voxel-wise metabolic information, i.e., the  $^{18}F$ -FDG influx rate constant ( $K_i$ ), after applying full kinetic- or Patlak analyses (49-51). In order to generate whole body parametric PET images, the slow kinetics of  $^{18}F$ -FDG require scanning for at least a duration of 45 to 60 min (52).

In current clinical practice, there are two ways to acquire whole body dynamic PET images noninvasively:

1. On a Biograph Vision PET/CT system where a combined acquisition of first 6 min of dynamic imaging over the heart, to obtain the arterial image derived input function (IDIF), followed by multiple whole body sweeps up to 60 min p.i.
2. On an LAFOV system where the long axial coverage captures the heart, to derive the IDIF, and all other organs of interest, including possible tumor lesions, within a single bed position.

For the analysis, a VOI is typically placed in the ascending aorta (53) to obtain the IDIF. Then, to determine  $K_i$  and the total blood distribution volume  $V$ , the measured tissue time-activity curve (TAC) from the PET image and the IDIF serve as input for a voxel-wise Patlak analysis according to Eq. 9 (54):

$$\frac{C(t_n)}{C_P(t_n)} = K_i \frac{\int_0^{t_n} C_P(\tau) d\tau}{C_P(t_n)} + V, t_n > t^*, n = 1 \dots N \quad Eq. 9$$

Where  $C(t)$  is the measured TAC at each voxel,  $C_P(t)$  the IDIF, and  $t_n$  with  $n=1 \dots N$

represents the mid-time points for the  $N$  dynamic PET frames.  $t^*$  is the time after which relative kinetic equilibrium between blood and the reversible compartment is assumed, i.e., when the Patlak plot becomes linear.

With regard to clinical advantages of whole body dynamic Patlak imaging over conventional static scans, parametric images can provide complementary information to standard SUV images, or rather filter information by deleting intravascular contributions to the PET signal, enabling easier detection and classification of small  $^{18}\text{F}$ -FDG avid lesions, particularly in high background uptake regions, such as the liver (55,56). However, new generation PET systems, including LAFOV systems, allow standard whole body static scans of less than 2 min (28,57,58). Including patient positioning and acquisition of a CT, this could lead to a total examination time of approximately 10 to 15 min. Taking into account patient comfort and desired patient throughput at different PET centers, dynamic whole body Patlak imaging may not be suitable for all patient studies; for diagnostics and staging, a simple static scan would do. However, for select patient groups, additional information to more accurately monitor treatment response may be required, especially when comparing to a baseline scan. In those cases  $^{18}\text{F}$ -FDG blood clearance changes may affect SUV-based quantification (45,48,56,59,60).

### Thesis aim

The aim of this thesis is to characterize the performance two innovative newly introduced PET/CT systems and to highlight the benefits and opportunities of these new PET/CT system technologies for direct clinical application and future scientific research.

### Thesis outline

This thesis starts with an extended introduction on digital PET. **Chapter 2** describes the technical principles regarding digital PET/CT systems, summarizes the performance characteristics for the three different commercially available systems, and reports on the resulting image quality, lesion detectability, and possibilities to reduce scan duration and/or lower the amount of radiotracer administration.

In 2018, the University Medical Center Groningen installed, as the first imaging facility worldwide, the digital SiPM-based Biograph Vision PET/CT (Siemens Healthineers). Therefore, **Chapter 3** evaluates PET/CT system performance conform the NEMA NU 2-2012 standard (61) with additional measurements described in the (at the time of study still unpublished) NEMA NU 2-2018 standard (62). Measurements were directly compared to results from its analog predecessor, the PMT-based Biograph mCT PET/CT (Siemens Healthineers), using existing literature.

**Chapter 4** continues on the work described in the previous chapter evaluating initial clinical experiences with the digital Biograph Vision PET/CT in terms of perceived image quality and semi-quantitative analysis in comparison with the Biograph mCT. To this aim, 20 oncological patients underwent a dual  $^{18}\text{F}$ -FDG PET/CT imaging protocol including a scan on both systems. Images were blindly reviewed by three nuclear medicine physicians, and semiquantitative analysis was performed on lesions and healthy tissues for comparison between systems.

Progressing on the foregoing chapter, **Chapter 5** aims to evaluate the effects of reduced scan duration in oncological  $^{18}\text{F}$ -FDG PET imaging on semiquantitative and subjective imaging parameters and its influence on clinical image reading. For this study, 30 patients underwent a 180 seconds per bed/position listmode PET acquisition which were subsequently reprocessed into additional images obtained with shorter scan durations. Semiquantitative lesion and healthy tissue uptake measurements were performed on each of the reconstructed images and image quality was visually evaluated by three nuclear medicine physicians.

**Chapter 6** focuses on image quality and activity optimization using  $^{89}\text{Zr}$  labeled mAb PET tracers. The difference in semiquantitative performance between the Biograph mCT and the Biograph Vision PET/CT was investigated. Hereto, 5 patients underwent immunoPET imaging on both systems and images were semi quantitatively analyzed through segmentation of tumor lesion(s) and healthy tissues. Furthermore, the effects of reducing scan duration using the Biograph Vision PET/CT on semiquantitative imaging parameters and its influence on visual image quality assessment were evaluated. Listmode PET data obtained from 15 patients, which were subsequently reprocessed to obtain images at shorter scan durations, were semiquantitatively analyzed and image quality was visually evaluated by three nuclear medicine physicians.

In 2021, the University Medical Center Groningen installed the LAFOV Biograph Vision Quadra PET/CT system (Siemens Healthineers). To provide the nuclear medicine field with a first impression of the improved image quality obtained with such a high-sensitivity system, **Chapter 7** showcases  $^{89}\text{Zr}$  immunoPET images of two patients obtained with the Biograph Vision Quadra PET/CT. For a complete overview, and a direct comparison of image quality, these two patients underwent a dual imaging protocol including one scan on the LAFOV Biograph Vision Quadra and the other scan on either the conventional analog Biograph mCT or digital Biograph Vision PET/CT system.

To test the new LAFOV system's compliance to current EARL standards for  $^{18}\text{F}$ -FDG tumor imaging (specified for conventional FOV PET systems) to facilitate multicenter research and harmonized clinical use, **Chapter 8** presents EARL phantom measurements with additional tests at various locations throughout the LAFOV and the use of shorter scan durations. Furthermore, clinical PET data of 10 oncological patients were collected to further explore and validate the effects of reducing scan duration on semiquantitative PET image biomarker accuracy and precision when using EARL-compliant reconstruction settings.

Since quantitative accuracy of SUV can be influenced by changes in plasma kinetics, e.g., due to treatment, and SUV derived from static images cannot distinguish between specific and nonspecific uptake, which are issues that could be overcome by dynamic  $^{18}\text{F}$ -FDG whole body (Patlak) imaging, **Chapter 9** focuses on this full quantitative imaging method. This study aims to reduce the total examination time of dynamic  $^{18}\text{F}$ -FDG whole body (Patlak) imaging, with data simulations, from up to 75 min to 30-60 min p.i. using a population averaged input function.

**Chapter 10** continues on the previous chapter by validating the use of a population-averaged input function to reduce examination time of the dynamic  $^{18}\text{F}$ -FDG whole body (Patlak) imaging procedure with dynamic whole body  $^{18}\text{F}$ -FDG PET data obtained using the LAFOV Biograph Vision Quadra PET/CT system. To this aim, twelve patients with suspected lung malignancy were included and underwent a 65 min dynamic PET acquisition. Full quantitative Patlak analysis was performed on both the entire 65 min scans, as well as on various shortened scan durations, using a population-averaged input function for comparison.

**Chapter 11** provides an overview of potential future research directions, potential developments in photon detection technology, and (more cost-effective) hardware developments in PET detectors.

**Chapters 12 and 13** present an English and Dutch summary (Nederlandse samenvatting) of the research described in this thesis, respectively.

## References

1. Jones T, Townsend D. History and future technical innovation in positron emission tomography. *J Med Imaging*. 2017;4:011013.
2. Berg E, Cherry SR. Innovations in instrumentation for Positron Emission Tomography. *Semin Nuc Med*. 2018;48:311-31.
3. Shukla AK, Kumar U. Positron emission tomography: an overview. *J Med Phys*. 2006;31:13-21.
4. Boellaard R, O'Doherty MJ, Weber WA, Mottaghy FM, Lonsdale MN, Stroobants SG, et al. FDG PET and PET/CT: EANM procedure guidelines for tumour PET imaging: version 1.0. *Eur J Nucl Med Mol Imaging*. 2010;37:181-200.
5. Juweid ME, Cheson BD. Positron-Emission Tomography and assessment of cancer therapy. *N Engl J Med*. 2006;354:496-507.
6. Basu S, Hess S, Braad PN. The basic principles of FDG-PET/CT Imaging. *PET Clin*. 2014;9:355-70.
7. Fletcher JW, Djulbegovic B, Soares HP, Siegel BA, Lowe VJ, Lyman GH, et al. Recommendations on the use of  $^{18}\text{F}$ -FDG PET in oncology. *J Nucl Med*. 2008;49:480-508.
8. Avril NE, Weber WA. Monitoring response to treatment in patients utilizing PET. *Radiol Clin North Am*. 2005;43:189-204.
9. Bastiaannet E, Groen B, Jager PL, Cobben DCP, van der Graaf WTA, Vaalburg W, et al. The value of FDG-PET in the detection, grading and response to therapy of soft tissue and bone sarcomas; a systematic review and meta-analysis. *Cancer Treat Rev*. 2004;30:83-101.
10. de Geus-Oei LF, Van Der Heijden HFM, Corstens FHM, Oyen WJG. Predictive and prognostic value of FDG-PET in nonsmall-cell lung cancer. A systematic review. *Cancer*. 2007;110:1654-64.
11. van De Watering FCJ, Rijpkema M, Perk L, Brinkmann U, Oyen WJG, Boerman OC. Zirconium-89 labeled antibodies: a new tool for molecular imaging in cancer patients. *Biomed Res Int*. 2014;203601.
12. Severin GW, Engle JW, Nickles RJ, Barnhart TE.  $^{89}\text{Zr}$  Radiochemistry for PET. *Med Chem*. 2015;7:389-94.
13. Zhang Y, Hong H, Cai W. PET tracers based on zirconium-89. *Curr Radiopharm*. 2011;4:131-9.
14. Jauw YWS, Menke-van der Houven van Oordt CW, Hoekstra OS, Hendrikse HN, Vugts DJ, Zijlstra JM, et al. Immuno-positron emission tomography with zirconium-89-labeled monoclonal antibodies in oncology: What can we learn from initial clinical trials? *Front Pharmacol*. 2016;7:1-15.
15. Conti M, Eriksson L. Physics of pure and non-pure positron emitters for PET: a review and a discussion. *EJNMMI Phys*. 2016;3:3-8.
16. Surti S. Update on Time-of-Flight PET Imaging. *J Nucl Med*. 2015;56:98-105.
17. van der Vos CS, Koopman D, Rijnsdorp S, Arends AJ, Boellaard R, van Dalen JA, et al. Quantification, improvement, and harmonization of small lesion detection with state-of-the-art PET. *Eur J Nucl Med Mol Imaging*. 2017;44:4-16.

18. Hutton BF, Erlandsson K, Thielemans K. Advances in clinical molecular imaging instrumentation. *Clin Transl Imaging*. 2018;6:31-45.
19. Conti M, Eriksson L, Westerwoudt V. Estimating image quality for future generations of TOF PET scanners. *IEEE Trans Nucl Sci*. 2013;60:87-94.
20. Karp JS, Surti S, Daube-Witherspoon ME, Muehllehner G. The benefit of time-of-flight in PET imaging: experimental and clinical results. *J Nucl Med*. 2015;6:790-5.
21. Vandenberghe S, Mikhaylova E, D'Hoe E, Mollet P, Karp JS. Recent developments in time-of-flight PET. *EJNMMI Phys*. 2016;3:3.
22. Slomka PJ, Pan T, Germano G. Recent advances and future progress in PET instrumentation. *Semin Nucl Med*. 2016;46:5-19.
23. Rausch I, Ruiz A, Valverde-Pascual I, Cal-González J, Beyer T, Carrio I. Performance evaluation of the Philips Vereos PET/CT System according to the NEMA NU2-2012 standard. *J Nucl Med*. 2018;60:561-7.
24. Surti S, Viswanath V, Daube-Witherspoon ME, Conti M, Casey ME, Karp JS. Benefit of improved performance with state-of-the art digital PET/CT for lesion detection in oncology. *Nucl Med*. 2020;61:1684-90.
25. van Sluis J, Boellaard R, Dierckx RAJO, Stormezand GN, Glaudemans AWJM, Noordzij W. Image quality and activity optimization in oncologic  $^{18}\text{F}$ -FDG PET using the digital Biograph Vision PET/CT system. *J Nucl Med*. 2020;61:764-71.
26. Vandenberghe S, Moskal P, Karp JS. State of the art in total body PET. *EJNMMI Phys*. 2020;7:35.
27. Karp JS, Viswanath V, Geagan MJ, Muehllehner G, Pantel AR, Parma MJ, et al. PennPET explorer: Design and preliminary performance of a whole-body imager. *J Nucl Med*. 2020;61:136-43.
28. Pantel AR, Viswanath V, Daube-witherspoon ME, Dubroff JG, Muehllehner G, Parma MJ, et al. PennPET Explorer: human imaging on a Whole-Body imager. *J Nucl Med*. 2020;61:144-51.
29. Spencer BA, Berg E, Schmall JP, Omidvari N, Leung EK, Abdelhafez YG, et al. Performance evaluation of the uEXPLORER Total-body PET/CT scanner based on NEMA NU 2-2018 with additional tests to characterize long axial field-of-view PET scanners. *J Nucl Med*. 2021;62:861-70.
30. Conti M, Aykac M, Bal H, Bendrien B, Bharkhada D, Cabello J, et al. Simulation and first measurements of a prototype ultra-long FOV PET/CT scanner. *Eur Assoc Nucl Med Annu Conf*. 2020;[abstract](OP-230):supplement 1.
31. Slart RHJA, Tsoumpas C, Glaudemans AWJM, Noordzij W, Willemsen ATM, Borra RJH, et al. Long axial field of view PET scanners: a road map to implementation and new possibilities. *Eur J Nucl Med Mol Imaging*. 2021;48:4236-45.
32. Surti S, Pantel AR, Karp JS. Total body PET: Why, how, what for? *IEEE Trans Radiat Plasma Med Sci*. 2021;4:283-92.
33. Wahl RL, Jacene H, Kasamon Y, Lodge MA. From RECIST to PERCIST: evolving considerations for PET response criteria in solid tumors. *J Nucl Med*. 2009;50:122-51.
34. Boellaard R, Delgado-Bolton R, Oyen WJG, Giammarile F, Tatsch K, Eschner W, et al. FDG PET/

- CT: EANM procedure guidelines for tumour imaging: version 2.0. *Eur J Nucl Med Mol Imaging*. 2014;42:328-54.
35. Vanderhoek M, Perlman SB, Jeraj R. Impact of the definition of peak standardized uptake value on quantification of treatment response. *J Nucl Med*. 2012;53:4-11.
36. Kinahan PE, Fletcher JW. PET/CT Standardized Uptake Values (SUVs) in clinical practice and assessing response to therapy. *Semin Ultrasound CT MR*. 2011;31:496-505.
37. Boellaard R, Krak NC, Hoekstra OS, Lammertsma AA. Effects of noise, image resolution, and ROI definition on the accuracy of standard uptake values: a simulation study. *J Nucl Med*. 2004;45:1519-27.
38. Krak NC, Boellaard R, Hoekstra OS, Twisk JWR, Hoekstra CJ, Lammertsma AA. Effects of ROI definition and reconstruction method on quantitative outcome and applicability in a response monitoring trial. *Eur J Nucl Med Mol Imaging*. 2005;32:294-301.
39. Frings V, De Langen AJ, Smit EF, Van Velden FHP, Hoekstra OS, Van Tinteren H, et al. Repeatability of metabolically active volume measurements with  $^{18}\text{F}$ -FDG and  $^{18}\text{F}$ -FLT PET in non-small cell lung cancer. *J Nucl Med*. 2010;51:1870-7.
40. Ilyas H, Mikhaeel NG, Dunn JT, Rahman F, Møller H, Smith D, et al. Defining the optimal method for measuring baseline metabolic tumour volume in diffuse large B cell lymphoma. *Eur J Nucl Med Mol Imaging*. 2018;45:1142-54.
41. Cottreau A-S, Hapdey S, Chartier L, Modzelewski R, Casanovas O, Itti E, et al. Baseline total metabolic tumor volume measured with fixed or different adaptive thresholding methods equally predicts outcome in peripheral T Cell Lymphoma. *J Nucl Med*. 2017;58:276-81.
42. Adams MC, Turkington TG, Wilson JM, Wong TZ. A systematic review of the factors affecting accuracy of SUV measurements. *Am J Roentgenol*. 2010;195:310-20.
43. Weber WA. Use of PET for monitoring cancer therapy and for predicting outcome. *J Nucl Med*. 2005;46:983-95.
44. Shankar LK, Hoffman JM, Bacharach S, Graham MM, Karp J, Lammertsma AA, et al. Consensus recommendations for the use of  $^{18}\text{F}$ -FDG PET as an indicator of therapeutic response in patients in National Cancer Institute Trials. *J Nucl Med*. 2006;47:1059-66.
45. Freedman NMT, Sundaram SK, Kurdziel K, Carrasquillo JA, Whatley M, Carson JM, et al. Comparison of SUV and Patlak slope for monitoring of cancer therapy using serial PET scans. *Eur J Nucl Med Mol Imaging*. 2003;30:46-53.
46. Huang SC. Anatomy of SUV. *Nucl Med Biol*. 2000;27:643-6.
47. Lammertsma AA, Hoekstra CJ, Giaccone G, Hoekstra OS. How should we analyse FDG PET studies for monitoring tumour response? *Eur J Nucl Med Mol Imaging*. 2006;33:S16-21.
48. Lammertsma AA. Forward to the past: the case for quantitative PET imaging. *J Nucl Med*. 2017;58:1019-24.
49. Karakatsanis NA, Lodge MA, Tahari AK, Zhou Y, Wahl RL, Rahmim A. Dynamic whole body PET parametric imaging: I. Concept, acquisition protocol optimization and clinical application. *Phys Med Biol*. 2014;49:1012-6.
50. Karakatsanis NA, Zhou Y, Lodge MA, Casey ME, Wahl RL, Zaidi H, et al. Generalized whole-

- body patlak parametric imaging for enhanced quantification in clinical PET. *Phys Med Biol.* 2015;60:8643-73.
51. Patlak CS, Blasberg RG. Graphical evaluation of blood-to-brain transfer constants from multiple-time uptake data. Generalizations. *J Cereb Blood Flow Metab.* 1985;5:584-90.
  52. Karakatsanis NA, Casey ME, Lodge MA, Rahmim A, Zaidi H. Whole-body direct 4D parametric PET imaging employing nested generalized Patlak expectation-maximization reconstruction. *Phys Med Biol.* 2016;61:5456-85.
  53. Weerd AP Van Der, Klein LJ, Boellaard R, Visser CA, Visser FC, Lammertsma AA. Image-derived input functions for determination of MRGlu in cardiac  $^{18}\text{F}$ -FDG PET scans. *J Nucl Med.* 2001;42:1622-9.
  54. Patlak CS, Blasberg RG. Graphical evaluation of blood-to-brain transfer constants from multiple-time uptake data. *J Cereb Blood Flow Metab.* 1983;5:584-90.
  55. Dias AH, Pedersen MF, Danielsen H, Munk OL, Gormsen LC. Clinical feasibility and impact of fully automated multiparametric PET imaging using direct Patlak reconstruction: evaluation of 103 dynamic whole-body  $^{18}\text{F}$ -FDG PET/CT scans. *Eur J Nucl Med Mol Imaging.* 2021;48:837-50.
  56. Hoekstra CJ, Hoekstra OS, Stroobants SG, Vansteenkiste J, Nuyts J, Smit EF, et al. Methods to monitor response to chemotherapy in non-small cell lung cancer with  $^{18}\text{F}$ -FDG PET. *J Nucl Med.* 2002;43:1304-9.
  57. Alberts I, Hünermund J, Prenosil G, Mingels C, Bohn KP, Viscione M, et al. Clinical performance of long axial field of view PET / CT : a head-to-head intra-individual comparison of the Biograph Vision Quadra with the Biograph Vision PET / CT. *Eur J Nucl Med Mol Imaging.* 2021;48:2395-404.
  58. Hu P, Zhang Y, Yu H, Chen S, Tan H, Qi C, et al. Total-body  $^{18}\text{F}$ -FDG PET/CT scan in oncology patients: how fast could it be? *Eur J Nucl Med Mol Imaging.* 2021;48:2384-94.
  59. Cheebsumon P, Velasquez LM, Hoekstra CJ, Hayes W, Kloet RW, Hoetjes NJ, et al. Measuring response to therapy using FDG PET: semi-quantitative and full kinetic analysis. *Eur J Nucl Med Mol Imaging.* 2011;38:832-42.
  60. Doot RK, Pierce LA, Byrd D, Elston B, Allberg KC, Kinahan PE. Biases in multicenter longitudinal PET standardized uptake value measurements. *Transl Oncol.* 2014;7:48-54.
  61. National Electrical Manufacturers Assoc. Performance measurements of positron emission tomographs. National Electrical Manufacturers Association. Rosslyn, VA, USA. NEMA Standards Publication NU 2-2012;2012.
  62. National Electrical Manufacturers Assoc. Performance measurements of positron emission tomographs. National Electrical Manufacturers Association. Rosslyn, VA, USA. NEMA Standards Publication NU 2-2018; 2018.





# Chapter 2

---

## Digital PET systems

Joyce van Sluis<sup>1</sup>, Adrienne H. Brouwers<sup>1</sup>, Ronald Boellaard<sup>1,2</sup>, and Walter Noordzij<sup>1</sup>

<sup>1</sup>Department of Nuclear Medicine and Molecular Imaging, University of Groningen, University Medical Center Groningen, Hanzeplein 1, 9713 GZ Groningen, The Netherlands

<sup>2</sup>Department of Radiology and Nuclear Medicine, Cancer Center Amsterdam, Amsterdam University Medical Centers, Free University of Amsterdam, De Boelelaan 1117, 1081 HV Amsterdam, The Netherlands

*Book chapter 'Digital PET systems' in Encyclopaedia of Nuclear Medicine, Volume 1. Basic concepts, radiopharmacy, and instrumentation. Elsevier. 2022;408-415.*



## **Abstract**

In the past decades, the main development in positron emission tomography (PET) technology has been detector design, specifically the adoption of solid-state technology. Conventional photomultiplier tubes have been replaced by compact detector elements commonly referred to as silicon-photomultipliers (SiPMs). At present, there are three commercially available PET/CT systems equipped with SiPM-based detectors. These so-called ‘digital’ PET/CT systems are the Philips Vereos PET/CT (Philips Healthcare), the Siemens Biograph Vision PET/CT (Siemens Healthineers), and the GE Discovery MI PET/CT (General Electric Healthcare). This chapter on digital PET describes the technical principles regarding digital PET/CT systems, summarizes the performance characteristics for the three different systems, and reports on the resulting image quality, lesion detectability, and possibilities to reduce scan duration and/or lower the amount of radiotracer administration.

## **Introduction**

Over the last decades, the main development in positron emission tomography (PET) detector design has been the adoption of solid-state technology (1). Conventional photomultiplier tubes (PMTs) have been replaced by solid-state read-out devices in recently introduced commercially available PET/CT systems. This detector technology has the advantage of being compact, but its insensitivity to a magnetic field makes it well-suited for PET coupled with Magnetic Resonance Imaging as well. The first clinical PET/MRI systems manufactured by Siemens (Siemens Healthineers) were equipped with avalanche photodiodes (APDs). More recently, further development of APDs resulted in the introduction of silicon-photomultipliers (SiPMs) which are implemented in the latest clinical PET/CT systems.

An APD is formed by a silicon p-n junction creating a depletion region free of mobile charge carriers. When a 511-keV photon is absorbed in a light-sensitive layer, silicon, an electron-hole pair is created (photo-electric effect). When applying a reverse bias to the photodiode, an electric field will be created across the depletion region causing these charge carriers to be accelerated towards the anode (holes), or cathode (electrons). This way, an absorbed photon will result in a net flow of current in a reverse-biased APD.

The applied electric field causes acceleration of electrons which in turn produce a secondary ionization, or avalanche, resulting in amplification of the electric signal. However this gain is not as high as with conventional PMTs. The slow rise time of the signal makes APDs unsuitable for implementation of time-of-flight (ToF). In ToF PET, the difference in the arrival times of the two photons on both detectors is

measured with high precision, which helps localize the point of annihilation (with a certain probability) along the line of response (2).

However, when the applied reverse-bias voltage is increased sufficiently (approaching the breakdown voltage) a created charge carrier will be accelerated to such an extent that it carries sufficient kinetic energy to create secondary charge pairs; this process is referred to as impact ionization. Accordingly, a single absorbed photon can trigger a self-perpetuating ionization cascade spreading through the silicon volume subjected to the electric field. Breakdown of the silicon occurs making it conductive, effectively amplifying the original electron-hole pair into a macroscopic current flow. This is called Geiger discharge; the APD operates in Geiger mode. Then, a single incoming light photon produces a large signal and the device is referred to as a single-photon avalanche diode (SPAD) of very compact size (10-100  $\mu\text{m}$ ) (3,4). Once a current is flowing it should be stopped or 'quenched'. Passive quenching is achieved through using a series of resistors which limit the current drawn by the diode during breakdown. This lowers the reverse voltage seen by the diode to a value below its breakdown voltage. The diode is then available to detect subsequent photons. Through this mechanism, a single SPAD functions as a photon-triggered switch, in either 'on' or 'off' state, resulting in a binary output. Proportional information regarding the photon flux is not available. This lack of proportionality is overcome in the SiPM. An SiPM is comprised of an array of (between 100 and 10000) SPADs which are read-out in parallel producing an electric signal proportional to the number of detected 511-keV photons in a small detector area (cell). The gain and detection efficiency is comparable to conventional PMTs while using a smaller operating voltage and running at a higher speed. An array of SiPMs can be used instead of the conventional array of PMTs (1).

Currently, there are three different commercially available 'digital' PET/CTs available which are equipped with SiPM-based PET detectors: the Siemens Biograph Vision PET/CT (Siemens Healthineers), the Philips Vereos PET/CT (Philips Healthcare), the GE Discovery MI PET/CT (General Electric Healthcare). Two different types of SiPM-based PET detectors are currently implemented in the abovementioned three systems. On the one hand there are so called analog SiPM-based detectors and on the other hand digital SiPM-based detectors or Digital Photon Counters (DPC).

The analog design incorporates the connection of multiple SiPM arrays together to sum the signals from each SiPM for a summed output (as implemented in the Biograph Vision and the GE Discovery MI PET/CT). The digital approach considers each SiPM separately to achieve a single readout for each SiPM (as used in the Philips Vereos PET/CT) (3).

## **Three digital PET/CT vendors**

The Siemens Biograph Vision PET/CT, the Philips Vereos PET/CT, and the GE Discovery MI PET/CT are presently the three commercially available systems equipped with SiPM-based detectors; so-called ‘digital’ PET/CT systems. Their system specific technical properties and associated performance characteristics will be described in the subsections below.

### **System features**

#### *The Philips Vereos PET/CT*

The whole body Philips Vereos PET/CT is a SiPM-based PET system coupled with a 64-slice helical CT scanner. The PET component of the Philips Vereos PET/CT consists of 18 detector elements arranged cylindrically into a single ring measuring 76.4 cm in diameter covering an axial length of 16.4 cm. A detector element consists of an array of 40 x 32 lutetium-yttrium-oxorthosilicate (LYSO) crystals (each crystal is 4 x 4 x 19 mm), which are individually coupled to SiPM detectors (1-to-1 coupling). An SiPM consists of 3200 APDs operated in Geiger mode. The arriving scintillation photons are read-out individually which is also known as digital SiPM or Digital Photon Counting (4,5).

#### *The Siemens Biograph Vision PET/CT*

The Siemens Biograph Vision PET/CT combines a 128-slice CT scanner with a whole body lutetium oxyorthosilicate PET system. The system has a 78-cm bore and the PET component contains 8 detector rings including 19 detector electronics assembly (DEA) units to form a ring; two adjacent detector blocks per DEA unit result in 38 blocks per ring. Each detector block contains a 4 x 2 arrangement of mini blocks which consist of a 5 x 5 array of 3.2 x 3.2 x 20 mm crystals coupled to an SiPM array of 16 x 16 mm. The arrangement of 4 x 2 miniblocks results in a 32-mm axial field-of-view (FOV) for 1 block. The system configuration which uses 8 blocks in the axial direction, results in a 25.6-cm axial FOV, or 26.1 cm including the spaces between the blocks. The detected photons are summed per SiPM detector to form a discrete output signal.

#### *The GE Discovery MI PET/CT*

The Discovery MI combines a 128-slice CT component with a 4-ring PET LYSO system providing a 20-cm axial FOV; a 3-ring configuration of this system is also available, however this book chapter only focuses on the 4-ring system with a larger axial FOV. Each PET ring uses 136 detector blocks, each of which comprises a 4 x 9 array of crystals coupled to a 3 x 6 array of SiPMs. The crystal elements are 4.0 x 5.3 x 25 mm, and each SiPM array is composed of 2 x 3 pixels with an active area

of 4 x 6 mm. Like in the Siemens Biograph Vision PET/CT the detected photons are summed per SiPM detector to form a discrete output signal.

## Performance characteristics

Evaluation of physical performance of PET systems is done according to NEMA standards published by the National Electrical Manufacturers Association. Performance measurements in the three currently available digital PET/CT systems were performed following the NEMA NU 2-2012 standard (6) and the NEMA NU 2-2018 standard (7). These performance measurements include spatial resolution, scatter fraction, sensitivity, count rate performance, image quality, coregistration accuracy, and timing resolution. An overview of the performance characteristics in terms of spatial resolution, sensitivity, count rate accuracy, scatter fraction, ToF performance, and coregistration error for the three digital systems is provided in Table 1.

**Table 1** Performance characteristics measured according to the NEMA NU 2-2012 and NEMA NU 2-2018 standards compared between systems (part 1).

Parameter	Distance*	Philips Vereos PET/CT (4)		Siemens Biograph Vision PET/CT (8)		GE Discovery MI PET/CT (9)	
		[mm FWHM]	[mm FWHM]	[mm FWHM]	[mm FWHM]	[mm FWHM]	[mm FWHM]
<b>Spatial resolution</b>							
Radial	1	4.3†	8.4†	3.5	6.8	4.0	8.5
	10	4.6	8.9	4.5	8.4	5.3	10.0
	20	5.8	10.4	5.8	10.5	7.5	13.4
Tangential	1	4.3†	8.4†	3.6	6.9	4.0	8.2
	10	4.4	9.0	3.9	7.0	4.2	8.8
	20	4.9	10.0	3.5	6.4	4.7	9.0
Axial	1	4.2	8.8	3.5	7.1	4.4	10.1
	10	4.4	9.1	4.3	8.7	5.6	11.8
	20	4.6	9.2	4.4	9.4	5.7	12.6
<b>Sensitivity [kcps/MBq]</b>							
	0	5.1		16.4		13.4	
	10	5.2		16.3		13.1	
<b>Accuracy [kcps at kbq/mL]</b>							
	Peak NECR	153 at 54.9		306 at 32.6		186 at 21.7	
	Peak true rate	733 at 64.6		1,306 at 54		827 at 34.8	
<b>Scatter fraction [%]</b>							
	At peak NECR	33.9		38.7		40.8	
	At low activity	31.7		37		NA	
<b>ToF resolution [ps]</b>							
		310		210		377	
<b>Coregistration error [mm]</b>							
		NA		1.25		NA	

\*Radial distance [cm] from the center of the FOV

†Average value of radial and tangential measurements

FWHM = full width at half maximum; FWTM = full width at tenth maximum; NA = not applicable



The performance characteristics regarding image contrast recovery and background variability (measured using the image quality phantom filled with a sphere to background ratio of 8:1) compared between systems is shown in Table 2.

**Table 2** Performance characteristics measured according to the NEMA NU 2-2012 and NEMA NU 2-2018 standards compared between systems (part 2).

Parameter	Philips Vereos PET/CT (4)		Siemens Biograph Vision PET/CT (8)		GE Discovery MI PET/CT (9)	
	Contrast [%]	Background variability [%]	Contrast [%]	Background variability [%]	Contrast [%]	Background variability [%]
<b>Sphere diameter</b>						
<i>[mm]</i>						
10	54.4	9.3	86.8	6.0	55.6	10.6
13	75.9	7.5	77.2	5.0	66.5	8.1
17	81.6	5.7	85.0	3.9	80.1	5.8
22	86.5	4.3	89.8	3.3	84.1	4.3
28	82.5	3.5	87.4	3.0	86.9	3.7
37	85.8	2.6	89.6	2.2	91.4	2.9
<b>Average lung residual [%]</b>	6.4		3.5		5.3	

## Image quality

With improved hardware implemented in digital PET/CT systems and associated improved performance characteristics, enhanced image quality of obtained clinical PET/CT acquisitions was expected. Improved image quality is caused by a better ToF (all three systems) and increased sensitivity due to a larger FOV with more axial coverage (Siemens Biograph Vision and GE Discovery MI systems). Different study groups investigated  $^{18}\text{F}$ -FDG PET/CT image quality and lesion detectability in oncology patients for the three PET/CT systems. Data were subsequently compared with a double scan performed on the analog predecessor of the specific system. The results of the studies on image quality for each vendor's digital PET/CT system is described in the subsections below.

## Clinical experiences and comparison with analog PET/CT

### *Philips Vereos PET/CT*

In this comparison study, 21 consecutive patients were included. All patients underwent a single injection of  $^{18}\text{F}$ -FDG activity and a dual-imaging protocol including a clinical PET/CT scan performed using the conventional analog Philips Gemini PET/CT (Philips Healthcare) followed by an acquisition using the digital

Philips Vereos PET/CT system. The obtained images using the digital system were scored significantly higher by two experienced interpreters in a (blinded for system type) side by side comparison regarding overall image quality (10). In 5 of 21 patients, lesions that were seen with the conventional Philips Gemini PET/CT were confirmed using the digital Vereos PET/CT. In addition, the digital system identified 8 additional  $^{18}\text{F}$ -FDG avid lesions initially missed using the conventional analog system. For visual comparison, patient images obtained using the two systems are shown in Figure 1.

Furthermore, semiquantitative analyses showed a significantly higher lesion  $\text{SUV}_{\text{max}}$  obtained from images acquired on the digital Vereos PET/CT; association with time-delay between the paired acquisitions was explored and subsequently ruled out at a 5% significance level (10).

In a similar study, 100 patients were included and underwent double PET/CT acquisitions using the conventional and digital system types after a single injection of  $^{18}\text{F}$ -FDG (11). Three nuclear medicine physicians scored the obtained images regarding image quality and evaluated differences in detectability using the two systems by counting the number of  $^{18}\text{F}$ -FDG avid lesions. In 54 patients, the readers regarded the images obtained using the digital Philips Vereos PET/CT system of improved image quality; in the remaining 46 patients image quality did not differ between systems. With respect to lesion detectability, in only 80 out of the 100 included patients lesions were found, and in 61 out of these 80 patients an equal number of lesions was detected on images obtained using both systems. In the remaining 19 patients, additional lesions were detected on images obtained using the digital Philips Vereos PET/CT compared to images obtained using the conventional Philips Gemini PET/CT (11).

### *Siemens Biograph Vision PET/CT*

In total, 20 consecutive patients referred for an oncologic clinical PET/CT were enrolled in this prospective comparison study. A single weight-based  $^{18}\text{F}$ -FDG injection was administered and patients underwent a dual-imaging protocol including a PET/CT acquisition on the digital Siemens Biograph Vision system and a PET/CT acquisition on the conventional analog Siemens Biograph mCT system (Siemens Healthineers) (12). 60 minutes postinjection, ten patients first underwent a scan on the conventional system immediately followed by the paired acquisition using the Siemens Biograph Vision PET/CT. In the other 10 patients, acquisition order was reversed to control for increase of specific tracer uptake in the tumor over time. PET/CT images were subsequently blindly evaluated by three experienced nuclear medicine physicians who were not aware of both the clinical indication of the

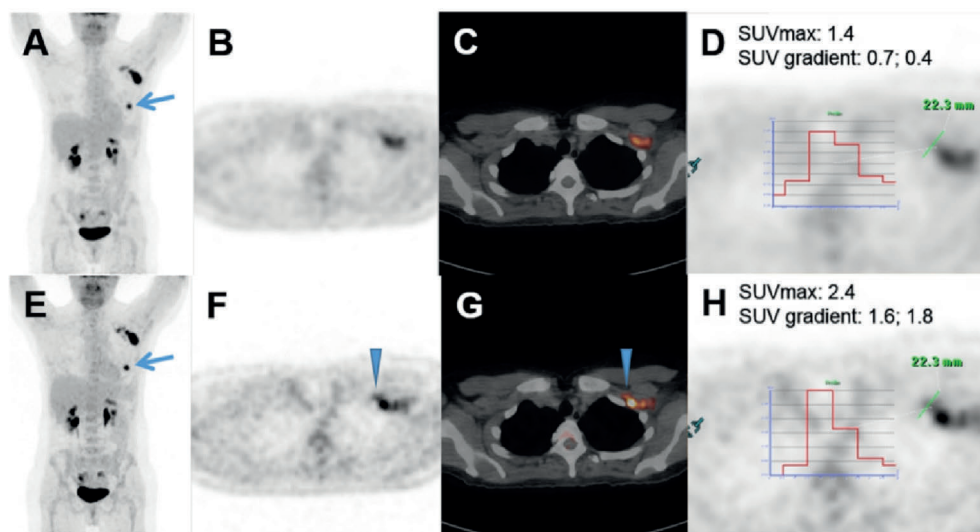


**Figure 1\*** Illustrative patient images obtained using the Philips Gemini PET/CT and the Philips Vereos PET/CT. A 47-year-old female with a history of breast cancer underwent a PET/CT acquisition for initial staging. The images acquired on the conventional Philips Gemini PET/CT are shown in the upper panel: (A) maximum intensity projection PET image showing the  $^{18}\text{F}$ -FDG avid primary breast tumor (arrow); (B) axial PET; (C) fused axial PET/CT; (D) count profile of a level III axillary lymph node.  $^{18}\text{F}$ -FDG avid lymph nodes were found at level I and II of the left axilla, however these were not confirmed as such by the readers. PET/CT staging was  $T_1N_1M_0$  (stage II). The images acquired on the digital Philips Vereos PET/CT are shown in the lower panel: (E) maximum intensity projection PET image; (F) axial PET; (G) fused axial PET/CT; (H) count profile of a level III axillary lymph node. Unlike on the images acquired using the conventional Gemini PET/CT, the readers identified this additional level III lymph node measuring  $0.9 \times 1.3$  cm on the PET/CT (triangle). PET/CT staging was  $T_1N_2M_0$  (stage III); no biopsy was obtained for this lesion. The additional level III lymph node measured a higher  $\text{SUV}_{\text{max}}$  and a sharper demarcation on the images obtained using the digital system (H) compared with images obtained using the conventional analog system (D). Subsequent biopsy of a level I axillary node showed evidence of metastatic disease. \*This figure was originally published in the *J Nucl Med*. Nguyen et al. Image quality and diagnostic performance of a digital PET prototype in patients with oncologic diseases: initial experience and comparison with analog PET. *J Nucl Med*. 2015;56:1378-85.

PET/CT examination and the PET/CT system on which the images were obtained. In addition, the nuclear medicine physicians counted the number of  $^{18}\text{F}$ -FDG avid lesions for assessment of lesion detectability between systems. Regarding semiquantitative analyses, lesion SUVs were obtained from the acquired images and compared between systems.

Images acquired on the Siemens Biograph Vision PET/CT were scored significantly higher on image quality with respect to images acquired using the Siemens Biograph mCT system. Moreover, in 7 out of 20 patients, one or more additional  $^{18}\text{F}$ -FDG avid lesions were found on the images obtained using the digital system which could not

be identified using the conventional analog PET/CT. To illustrate, example patient images are shown in Figure 2. Semiquantitative lesion measurement comparison between images obtained from the two systems showed a slight increase in lesion  $SUV_{max}$  (not significant) when using the Siemens Biograph Vision PET/CT. The slight increase in  $SUV_{max}$  using the digital system can be attributed to a higher spatial resolution and the use of smaller voxel sizes resulting in less partial volume effect and herewith a higher contrast recovery (12).

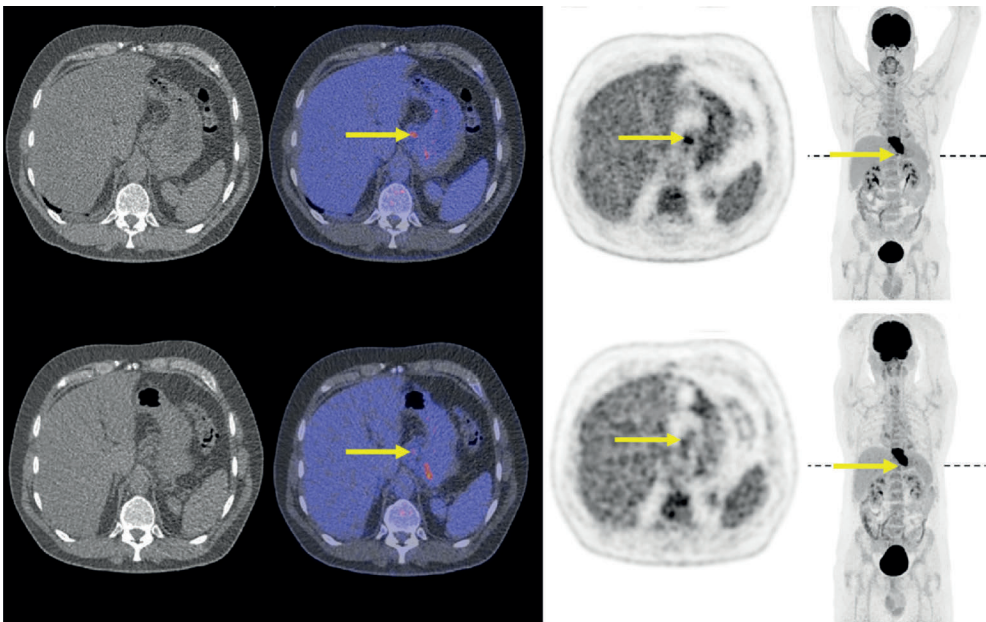


**Figure 2\*** Illustrative patient images obtained using the Siemens Biograph mCT PET/CT and the Siemens Biograph Vision PET/CT. Illustrative transaxial CT, fused PET/CT, PET, and maximum intensity projection PET images (from left to right) acquired on the Siemens Biograph Vision PET/CT (top row) and Siemens Biograph mCT (bottom row) of a 59-year-old male (weight, 106 kg) with metastasized esophageal cancer. The position of the transaxial slice is indicated on the maximum intensity projection PET (dashed line). Arrows indicate a small lesion found on the Siemens Biograph Vision images that did not appear as such on the Siemens Biograph mCT images. \*This figure was originally published in the *J Nucl Med.* van Sluis et al. Image quality and semiquantitative measurements on the Biograph Vision PET/CT system: initial experiences and comparison with the Biograph mCT. *J Nucl Med.* 2020;61:129-35.

### GE Discovery MI PET/CT

A total of 50 oncology patients were enrolled in this image quality comparison study. After a single injection of  $^{18}\text{F}$ -FDG activity, the dual-imaging protocol consisted of a first scan on the conventional PMT-based analog GE Discovery 600 PET/CT or

GE Discovery 690 PET/CT (General Electric Healthcare), followed by a second acquisition on the digital GE Discovery MI PET/CT.

Images obtained using the digital system were scored significantly higher regarding visual image quality than images obtained using the conventional PET/CT by two nuclear medicine physicians that were blinded for the PET/CT system used. In addition, PET/CT scans acquired using the digital GE Discovery MI PET/CT identified all lesions seen on images obtained using the conventional PET/CT system, as well as 37 additional  $^{18}\text{F}$ -FDG avid lesions in 14 out of 50 patients (28%) (13). For illustrative purposes, example patient images are shown in Figure 3. Semiquantitative analyses showed a significant increase in mean lesion  $\text{SUV}_{\text{max}}$ . Increase in  $\text{SUV}_{\text{max}}$  was suggested to be a result of increased sensitivity of the digital system. However, as all acquisitions on the Discovery MI system were performed after conventional PET/CT images were obtained, the increase in  $\text{SUV}_{\text{max}}$  can partially be attributed to increased uptake time and herewith increased lesion-to-background ratio (13).

### **Scan duration and activity reduction**

Due to the increased sensitivity of digital PET/CT systems, shorter scan durations and/or lower activity administrations can be achieved. To which extent the improved performance characteristics of the different digital systems allow such reductions has been explored by different research groups and their results are reported in the subsections below.

#### *Philips Vereos PET/CT*

To date, no clinical studies have been published to test the possibilities of reducing scan time and/or activity administration using the Philips Vereos PET/CT.

#### *Siemens Biograph Vision PET/CT*

In this prospective study, 30 oncological patients were enrolled. Three different malignancies were included to form homogeneous groups for optimal comparison of quantitative parameters (14). PET listmode data were acquired using the Siemens Biograph Vision PET/CT at 180 seconds per bed position (s/bp). Reprocessing of listmode data allows recombination of PET data and timing information which was performed to simulate PET data acquired at reduced scan duration which is equivalent to a lower amount of injected activity; reprocessed listmode data resulted in additional PET images at 10, 30, 60, and 120 s/bp. Patient images illustrating PET data acquired at different scan durations are shown in Figure 4. Images acquired at 60 s/bp were semiquantitatively still comparable to images obtained at 180 s/bp and three nuclear medicine physicians agreed on the diagnostic image quality of the images obtained with a factor 3 reduction in acquisition time (14).

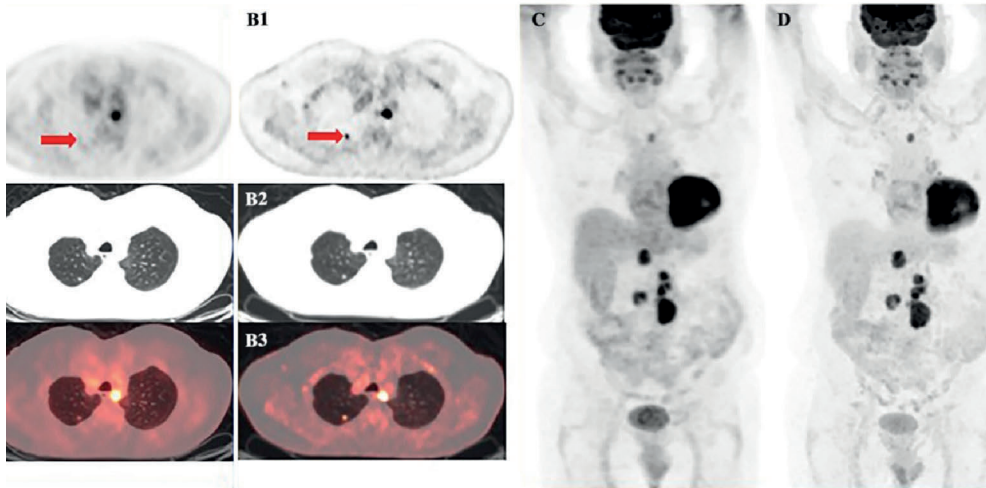


**Figure 3\*** Illustrative patient images obtained using the GE Discovery 690 PET/CT and the GE Discovery MI PET/CT. A 79-year-old-male with renal cancer underwent PET/CT acquisition 34 minutes after conventional PET/CT acquisition, 104 min after  $^{18}\text{F}$ -FDG injection. Discovery MI PET/CT images show a significant increase in  $\text{SUV}_{\text{max}}$  (red arrow). (A1) Axial PET obtained using the Discovery 690 PET/CT; (A2) Axial CT obtained using the Discovery 690 PET/CT; (A3) Axial fused image obtained using the Discovery 690 PET/CT; (B1) Axial PET obtained using the Discovery MI PET/CT; (B2) Axial CT obtained using the Discovery MI PET/CT; (B3) Axial fused image obtained using the Discovery MI PET/CT; (C) maximum-intensity-projection PET image obtained using the Discovery 690 PET/CT; (D) maximum-intensity-projection PET image obtained using the Discovery MI PET/CT. \*This figure was originally published in PLoS one. Baratto et al.  $^{18}\text{F}$ -FDG silicon photomultiplier PET/CT: a pilot study comparing semiquantitative measurements with standard PET/CT. PLoS ONE. 2017.

### GE Discovery MI PET/CT

For this study, a total of 58 oncology patients were enrolled. Patients with different cancer types were included consecutively to capture a realistic clinical representation (15). Listmode data were acquired using the GE Discovery MI PET/CT with a reference standard acquisition time between 180 and 210 s/bp depending on BMI as recommended by the manufacturer. Reprocessing of listmode data resulted in additional PET images at 30, 60, 90, and 120 s/bp. Example patient images acquired using various acquisition times are shown in Figure 5.

A factor of 2 reduction in acquisition time (from 180 to 90 s/bp) retained sufficient image quality as rated blindly by two experienced nuclear medicine physicians (15). Furthermore, semiquantitative analysis performed on a single representative lesion per patient identified by one of the nuclear medicine physicians showed acceptable mean percentage change in lesion  $\text{SUV}_{\text{max}}$  of 0.95% on images acquired 90 s/bp relative to images acquired at 180 s/bp.

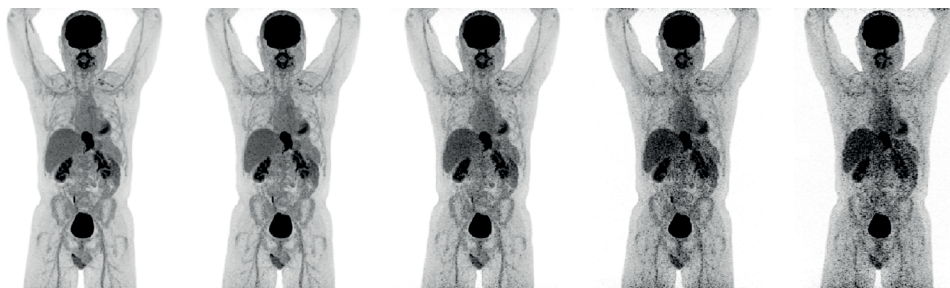


**Figure 4\*** Maximum intensity projection PET images of a 52-year-old male (weight, 86 kg) with esophageal cancer. Images were acquired at 180, 120, 60, 30, and 10 s/bp (from left to right respectively). \*This figure was adapted from *J Nucl Med. van Sluis et al. Image quality and activity optimization in oncologic  $^{18}\text{F}$ -FDG PET using the digital Biograph Vision PET/CT system. J Nucl Med. 2020;61:764-71.*

## Future perspectives and new research

The latest development in PET/CT system design has been the introduction of the so-called total-body PET/CT system which hold promising opportunities for the future. Although also equipped with SiPM-based detectors, these systems were left out of the comparison in this chapter to only focus on clinical state of the art PET/CT systems. Such a total body PET/CT design, surrounding the patient with many more detectors in the axial FOV, comes with two major improvements (16):

1. Longer axial extent of the FOV resulting in higher detection efficiency as more photon pairs are captured
2. One bed position covers a much larger proportion of the patient, thus the same time frame can cover more anatomy

Three total body systems have just been released on the (commercial) market. These are the PennPET Explorer (University of Pennsylvania) (17) with a 70-cm-long axial FOV, the uEXPLORER (United Imaging Healthcare) (18) which has a 194-cm-long axial FOV, and the Siemens Biograph Vision Quadra PET/CT (Siemens Healthineers) (19) with a 102-cm-long axial FOV.

Improved performance characteristics of these total body PET/CT systems will allow an even larger reduction in scan time and/or amount of radiotracer administration, but these systems come with many other opportunities that can be explored.

The improved sensitivity of total body PET can be used for example to improve image quality with long lived isotopes such as  $^{89}\text{Zr}$  for immunoPET imaging. A substantial improvement in image quality could allow a reduction in  $^{89}\text{Zr}$  activity administration which would make this radionuclide suitable for other applications besides oncology, for example inflammatory diseases. In addition, because of the increased sensitivity,

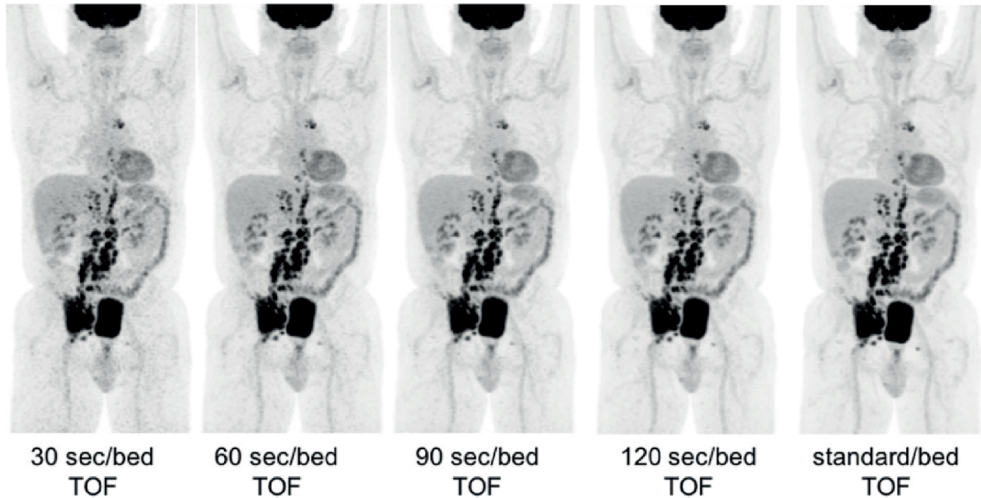


**Figure 5\*** Maximum intensity projection PET images acquired 71 min after injection of 423.3 MBq of  $^{18}\text{F}$ -FDG and reconstructed at various s/bp (BMI 26.6). \*This figure was originally published in *EJNMMI Physics*. Sonni et al. Initial experience with a SiPM-based PET/CT scanner: influence of acquisition time on image quality. *EJNMMI Phys.* 2018;5:9.

radiotracers could be followed longer over time postinjection. Furthermore, the larger FOV captures all relevant organs of interest and pharmacokinetic behavior of radioactive tracers can be observed (noninvasively) in more detail using whole body dynamic imaging; this holds promising future prospects for application in research and clinical practice.

## General conclusions

With the implementation of SiPM-based detectors in digital PET/CT systems, improved performance characteristics ensure better image quality with respect to conventional systems equipped with PMTs. Enhanced image quality leads to improved lesion detectability and possibilities to reduce scan duration for a higher patient throughput and/or lower the amount of radiotracer administration to reduce radiation exposure.

## References

1. Hutton BF, Erlandsson K, Thielemans K. Advances in clinical molecular imaging instrumentation. *Clin Transl Imaging*. 2018;6:31-45.
2. Vandenberghe S, Mikhaylova E, D'Hoe E, Mollet P, Karp JS. Recent developments in time-of-flight PET. *EJNMMI Phys*. 2016;3:3.
3. Slomka PJ, Pan T, Germano G. Recent advances and future progress in PET instrumentation. *Semin Nucl Med*. 2016;46:5-19.
4. Rausch I, Ruiz A, Valverde-Pascual I, Cal-González J, Beyer T, Carrio I. Performance evaluation of the Philips Vereos PET/CT System according to the NEMA NU2-2012 standard. *J Nucl Med*. 2018;60:561-7.
5. Zhang J, Maniawski P, Knopp M V. Performance evaluation of the next generation solid-state digital photon counting PET/CT system. *EJNMMI Res*. 2018;8:97.
6. National Electrical Manufacturers Assoc. Performance measurements of positron emission tomographs. National Electrical Manufacturers Association. Rosslyn, VA, USA. NEMA Standards Publication NU 2-2012; 2012.
7. National Electrical Manufacturers Assoc. Performance measurements of positron emission tomographs. National Electrical Manufacturers Association. Rosslyn, VA, USA. NEMA Standards Publication NU 2-2018; 2018.
8. van Sluis J, de Jong J, Schaar J, Noordzij W, Snick P Van, Dierckx R, et al. Performance characteristics of the digital Biograph Vision PET/CT system. *J Nucl Med*. 2019;60:1031-6
9. Hsu DFC, Ilan E, Peterson WT, Uribe J, Lubberink M, Levin CS. Studies of a next-generation silicon-photomultiplier-based time-of-flight PET/CT System. *J Nucl Med*. 2017;58:1511-8.
10. Nguyen NC, Vercher-Conejero JL, Sattar A, Miller MA, Maniawski PJ, Jordan DW, et al. Image quality and diagnostic performance of a digital PET prototype in patients with oncologic diseases: initial experience and comparison with analog PET. *J Nucl Med*. 2015;56:1378-85.
11. López-Mora DA, Flotats A, Fuentes-Ocampo F, Camacho V, Fernández A, Ruiz A, et al. Comparison of image quality and lesion detection between digital and analog PET/CT. *Eur J Nucl Med Mol Imaging*. 2019;46:1383-90.
12. van Sluis J, Boellaard R, Somasundaram A, van Snick JH, Borra RJH, Dierckx RAJO, et al. Image quality and semiquantitative measurements on the biograph vision PET/CT system: initial experiences and comparison with the biograph mCT. *J Nucl Med*. 2020;61:129-35.
13. Baratto L, Park SY, Hatami N, Davidzon G, Srinivas S, Gambhir SS, et al.  $^{18}\text{F}$ -FDG silicon photomultiplier PET/CT: a pilot study comparing semi-quantitative measurements with standard PET/CT. *PLoS One*. 2017;12:1-13.
14. van Sluis J, Boellaard R, Dierckx RAJO, Stormezand GN, Glaudemans AWJM, Noordzij W. Image quality and activity optimization in oncologic  $^{18}\text{F}$ -FDG PET using the digital Biograph Vision PET/CT system. *J Nucl Med*. 2020;61:764-71.
15. Sonni I, Baratto L, Park S, Hatami N, Srinivas S, Davidzon G, et al. Initial experience with a

- SiPM-based PET/CT scanner: influence of acquisition time on image quality. *EJNMMI Phys.* 2018;5:9.
16. Vandenberghe S, Moskal P, Karp JS. State of the art in total body PET. *EJNMMI Phys.* 2020;7:35.
  17. Karp JS, Viswanath V, Geagan MJ, Muehllehner G, Pantel AR, Parma MJ, et al. PennPET explorer: Design and preliminary performance of a whole-body imager. *J Nucl Med.* 2020;61:136-43.
  18. Spencer BA, Berg E, Schmall JP, Omidvari N, Leung EK, Abdelhafez YG, et al. Performance evaluation of the uEXPLORER Total-body PET/CT scanner based on NEMA NU 2-2018 with additional tests to characterize long axial field-of-view PET scanners. *J Nucl Med.* 2021;62:861-70.
  19. Conti M, Aykac M, Bal H, Bendrien B, Bharkhada D, Cabello J, et al. Simulation and first measurements of a prototype ultra-long FOV PET/CT scanner. *Eur Assoc Nucl Med Annu Conf.* 2020;[abstract](OP-230):supplement 1.





# Chapter 3

---

## Performance characteristics of the digital Biograph Vision PET/CT system

Joyce van Sluis<sup>1</sup>, Johan R. de Jong<sup>1</sup>, Jenny Schaar<sup>1</sup>, Walter Noordzij<sup>1</sup>, Johannes H. van Snick<sup>1</sup>, Rudi A.J.O. Dierckx<sup>1</sup>, Ronald J.H. Borra<sup>1</sup>, Antoon T.M. Willemsen<sup>1</sup>, and Ronald Boellaard<sup>1,2</sup>

<sup>1</sup>Department of Nuclear Medicine and Molecular Imaging, University of Groningen, University Medical Center Groningen, Hanzeplein 1, 9713 GZ Groningen, The Netherlands

<sup>2</sup>Department of Radiology and Nuclear Medicine, Cancer Center Amsterdam, Amsterdam University Medical Centers, Free University of Amsterdam, De Boelelaan 1117, 1081 HV Amsterdam, The Netherlands

*J Nucl Med. 2019;60:1031-1036.*



## **Abstract**

This study evaluated the performance of the digital Biograph Vision PET/CT system according to the NEMA NU 2-2012 standard (published by the National Electrical Manufacturers Association (NEMA)) to allow for a reliable, reproducible, and intersystem comparable performance measurement.

**Methods** The new digital PET/CT system features silicon photomultiplier-based detectors with 3.2-mm lutetium oxyorthosilicate crystals and full coverage of the scintillator area. The PET components incorporate 8 rings of 38 detector blocks, and each block contains 4 x 2 mini blocks. Each mini block consists of a 5 x 5 lutetium oxyorthosilicate array of 3.2 x 3.2 x 20 mm crystals coupled to a silicon photomultiplier array of 16 x 16 mm, resulting in an axial field-of-view of 26.1 cm. In this study, PET/CT system performance was evaluated for conformation with the NEMA NU 2-2012 standard, with additional measurements described in the new NEMA NU 2-2018 standard. Spatial resolution, sensitivity, count rate performance, accuracy of attenuation and scatter correction, image quality, coregistration accuracy, and Time-of-Flight performance were determined. Measurements were directly compared with results from its predecessor, the Biograph mCT Flow, using existing literature. Moreover, feasibility to comply with the European Association of Nuclear Medicine Research Ltd. (EARL) criteria was evaluated, and some illustrative patient PET images were obtained.

**Results** The Biograph Vision showed a transverse and axial spatial resolution of 3.6 and 3.5 mm, respectively, in full width at half maximum at a 1-cm offset from the center of the field-of-view (measured with a  $^{22}\text{Na}$  0.25-mm point source), a NEMA sensitivity of 16.4 kcps/MBq, and a NEMA peak noise-equivalent count rate of 306 kcps at 32 kBq/mL. Time-of-Flight resolution varied from 210 to 215 as count rate increased up to the peak noise-equivalent count rate. The overall image contrast seen with the NEMA image quality phantom ranged from 77.2% to 89.8%. Furthermore, the system was able to comply with the current and future EARL performance criteria.

**Conclusion** The Biograph Vision outperforms the analog Biograph mCT Flow, and the system is able to meet European harmonizing performance standards.

## **Introduction**

PET plays a key role in diagnosis and evaluation of medical conditions. Since 1998, when the first hybrid PET/CT system became operational (1), advances in PET technology have been significant. The implementation of fast lutetium oxyorthosilicate crystals (2) allowed for shorter coincidence timing windows and

enabled Time-of-Flight (ToF) imaging (3-5), and the use of an extended axial field-of-view (FOV) increased volume sensitivity (6).

Evaluation of the physical performance of PET systems using NEMA NU 2-2012 (published by the National Electrical Manufacturers Association (NEMA)) allows for reproducible and accepted comparisons between PET systems (7).

The digital Biograph Vision PET/CT system (Siemens Healthineers) introduces silicon photomultiplier (SiPM)-based detectors with 3.2-mm lutetium oxyorthosilicate crystals and full coverage between the crystal and the SiPMs. The Vision is the third commercially available digital system, with the other two being the Vereos (Philips Healthcare) (8,9) and the Discovery MI (GE Healthcare) (10).

The purpose of this study was to evaluate the performance of the Vision according to both the NEMA NU 2-2012 (7) and the NEMA NU 2-2018 standards (11). Results were compared with data from the analog Biograph mCT Flow system (12). Spatial resolution, sensitivity, scatter fraction, noise-equivalent count rate (NECR), image quality, and accuracy of attenuation and scatter corrections were evaluated following the NEMA NU-2 2012 protocol. ToF resolution and coregistration accuracy were determined according to the NEMA NU-2 2018 standard. The feasibility of complying with the European Association of Nuclear Medicine Research Ltd. (EARL) criteria was explored, and some first illustrative patient images were obtained.

## **Materials and methods**

### **Biograph Vision PET/CT system**

The Vision combines a 128-slice CT scanner with a whole body lutetium oxyorthosilicate PET system. The system has a 78-cm bore and 227-kg table capacity. The PET component contains 8 detector rings and 19 detector electronics assembly units to form a ring. Two adjacent detector blocks per detector electronics assembly unit result in 38 blocks per ring. Each detector block contains a 4 x 2 arrangement of mini blocks. A mini block consists of a 5 x 5 lutetium oxyorthosilicate array of 3.2 x 3.2 x 20 mm crystals coupled to an SiPM array. Each SiPM array is 16 x 16 mm and has 16 output channels.

The arrangement of 4 x 2 mini blocks, with 2 mini blocks in the axial direction, results in a 32-mm axial FOV for 1 block. This configuration, which uses 8 blocks in the axial direction, has a 25.6-cm axial FOV, or 26.1 cm including the packing spaces between the blocks.

The design of the detector is based on a square array of small crystals whose area is fully covered by SiPM detector elements, exploiting the full potential of SiPMs. The 3.2-mm crystal size allows for a high system spatial resolution, whereas the full coverage optimizes light collection and enables improved timing resolution and signal-to-noise ratio (13).

## Measurements

Performance measurements included spatial resolution, scatter fraction, sensitivity, count rate performance, image quality, coregistration accuracy, and timing resolution. All measurements were conducted according to the NEMA NU 2-2012 and NEMA NU 2-2018 standards. Acquisition and reconstruction protocols, as well as NEMA analysis software, were provided by the manufacturer. All reported metrics conform with the specifications and definitions provided in the NEMA NU 2 standards.

### *Spatial resolution*

NEMA NU 2-2012 specifies using a  $^{18}\text{F}$ -FDG point source smaller than 1 x 1 x 1 mm. However, for measuring the spatial resolution on the Vision with smaller crystals, a smaller point source could improve test results (14). NEMA NU 2-2018 therefore recommends purchasing a  $^{22}\text{Na}$  point source (11). Thus, a 74-kBq, 0.25-mm-diameter spheric  $^{22}\text{Na}$  point source (Eckert and Ziegler Isotope Products) was used.

To comply with the NEMA NU 2-2012 standard, measurements were also performed using an  $^{18}\text{F}$ -FDG point source. At the start of data acquisition, a point source of 3.7 kBq of  $^{18}\text{F}$ -FDG with a length of about 0.3 mm was prepared in a 0.5-mL syringe (Hamilton Co.). The activity at the start of acquisition was sufficiently low to keep deadtime losses and randoms below 5% of total events. Data were acquired at several positions in the FOV (in x, y, and z directions of 0, 1, and 3.3 cm [ $\approx \frac{1}{8}$  FOV<sub>Z</sub>]; 0, 1, and 13 cm [ $\approx \frac{1}{2}$  FOV<sub>Z</sub>]; 0, 10, and 3.3 cm; 0, 10, and 13 cm; 0, 20, and 3.3 cm; and 0, 20, and 13 cm, respectively). At least  $2 \times 10^6$  coincidence counts were acquired in each position.

The obtained sinogram data were Fourier-rebinned and reconstructed by filtered backprojection using only a standard ramp filter into a 880 x 880 x 307 matrix with a 0.8 x 0.8 x 0.8 mm voxel size. The data were reconstructed without attenuation and scatter correction. The spatial resolution was determined according to NEMA NU 2-2012 as the full width at half maximum (FWHM) of the point-spread function (PSF) (7).

### *Scatter fraction, count losses, and randoms measurement*

The phantom used for these measurements was a 70-cm-long polyethylene cylinder (20-cm diameter), with a line source inserted axially into the cylinder 4.5 cm radially from the center. At the start of data acquisition, the line source was filled with 1.2 GBq of  $^{18}\text{F}$ -FDG to achieve count rates beyond the expected peak of the NECR. Data were acquired for over 12 h, resulting in 35 frames, each with a 240-s acquisition time and an interframe delay of 960 s. To account for randoms, online randoms subtraction was applied using the delayed-coincidence-time-window technique (15). Subsequently, scatter fraction and NECR were determined (7).

### *Sensitivity*

Sensitivity was measured using a 70-cm-long polyethylene tube (inner diameter, 1 mm; outer diameter, 3 mm) filled with 5.07 MBq of  $^{18}\text{F}$ -FDG (at acquisition start) and placed inside 5 concentric aluminum sleeves of equal length with known diameters (7). Five data sets were acquired associated with each of the 5 sleeves (starting with all 5 aluminum sleeves and finishing with a single sleeve) for 300 s each. The measurements were conducted at the center of the transaxial FOV and repeated at a 10-cm radial offset. Randoms subtraction was applied using the delayed-coincidence-time-window measurement. Next, the system sensitivity was computed (7).

### *Accuracy of count losses and randoms corrections*

This evaluation used data acquired from the scatter fraction and count rate measurements. Data were corrected for dead time, randoms, scatter, and attenuation (7). The parameters of the low-dose CT scan used for attenuation correction were an x-ray tube current of 80 mAs, a tube voltage of 120 kV, and a spiral pitch factor of 0.8. Scatter was corrected using the extended single-scatter simulation algorithm (16), which discriminates the scattered annihilation radiation according to its differential ToF.

Subsequently, the corrected data were reconstructed using the standard provided whole body reconstruction algorithm, that is, an ordinary Poisson ordered-subset expectation maximization (OP-OSEM) 3-dimensional (3D) iterative algorithm (17) with 8 iterations, 5 subsets, and no filtering. An image matrix size of 220 x 220 was used. By extrapolating the true rate for low activity concentrations (where count losses and randoms can be neglected), count rate accuracy was estimated.

### *Image quality, accuracy of attenuation, and scatter corrections*

The PET NEMA NU2 image quality phantom (IQ phantom) (PTW) was used to evaluate image quality. The background activity concentration at the start of data acquisition was 5.7 kBq/mL  $^{18}\text{F}$ -FDG. The 4 smallest spheres were filled with a sphere-to-background ratio of 8:1 for the first set of scans and 4:1 for the second set of scans. The remaining 2 largest spheres were filled with nonradioactive water. The IQ phantom was positioned with all spheres aligned in the axial and transaxial center of the FOV. For simulation of a clinical situation with activity outside the FOV, the cylindrical scatter phantom was placed axially next to the IQ phantom (7). The line source inside the scatter phantom was filled with approximately 116 MBq of  $^{18}\text{F}$ -FDG at the start of both data acquisitions.

Two sequential measurements of 240 s each were acquired for a single bed position after a low-dose CT scan for attenuation correction. Acquisitions were done to



simulate a whole body scan (emission and transmission) of 100 cm total axial imaging distance in 30 min of emission imaging. All data were corrected for random coincidences (smoothed random correction), normalization, decay, dead-time losses, scatter, and attenuation. The data were reconstructed using an OP-OSEM 3D-iterative algorithm with 8 iterations and 5 subsets, applying PSF and ToF into a 440 x 440 matrix with a voxel size of 1.6 x 1.6 x 1.6 mm. The percentages contrast obtained for hot and cold spheres, the background count variability for each sphere, and the accuracies of attenuation and scatter corrections were evaluated.

### *Coregistration accuracy*

For measurement of coregistration accuracy, a vial was filled with 59.6 MBq of  $^{18}\text{F}$ -FDG activity (in 0.1 mL at data acquisition start) and CT contrast (240 mg/mL) to a volume of no more than 1.4 mL. In total, 115 kg in nine 11.5-kg increments (which includes the weight of the 11.5-kg L-fixtured) were placed on the patient bed. The foam holders provided by the manufacturer were positioned on the L-fixtured at 6 locations, 3 points on each of 2 transaxial planes. In the transverse direction (with the coordinate system origin  $x$  and  $y = 0$  and  $0$  cm, respectively), the foam holders were placed at nominal locations of 0 and 1 cm, 0 and 20 cm, and 20 and 0 cm on the  $x$  and  $y$  axes, respectively. In the axial direction (with the coordinate system origin  $z = 0$ , located at the edge of the PET axial FOV), the foam holders were placed in the center of the PET axial FOV ( $z = \frac{1}{2}$  PET axial FOV) and at 5 and 100 cm from the tip of the patient table (11). Per location, a low-dose CT scan was performed first and followed by a 3-min PET scan. The total of 6 measurements was performed to determine the centroid within the PET and CT data sets and, subsequently, to calculate the length of the 3D vector between the CT centroid and the PET centroid (i.e., the coregistration error) (11).

### *Timing resolution*

The ToF resolution was calculated using the acquired scatter data used for NECR performance, according to a new proposed method (11,18). The timing resolution was calculated as the FWHM of the time distribution of events, after correction for scatter, randoms, and the position of the line source.

### *EARL performance*

EARL performance on the Vision was measured to evaluate its ability to meet current EARL guidelines and foreseen 2019 EARL guidelines (19-22). Measurements were conducted according to EARL standard operating procedures (23). The images were reconstructed using an OP-OSEM 3D-iterative algorithm with 4 iterations and 5 subsets, applying ToF, into an image matrix size of 220 x 220, resulting in a voxel

size of 3.3 x 3.3 x 1.6 mm. This reconstruction was repeated with 8 iterations, a 5-mm FWHM Gaussian filter, and an image matrix size of 220 x 220. Additional reconstructions applied resolution modeling, with and without a 7-mm FWHM Gaussian filter and with matrix sizes of both 220 x 220 and 440 x 440. Reconstructions were performed with corrections for attenuation, scatter, normalization, decay, and dead time. Moreover, all (nonsmoothed) reconstructed images were filtered using Gaussian kernels with a FWHM ranging from 1 to 10 mm in 1-mm steps to derive the optimal combination of reconstruction methods, settings, and filtering to achieve EARL-compliant performance. The latter procedure will allow the definition of EARL-compliant reconstruction protocols for the Vision.

To provide the reader with insight on a possible activity or scantime reduction that may be applied in clinical settings, EARL decay measurements were performed according to a previously published method (24).

### *Patient study*

A patient study is included to provide the reader with a first impression on clinical performance. We do not intend to provide a detailed and valid intersystem comparison. A 67-y-old woman (1.64 m tall and weighing 73.1 kg) diagnosed with parkinsonism was injected with 200 MBq of  $^{18}\text{F}$ -FDG. At 30 min after injection, a brain PET/CT study was first performed on an mCT system for 15 min and then repeated on the Vision (~5 min after the completion of the mCT study). Data from the mCT were reconstructed using 3D-ToF OP-OSEM with 6 iterations, 21 subsets, and resolution modeling. No filter was used, and the resulting image size was 400 x 400 with a voxel size of 2 x 2 x 2 mm. Data acquired on the Vision were reconstructed using 3D-ToF OP-OSEM with 8 iterations and 5 subsets, with resolution modeling into a 440 x 440 image matrix with a voxel size of 1.6 x 1.6 x 1.6 mm.

Another patient, a 56-y-old woman (1.54 m tall and weighing 67.3 kg) diagnosed with metastasized non-small cell lung carcinoma was injected with 215 MBq of  $^{18}\text{F}$ -FDG. At 60 min after injection, a whole body PET/CT study was performed on an mCT system using 3-min PET acquisitions per bed position. Data were reconstructed using 3D-ToF OP-OSEM with 3 iterations, 21 subsets, and resolution modeling. A Gaussian filter of 5 mm was applied to the reconstructed images, and the resulting image size was 400 x 400 with a voxel size of 2 x 2 x 2 mm. Subsequently, measurements were repeated on the Vision using 3-min PET acquisitions per bed position. The vendor-recommended reconstruction protocol was applied, that is, 3D-ToF OP-OSEM with 4 iterations, 5 subsets, resolution modeling, no filtering, an image matrix size of 220 x 220, and a voxel size of 3.3 x 3.3 x 1.6 mm.

The patient study was approved by the medical ethics review board of the University Medical Center Groningen, and both patients provided written informed consent.

## Results

### NEMA measurements

#### *Spatial resolution, sensitivity, coregistration accuracy, and timing resolution*

The spatial resolutions are summarized in Table 1, listing FWHM and full-width-at-tenth-maximum values at 1, 10, and 20 cm. The sensitivity values for both the 0- and the 10-cm off-center position, the maximum coregistration error, and the calculated timing resolution are also given in Table 1. These results show an average sensitivity increase of 70.3% for the Vision compared with the mCT Flow. The observed ToF of 210 ps worsens only 5 ps from low count rate up to peak NECR (Table 1; Fig. 1). In addition, the axial sensitivity profiles for both the 0- and the 10-cm off-center positions are shown in Figure 2.

**Table 1** NEMA NU 2-2012 measurement results and some additional results according to the NEMA NU 2-2018 standard acquired on the Vision with a direct comparison to published results from the mCT FLOW (12).

Parameter	*Distance	Measured (Vision)				Published (mCT Flow)	
		<sup>22</sup> Na	<sup>18</sup> F-FDG	<sup>22</sup> Na	<sup>18</sup> F-FDG	<sup>18</sup> F-FDG	<sup>18</sup> F-FDG
Spatial Resolution		[mm FWHM]		[mm FWTM]		[mm FWHM]	[mm FWTM]
Radial	1	3.5	3.7	6.8	7.4	4.3	8.6
	10	4.5	4.6	8.4	8.8	5.2	9.3
	20	5.8	6.0	10.5	11.1	5.6	9.8
Tangential	1	3.6	3.7	6.9	7.2	4.3	8.6
	10	3.9	3.9	7.0	7.3	4.7	9.7
	20	3.5	3.6	6.4	7.0	6.5	12.7
Axial	1	3.5	3.8	7.1	7.6	4.3	8.6
	10	4.3	4.3	8.7	9.2	5.9	11.1
	20	4.4	4.6	9.4	10.2	7.8	13.7
Sensitivity						[kcps/MBq]	
	0			16.4		9.6	
	10			16.3		9.6	
Parameter		Measured (Vision)				Published (mCT Flow)	
Accuracy						[kcps] @ [kBq/ml]	
Peak NECR		306 @ 32.6				185 @ 29	
Peak true rate		1306 @ 54				634 @ 42.4	
Scatter Fraction						[%]	
	[%]@ peak NECR	38.7				33.4	
	[%]@ low activity	37				33.5	
ToF Resolution						[ps]	
		210				540	
Max Coregistration Error						[mm]	
		1.25				n/a	

\*radial distance in [cm] from center FOV

FWHM = full width at half maximum; FWTM = full width at tenth maximum

*Scatter fraction, count losses, and randoms measurement*

Peak NECR and scatter fractions at peak NECR and at low activity levels are given in Table 1. Figure 1 shows plots of the trues, randoms, prompts, and scatter event rates next to the scatter fraction curve as a function of activity. In addition, the NECR as a function of activity concentration is shown.

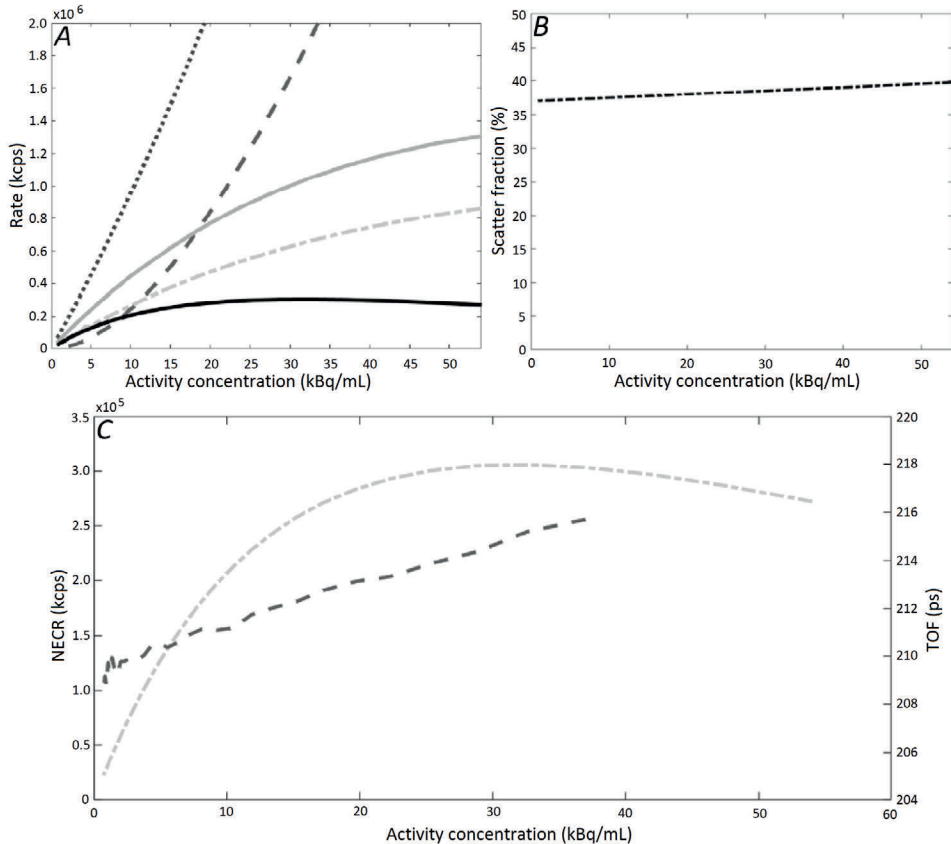


**Figure 1** (A) Plots of prompts (dotted line), randoms (dashed line), trues (grey solid line), scatter event rates (dashed-dotted line), and NECR (black solid line). (B) Scatter fraction as function of activity concentration. (C) NECR (dashed-dotted line) and ToF (dashed line) as function of activity concentration.

The trues rate was 1,306 kcps at 54 kBq/mL, and the accuracy mean bias was 2.9%. Figure 3 shows a plot of the maximum and minimum relative count rate error for the different activity concentrations.

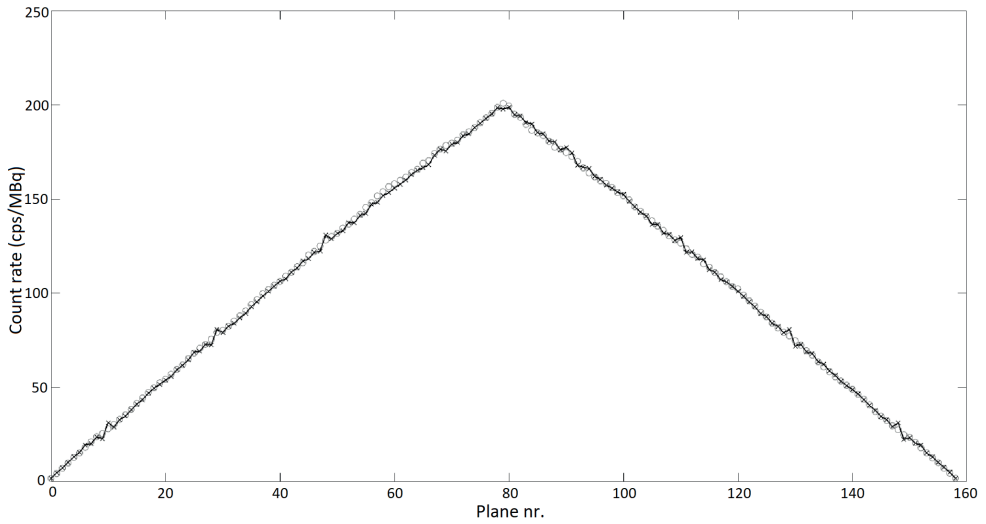


**Figure 2** The axial sensitivity profiles for both the 0- and 10-cm off-center positions. The 0-cm off-center positions are indicated with the gray circles, whereas the black crosses represent the 10-cm off-center.

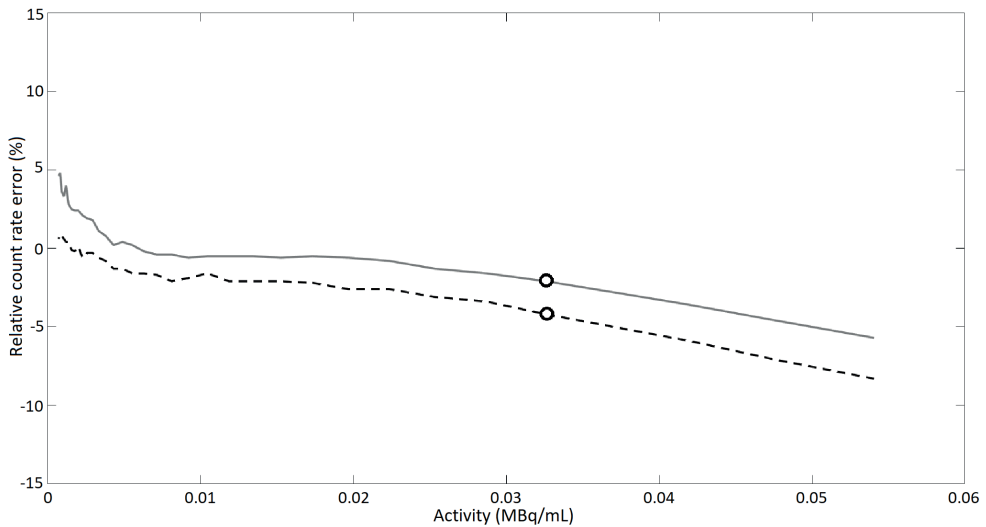


**Figure 3** Maximum (solid line) and minimum (dashed line) relative count rate error for different activity concentrations, and maximum and minimum bias values (circles) at activity concentration of peak NECR.

**Table 2** Contrast, background variability, and average lung residual for 8:1 sphere-to-background ratio on Vision, directly compared with published results from mCT Flow. mCT Flow measurements include effect of low-resolution matrix and postreconstruction 3-mm Gaussian filter (12).

Sphere size [mm]	Contrast [%]		Background variability [%]	
	Vision	mCT Flow	Vision	mCT Flow
10	86.8	41.9	6.0	6.3
13	77.2	63.1	5.0	5.4
17	85.0	68.1	3.9	4.4
22	89.8	76.6	3.3	3.6
28	87.4	71.3	3.0	3.0
37	89.6	77.7	2.2	2.4
Av. lung residual [%]	3.5	12.1		

**Table 3** Contrast, background variability, and average lung residual for 4:1 sphere-to-background ratio on Vision, directly compared with published results from mCT Flow. mCT Flow measurements include effect of low-resolution matrix and postreconstruction 3-mm Gaussian filter (12).

Sphere size [mm]	Contrast [%]		Background variability [%]	
	Vision	mCT Flow	Vision	mCT Flow
10	93.1	28.3	6.4	6.9
13	73.5	47.9	5.0	6.8
17	79.0	58.4	4.0	5.6
22	87.0	70.8	3.1	4.7
28	86.3	67.0	2.7	3.8
37	89.4	76.9	2.2	2.9
Av. lung residual [%]	3.4	12.3		

### Image quality, accuracy of attenuation, and scatter corrections

Tables 2 and 3 show the percentage contrast, background variability, and average lung residual for the 8:1 and 4:1 sphere-to-background ratios.

### Additional measurements

#### EARL compliance

Figures 4 and 5 show SUV recovery coefficients as a function of the sphere sizes in the NEMA IQ phantom for various reconstruction protocols according to the current EARL performance criteria (19,20) and foreseen new EARL performance criteria (21,22), respectively.

EARL compliance was achieved by using 3D-ToF OP-OSEM with 4 or 8 iterations and 5 subsets, with a 5-mm FWHM Gaussian filter and an image matrix size of 220 x 220, or by using 3D-ToF OP-OSEM with resolution modeling and the same reconstruction settings as above but with a 7-mm FWHM Gaussian filter and an image matrix size of 220 x 220 or 440 x 440. For the foreseen new EARL specifications,

compliance can be achieved either by using 3D-ToF OP-OSEM with 4 or 8 iterations and 5 subsets, a matrix of 220 x 220, and no additional filtering or by using 3D-ToF OP-OSEM with resolution modeling, a Gaussian filter of 5-mm FWHM, and an image matrix size of either 220 x 220 or 440 x 440, although at present borderline results were seen using  $SUV_{peak}$  recoveries. There is no  $SUV_{peak}$  upper and lower limit according to current EARL specifications; therefore, these limits cannot be shown in Figure 4C.

For illustrative purposes, the  $SUV_{max}$  and  $SUV_{mean}$  recovery coefficients without filtering, and with and without additional PSF resolution modeling (not EARL-compliant), are shown in Supplemental Figures 1 and 2 (supplemental materials are available at <http://jnm.snmjournals.org>). In addition, the results of the EARL decay measurements (24) to provide first insights on possible activity or scan time reduction are shown in Supplemental Tables 1-3; these results suggest that for EARL-compliant reconstructions, a reduction in the activity and scan duration product by a factor of 8, compared with current recommendations, seems feasible.

### *Example patient images*

Supplemental Figures 3 and 4 illustrate some clinical example images obtained with the Vision and the mCT.

## **Discussion**

### **NEMA measurements**

#### *Spatial resolution*

The spatial resolution (FWHM) of the Vision (with  $^{18}F$ -FDG) was better than that of the mCT Flow. The transaxial spatial resolution of the Vision was better than that of the mCT Flow, at 0.6, 0.6, and 1.2 mm at the 1-, 10-, and 20-cm radial positions, respectively. This improvement can be explained by the smaller 3.2-mm lutetium oxyorthosilicate crystals, with respect to the 4-mm crystals of the mCT Flow. The improvement in axial resolution away from the center of the system is probably to be attributed to an advanced rebinning technique introduced in the Vision (25).

With such small crystals, the resolution measurement depends on the ability to build a smaller point source. As the mean positron range of  $^{22}Na$  and  $^{18}F$ -FDG is similar (26), the difference in spatial resolution measurement can be attributed to the source dimension. Preparing a small source with  $^{18}F$ -FDG is challenging; therefore, the NEMA NU 2-2018 recommends purchasing a  $^{22}Na$  source to measure the spatial resolution. Hence, we also used the  $^{22}Na$  point source in our experiments.

#### *Sensitivity and timing resolution*

The improved ToF resolution of 210 ps can be translated to more effective noise

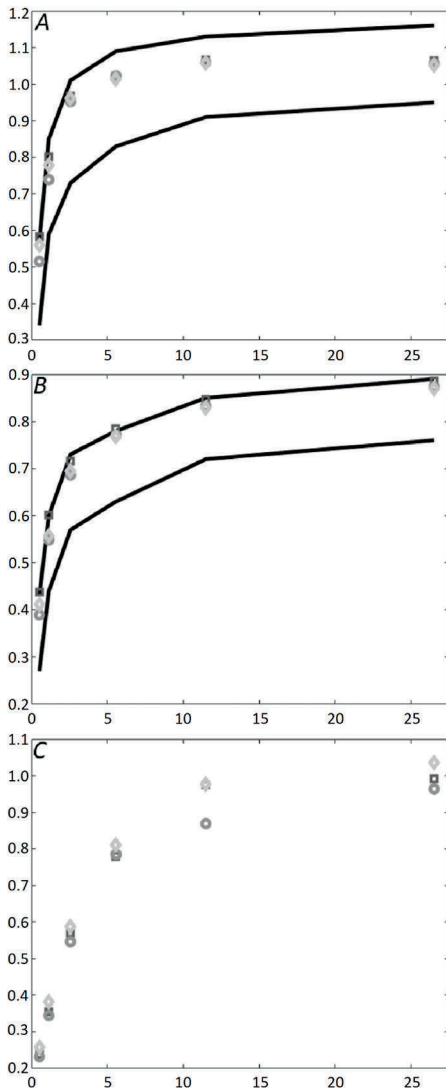


**Figure 4** SUV recovery coefficients as function of sphere size in IQ phantom for various reconstruction protocols. Square = 3D-ToF OP-OSEM with 4 iterations, 5 subsets, and 5-mm Gaussian filter into matrix size of  $220 \times 220$ ; circle = "square" but with 7-mm Gaussian filter and addition of PSF; diamond = "circle" but with image size of  $440 \times 440$ . According to EARL specifications,  $SUV_{max}$  (A),  $SUV_{mean}$  (B), and  $SUV_{peak}$  (C) recoveries are shown. Lines illustrate upper and lower limits.  $SUV_{peak}$  limits are not provided here since these are not included in current EARL guidelines.

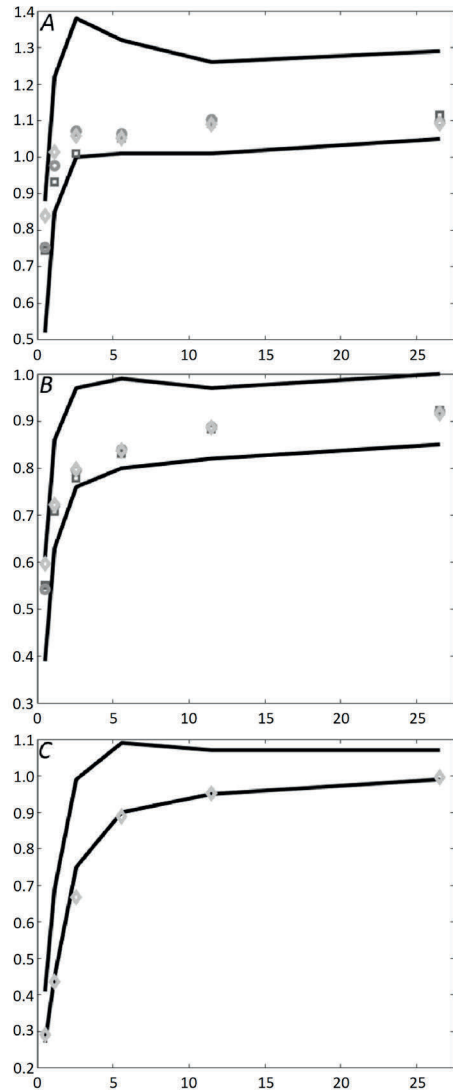


**Figure 5** SUV recovery coefficients as function of sphere size in IQ phantom for various reconstruction protocols. Square = 3D-ToF OP-OSEM with 4 iterations, 5 subsets, and 4-mm Gaussian filter into matrix size of  $220 \times 220$ ; circle = "square" but with 5-mm Gaussian filter and addition of PSF; diamond = "circle" but with image size of  $440 \times 440$ . According to EARL 2019 specifications,  $SUV_{max}$  (A),  $SUV_{mean}$  (B), and  $SUV_{peak}$  (C) recoveries are shown. Lines illustrate upper and lower limits.

reduction or better contrast enhancement in comparison to the mCT Flow (27). The higher sensitivity of the Vision may allow for reduction in dose or scan time in future clinical application (Supplemental Tables 1-3 provide first insights regarding dose or scan-time reduction).

### *Scatter fraction, count losses, and randoms measurement*

The peak NECR increased 65% when measured on the Vision, compared with the mCT Flow. Because of the extended axial FOV of the new system and a greater acceptance angle, a small increase in scatter fraction can be expected. The true counts captured on the Vision have increased with respect to its predecessor (~770 kcps at 20 kBq/mL for the Vision and 440 at 20 kBq/mL for the mCT Flow). The increase in true count rate is assumed to result from a lower dead time and a higher sensitivity on the Vision than on the mCT Flow; therefore, the Vision relatively outperforms its predecessor on this aspect.

### *Image quality and quantification*

A higher percentage contrast for the 10-mm sphere was seen. This higher contrast recovery for the smallest sphere is likely caused by the Gibbs artifact from the use of PSF reconstructions.

## **Additional measurements**

### *EARL*

By using standard available reconstruction settings, it is possible to set up a reconstruction protocol, both with and without resolution modeling, that complies with both current and foreseen future EARL specifications. The default whole body reconstruction protocol may result in voxels smaller than 3 mm in any direction (especially slice thickness), which is noncompliant with current EARL criteria (19,20). In the foreseen new EARL performance criteria, this restriction will no longer be applicable and the use of PSF reconstruction will be permitted (21,22).

### *Patient study*

The 2 initial PET studies that were performed were intended to provide the reader with a first glance at the image quality obtained with the Vision and should not be considered a scientifically valid comparison of clinical system performance.

## **Conclusion**

The Vision had a transverse and axial spatial resolution of 3.6 and 3.5 mm, respectively, at a 1-cm offset from the center of the FOV (measured with a  $^{22}\text{Na}$  source), compared

with respective values of 4.3 and 4.3 mm for the mCT Flow. Moreover, compared with the mCT Flow, the Vision had a 70.3% increase in sensitivity, a 65% higher peak NECR, and a higher contrast recovery. Finally, the timing resolution improved from 540 ps on the mCT Flow to 210 ps on the Vision. The Vision outperformed the analog mCT Flow in every NEMA performance test that was evaluated.

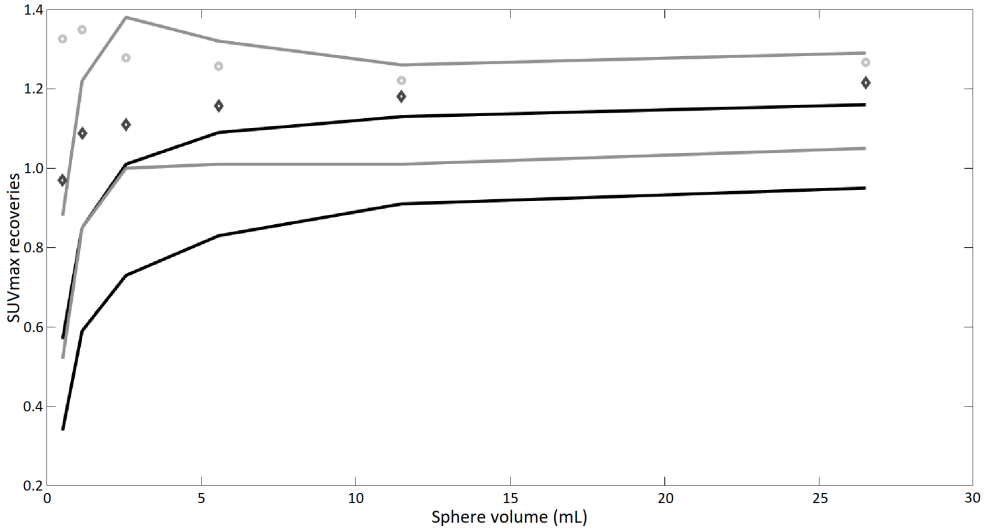
## References

1. Beyer T, Townsend DW, Brun T, Kinahan PE, Charron M, Roddy R, et al. A combined PET/CT scanner for clinical oncology. *J Nucl Med.* 2000;41:1369-1379.
2. Melcher CL. Scintillation crystals for PET. *J Nucl Med.* 2000;41:1051-1055.
3. Moses WW. Time of Flight in PET Revisited. *IEEE Trans Nucl Sci.* 2003;50:1325-1330.
4. Surti S, Kuhn A, Werner ME, Perkins AE, Kolthammer J, Karp JS. Performance of Philips Gemini TF PET/CT scanner with special consideration for its time-of-flight imaging capabilities. *J Nucl Med.* 2007;48:471-480.
5. Jakoby BW, Bercier Y, Conti M, Casey ME, Bendriem B, Townsend DW. Physical and clinical performance of the mCT time-of-flight PET/CT scanner. *Phys Med Biol.* 2011;56:2375-2389.
6. Jakoby BW, Bercier Y, Watson CC, Bendriem B, Townsend DW. Performance characteristics of a new LSO PET/CT scanner with extended axial field-of-view and PSF reconstruction. *IEEE Trans Nucl Sci.* 2009;56:633-639.
7. National Electrical Manufacturers Assoc. Performance measurements of positron emission tomographs. NEMA Standards Publication NU 2-2012. Rosslyn, USA: National Electrical Manufacturers Association. 2012.
8. Nguyen NC, Vercher-Conejero JL, Sattar A, Miller MA, Maniawski PJ, Jordan DW, et al. Image quality and diagnostic performance of a digital PET prototype in patients with oncologic diseases: Initial experience and comparison with analog PET. *J Nucl Med.* 2015;56:1378-1385.
9. Rausch I, Ruiz A, Valverde-Pascual I, Cal-González J, Beyer T, Carrio I. Performance evaluation of the Philips Vereos PET/CT system according to the NEMA NU2-2012 standard. *J Nucl Med.* October 25, 2018;60:1684-90.
10. Hsu DFC, Ilan E, Peterson WT, Uribe J, Lubberink M, Levin CS. Studies of a next-generation silicon-photomultiplier-based time-of-flight PET/CT system. *J Nucl Med.* 2017;58:1511-1518.
11. National Electrical Manufacturers Assoc. Performance measurements of positron emission tomographs. NEMA Standards Publication NU 2-2018. Rosslyn, VA, USA: National Electrical Manufacturers Association. 2018.
12. Rausch I, Cal-González J, Dapra D, Gallowitsch HJ, Lind P, Beyer T, et al. Performance evaluation of the Biograph mCT Flow PET/CT system according to the NEMA NU2-2012 standard. *EJNMMI Phys.* 2015;2:1-17.
13. Surti S. Update on time-of-flight PET imaging. *J Nucl Med.* 2015;56:98-105.
14. St. James ST, Thompson CJ. Investigation of the block effect in LSO detectors. *IEEE Nucl Sci Symp Conf Rec.* 2005;5:2474-2477.
15. Watson CC, Casey ME, Eriksson L, Mulnix T, Adams D, Bendriem B. NEMA NU 2 performance tests for scanners with intrinsic radioactivity. *J Nucl Med.* 2004;45:822-826.
16. Watson CC. Extension of single scatter simulation to scatter correction of time-of-flight PET. *IEEE Trans Nucl Sci.* 2007;54:1679-1686.
17. Varrone A, Sjöholm N, Eriksson L, Gulyás B, Halldin C, Farde L. Advancement in PET quantification using 3D-OP-OSEM point spread function reconstruction with the HRRT. *Eur J*

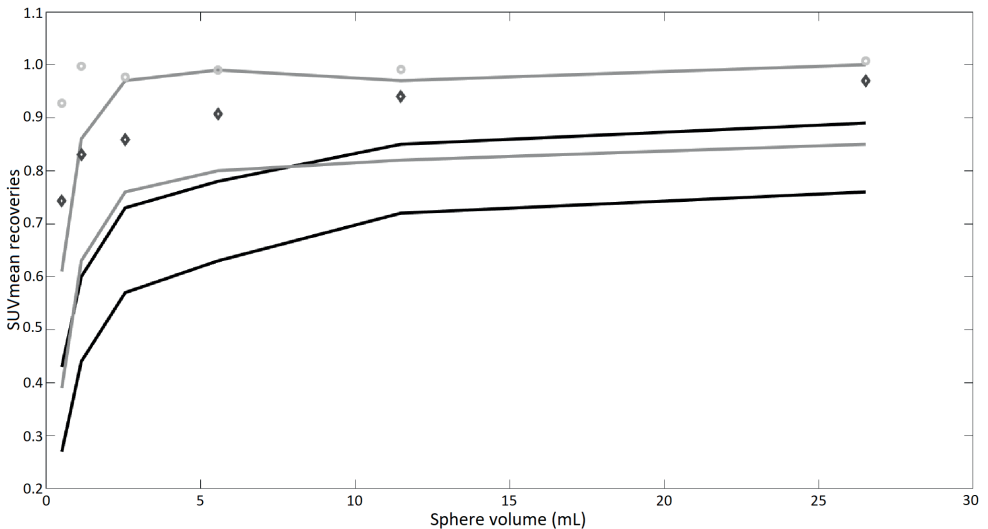
- Nucl Med Mol Imaging. 2009;36:1639-1650.
18. Wang G-C, Li X, Niu X, Du H, Balakrishnan K, Ye H, et al. PET timing performance measurement method using NEMA NEC Phantom. *IEEE Trans Nucl Sci.* 2016;63:1335-1342.
  19. Boellaard R, O'Doherty MJ, Weber WA, Mottaghy FM, Lonsdale MN, Stroobants SG, et al. FDG PET and PET/CT: EANM procedure guidelines for tumour PET imaging: version 1.0. *Eur J Nucl Med Mol Imaging.* 2010;37:181-200.
  20. Boellaard R, Delgado-Bolton R, Oyen WJG, Giammarile F, Tatsch K, Eschner W, et al. FDG PET/CT: EANM procedure guidelines for tumour imaging: version 2.0. *Eur J Nucl Med Mol Imaging.* 2014;42:328-354.
  21. Kaalep A, Sera T, Rijnsdorp S, Yaqub M, Talsma A, Lodge MA, et al. Feasibility of state of the art PET/CT systems performance harmonisation. *Eur J Nucl Med Mol Imaging.* 2018;45:1-18.
  22. Boellaard R. New developments of EANM oncology PET/CT guidelines and update of the EARL accreditation standards. Presented at the EANM congress 2018. Website of EANM Research Ltd. [http://earl.eanm.org/cms/website.php?id=/en/projects/fdg\\_pet\\_ct\\_accreditation/accreditation\\_specifications.htm](http://earl.eanm.org/cms/website.php?id=/en/projects/fdg_pet_ct_accreditation/accreditation_specifications.htm). Accessed November 7, 2018.
  23. Manual for EARL FDG-PET/CT accreditation Version 1.2. EANM Research Ltd. March 2017.
  24. Boellaard R, Willemsen A, Arends B, Visser EP. EARL procedure for assessing PET/CT system specific patient FDG activity preparations for quantitative FDG PET/CT studies. April 2013. Pdf of the standard operating procedure. [http://earl.eanm.org/html/img/pool/EARL-procedure-for-optimizing-FDG-activity-for-quantitative-FDG-PET-studies\\_version\\_1\\_1.pdf](http://earl.eanm.org/html/img/pool/EARL-procedure-for-optimizing-FDG-activity-for-quantitative-FDG-PET-studies_version_1_1.pdf). Accessed October 18, 2018.
  25. Vandenberghe S, Daube-Witherspoon ME, Lewitt RM, Karp JS. Fast reconstruction of 3D time-of-flight PET data by axial rebinning and transverse mashing. *Phys Med Biol.* 2006;51:1603-1621.
  26. Jødal L, Le Loirec C, Champion C. Positron range in PET imaging: Non-conventional isotopes. *Phys Med Biol.* 2014;59:7419-7434.
  27. Karp JS, Surti S, Daube-Witherspoon ME, Muehllehner G. The benefit of time-of-flight in PET imaging: Experimental and clinical results. *J Nucl Med.* 2015;6:790-795.



## Supplemental data



**Supplemental Figure 1**  $SUV_{max}$  recovery coefficients as function of the sphere sizes in the NEMA NU2 IQ phantom using 4 iterations, 5 subsets, applying ToF, no filter (nonEARL), with (circle) and without (diamond) PSF resolution modeling. For comparison, the upper- and lower limits of  $SUV_{max}$  recoveries as described by current EARL guidelines (EARL1 (solid black lines)) and EARL 2019 guidelines (EARL2 (solid gray lines)) have been included.



**Supplemental Figure 2**  $SUV_{mean}$  recovery coefficients as function of the sphere sizes in the NEMA NU2 IQ phantom using 4 iterations, 5 subsets, applying ToF, no filter (nonEARL), with (circle) and without (diamond) PSF resolution modeling. For comparison, the upper- and lower limits of  $SUV_{mean}$  recoveries as described by current EARL guidelines (EARL1 (solid black line)) and EARL 2019 guidelines (EARL2 (solid gray line)) have been included.

**Supplemental Table 1** Current EANM recommendations for FDG administration (20) describe for a patient of 75 kg in weight for the Vision with a bed overlap of 49.7% to administer  $7 \text{ MBq} \cdot \text{min} \cdot \text{bed}^{-1} \cdot \text{kg}^{-1}$ . This equals  $3.5 \text{ MBq} \cdot \text{kg}$  for scanning 2 min per bed position and  $2.33 \text{ MBq} \cdot \text{kg}$  for scanning 3 min per bed position. Following the standard operating procedure “EARL procedure for assessing PET/CT system specific patient FDG activity preparations for quantitative FDG PET/CT studies” (23) results were obtained for 15, 30, 60, 120, and 300 s of scan time, respectively, using the EARL1 reconstruction with 4 iterations, 5 subsets, a matrix size of 220, applying PSF and ToF, and a Gaussian filter of 7 mm. Results indicated in green represent coefficient of variation values of <15%. The corresponding activity dose and scan duration provide a first insight in applicable activity dose and scan duration for clinical practice. Translating this to continuous bed motion (Flow) scanning versus step-and-shoot for a typical whole body scan of ~105 cm: with an axial FOV of 26.3 cm and a bed overlap of 49.7%, 105 cm means 8 total beds. 8 total beds in 1 min per bed position step-and-shoot acquisition (see \*) corresponds to 8 minutes scan duration. Conversion of the above mentioned step-and-shoot acquisition to continuous bed motion (without overlap) equals a table speed of ~2.2 mm/s.

**EARL1: PSF ToF 4i5s m220 G7**

Activity [MBq/kg]/Duration [s]		15	30	60	120	300
T0	4.00	14	10	9	7	4
T0+1h	2.73	15	11	9	7	4
T0+2h	1.87	18	13	10	8	5
T0+3h	1.29	22	16	11	8	6
T0+4h	0.88 *	26	19	14	10	7
T0+5h	0.56	32	26	18	13	8
T0+6h	0.41	37	30	21	15	10

\*For scanning 1 min per bed position on the Vision, FDG administration can be decreased by a factor ~8

**Supplemental Table 2** Following the standard operating procedure “EARL procedure for assessing PET/CT system specific patient FDG activity preparations for quantitative FDG PET/CT studies” (23) results were obtained for 15, 30, 60, 120, and 300 s of scan time, respectively, using the EARL2 reconstruction with 4 iterations, 5 subsets, a matrix size of 220, applying PSF and ToF, and a Gaussian filter of 5 mm. Results indicated in green represent coefficient of variation values of <15%. The corresponding activity dose and scan duration provide a first insight in applicable activity dose and scan duration for clinical practice.

**EARL2: PSF ToF 4i5s m220 G5**

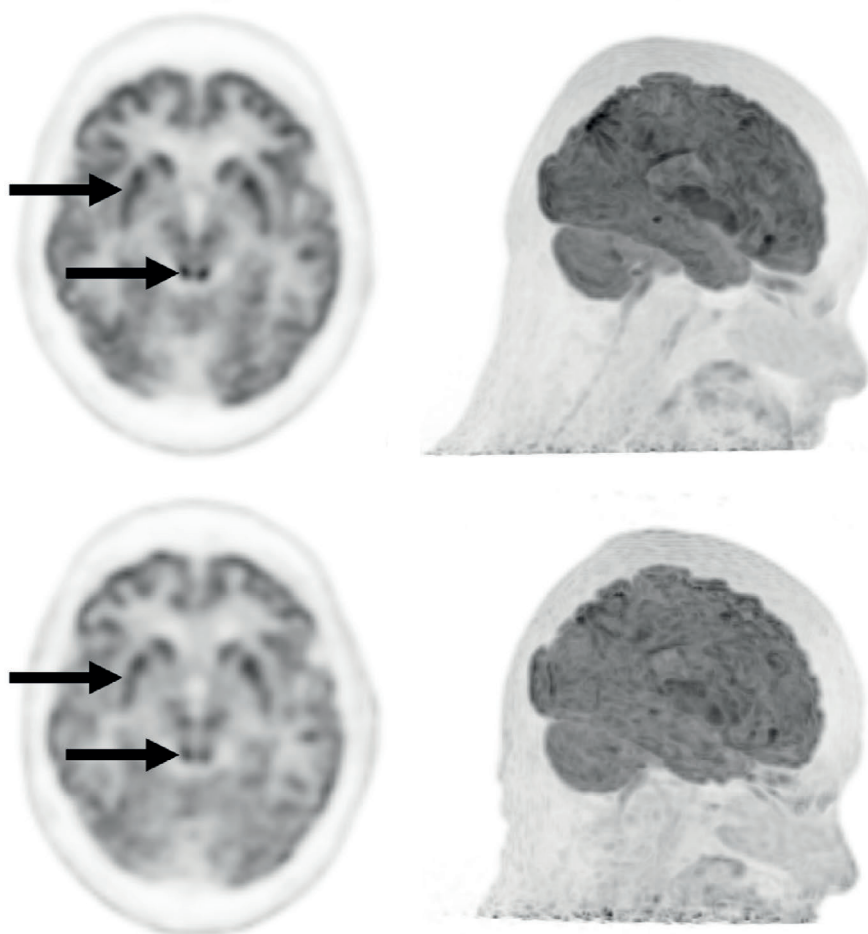
Activity [MBq/kg]/Duration [s]		15	30	60	120	300
T0	4.00	20	14	10	7	5
T0+1h	2.73	22	17	12	9	6
T0+2h	1.87 *	26	20	14	11	7
T0+3h	1.29	33	24	16	11	8
T0+4h	0.88	42	29	21	15	10
T0+5h	0.56	48	38	26	18	12
T0+6h	0.41	56	43	29	22	13

\*For scanning 1 min per bed position on the Vision, FDG administration can be decreased by a factor ~4

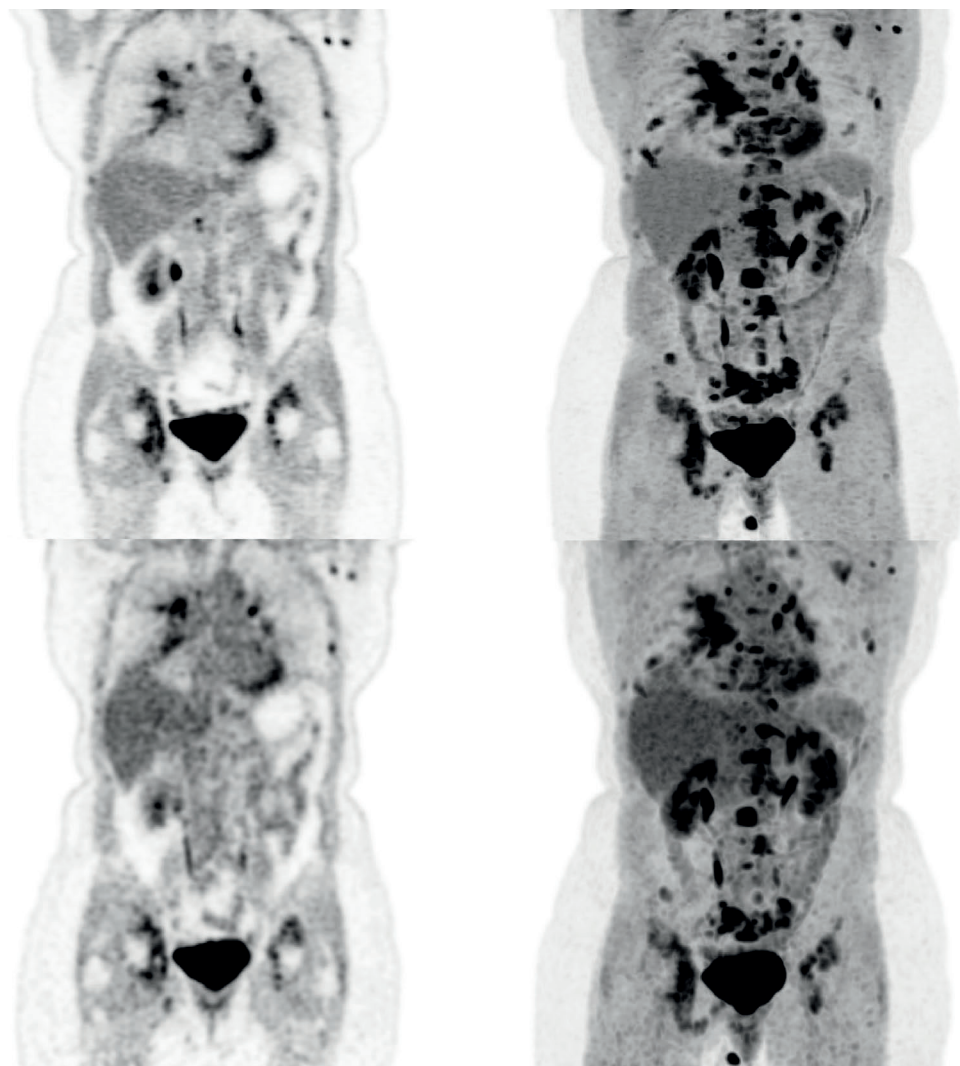


**Supplemental Table 3** Following the standard operating procedure “EARL procedure for assessing PET/CT system specific patient FDG activity preparations for quantitative FDG PET/CT studies” (23) results were obtained for 15, 30, 60, 120, and 300 s of scan time, respectively, using the vendor recommended reconstruction protocol with 4 iterations, 5 subsets, a matrix size of 440, applying PSF and ToF. Results indicated in green represent coefficient of variation values of <15%. The corresponding activity dose and scan duration provide a first insight in applicable activity dose and scan duration for clinical practice.

<b>Vendor recommended: PSF ToF 4i5s m440 all pass</b>						
	Activity [MBq/kg]/Duration [s]	15	30	60	120	300
T0	4.00	52	35	25	18	11
T0+1h	2.73	61	44	31	23	14
T0+2h	1.87	76	53	37	27	17
T0+3h	1.29	87	63	43	31	20
T0+4h	0.88	119	84	59	39	24
T0+5h	0.56	138	97	64	45	28
T0+6h	0.41	166	114	77	56	35



**Supplemental Figure 3** Brain images acquired on the Biograph Vision (upper row) and images acquired on the Biograph mCT (lower row). Data acquired on the Vision were reconstructed using 3D-ToF OP-OSEM with 8 iterations and 5 subsets, with resolution modeling into a  $440 \times 440$  matrix with a size of  $1.6 \times 1.6 \times 1.6$  mm. Data from the mCT were reconstructing using 3D-ToF OP-OSEM with 6 iterations, 21 subsets, and resolution modeling. The resulting image size was  $400 \times 400$  with a voxel size of  $2 \times 2 \times 2$  mm. For both reconstruction protocols, no filter was used. The black arrows indicate the striatum and thalamus. In the images acquired on the Vision a more clear demarcation of the striatum and thalamus can be observed.



**Supplemental Figure 4** Illustrative coronal images (left column) and maximum intensity projection images (right column) acquired on the Biograph Vision (upper row) and on the Biograph mCT (lower row) of a 56-year old female patient with metastasized non-small cell lung carcinoma. On visual inspection, the difference in tissue structures is more clearly defined in images obtained from the new digital Biograph Vision. It should be noted that a 2 mm Gaussian filter was applied on the images acquired on the Biograph mCT in contrast to the images acquired on the Biograph Vision. Also, an approximate 20-30 longer uptake time applies to the scans performed on the Biograph Vision in comparison to the scans performed on the Biograph mCT system. These differences in reconstruction and  $^{18}\text{F}$ -FDG uptake time may result in relatively small differences in image quality.





# Chapter 4

---

## Image quality and semiquantitative measurements on the Biograph Vision PET/CT system: initial experiences and comparison with the Biograph mCT

Joyce van Sluis<sup>1</sup>, Ronald Boellaard<sup>1,2</sup>, Ananthi Somasundaram<sup>1</sup>, Johannes H. van Snick<sup>1</sup>, Ronald J.H. Borra<sup>1</sup>, Rudi A.J.O. Dierckx<sup>1</sup>, Gilles N. Stormezand<sup>1</sup>, Andor W.J.M. Glaudemans<sup>1</sup>, and Walter Noordzij<sup>1</sup>

<sup>1</sup>Department of Nuclear Medicine and Molecular Imaging, University of Groningen, University Medical Center Groningen, Hanzeplein 1, 9713 GZ Groningen, The Netherlands

<sup>2</sup>Department of Radiology and Nuclear Medicine, Cancer Center Amsterdam, Amsterdam University Medical Centers, Free University of Amsterdam, De Boelelaan 1117, 1081 HV Amsterdam, The Netherlands

*J Nucl Med.* 2020;61:129-135.



## **Abstract**

In May 2018, the Biograph Vision PET/CT system was installed at the University Medical Center Groningen. This study evaluated the initial experiences with this new PET/CT system in terms of perceived image quality and semiquantitative analysis in comparison to the Biograph mCT as a reference.

**Methods** In total, 20 oncologic patients were enrolled and received a single 3 MBq/kg injected dose of  $^{18}\text{F}$ -FDG followed by a dual-imaging PET scan. Ten patients were scanned on the Biograph mCT first, whereas the other 10 patients were scanned on the Biograph Vision first. The locally preferred clinically reconstructed images were blindly reviewed by 3 nuclear medicine physicians and scored (using a Likert scale of 1-5) on tumor lesion demarcation, overall image quality, and image noise. In addition, these clinically reconstructed images were used for semiquantitative analysis by measurement of SUVs in tumor lesions. Images acquired using reconstructions conform with the European Association of Nuclear Medicine Research Ltd. (EARL) specifications were also used for measurements of SUV in tumor lesions and healthy tissues for comparison between systems.

**Results** The  $^{18}\text{F}$ -FDG dose received by the 14 men and 6 women (age range, 36-84; mean  $\pm$  SD, 61  $\pm$  16 y) ranged from 145 to 405 MBq (mean  $\pm$  SD, 268  $\pm$  59.3). Images acquired on the Biograph Vision were scored significantly higher on tumor lesion demarcation, overall image quality, and image noise than images acquired on the Biograph mCT ( $P < 0.001$ ). The overall interreader agreement showed a Fleiss  $\kappa$  of 0.61 (95% confidence interval, 0.53-0.70). Furthermore, the SUVs in tumor lesions and healthy tissues agreed well (within 95%) between PET/CT systems, particularly when EARL-compliant reconstructions were used on both systems.

**Conclusion** In this initial study, the Biograph Vision showed improved image quality compared with the Biograph mCT in terms of lesion demarcation, overall image quality, and visually assessed signal-to-noise ratio. The 2 systems are comparable in semiquantitatively assessed image biomarkers in both healthy tissues and tumor lesions. Improved quantitative performance may, however, be feasible using the clinically optimized reconstruction settings.

## **Introduction**

PET integrated with CT is a standard of care used in oncology (1-3) and many other indications, such as infectious diseases, cardiology, and neurology. In oncology, PET/CT is a commonly used and rapidly evolving technique for, among others, differentiation between benign and malignant tumors, cancer staging, primary tumor definition, therapy prediction and guidance, and radiation therapy planning (1,3).

Improvements in PET instrumentation over the years include the use of fast lutetium oxyorthosilicate crystals permitting shorter coincidence timing windows (4,5), new reconstruction methods with time-of-flight (ToF) application (5-9) for improved image signal-to-noise ratio, and expansion of the axial field-of-view for increased volume sensitivity and axial coverage (9). Recently, silicon photomultiplier (SiPM)-based detectors emerged, offering several advantages over photomultiplier tubes such as more compact size, higher intrinsic time resolution, and higher photon detection efficiency, making them favorable for coupling with ToF reconstruction (10,11).

The most commonly used PET radiotracer at present is  $^{18}\text{F}$ -FDG, a glucose analog, for which accumulation in tissue is proportional to glucose utilization (1). Based on increased glucose uptake and glycolysis of specific tumors,  $^{18}\text{F}$ -FDG PET/CT has been proven to be essential in detecting cancer, staging it, planning its therapy, and evaluating the response (12-16).

In May 2018, the first SiPM-based Biograph Vision PET/CT system (Siemens Healthineers) was installed at the Department of Nuclear Medicine and Molecular Imaging at the University Medical Center Groningen. The 3.2-mm crystal size allows for a high system spatial resolution, and full coverage of the small crystals by the SiPM detector elements optimizes light collection, enabling improved timing resolution and signal-to-noise ratio (17).

The main purpose of this study was to evaluate initial clinical experiences and to explore whether the system yields improved image quality and diagnostic performance (i.e., lesion demarcation, overall image quality, and visually assessed signal-to-noise ratio) in comparison with its predecessor, the Biograph mCT (Siemens Healthineers). Therefore, a comparison between whole body  $^{18}\text{F}$ -FDG clinical images obtained on the Biograph Vision and the Biograph mCT -both being systems of the same vendor- has been explored both visually and semiquantitatively.

## **Materials and methods**

### **Patient population**

Between June and August 2018, 20 patients who were referred to the Department of Nuclear Medicine and Molecular Imaging for oncologic clinical PET/CT were enrolled in this prospective study.

Patients with a glucose level equal to or over 198 mg/dL before  $^{18}\text{F}$ -FDG injection were excluded, as were pregnant women and patients unable to lie still for the duration of the examination.

The local medical ethics review board of the University Medical Center Groningen waived the need for formal ethical review (waiver number METc2017/489) on review of the study protocol. In addition, patients were informed about the study aims, procedures, and the need to acquire an additional low-dose CT scan (~1 mSv)

and gave written informed consent to participate.

### **Imaging protocol**

All patients received a single intravenous injection of a weight-based dose of  $^{18}\text{F}$ -FDG (3 MBq/kg, according to European Association of Nuclear Medicine guidelines) (18) and then underwent a dual-imaging PET protocol, including a PET/CT scan on the Biograph Vision and a PET/CT scan on the Biograph mCT. Ten patients first underwent acquisition on the Biograph mCT at 60 min after injection, followed immediately by image acquisition using the Biograph Vision at approximately 90 min after injection. In the other 10 patients, the order was switched to control for increased radiotracer uptake in the tumor over time, possibly influencing image quality. Since the PET/CT systems at the Department of Nuclear Medicine and Molecular Imaging at the University Medical Center Groningen are accredited for  $^{18}\text{F}$ -FDG PET/CT imaging by the European Association of Nuclear Medicine Research Ltd. (EARL), the EARL imaging protocol is followed strictly. This protocol recommends that the scan start at 60 min after injection (1,19). Second scans were done immediately after the first; therefore,  $^{18}\text{F}$ -FDG uptake time and interval between scans were comparable for all 20 patients.

Patients were instructed to fast and avoid strenuous exercise for at least 4-6 h before the  $^{18}\text{F}$ -FDG injection. At the time of injection, blood glucose levels were no more than 198 mg/dL. A standard low dose CT scan was obtained from the vertex to the mid-thighs and used for attenuation correction. On the Biograph Vision, the parameters were an x-ray tube current of 43 mAs, a tube voltage of 100 kV, and a spiral pitch factor of 1. On the 40- and 64-slice Biograph mCT, the respective parameters were an x-ray tube current of 103 and 99 mAs, a tube voltage of 140 and 140 kV, and a spiral pitch factor of 1 and 1.5. Afterward, an emission PET scan was acquired at 3 min per bed position in listmode. All scans were acquired during normal breathing without respiratory motion gating or correction.

Images acquired on the Biograph Vision were reconstructed using the vendor-recommended, clinically most relevant reconstruction protocol -that is, an ordinary Poisson ordered-subset expectation maximization (OP-OSEM) 3-dimensional (3D) iterative algorithm (20) with 4 iterations and 5 subsets, with application of ToF, resolution modeling, and no filtering. The resulting PET images had an image matrix of 440 x 440 with a voxel size of 1.6 x 1.6 x 1.5 mm. Images acquired on the Biograph mCT were reconstructed using the locally preferred clinical reconstruction protocol: 3D ToF OP-OSEM with 3 iterations, 21 subsets, and resolution modeling. A Gaussian filter of 5 mm was applied to the reconstructed images, and the resulting image matrix was 400 x 400 with a voxel size of 2 x 2 x 2 mm. In addition, EARL reconstructions (1,19) were obtained for both the Biograph Vision and the Biograph

mCT. Images acquired on the Biograph Vision were reconstructed to comply with EARL using 3D ToF OP-OSEM with 4 iterations and 5 subsets, with application of resolution modeling and a Gaussian filter of 7 mm. The resulting image matrix was 440 x 440 with a voxel size of 1.6 x 1.6 x 1.5 mm. The EARL reconstruction for images obtained from the Biograph mCT used 3D ToF OP-OSEM with 3 iterations and 21 subsets, resolution modeling, and a Gaussian filter of 6.5 mm, for a resulting image matrix of 256 x 256 with a voxel size of 3.2 x 3.2 x 2 mm.

### Qualitative image analysis

The acquired images were independently reviewed and analyzed using a dedicated Syngo.via VB30 workstation (Siemens Healthineers). All PET images acquired from the recommended clinical reconstruction protocols were blindly evaluated by 3 experienced nuclear medicine physicians (with 15, 5, and 10 y of experience in interpreting PET scans). The readers were not aware of the clinical indication for the PET/CT exam.

Readers were allowed to manually adjust the standard window settings. Subsequently, they assessed the following quality criteria based on 5-point Likert scales: tumor lesion demarcation (ranging from 1 [lesion cannot be confirmed] to 5 [excellent lesion margin demarcation]), overall image quality (ranging from 1 [poor overall image quality] to 5 [excellent overall image quality]), and image noise (ranging from 1 [enormous image noise] to 5 [no perceivable image noise]) (10,21). In addition, per clinically recommended reconstruction, the number of suggestive  $^{18}\text{F}$ -FDG-avid lesions was counted.

In cases of large assessment differences between readers, the specific images were discussed in a consensus meeting.

### Semiquantitative image analysis

Semiquantitative analyses were performed using the quAntitative onCology moleCUlar Analysis suiTE (ACCURATE) (22). Using the EARL-reconstructed images, 0.5-mL spheric volumes of interest were placed in healthy tissues (aortic arch, semioval center [white matter], lung, left ventricle of the heart, parotid gland, quadriceps femoris muscle, spleen). From these volumes of interest,  $\text{SUV}_{\text{max}}$ ,  $\text{SUV}_{\text{peak}}$ , and  $\text{SUV}_{\text{mean}}$  were obtained. In addition, using the EARL-reconstructed images and the locally preferred clinical reconstructed images, volumes of interest were placed in the different lesions per patient (with an overall maximum of 5 lesions per patient and a maximum of 2 in the same tissue type). For reference-tissue purposes, a 3-mL spheric volume of interest was placed in the liver. From these measurements, the  $\text{SUV}_{\text{max}}$ ,  $\text{SUV}_{\text{peak}}$ , and  $\text{SUV}_{\text{mean}}$  were compared between systems.

## Statistical analysis

Statistical analysis was performed with SPSS Statistics, version 25.0 (IBM Corp.). Scoring of the images acquired on the 2 PET/CT systems was compared pairwise using a 2-tailed paired-samples t test. For interreader agreement on tumor lesion demarcation, overall image quality, and image noise, the original 5-point scores were reassigned to 3-point scores (1 + 2 became 1, 3 became 2, and 4 + 5 became 3). Interreader agreement was subsequently evaluated using the k statistic. Bland-Altman plot analysis was performed to assess the agreement regarding  $SUV_{max}$ ,  $SUV_{peak}$ , and  $SUV_{mean}$  obtained in healthy tissues and in lesions between the 2 systems. Subsequently, equivalence tests were done on each of the healthy tissues and on the tumor lesions to quantify agreement on SUV between the systems. Furthermore, using partial correlation, the relation between SUV and the interval between scans was evaluated.

## Results

In total, 20 oncologic patients (14 men and 6 women; age range, 36-84; mean  $\pm$  SD,  $61 \pm 16$  y) were enrolled in the study. To simulate the actual clinical experience, different cancer types were included. Table 1 shows relevant demographic and clinical information. The injected  $^{18}F$ -FDG dose ranged from 145 to 405 MBq (mean  $\pm$  SD,  $268 \pm 59.4$  MBq). All patients had a blood glucose level of no more than 198 mg/dL before dose administration. To control for the possibility that increased  $^{18}F$ -FDG tumor uptake over time might influence image quality, the first 10 patients were scanned on the Biograph mCT first, whereas the other 10 patients were scanned on the Biograph Vision first. The interval between the start of the first and second scans ranged from 24 to 60 min (mean  $\pm$  SD,  $37 \pm 7.7$  min).

### Qualitative image quality

The average scores of the 3 readers for the Biograph mCT images versus the Biograph Vision images were  $3.3 \pm 1.0$  versus  $4.3 \pm 0.80$  for lesion demarcation,  $3.4 \pm 0.90$  versus  $4.3 \pm 0.80$  for overall image quality, and  $3.4 \pm 0.70$  versus  $3.9 \pm 0.70$  for image noise. Images acquired on the Biograph Vision were scored significantly higher on tumor lesion demarcation (median 5), overall image quality (median 4), and image noise (median 4) than images acquired on the Biograph mCT (medians of 3, 3, and 3, respectively;  $P < 0.01$ ). The overall interreader agreement showed a Fleiss  $\kappa$  of 0.61 (95% confidence interval, 0.53-0.70). Example images of patients of standard weight (91 and 101 kg) are shown in Figures 1 and 2. Supplemental Figures 1 and 2 show images of a lighter-weight (53 kg) and a heavier-weight (139 kg) patient, respectively (supplemental materials are available at <http://jnm.snmjournals.org>).

**Table 1** Demographic and clinical data of all study participants.

Patient #	Age [y]	Sex	Weight [kg]	Disease	Injected $^{18}\text{F}$ -FDG dose [MBq]	Time delay [min]*
1	40	F	73	Ovarian cancer	230	28
2	69	M	90	Colon cancer	270	40
3	79	M	90	Lung cancer	305	38
4	49	M	97.5	Lung cancer	305	40
5	36	M	79.5	Sarcoidosis	220	42
6	84	M	91	Lung cancer	270	42
7	66	F	101	Thyroid cancer	300	29
8	75	M	88.2	Multiple myeloma	280	60
9	66	F	72	Breast cancer	215	32
10	74	M	139	Melanoma	405	33
11	59	M	106	Esophageal cancer	305	30
12	84	M	73	Esophageal cancer	220	33
13	59	M	104	Oropharyngeal cancer	320	37
14	77	M	62	Colon cancer	200	39
15	62	M	77	Esophageal cancer	240	46
16	63	M	105	Lymphoma	300	41
17	52	F	115	Lymphoma	355	36
18	60	F	89	Esophageal cancer	235	35
19	47	F	53	Lung cancer	145	36
20	25	M	79	Testicular cancer	235	24

\*Time delay between the first and second scan in minutes. Images were acquired on the Biograph mCT first for the first ten patients. For the other ten patients images were acquired on the Biograph Vision first

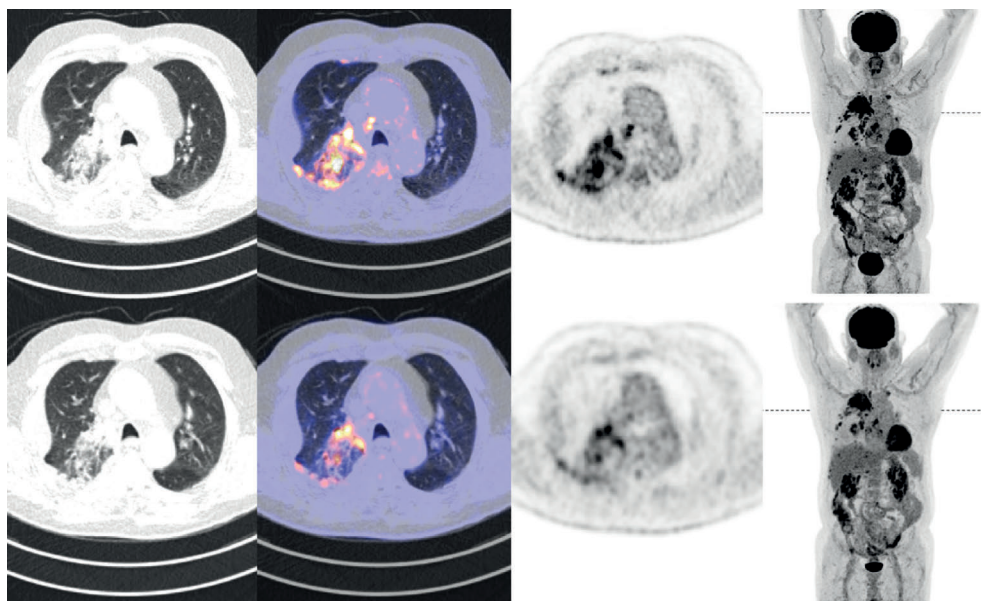


**Figure 1** Transaxial CT, fused PET/CT, PET, and maximum intensity projection PET images (from left to right) acquired on the Biograph Vision (top) and the Biograph mCT (bottom) for an 84-y-old male (weight, 91 kg) with metastasized non-small cell lung carcinoma. Position of the transaxial slice is indicated on the maximum intensity projection images (dashed line).

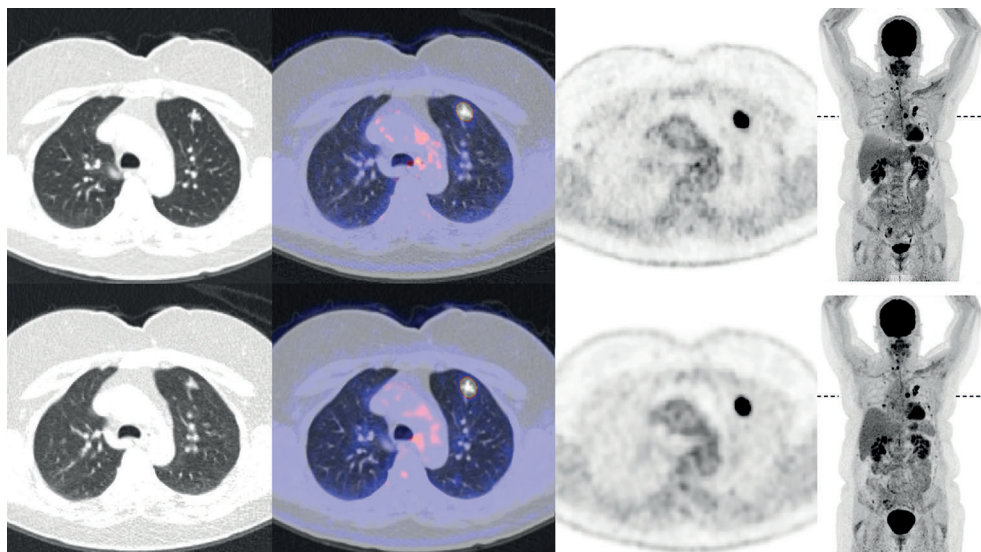


**Figure 2** Transaxial CT, PET/CT, PET, and maximum intensity projection PET images (from left to right) acquired on the Biograph Vision (top) and the Biograph mCT (bottom) for a 66-y-old female (weight, 101 kg) with metastasized thyroid cancer. Position of the transaxial slice is indicated on the maximum intensity projection images (dashed line).

In 7 of the 20 patients, one or more  $^{18}\text{F}$ -FDG-avid lesions not seen on the Biograph mCT images were identified on the Biograph Vision images. These additional lesions all measured below 0.75 cm in diameter and were located in areas with significant motion, such as the lungs and near the diaphragm. Figures 3 and 4 show examples of the additional lesions found on the Biograph Vision images.

### Semiquantitative image quality

The results of the equivalence tests of SUV in healthy tissue matched per patient are presented in Table 2. The SUVs in tumor lesions and healthy tissues agreed well between the 2 PET/CT systems when EARL-compliant reconstructions were used. Bland-Altman plots displaying agreement in  $\text{SUV}_{\text{max}}$  in normal tissues between the 2 systems are shown in Supplemental Figure 3. The results of the equivalence tests for  $\text{SUV}_{\text{max}}$ ,  $\text{SUV}_{\text{peak}}$ , and  $\text{SUV}_{\text{mean}}$  in tumor lesions are presented in Table 3; there was no significant difference between the 2 systems. Agreement in tumor lesion  $\text{SUV}_{\text{max}}$ ,  $\text{SUV}_{\text{peak}}$ , and  $\text{SUV}_{\text{mean}}$  between the 2 systems is shown in Bland-Altman plots in Figure 5. Scatterplots of lesion SUVs from images obtained on the 2 systems are displayed in Supplemental Figure 4.  $\text{SUV}_{\text{max}}$ ,  $\text{SUV}_{\text{peak}}$ , and  $\text{SUV}_{\text{mean}}$  distributions between EARL-compliant and clinically reconstructed images acquired on the 2 systems are shown in boxplots in Figure 6.

Partial correlation testing showed no significant correlation between normal-tissue

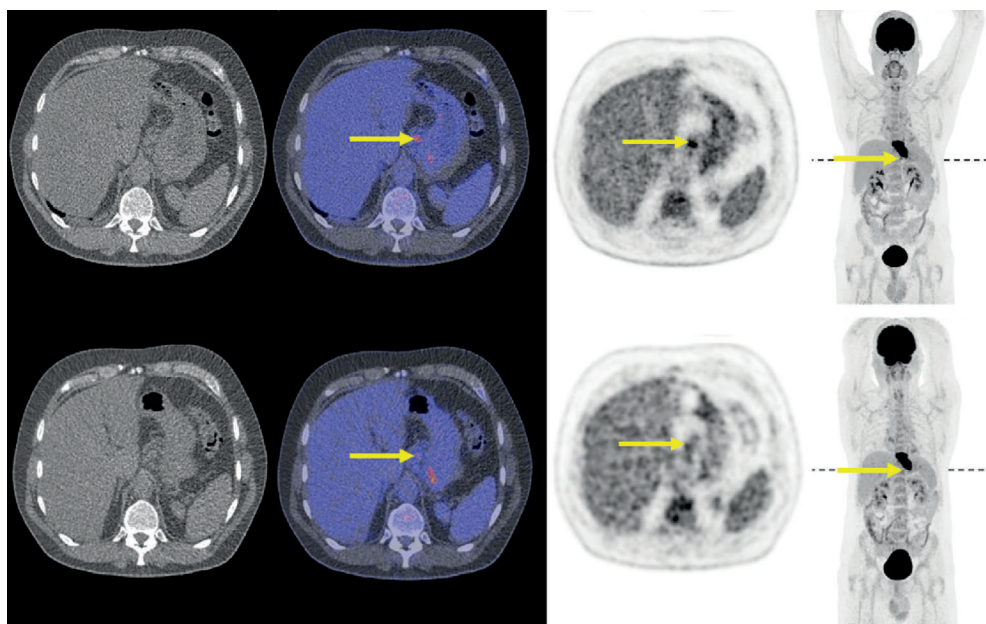


**Figure 3** Transaxial CT, PET/CT, PET, and maximum intensity projection PET images (from left to right) acquired on the Biograph Vision (top) and the Biograph mCT (bottom) for a 59-y-old male (weight, 106 kg) with metastasized esophageal cancer. Position of the transaxial slice is indicated on the maximum intensity projection images (dashed line). Arrows indicate a small lesion found on the Biograph Vision images that did not appear as such on the Biograph mCT images.

$SUV_{max}$ ,  $SUV_{peak}$ , or  $SUV_{mean}$  and the interval between imaging on the 2 systems, nor was there a correlation between lesion  $SUV_{max}$ ,  $SUV_{peak}$ , or  $SUV_{mean}$  and the interval.

Furthermore, SUVs of additional lesions found on the Biograph Vision images were compared with SUVs obtained from the Biograph mCT images.  $SUV_{max}$  ranged from 4.5 to 34.5 (median, 7.5) for the Biograph Vision and from 2.1 to 8.7 (median, 2.9) for the Biograph mCT.  $SUV_{peak}$  and  $SUV_{mean}$  were similar between the 2 systems.

## Discussion

This study evaluated initial experiences with the Biograph Vision and found that it outperforms its predecessor, the Biograph mCT, in terms of visually assessed image quality, tumor lesion demarcation, overall image quality, and signal-to-noise ratio. Semiquantitative analyses showed both systems to be comparable in assessing biomarkers in both healthy tissues and tumor lesions. Furthermore, in 7 of 20 patients, one or more  $^{18}F$ -FDG-avid lesions not found on the Biograph mCT images were identified on the Biograph Vision images, a result that could have important clinical consequences.

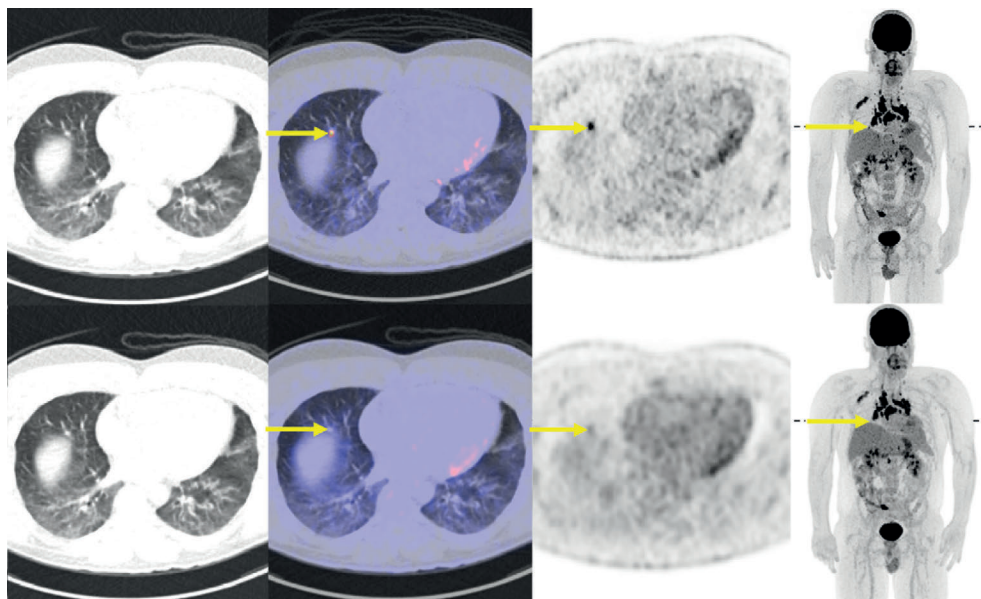


**Figure 4** Transaxial CT, PET/CT, PET, and maximum intensity projection PET images (from left to right) acquired on the Biograph Vision (top) and the Biograph mCT (bottom) for a 36-y-old male (weight, 69 kg) with sarcoidosis. Position of the transaxial slice is indicated on the maximum intensity projection images (dashed line). Arrows indicate a small lesion found on the Biograph Vision images that did not appear as such on the Biograph mCT images.

**Table 2** Difference in SUVs in healthy organ tissues.

Organs	Mean difference mCT-Vision SUV $\pm$ SD	95% CI	P	Equivalence	
<u>Aortic arch</u>	SUV <sub>max</sub>	-0.01 $\pm$ 0.47	-0.23; 0.21	0.921	Equivalent
	SUV <sub>peak</sub>	-0.04 $\pm$ 0.49	-0.23; 0.23	0.991	Equivalent
	SUV <sub>mean</sub>	-0.11 $\pm$ 0.43	-0.21; 0.20	0.966	Equivalent
<u>Semioval center</u>	SUV <sub>max</sub>	-0.36 $\pm$ 0.83	-0.40; 0.39	0.985	Equivalent
	SUV <sub>peak</sub>	-0.31 $\pm$ 0.87	-0.41; 0.40	0.994	Equivalent
	SUV <sub>mean</sub>	0.01 $\pm$ 0.43	-0.20; 0.20	0.997	Equivalent
<u>Liver</u>	SUV <sub>max</sub>	0.38 $\pm$ 0.28	-0.13; 0.13	0.956	Equivalent
	SUV <sub>peak</sub>	-0.11 $\pm$ 0.41	-0.19; 0.20	0.968	Equivalent
	SUV <sub>mean</sub>	0.04 $\pm$ 0.28	-0.13; 0.13	0.992	Equivalent
<u>Lung</u>	SUV <sub>max</sub>	0.08 $\pm$ 0.15	-0.07; 0.07	0.964	Equivalent
	SUV <sub>peak</sub>	0.02 $\pm$ 0.13	-0.06; 0.06	0.991	Equivalent
	SUV <sub>mean</sub>	0.04 $\pm$ 0.12	-0.06; 0.05	0.867	Equivalent
<u>Left ventricle of the heart</u>	SUV <sub>max</sub>	0.01 $\pm$ 0.65	-0.31; 0.30	0.973	Equivalent
	SUV <sub>peak</sub>	-0.16 $\pm$ 0.68	-0.32; 0.32	0.987	Equivalent
	SUV <sub>mean</sub>	0.04 $\pm$ 0.53	-0.25; 0.25	0.993	Equivalent
<u>Parotid gland</u>	SUV <sub>max</sub>	0.66 $\pm$ 0.97	-0.45; 0.45	0.996	Equivalent
	SUV <sub>peak</sub>	0.17 $\pm$ 0.52	-0.25; 0.24	0.982	Equivalent
	SUV <sub>mean</sub>	0.57 $\pm$ 0.85	-0.40; 0.39	0.979	Equivalent
<u>Quadriceps muscle</u>	SUV <sub>max</sub>	0.20 $\pm$ 0.30	-0.14; 0.14	0.977	Equivalent
	SUV <sub>peak</sub>	0.09 $\pm$ 0.23	-0.11; 0.11	0.992	Equivalent
	SUV <sub>mean</sub>	0.07 $\pm$ 0.16	-0.07; 0.07	0.988	Equivalent
<u>Spleen</u>	SUV <sub>max</sub>	0.07 $\pm$ 0.32	-0.15; 0.15	0.973	Equivalent
	SUV <sub>peak</sub>	0.00 $\pm$ 0.30	-0.14; 0.14	0.995	Equivalent
	SUV <sub>mean</sub>	0.04 $\pm$ 0.32	-0.15; 0.15	0.995	Equivalent

**Table 3** Difference in SUVs in tumor lesions.

	Mean difference mCT-Vision SUV±SD	95% CI	P	Equivalence	
<u>Lesions (EARL)</u>	SUV <sub>max</sub>	0.09 ± 4.09	-1.24; 1.17	0.956	Equivalent
	SUV <sub>peak</sub>	0.07 ± 2.32	-0.69; 0.67	0.985	Equivalent
	SUV <sub>mean</sub>	0.67 ± 5.41	-1.60; 1.58	0.988	Equivalent
<u>Lesions (clinical)</u>	SUV <sub>max</sub>	-6.30 ± 11.75	-3.52; 3.38	0.969	Equivalent
	SUV <sub>max</sub> *			<0.001	Not Equivalent
	SUV <sub>peak</sub>	0.62 ± 4.04	-1.27; 1.10	0.885	Equivalent
	SUV <sub>mean</sub>	-2.68 ± 6.43	-1.90; 1.90	0.991	Equivalent

\*Since the difference between measured SUVmax from the locally preferred clinical reconstructed images between systems was not normally distributed (but skewed), the results of the Wilcoxon signed-rank test were included as well

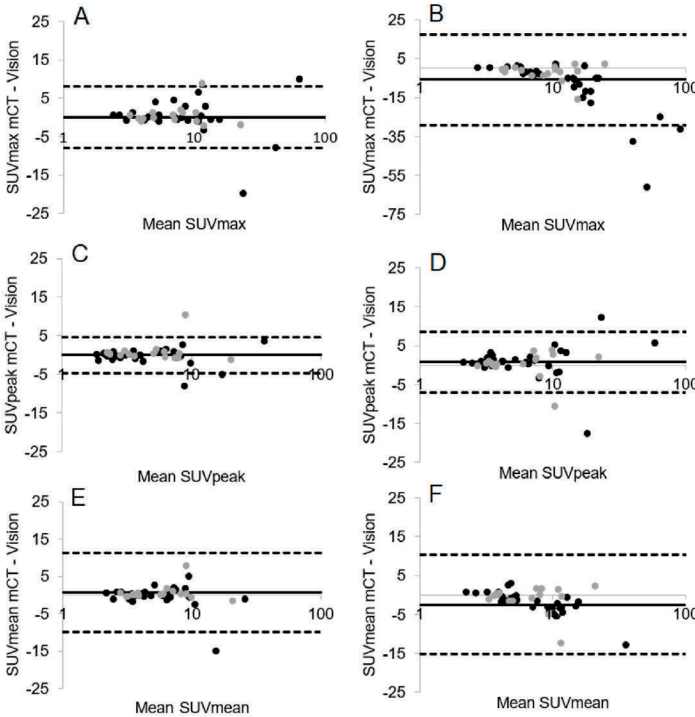


**Figure 5** (A) Bland-Altman plot of Biograph mCT and Biograph Vision SUV<sub>max</sub> lesion differences using EARL-compliant image reconstructions (SUV<sub>max</sub> on Biograph mCT minus SUV<sub>max</sub> on Biograph Vision) against mean SUV<sub>max</sub> (mean SUV<sub>max</sub> between systems) (C) Bland-Altman plot of SUV<sub>peak</sub> lesion differences against mean SUV<sub>peak</sub>; (E) Bland-Altman plot of SUV<sub>mean</sub> lesion differences against mean SUV<sub>mean</sub>. Mean difference is illustrated by the solid line, upper and lower limits of agreement are shown by dashed lines. Measurements performed on the Biograph mCT first and Biograph Vision first are illustrated with black and grey dots, respectively. For direct comparison with lesion SUV differences obtained from locally preferred clinically reconstructed images, see the plots in B, D, and F.

Recent technical developments in PET instrumentation have likely contributed to the improved quality observed in images acquired on the Biograph Vision (23). The introduction of SiPM detectors in commercially available PET/CT systems is of clinical importance because of the potential advantages of this new technology. SiPM-based photodetectors are characterized by superior timing resolution, enabling improved ToF estimation (24), and efficient photon detection.



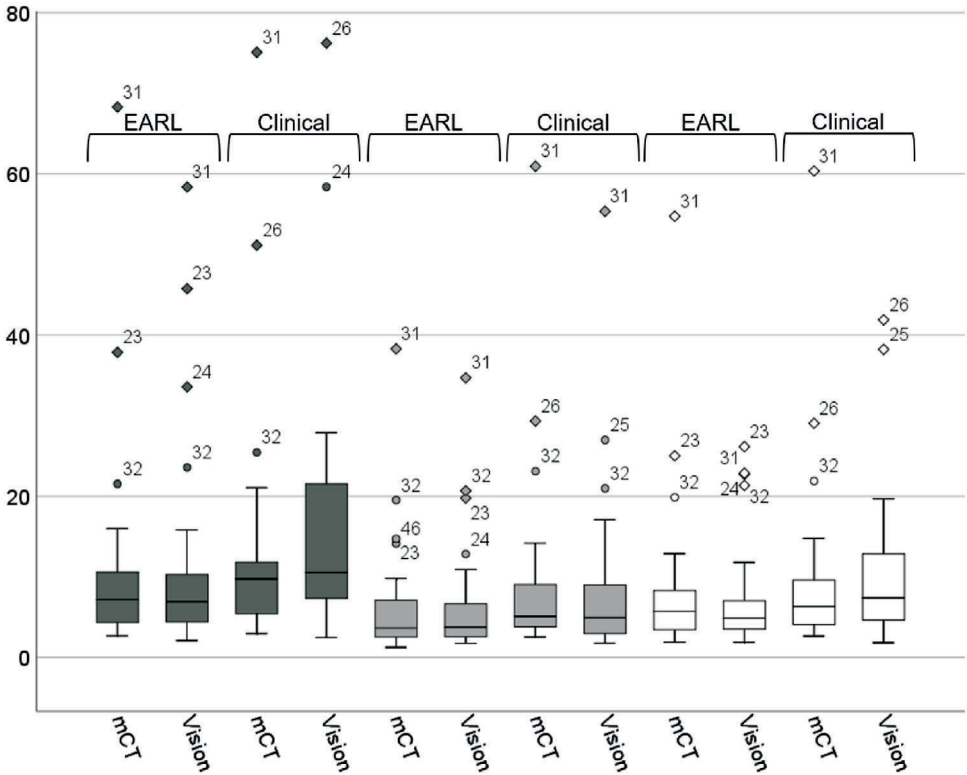


**Figure 6** Boxplots showing  $SUV_{max}$  (dark gray),  $SUV_{peak}$  (light gray), and  $SUV_{mean}$  (white) distributions between EARL-compliant and locally preferred clinically reconstructed images acquired on the Biograph mCT and the Biograph Vision. Dots represent outliers; diamonds represent extreme outliers. For clarity, the y-axis was set from 0 to 80; consequently, a few outliers are not visible (but can be found in the Bland-Altman plots in Fig. 5).

The performance characteristics of the most recently developed SiPM-based PET/CT system, the Biograph Vision, were evaluated and published recently by our group (25). Spatial resolution, sensitivity, count rate performance, accuracy of attenuation and scatter correction, ToF performance, and image quality were evaluated according to the National Electrical Manufacturers Association (NEMA) NU-2 2012 and NEMA NU-2 2018 standards, showing improved performance with regard to its predecessor, the Biograph mCT (25). Of all the current commercially available PET/CT systems, the Biograph Vision also outperforms other SiPM-based systems. For instance, it has a timing resolution of 210 ps, compared with 310 ps for the Vereos (Philips Healthcare) (26) and 375 ps for the Discovery MI (GE Healthcare) (3). The sensitivity of the Biograph Vision has also improved with regard to the other available SiPM-based systems, at 16.4 kcps/MBq for the Biograph Vision as opposed to 5.2 kcps/MBq for the Vereos and 13.7 kcps/MBq for the Discovery MI.

The benefits of higher sensitivity and improved ToF resolution are a higher signal-to-noise ratio (especially for heavy patients), higher overall image quality, higher lesion detectability, and more accurate image quantification (24). Three of these categories have been qualitatively assessed in this study to see whether theoretic and expected improvement in image quality also translates to an improved perceived image quality in clinical practice. The Biograph Vision scored significantly higher than the Biograph mCT on lesion demarcation, overall image quality, and image noise.

With regard to the semiquantitative measurements, good agreement in SUV in tumor lesions and in healthy tissues was seen between the Biograph Vision and the Biograph mCT when EARL-compliant reconstructions were used, as well as when the locally preferred clinical image reconstructions were used. Because of the balanced order in which the dual scans were performed (10 patients being scanned first on the Biograph mCT and the other 10 being scanned first on the Biograph Vision) and because the EARL guidelines for tumor imaging were followed, the interval between the 2 scans had no significant influence on the normal tissue or lesion SUVs. When the locally preferred clinical reconstruction settings are used on the Biograph Vision, the higher spatial resolution of the system and the use of smaller voxel sizes result in less of a partial-volume effect; a higher contrast recovery is obtained, resulting in a slight increase in  $SUV_{max}$  (not significant, however [Figs. 5 and 6; Table 3]). Moreover, the SUVs from the locally preferred clinical reconstructed images were higher, overall, than those from the EARL-compliant images (Fig. 5). The occasional increase in  $SUV_{max}$  in the locally preferred clinical reconstructed images of Figure 5 can be explained by the characteristics of the lesions. If the  $SUV_{max}$  is already high ( $>10$ ) on Biograph mCT images, it will be even higher on Biograph Vision images (because of its higher spatial resolution and smaller voxel size).

The perceived improvement in image quality with the Biograph Vision resulted in identification of one or more additional  $^{18}F$ -FDG-avid lesions in 7 of 20 patients. The additional lesions were all below 0.75 cm in diameter and were located in areas with significant motion, such as the lungs and near the diaphragm. In 1 patient, an additional lesion that was found resulted in upstaging of the disease. In none of the patients therapy was altered, since the additional lesions were near the primary tumor or numerous other small metastases were already considered. However, this study had only a small sample size. Nevertheless, these initial findings suggest that the Biograph Vision would be beneficial for detecting small lesions that could have a clinical impact, such as by changing the disease stage or leading to a different choice of therapy.

Because we believe that comparisons between the 2 systems would be more valid if the groups of oncologic disease were more homogeneous, future such studies are warranted to more deeply explore lesion quantification.

## **Conclusion**

In this initial study, we found that perceived image quality is better with the Biograph Vision than the Biograph mCT: tumor lesions were more sharply demarcated, image quality higher, and signal-to-noise ratio better. Regarding semiquantitative image quality, the 2 systems performed comparably for imaging healthy tissues and tumor lesions. Improved quantitative performance may, however, be feasible using clinically optimized reconstruction settings. Future studies including more homogeneous groups of oncologic disease are warranted to validate our findings and to assess the potential clinical impact of PET imaging using the Biograph Vision.

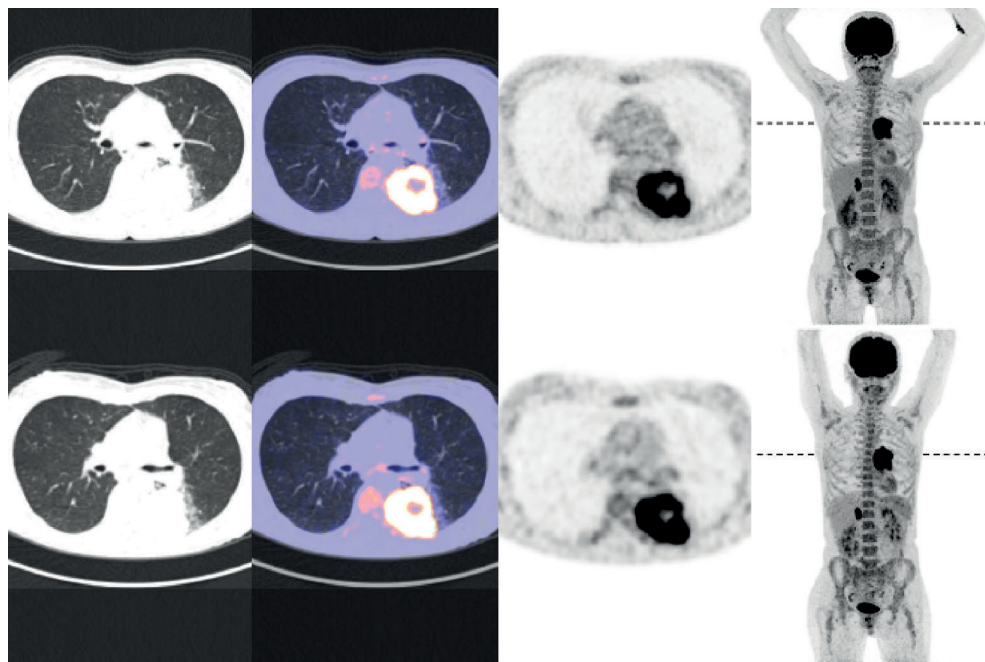
## References

1. Boellaard R, Delgado-Bolton R, Oyen WJG, Giammarile F, Tatsch K, Eschner W, et al. FDG PET/CT: EANM procedure guidelines for tumour imaging: version 2.0. *Eur J Nucl Med Mol Imaging*. 2015;42:328-354.
2. Slomka PJ, Pan T, Germano G. Recent advances and future progress in PET instrumentation. *Semin Nucl Med*. 2016;46:5-19.
3. Hsu DFC, Ilan E, Peterson WT, Uribe J, Lubberink M, Levin CS. Studies of a next-generation silicon-photomultiplier-based time-of-flight PET/CT system. *J Nucl Med*. 2017;58:1511-1518.
4. Melcher CL. Scintillation crystals for PET. *J Nucl Med*. 2000;41:1051-1055.
5. Rausch I, Cal-González J, Dapra D, Gallowitsch HJ, Lind P, Beyer T, et al. Performance evaluation of the Biograph mCT Flow PET/CT system according to the NEMA NU2-2012 standard. *EJNMMI Phys*. 2015;2:26.
6. Moses WW. Time of flight in PET revisited. *IEEE Trans Nucl Sci*. 2003;50:1325-1330.
7. Surti S, Kuhn A, Werner ME, Perkins AE, Kolthammer J, Karp JS. Performance of Philips Gemini TF PET/CT scanner with special consideration for its time-of-flight imaging capabilities. *J Nucl Med*. 2007;48:471-480.
8. Jakoby BW, Bercier Y, Conti M, Casey ME, Bendriem B, Townsend DW. Physical and clinical performance of the mCT time-of-flight PET/CT scanner. *Phys Med Biol*. 2011;56:2375-2389.
9. Jakoby BW, Bercier Y, Watson CC, Bendriem B, Townsend DW. Performance characteristics of a new LSO PET/CT scanner with extended axial field-of-view and PSF reconstruction. *IEEE Trans Nucl Sci*. 2009;56:633-639.
10. Sonni I, Baratto L, Park S, Hatami N, Srinivas S, Davidzon G, et al. Initial experience with a SiPM-based PET/CT scanner: influence of acquisition time on image quality. *EJNMMI Phys*. 2018;5:9.
11. Ullah MN, Pratiwi E, Cheon J, Choi H, Yeom JY. Instrumentation for time-of-flight positron emission tomography. *Nucl Med Mol Imaging*. 2016;50:112-122.
12. Almuhaideb A, Papathanasiou N, Bomanji J. <sup>18</sup>F-FDG PET/CT imaging in oncology. *Ann Saudi Med*. 2011;31:3-13.
13. Avril NE, Weber WA. Monitoring response to treatment in patients utilizing PET. *Radiol Clin North Am*. 2005;43:189-204.
14. Bastiaannet E, Groen B, Jager PL, Cobben DCP, van der Graaf WTA, Vaalburg W, et al. The value of FDG-PET in the detection, grading and response to therapy of soft tissue and bone sarcomas; a systematic review and meta-analysis. *Cancer Treat Rev*. 2004;30:83-101.
15. Borst GR, Belderbos JSA, Boellaard R, Comans EFI, de Jaeger K, Lammertsma AA, et al. Standardised FDG uptake: a prognostic factor for inoperable non-small cell lung cancer. *Eur J Cancer*. 2005; 41:1533-1541.
16. de Geus-Oei L-F, van der Heijden HFM, Corstens FHM, Oyen WJG. Predictive and prognostic value of FDG-PET in nonsmall-cell lung cancer. *Cancer*. 2007; 110:1654-1664.
17. Surti S. Update on time-of-flight PET imaging. *J Nucl Med*. 2015;56:98-105.

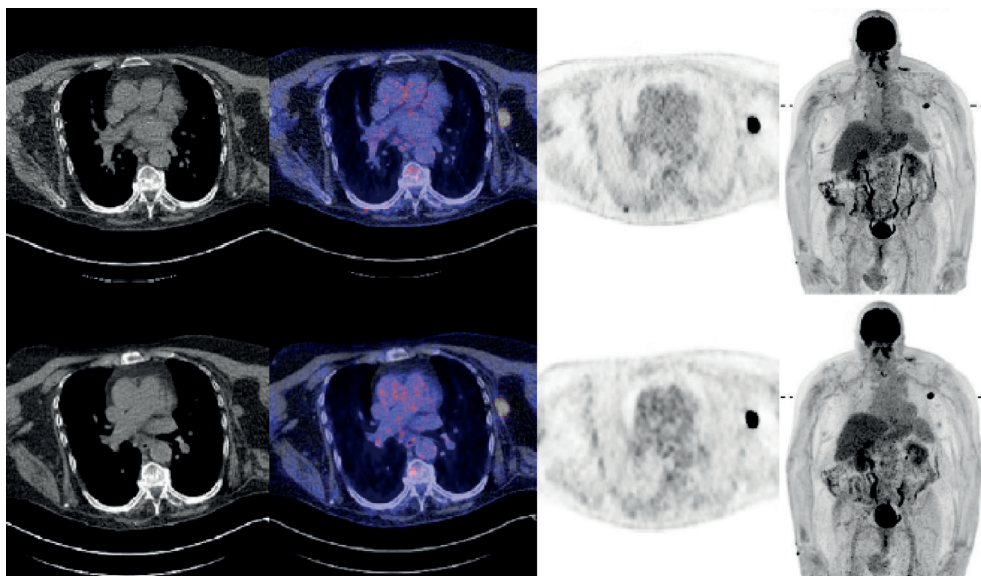


18. Boellaard R, O'Doherty MJ, Weber WA, Mottaghy FM, Lonsdale MN, Stroobants SG, et al. FDG PET/CT: EANM procedure guidelines for tumour imaging-version 1.0. *Eur J Nucl Med Mol Imaging*. 2010;37:181-200.
19. Boellaard R. EANM FDG PET/CT accreditation specifications for SUV recovery coefficients. EANM Research Ltd. website. [http://earl.eanm.org/cms/website.php?id5/en/projects/fdg\\_pet\\_ct\\_accreditation/accreditation\\_specifications.htm](http://earl.eanm.org/cms/website.php?id5/en/projects/fdg_pet_ct_accreditation/accreditation_specifications.htm). Published January 2017. Accessed August 1, 2019.
20. Varrone A, Sjöholm N, Eriksson L, Guly'as B, Halldin C, Farde L. Advancement in PET quantification using 3D-OP-OSEM point spread function reconstruction with the HRRT. *Eur J Nucl Med Mol Imaging*. 2009;36:1639-1650.
21. Lenga L, Czwikla R, Wichmann JL, Leithner D, Albrecht MH, Booz C, et al. Dual-energy CT in patients with colorectal cancer: improved assessment of hypoattenuating liver metastases using noise-optimized virtual monoenergetic imaging. *Eur J Radiol*. 2018;106:184-191.
22. Boellaard R. Quantitative oncology molecular analysis suite: ACCURATE [abstract]. *J Nucl Med*. 2018;59(suppl 1):1753.
23. Hutton BF, Erlandsson K, Thielemans K. Advances in clinical molecular imaging instrumentation. *Clin Transl Imaging*. 2018;6:31-45.
24. Vandenberghe S, Mikhaylova E, D'Hoe E, Mollet P, Karp JS. Recent developments in time-of-flight PET. *EJNMMI Phys*. 2016;3:3.
25. van Sluis J, de Jong JR, Schaar J, Noordzij W, van Snick JH, Dierckx RAJO, et al. Performance characteristics of the digital Biograph Vision PET/CT system. *J Nucl Med*. 2019;60:1031-1036.
26. Rausch I, Ruiz A, Valverde-Pascual I, Cal-González J, Beyer T, Carrio I. Performance evaluation of the Philips Vereos PET/CT system according to the NEMA NU2-2012 standard. *J Nucl Med*. 2019;60:561-567.

## Supplemental data

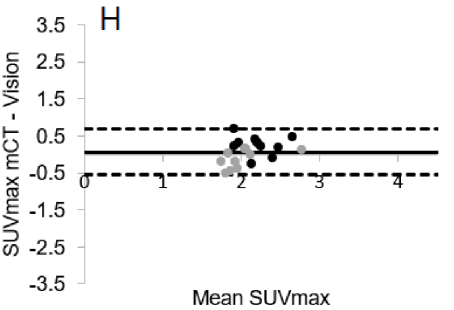
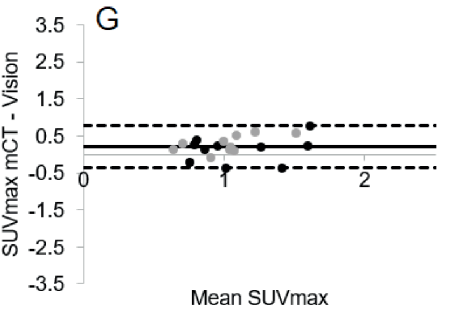
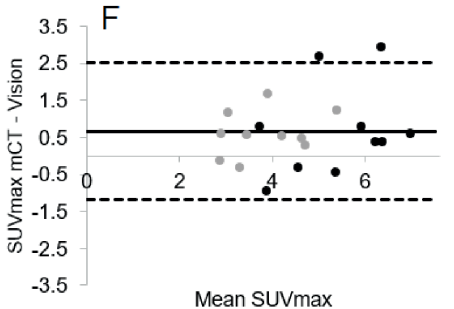
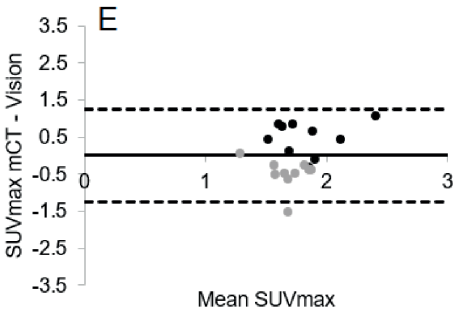
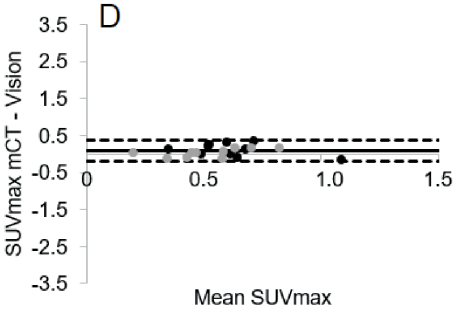
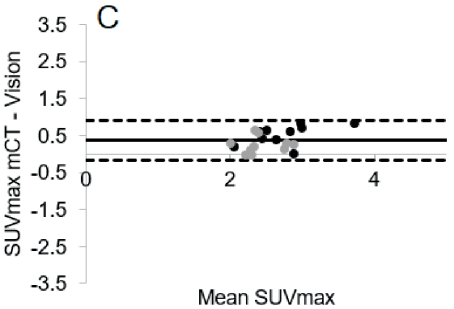
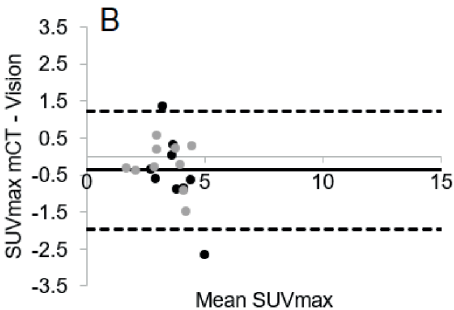
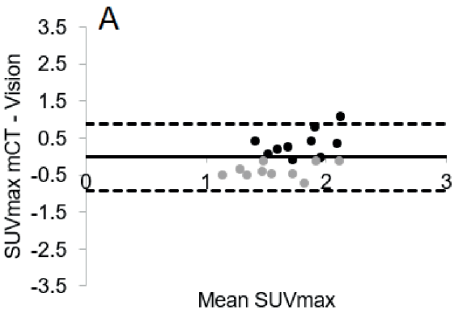


**Supplemental Figure 1** Illustrative transaxial CT, fused PET/CT, PET, and maximum intensity projection PET images (from left to right) acquired on the Biograph Vision (upper row) and acquired on the Biograph mCT (lower row) of a 47-year old female patient (weight 53 kg) with metastasized non-small cell lung carcinoma. The position of the transaxial slice is indicated on the maximum intensity projection images (dashed line).

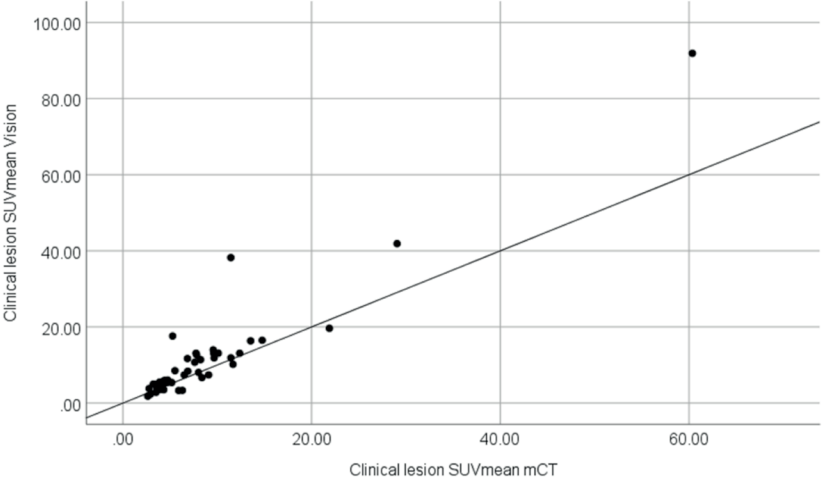
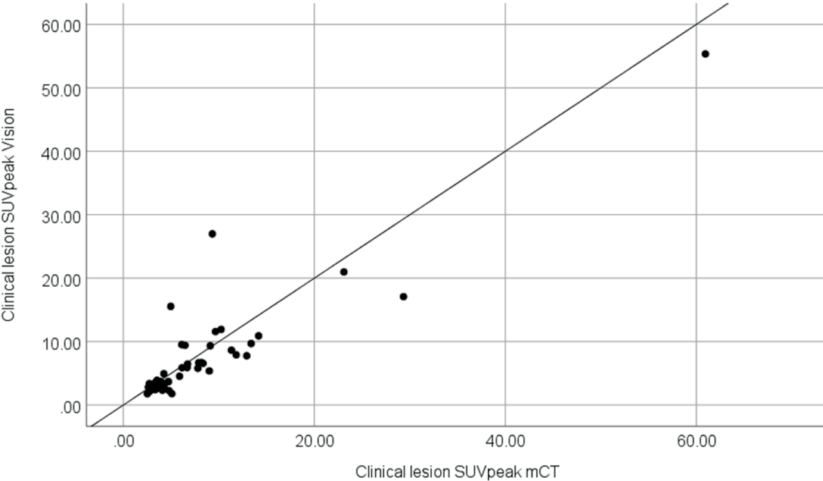
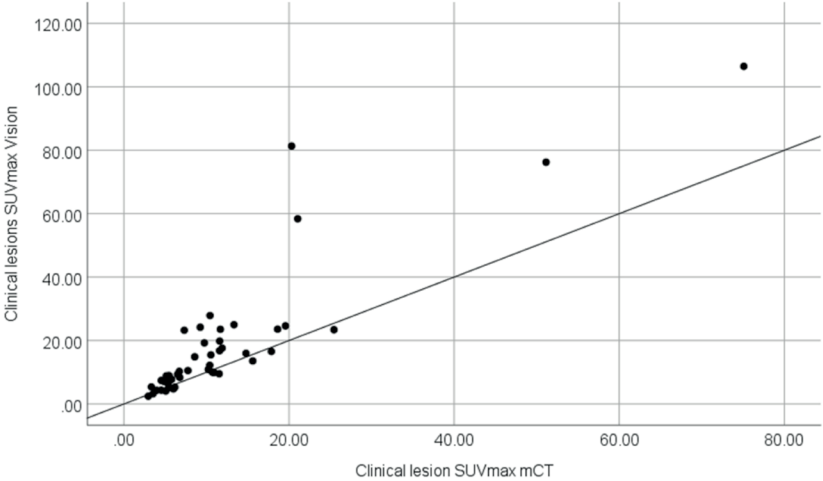


**Supplemental Figure 2** Illustrative transaxial CT, fused PET/CT, PET, and maximum intensity projection PET images (from left to right) acquired on the Biograph Vision (upper row) and acquired on the Biograph mCT (lower row) of a 74-year old male patient (weight 139 kg) with metastasized melanoma. The position of the transaxial slice is indicated on the maximum intensity projection images (dashed line).

**Supplemental Figure 3** → Bland-Altman plots of Biograph mCT and Biograph Vision  $SUV_{max}$  measurement differences ( $SUV_{max}$  measured on the mCT minus  $SUV_{max}$  measured on the Vision) plotted against the mean  $SUV_{max}$  (the mean  $SUV_{max}$  between systems). The mean difference between  $SUV_{max}$  measurement differences is illustrated by the horizontal solid black line and the upper and lower limits of agreement are shown by the dashed horizontal lines. The measurements performed on the Biograph mCT first and the Biograph Vision first are illustrated with the black and gray dots, respectively. The individual plots represent the different healthy tissues of the measurement: aortic arch (A), semioval center (B), liver (C), lung (D), left ventricle of the heart (E), parotid gland (F), quadriceps muscle (G), and spleen (H). At least 96% of the difference scores fell within the 95% limits of agreement.



**Supplemental Figure 4** → Scatter plots demonstrating a higher lesion  $SUV_{max}$  (A) obtained from the Biograph Vision images with respect to the Biograph mCT images. Similar lesion  $SUV_{peak}$  (B) and  $SUV_{mean}$  (C) are observed between systems.





# Chapter 5

---

## Image quality and activity optimization in oncologic $^{18}\text{F}$ -FDG PET using the digital Biograph Vision PET/CT system

Joyce van Sluis<sup>1</sup>, Ronald Boellaard<sup>1,2</sup>, Rudi A.J.O. Dierckx<sup>1</sup>, Gilles N. Stormezand<sup>1</sup>, Andor W.J.M. Glaudemans<sup>1</sup>, and Walter Noordzij<sup>1</sup>

<sup>1</sup>Department of Nuclear Medicine and Molecular Imaging, University of Groningen, University Medical Center Groningen, Hanzeplein 1, 9713 GZ Groningen, The Netherlands

<sup>2</sup>Department of Radiology and Nuclear Medicine, Cancer Center Amsterdam, Amsterdam University Medical Centers, Free University of Amsterdam, De Boelelaan 1117, 1081 HV Amsterdam, The Netherlands

*J Nucl Med.* 2020;61:764-771.



## **Abstract**

The first Biograph Vision PET/CT system (Siemens Healthineers) was installed at the University Medical Center Groningen. Improved performance of this system could allow for a reduction in activity administration or scan duration. This study evaluated the effects of reduced scan duration in oncologic  $^{18}\text{F}$ -FDG PET imaging on quantitative and subjective imaging parameters and its influence on clinical image interpretation.

**Methods** Patients referred for a clinical PET/CT scan were enrolled in this study, received a weight-based  $^{18}\text{F}$ -FDG injected activity, and underwent listmode PET acquisition at 180 s per bed position (s/bp). Acquired PET data were reconstructed using the vendor-recommended clinical reconstruction protocol (hereafter referred to as “clinical”), using the clinical protocol with additional 2-mm Gaussian filtering (hereafter referred to as “clinical+G2”), and -in conformance with European Association of Nuclear Medicine Research Ltd. (EARL) specifications- using different scan durations per bed position (180, 120, 60, 30, and 10 s). Reconstructed images were quantitatively assessed for comparison of SUVs and noise. In addition, clinically reconstructed images were qualitatively evaluated by 3 nuclear medicine physicians.

**Results** In total, 30 oncologic patients (22 men, 8 women; age: 48-88 y [range],  $67 \pm 9.6$  y [mean  $\pm$  SD]) received a single weight-based (3 MBq/kg)  $^{18}\text{F}$ -FDG injected activity (weight: 45-123 kg [range],  $81 \pm 15$  kg [mean  $\pm$  SD]; activity: 135-380 MBq [range],  $241 \pm 47.3$  MBq [mean  $\pm$  SD]). Significant differences in lesion  $\text{SUV}_{\text{max}}$  were found between the 180-s/bp images and the 30- and 10-s/bp images reconstructed using the clinical protocols, whereas no differences were found in lesion  $\text{SUV}_{\text{peak}}$ . EARL-compliant images did not show differences in lesion  $\text{SUV}_{\text{max}}$  or  $\text{SUV}_{\text{peak}}$  between scan durations. Quantitative parameters showed minimal deviation ( $\sim 5\%$ ) in the 60-s/bp images. Therefore, further subjective image quality assessment was conducted using the 60-s/bp images. Qualitative assessment revealed the influence of personal preference on physicians’ willingness to adopt the 60-s/bp images in clinical practice. Although quantitative PET parameters differed minimally, an increase in noise was observed.

**Conclusion** With the Biograph Vision PET/CT system for oncologic  $^{18}\text{F}$ -FDG imaging, scan duration or activity administration could be reduced by a factor of 3 or more with the use of the clinical+G2 or the EARL-compliant reconstruction protocol.

## **Introduction**

PET integrated with CT is a noninvasive imaging method widely used in oncology (1-3) and many other indications, providing both anatomic information and metabolic information (4). In oncology, PET/CT is a rapidly evolving technique for diagnosis, cancer staging, radiation therapy planning, prognosis, and treatment response monitoring (1,3,5).

Recently introduced PET/CT systems are equipped with silicon photomultiplier-based detectors with improved detection capabilities that might contribute to enhanced diagnostic performance but could also allow for a reduction in activity administration or scan duration (3,6-8). The first silicon photomultiplier-based detector Biograph Vision PET/CT system (Siemens Healthineers) was installed at the Department of Nuclear Medicine and Molecular Imaging at the University Medical Center Groningen in May 2018.

Despite its frequent and widespread use in oncologic imaging, PET/CT is associated with some radiation exposure, particularly relevant for young lymphoma patients (9). A pilot phantom study investigating the possibility of activity reduction using the Biograph Vision PET/CT system (Supplemental Tables 1 and 2; supplemental materials are available at <http://jnm.snmjournals.org>) (6) showed that  $^{18}\text{F}$ -FDG administration can be decreased by a factor of approximately 8 for scanning at 60 s per bed position (s/bp) using European Association of Nuclear Medicine Research Ltd. (EARL)-compliant reconstructions (1,10). Lowering the injected activity results in a decrease in radiation exposure for young patients as well as medical staff but can also reduce  $^{18}\text{F}$ -FDG costs. On the other hand, shorter scan times can increase patient throughput, in turn increasing cost-effectiveness.

To our knowledge, scan duration or activity optimization has not yet been explored for the Biograph Vision PET/CT system. Therefore, to further clinically validate the findings obtained from our phantom measurements, the effects of scan duration or administered activity reduction in  $^{18}\text{F}$ -FDG PET imaging on quantitative and subjective imaging parameters and its influence on clinical image interpretation were evaluated in this study.

## **Materials and methods**

### **Patient population**

Patients referred for an oncologic clinical PET/CT were enrolled in this prospective study. For optimal comparison of quantitative parameters, 3 different malignancies were selected to form homogeneous groups: non-small cell lung carcinoma (NSCLC), esophageal cancer, and lymphoma. Patients with a glucose level of greater than or equal to 198 mg/dL before  $^{18}\text{F}$ -FDG administration were excluded from participation in this study.



According to the Dutch Medical Research Involving Human Subjects Act, the local medical ethics committee exempted approval without additional procedures (waiver number: METc2017/489). No additional informed consent was required. Patient information was anonymized before data analysis.

### **Imaging protocol**

In accordance with European Association of Nuclear Medicine guidelines for tumor imaging, patients received a weight-based bolus injection of  $^{18}\text{F}$ -FDG activity (3 MBq/kg) via intravenous infusion (1,11). The syringe and catheter were not measured after the injection for any residual activity. Approximately 60 min after injection (mean  $\pm$  SD, 62  $\pm$  5), patients underwent a listmode PET/CT imaging protocol on the Biograph Vision system.

Patients were instructed to avoid strenuous exercise for 24 h and to fast for at least 4-6 h before  $^{18}\text{F}$ -FDG activity administration. At the time of  $^{18}\text{F}$ -FDG injection, blood glucose levels measured less than or equal to 198 mg/dL. A standard low-dose CT (an x-ray tube current of 43 mAs, a tube voltage of 100 kV, and a spiral pitch factor of 1) scan was acquired from the vertex to the mid-thigh and used for attenuation correction. A consecutive emission PET scan was acquired at 180 s/bp in listmode. All scans were obtained during normal breathing.

Subsequently, PET listmode data were reprocessed to produce additional sets of sinograms: 10, 30, 60, and 120 s/bp. Three different reconstruction protocols were used to reconstruct the PET images for each of the 5 scan durations. The vendor-recommended clinical reconstruction protocol involved an ordinary Poisson ordered-subset expectation maximization 3-dimensional iterative algorithm (12) using 4 iterations, 5 subsets, time-of-flight application, and resolution modeling, without filtering (hereafter referred to as “clinical”) and with 2-mm Gaussian filtering (hereafter referred to as “clinical+G2”). The resulting image size was 440 x 440, with a voxel size of 1.6 x 1.6 x 1.5 mm. In addition, EARL1- and EARL2-compliant reconstructions (1,10) were obtained using 3-dimensional ordinary Poisson ordered-subset expectation maximization, time-of-flight application, 4 iterations, 5 subsets, resolution modeling, and Gaussian filters of 7 and 5 mm, respectively. The resulting image size was 220 x 220, with a voxel size of 3.3 x 3.3 x 1.5 mm. All scans were acquired during normal breathing without respiratory motion gating or correction.

### **Quantitative image analysis**

Reconstructed PET images were analyzed using the quAntitative onCology moleCUlaR Analysis suiTE (ACCURATE), version v03012019 (13). Two semiautomated tumor delineation methods were used to segment and analyze individual lesions per image (with a maximum of the 10 hottest lesions). The first

semiautomated method was based on a fixed SUV threshold of 4.0 g/mL (SUV = 4), whereas the other method, the so-called majority vote (MV2), was based on agreement in tumor delineation between multiple semiautomated methods (14). For clarity, an illustrative clinical image example and a schematic overview of the MV2 method are shown in Supplemental Figures 1 and 2, respectively. If the semiautomated methods were incapable of delineating the lesion, then a 1-mL spheric volume of interest (VOI) was manually placed on (the hottest part in) the lesion. Analyses were performed using  $SUV_{\max}$  and  $SUV_{\text{peak}}$  measurements derived from the 2 semiautomated delineation methods or manual VOI placement.

In addition, for each image, a 3-mL spheric VOI was placed in the liver, where activity distribution was almost uniform, as a reference and to characterize image noise using the SD of the voxel values within the VOI.

### Qualitative image analysis

Images obtained at 180 s/bp and at a shorter scan duration (i.e., 60 s/bp) using the clinical reconstruction protocols were qualitatively evaluated. The 60-s/bp data were chosen because, at this shorter duration, the images were quantitatively still comparable to those at 180 s/bp (as will be shown later). Three experienced nuclear medicine physicians with 15, 5, and 10 y of experience in interpreting PET scans (Andor W.J.M. Glaudemans, Gilles N. Stormezand, and Walter Noordzij, respectively) independently reviewed the reconstructed images using a dedicated syngo.via VB30 (Siemens Healthineers) workstation. Interpreters were not unaware of scan duration. Images reconstructed according to the clinical protocol were evaluated first. After 4 wk, images reconstructed according to the clinical+G2 protocol were evaluated. Images were scored on the basis of 5-point Likert scales with regard to the following characteristics: image noise, lesion margin demarcation, and overall image quality. In addition, the number of avid  $^{18}\text{F}$ -FDG lesions per image was counted to assess possible missed lesions in shorter scan durations, and TNM staging was performed.

### Statistical analysis

Analyses were performed with SPSS Statistics, version 25.0 (IBM Corp.). For each reconstruction method, the lesion SUVs at each scan duration (120, 60, 30, and 10 s/bp) were compared with the lesion SUVs of images acquired at 180 s/bp using a repeated-measures ANOVA with post hoc Bonferroni adjustment for pairwise comparison. A *P* value of less than 0.05 was considered significant. Pairwise comparisons were also performed to assess the differences between each lesion's  $SUV_{\max}$  derived from the 180-s/bp images and shorter scan durations.

All quantitative analyses were performed once for the quantitative parameters obtained using the SUV = 4 semiautomated delineation method and once for the

parameters obtained using the MV2 semiautomated delineation method. Furthermore, qualitative Likert scale scores for the images were compared pairwise using a 2-tailed paired-samples t test; in addition, inter-interpreter agreement was evaluated using  $\kappa$  statistic.

## Results

A total of 30 oncology patients (22 men, 8 women; age: 48-88 y [range],  $67 \pm 9.6$  y [mean  $\pm$  SD]) received a single weight-based (3 MBq/kg) bolus of  $^{18}\text{F}$ -FDG injected activity (weight: 45-123 kg [range],  $81 \pm 15$  kg [mean  $\pm$  SD]; activity: 135-380 MBq [range],  $241 \pm 47.3$  MBq [mean  $\pm$  SD]) via intravenous infusion. For optimal quantitative comparison, 3 homogeneous groups were formed and consisted of 15 NSCLC patients, 9 patients with lymphoma, and 6 patients with esophageal cancer. Table 1 shows relevant demographic and clinical information.

**Table 1** Demographic and clinical data of all included patients.

Patient #	Age [y]	Sex	Weight [kg]	Disease	Injected $^{18}\text{F}$ -FDG activity [MBq]
1	74	M	75	NSCLC	215
2	74	M	87	NSCLC	270
3	70	M	66	NSCLC	195
4	65	M	87	NSCLC	265
5	61	M	77	NSCLC	231
6	62	M	91	NSCLC	275
7	59	F	70	NSCLC	220
8	67	F	85	NSCLC	260
9	79	M	90	NSCLC	265
10	63	M	76	NSCLC	205
11	61	F	87	NSCLC	260
12	53	F	45	NSCLC	135
13	81	M	58	NSCLC	160
14	88	M	88	NSCLC	264
15	69	F	76	NSCLC	220
16	77	F	71	Lymphoma	210
17	48	M	82	Lymphoma	240
18	75	M	80	Lymphoma	245
19	61	M	90	Lymphoma	280
20	62	F	68	Lymphoma	220
21	62	M	88	Lymphoma	260
22	72	M	86	Lymphoma	270
23	70	F	58	Lymphoma	180
24	64	M	90	Lymphoma	280
25	60	M	106	Esophageal cancer	305
26	77	M	62	Esophageal cancer	200
27	58	M	123	Esophageal cancer	380
28	84	M	73	Esophageal cancer	220
29	70	M	101	Esophageal cancer	290
30	52	M	86	Esophageal cancer	260

## Quantitative image analysis

For each of the 30 patients, a total of 20 images were obtained (4 reconstruction methods times 5 scan durations times 30 patients, resulting in 600 images). Tumor segmentations were performed on each of the 600 images individually. In total, 4,076 tumor segmentations were made; approximately 100 tumor lesions were segmented using 2 semiautomated segmentation methods ( $SUV = 4$  and MV2) for each reconstructed scan duration and each reconstruction method, resulting in 40 segmentations per lesion. A total of 352 lesion segmentations could not be made by the  $SUV = 4$  method, whereas the MV2 method was unsuccessful in capturing 1,155 lesion segmentations. The median lesion  $SUV_{max}$  was 8.7 (range, 1.7-57), and the median lesion  $SUV_{peak}$  was 3.9 (range, 0.2-59).

The results of the lesion  $SUV_{max}$  comparisons between different scan durations obtained using the  $SUV = 4$  and the MV2 semiautomated lesion delineation methods for the 4 different reconstruction protocols are shown in boxplots in Figure 1. Similarly, the results of the lesion  $SUV_{peak}$  comparisons are shown in Figure 2. Differences in  $SUV_{max}$  comparisons per lesion between measurements derived from the 180-s/bp images and measurements obtained at shorter scan durations for the 4 different reconstruction protocols, delineated using both semiautomated methods, are shown in boxplots in Figure 3.

The median lesion  $SUV_{max}$  obtained at shorter scan durations -120, 60, 30, and 10 s/bp- were each directly compared with the median lesion  $SUV_{max}$  obtained from the 180-s/bp images. These comparisons were done twice for both semiautomated delineation methods. The results are shown in Table 2. This clarifies the difference in median  $SUV_{max}$  between the shorter scan durations and the 180-s/bp images.

When the clinical and clinical+G2 reconstruction settings were used, significant differences in lesion  $SUV_{max}$  were found between the 180-s/bp images ( $P < 0.01$ ; 95% CI, 0.50-5.91) and the 10-s/bp images ( $P < 0.001$ ; 95% CI, 0.85-3.65) when delineated with the  $SUV = 4$  method. In addition, when the clinical+G2 reconstruction setting was used, significant differences in lesion  $SUV_{max}$  were found between the 60-s/bp images and the 10-s/bp images ( $P < 0.05$ ; 95% CI, 0.24-3.42).

When delineations were performed with the MV2 method, significant differences were found in lesion  $SUV_{max}$  in the clinically reconstructed images between the 180-s/bp images and both the 30-s/bp images ( $P < 0.05$ ; 95% CI, 0.12-4.10) and the 10-s/bp images ( $P < 0.001$ ; 95% CI, 0.99-5.85). Significant differences were also found between the 120-s/bp images and both the 30-s/bp images ( $P < 0.05$ ; 95% CI, 0.30-3.38) and the 10-s/bp images ( $P < 0.05$ ; 95% CI, 0.47-5.83) as well as between the 60-s/bp images and the 30-s/bp images ( $P < 0.001$ ; 95% CI, 0.43-2.09). Between the images obtained using the clinical+G2 reconstruction method, significant differences in lesion  $SUV_{max}$  were found between the 180-s/bp images and the

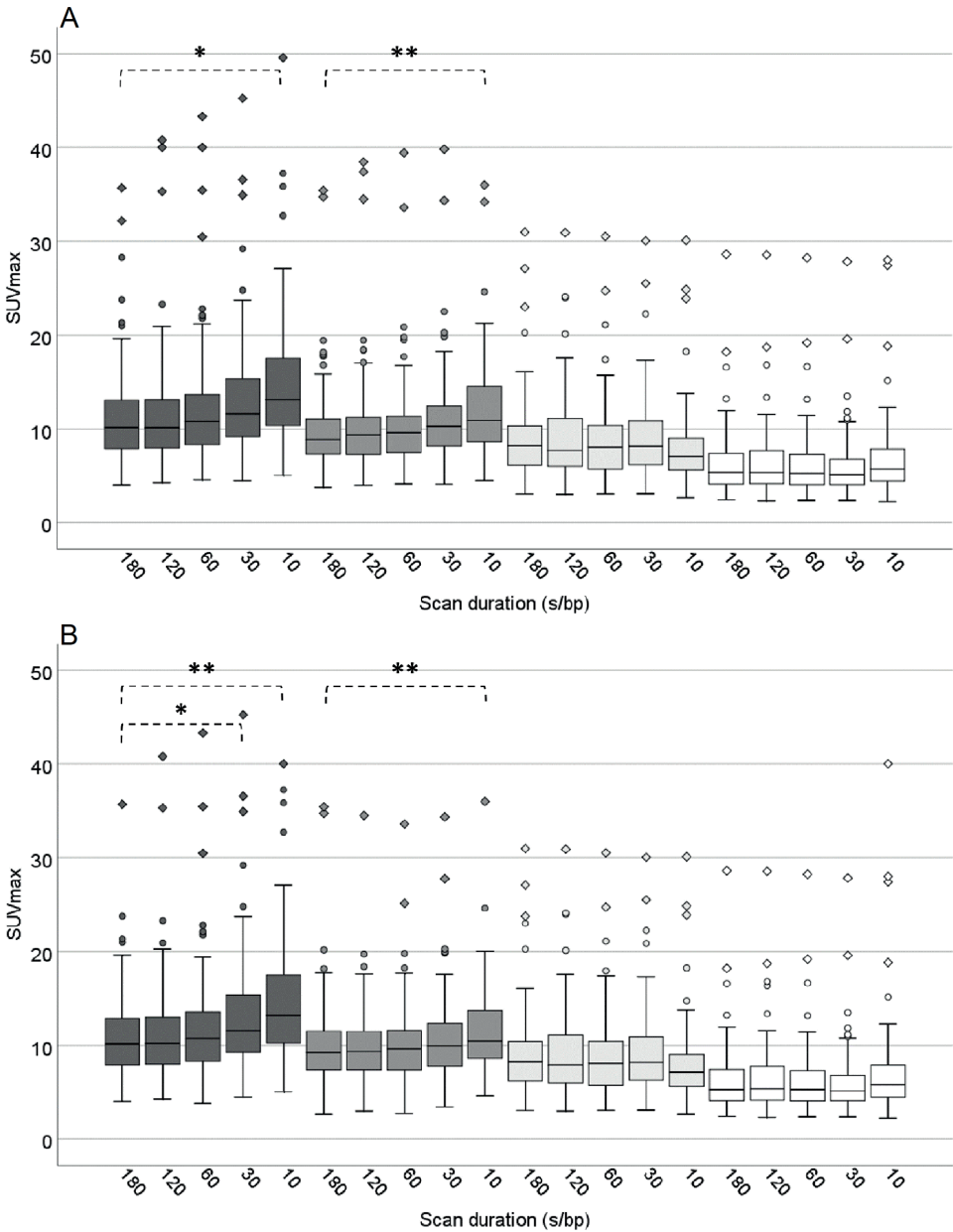


**Figure 1** Boxplots showing spread of lesion  $SUV_{max}$  obtained from clinical (dark gray), clinical+G2 (gray), EARL2-compliant (light gray), and EARL1-compliant (white) image reconstructions at different scan durations. Quantitative analyses were performed using  $SUV = 4$  (A) and MV2 (B) semiautomated lesion delineation methods. Outliers are illustrated with circles, and diamonds represent extreme outliers. Single asterisks and double asterisks indicate significant differences between scan durations at  $P < 0.05$  and  $P < 0.001$ , respectively.

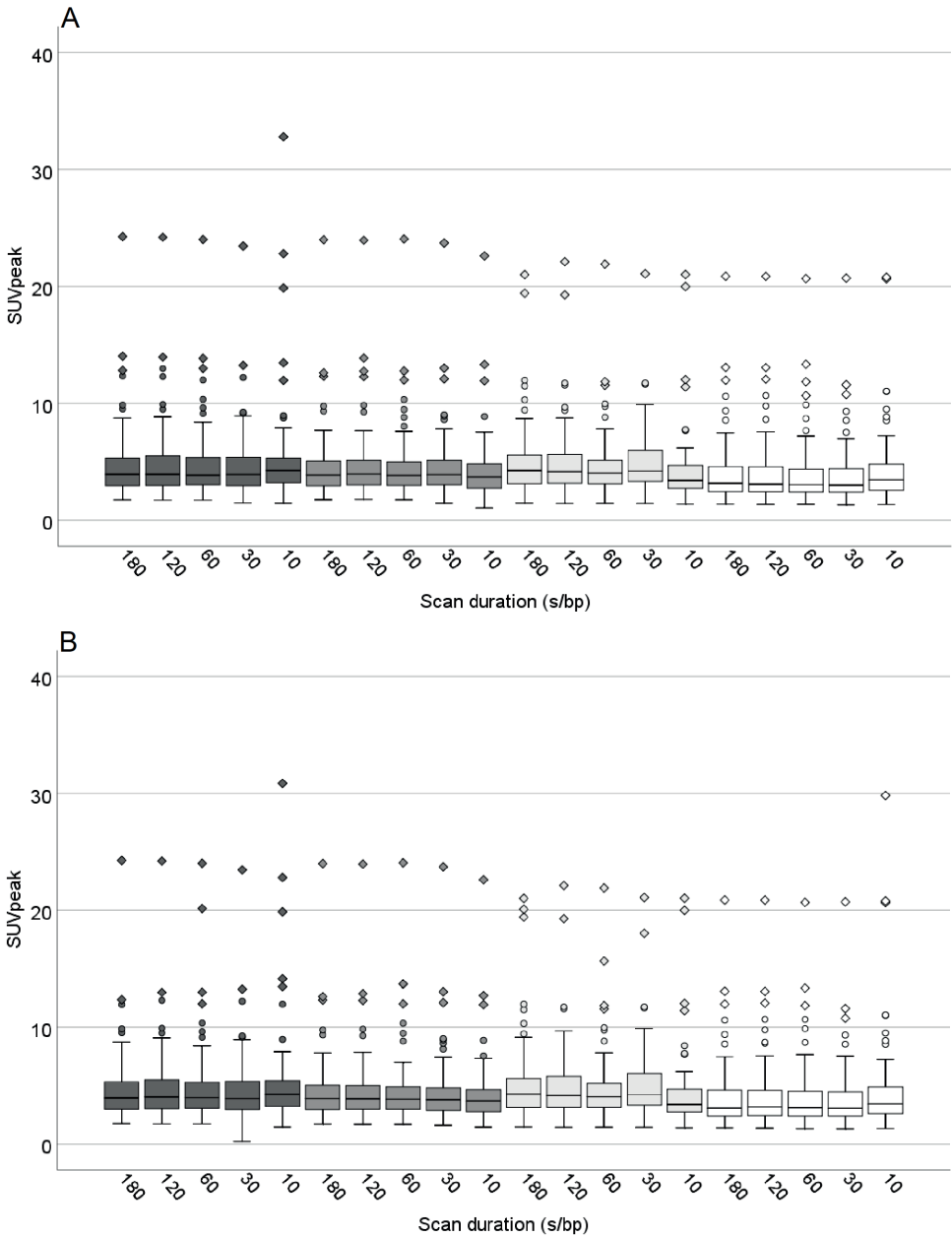


**Figure 2** Boxplots showing spread of lesion  $SUV_{peak}$  obtained from clinical (dark gray), clinical+G2 (gray), EARL2-compliant (light gray), and EARL1-compliant (white) image reconstructions at different scan durations. Quantitative analyses were performed using  $SUV = 4$  (A) and MV2 (B) semiautomated lesion delineation methods. Outliers are illustrated with circles, and diamonds represent extreme outliers.



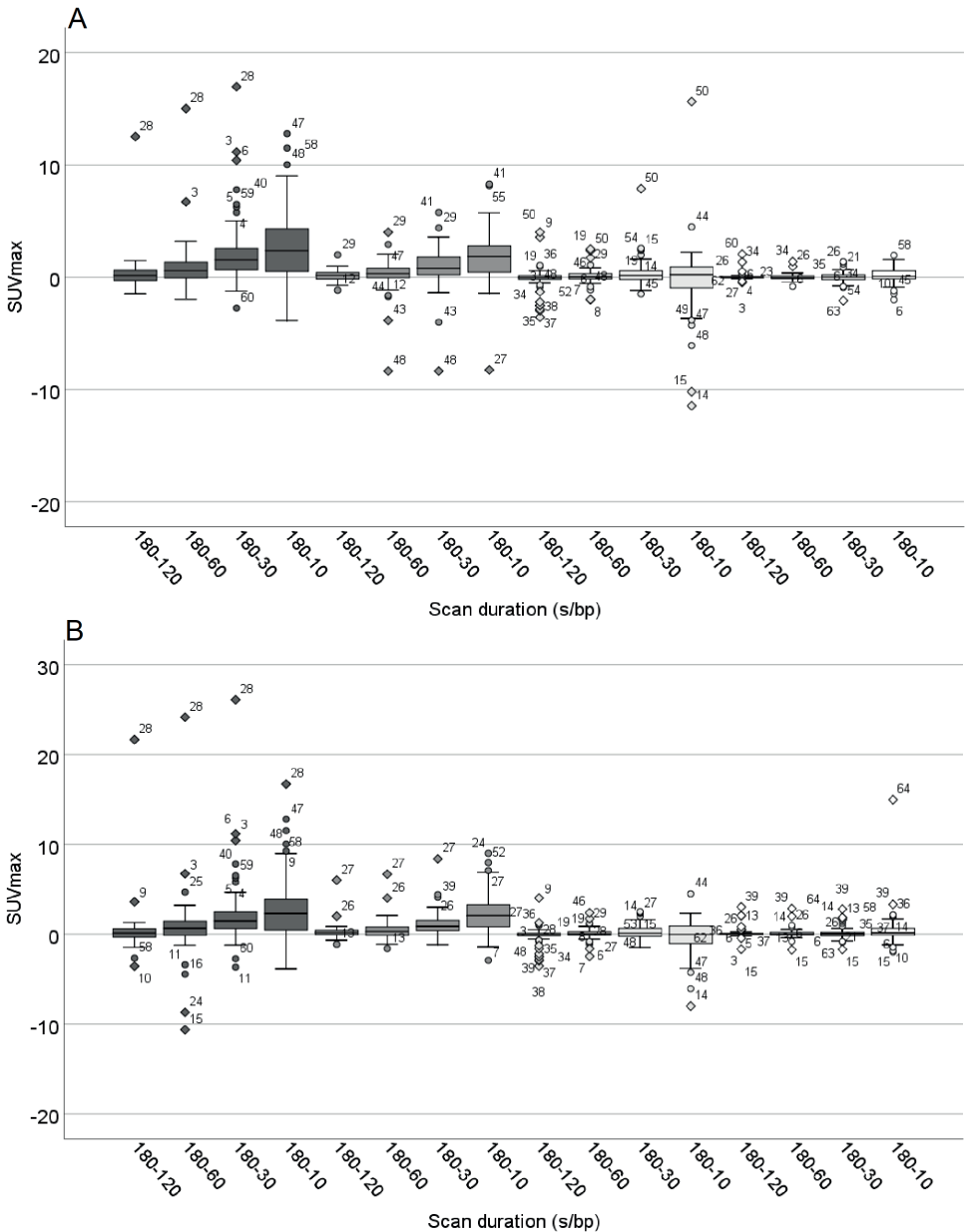


**Figure 3** Boxplots showing spread of  $SUV_{max}$  differences per lesion between 180 s/bp and shorter scan durations obtained from clinical (dark gray), clinical+G2 (gray), EARL2-compliant (light gray), and EARL1-compliant (white) image reconstructions. Quantitative analyses were performed using  $SUV = 4$  (A) and  $MV2$  (B) semiautomated lesion delineation methods. Outliers are illustrated with circles, diamonds represent extreme outliers, and numbers indicate lesion numbers.

**Table 2** Median lesion  $SUV_{max}$  scores derived from images obtained using the clinical and clinical+G2 reconstruction settings, delineated with both the  $SUV = 4$  and MV2 semiautomated delineation method. Bias is the percentage difference between median  $SUV_{max}$  at shorter scan durations and the median  $SUV_{max}$  of the 180 s/bp images.

Scan duration [s/bp]	SUV = 4		MV2	
	Median $SUV_{max}$	Bias [%]	Median $SUV_{max}$	Bias [%]
<u>clinical</u>				
180	10.39	n.a.	10.27	n.a.
120	10.43	0.4	10.28	0.1
60	10.99	5.8	10.83	5.5
30	11.79	13.5	11.63	13.3
10	13.14	26.5	13.20	28.6
<u>clinical+G2</u>				
180	9.33	n.a.	9.44	n.a.
120	9.71	4.2	9.61	1.9
60	10.02	7.4	9.88	4.7
30	10.61	13.7	10.33	9.5
10	11.67	25.2	11.30	19.8

10-s/bp images ( $P < 0.05$ ; 95% CI, 0.02-0.28) as well as between the 120-s/bp images and the 10-s/bp images ( $P < 0.05$ ; 95% CI, 0.31-3.85) and between the 60-s/bp images and both the 30-s/bp images ( $P < 0.001$ ; 95% CI, 0.39-1.05) and the 10-s/bp images ( $P < 0.05$ ; 95% CI, 0.21-4.20).

No significant differences were found between lesion  $SUV_{peak}$  at different scan durations. Furthermore, EARL1- and EARL2-compliant image reconstructions did not show any significant differences in  $SUV_{max}$  or  $SUV_{peak}$  in comparisons between all different scan durations.

### Qualitative image analysis

From the quantitative analysis, the shorter scan duration that still quantitatively resembled the values obtained from the 180-s/bp images reconstructed according to the clinical and clinical+G2 protocols (deviation of ~5%) was found to be the 60-s/bp option (Fig. 1; Table 2). Therefore, further clinical qualitative evaluations were conducted with the 180-s/bp images and the 60-s/bp images. For illustrative purposes, Figure 4 shows an example of patient PET images acquired using the 4 reconstruction protocols at different scan durations ranging from 180 s/bp to 10 s/bp. Figures 5 and 6 show examples of reconstructed patient PET images obtained using the 4 different reconstruction settings at 180 s/bp versus 60 s/bp.

All 180-s/bp images reconstructed using the clinical reconstruction protocol were scored significantly higher than the images acquired at 60 s/bp on noise, lesion demarcation, and overall image quality ( $P < 0.001$ ; 95% CI of 2.25-2.55, 2.03-2.35, and 2.20-2.58, respectively). When the clinical+G2 reconstruction protocol was used, images obtained at 180 s/bp were scored higher than the 60-s/bp images as



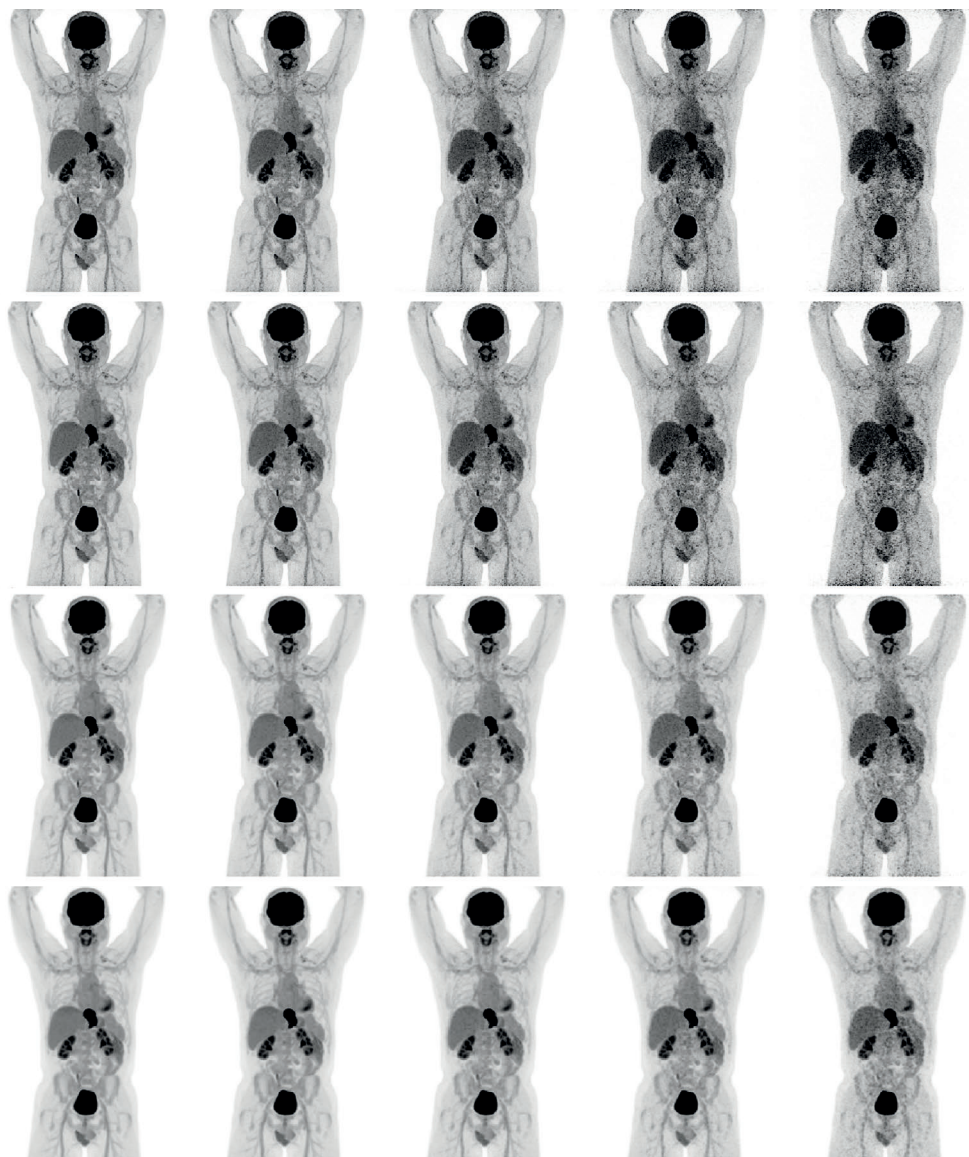


**Figure 4** Maximum intensity projection PET images of 52-y-old male (weight, 86 kg) with esophageal cancer. Images were acquired at 180, 120, 60, 30, and 10 s/bp (from left to right, respectively) using clinical, clinical+G2, EARL2-compliant, and EARL1-compliant reconstruction protocols (from top to bottom, respectively).

well. In addition, the filtered images were more highly valued with respect to their unfiltered counterparts ( $P < 0.001$ ; 95% CI of 2.87-3.20, 3.02-3.24, and 3.16-3.35, respectively). For images reconstructed according to the clinical protocol, the Fleiss  $\kappa$  statistic did not show significant inter-interpretor agreement. For the clinically



**Figure 5** Maximum intensity projection PET images of 62-y-old female (weight, 68 kg) with metastasized NSCLC. Images were acquired at 180 s/bp (top row) and 60 s/bp (bottom row) and reconstructed using clinical, clinical+G2, EARL2-compliant, and EARL1-compliant protocols (from left to right, respectively).

reconstructed images with additional 2-mm filtering, inter-interpretation agreement was good regarding the evaluation of noise, lesion demarcation, and overall image quality, with  $\kappa$  values of 0.65 ( $P < 0.001$ ; 95% CI, 0.57-0.74), 0.64 ( $P < 0.001$ ; 95% CI, 0.56-0.73), and 0.72 ( $P < 0.001$ ; 95% CI, 0.64-0.81), respectively.

With regard to the images reconstructed according to the clinical protocol, in 5 of 30 cases, reducing the scan duration from 180 s/bp to 60 s/bp resulted in missed lesions, changing the TNM staging of the disease. In 2 of these cases, the change in TNM staging would have influenced the choice of therapy. In these 2 cases, 2 NSCLC patients, the missed lesions were specifically a contralateral lung nodule in 1 patient and a distant liver metastasis in the other. There was no inter-interpretation agreement on exchanging the 180-s/bp images for the shorter acquisition time, since the interpreting physicians were willing to exchange the 180-s/bp images for the 60-s/bp images in 27, 8, and 23 cases, respectively.

Concerning the images reconstructed using the clinical+G2 protocol, in 1 of 30 cases, reducing the scan duration from 180 s/bp to 60 s/bp resulted in a missed lesion,



**Figure 6** Maximum intensity projection PET images of 61-y-old male (weight, 77 kg) with metastasized NSCLC. Images were acquired at 180 s/bp (top row) and 60 s/bp (bottom row) and reconstructed using clinical, clinical+G2, EARL2-compliant, and EARL1-compliant protocols (from left to right, respectively).

changing the TNM staging of the disease. This missed lesion would not have had any influence on the therapy choice for this patient, as it was 1 of 3 small locoregional lymph node metastases from a primary esophageal carcinoma. There was no inter-interpreter agreement on exchanging the 180-s/bp images for the shorter acquisition time, since the interpreting physicians were willing to exchange the 180 s/bp images for the 60-s/bp images in 13, 24, and 21 cases, respectively.

The results of the noise quantification through calculation of the coefficient of variation obtained from the 3-mL liver VOIs in each image are shown in Figure 7. Here, a difference in the amount of image noise between images obtained at 180 s/bp and images obtained at 60 s/bp can be observed for all 4 reconstruction protocols.

## **Discussion**

In the present study, we explored the effect of scan time reduction on quantitative PET image parameters and image quality using the digital Biograph Vision PET/CT system. Administered  $^{18}\text{F}$ -FDG activity can be adjusted proportionally to shorter

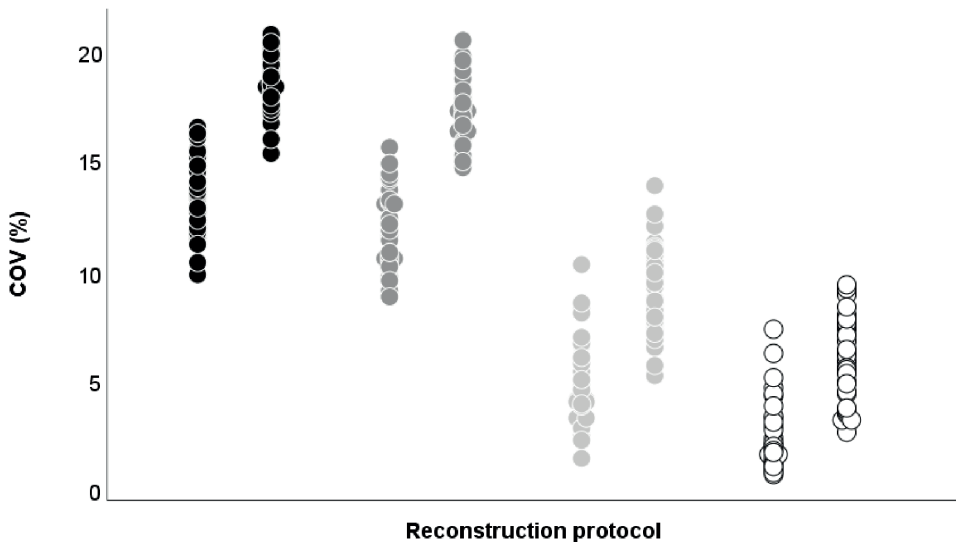


**Figure 7** Liver coefficient of variation (COV) obtained from clinical (black), clinical+G2 (gray), EARL2-compliant (light gray), and EARL1-compliant (white) image reconstructions at 180 s/bp (left column) vs. 60 s/bp (right column).

scan times per bed position (with an added 10% for compensation of lower noise-equivalent count rates per MBq at higher activity concentrations) (5). The results obtained using the clinical protocols suggest that with a minimal bias (~5%) for quantitative image parameters, reducing scan time or activity by a factor of 3 when using the clinical and clinical+G2 reconstruction protocols is feasible. When EARL-compliant reconstructions are applied, even further reductions are potentially achievable (6).

The quality of PET images obtained at a reduced scan duration was evaluated by 3 nuclear medicine physicians to assess its impact in clinical practice. From this evaluation it became apparent that personal preference is an essential element contributing to physicians' willingness to adopt the shorter scan duration for diagnosing in clinical practice. Although quantitative PET parameters differed minimally, a substantial increase in noise was observed (Fig. 7). The extent to which this increase in noise is disturbing to physicians is decisive for the scoring of image quality and for the consideration of working with the shorter scan duration. The addition of a small Gaussian filter of 2 mm to the reconstruction protocol in the 60-s/bp image setting diminished the influence of image noise without notably affecting the apparent spatial resolution (15).

With the clinical+G2 reconstruction protocol, a reduction of scan time or injected activity could have led to downstaging in only 1 of 30 cases, as indicated by 2 of 3 nuclear medicine specialists. The 3 nuclear medicine physicians evaluated the images

obtained with the shorter scan duration as they would have evaluated the 180-s/bp images. With extra time being taken, the missed lesion might not be overlooked in the 60-s/bp images. A trade-off between increasing patient throughput or reducing radiation exposure and possibly reserving more time for image interpretation is a factor that needs to be taken into consideration.

With regard to other commercially available digital PET/CT systems, a comparable study stated that a reduction in activity or scan time to 90 s/bp (which equals a factor of 2) is feasible when the Discovery MI PET/CT system (GE Healthcare) is used (16). For the Vereos PET/CT system (Philips Healthcare), a similar study on activity optimization has not been conducted yet.

To our knowledge, this is the first study to explore scan duration or activity optimization and image quality using the digital Biograph Vision PET/CT system. Lowering the injected activity by a factor of 3 will result in a decrease in radiation exposure for patients (particularly important for young lymphoma patients) as well as medical staff and will also reduce  $^{18}\text{F}$ -FDG costs while maintaining quantitative PET performance. For institutions more interested in increased patient throughput, shorter scan times (down to ~6 min for a whole body scan) in combination with an activity prescription of 3 MBq/kg are feasible with the Biograph Vision PET/CT system, in turn also increasing cost-effectiveness. However, with increasing patient throughput, there is also more demand for peripheral sources, such as preparation rooms, staff, and time for reporting. For pediatric purposes, both reducing activity and scanning faster are of high clinical importance, as radiation exposure should be kept to the bare minimum in this patient population; in addition, faster scanning decreases the need for anesthetics.

## **Conclusion**

When the Biograph Vision PET/CT system is used for oncologic  $^{18}\text{F}$ -FDG imaging, it is acceptable to reduce scan duration or activity administration by a factor of 3 (compared with European Association of Nuclear Medicine activity prescriptions (1)) for routine clinical imaging when using the clinical+G2 reconstruction protocol. When applying EARL-compliant reconstructions, further reductions are achievable, depending on local preferences.

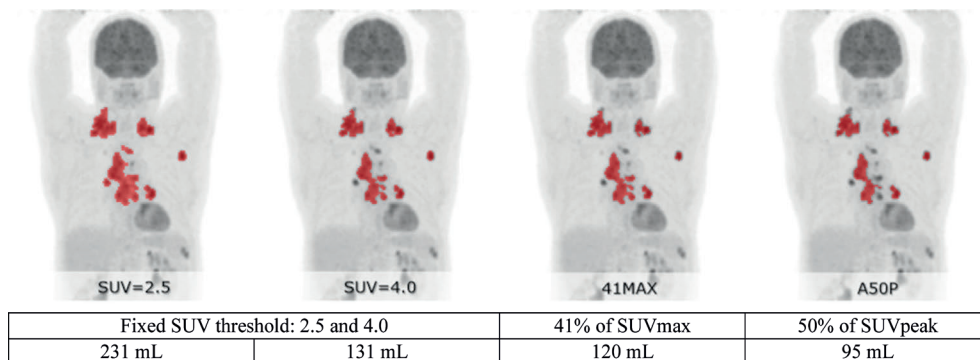
A reduction of injected activity will decrease radiation exposure for patients as well as for medical staff. In addition, for institutions without the ability to produce their own  $^{18}\text{F}$ -FDG, activity reduction will lower the costs of PET/CT imaging. Alternatively, a faster scan time increases patient throughput, resulting in a higher cost efficiency for PET centers.

## References

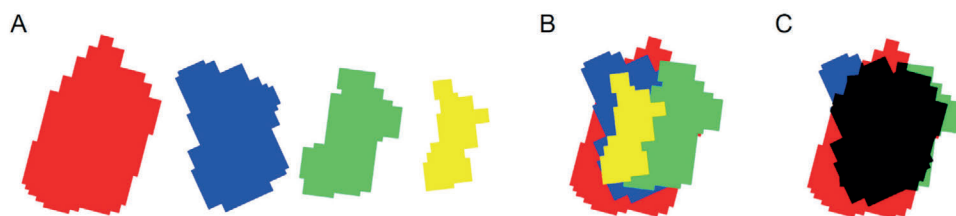
1. Boellaard R, Delgado-Bolton R, Oyen WJG, Giammarile F, Tatsch K, Eschner W, et al. FDG PET/CT: EANM procedure guidelines for tumour imaging: version 2.0. *Eur J Nucl Med Mol Imaging*. 2015;42:328-354.
2. Slomka PJ, Pan T, Germano G. Recent advances and future progress in PET instrumentation. *Semin Nucl Med*. 2016;46:5-19.
3. Hsu DFC, Ilan E, Peterson WT, Uribe J, Lubberink M, Levin CS. Studies of a next generation silicon-photomultiplier-based time-of-flight PET/CT system. *J Nucl Med*. 2017;58:1511-1518.
4. Townsend DW. Dual-modality imaging: combining anatomy and function. *J Nucl Med*. 2008;49:938-955.
5. Boellaard R, Oyen WJG, Hoekstra CJ, Hoekstra OS, Visser EP, Willemsen ATM, et al. The Netherlands protocol for standardisation and quantification of FDG whole body PET studies in multi-centre trials. *Eur J Nucl Med Mol Imaging*. 2008;35:2320-2333.
6. van Sluis J, de Jong JR, Schaar J, Noordzij W, van Snick JH, Dierckx RAJO, et al. Performance characteristics of the digital Biograph Vision PET/CT system. *J Nucl Med*. 2019;60:1031-1036.
7. Nguyen NC, Vercher-Conejero JL, Sattar A, Miller MA, Maniawski PJ, Jordan DW, et al. Image quality and diagnostic performance of a digital PET prototype in patients with oncologic diseases: initial experience and comparison with analog PET. *J Nucl Med*. 2015;56:1378-1385.
8. Rausch I, Ruiz A, Valverde-Pascual I, Cal-González J, Beyer T, Carrio I. Performance evaluation of the Philips Vereos PET/CT System according to the NEMA NU2-2012 standard. *J Nucl Med*. 2019;60:561-567.
9. Karakatsanis NA, Fokou E, Tsoumpas C. Dosage optimization in positron emission tomography: state-of-the-art methods and future prospects. *Am J Nucl Med Mol Imaging*. 2015;5:527-547.
10. Boellaard R. New developments of EANM oncology PET/CT guidelines and update of the EARL accreditation standards presentation. [http://earl.eanm.org/html/img/pool/New\\_EARL\\_project\\_and\\_update\\_of\\_FDG\\_standard\\_Oct2018.pdf](http://earl.eanm.org/html/img/pool/New_EARL_project_and_update_of_FDG_standard_Oct2018.pdf). Accessed April 6, 2020.
11. Boellaard R, O'Doherty MJ, Weber WA, Mottaghy FM, Lonsdale MN, Stroobants SG, et al. FDG PET and PET/CT: EANM procedure guidelines for tumour PET imaging: version 1.0. *Eur J Nucl Med Mol Imaging*. 2010;37:181-200.
12. Varrone A, Sjöholm N, Eriksson L, Guly'as B, Halldin C, Farde L. Advancement in PET quantification using 3D-OP-OSEM point spread function reconstruction with the HRRT. *Eur J Nucl Med Mol Imaging*. 2009;36:1639-1650.
13. Boellaard R. Quantitative oncology molecular analysis suite: ACCURATE [abstract]. *J Nucl Med*. 2018;59(suppl 1):1753.
14. Kolinger GD, Váñez García D, Kramer GM, Frings V, Smit EG, de Langen AJ, et al. Repeatability of [<sup>18</sup>F]FDG PET/CT total metabolic active tumour volume and total tumour burden in NSCLC patients. *EJNMMI Res*. 2019;9:14.
15. Armstrong IS, Kelly MD, Williams HA, Matthews JC. Impact of point spread function modelling



- and time of flight on FDG uptake measurements in lung lesions using alternative filtering strategies. *EJNMMI Phys.* 2014;1:99.
16. Sonni I, Baratto L, Park S, Hatami N, Srinivas S, Davidzon G, et al. Initial experience with a SiPM-based PET/CT scanner: influence of acquisition time on image quality. *EJNMMI Phys.* 2018;5:9.



**Supplemental Figure 1** Clinical example of the segmentation performance of the four standard methods comprising the MV2 delineation method. Clear differences in the segmentation volumes can be observed (in red) for the SUV = 2.5, SUV = 4.0, 41MAX, and A50P method (from left to right).



**Supplemental Figure 2** Illustration of the four different segmentation volumes obtained from a single lesion using the four standard segmentation methods comprising the MV2 delineation method: SUV = 2.5 (red), SUV = 4.0 (blue), 41MAX (green), and A50P (yellow) (A). The MV2 method uses the different segmentations of the four methods involved and overlaps the different volumes to evaluate the agreement (B). The resulting MV2 segmentation (black) agrees between at least two of the standard delineation methods.



# Chapter 6

---

## Optimization of scan duration and image quality in oncological $^{89}\text{Zr}$ immunoPET imaging using the Biograph Vision PET/CT

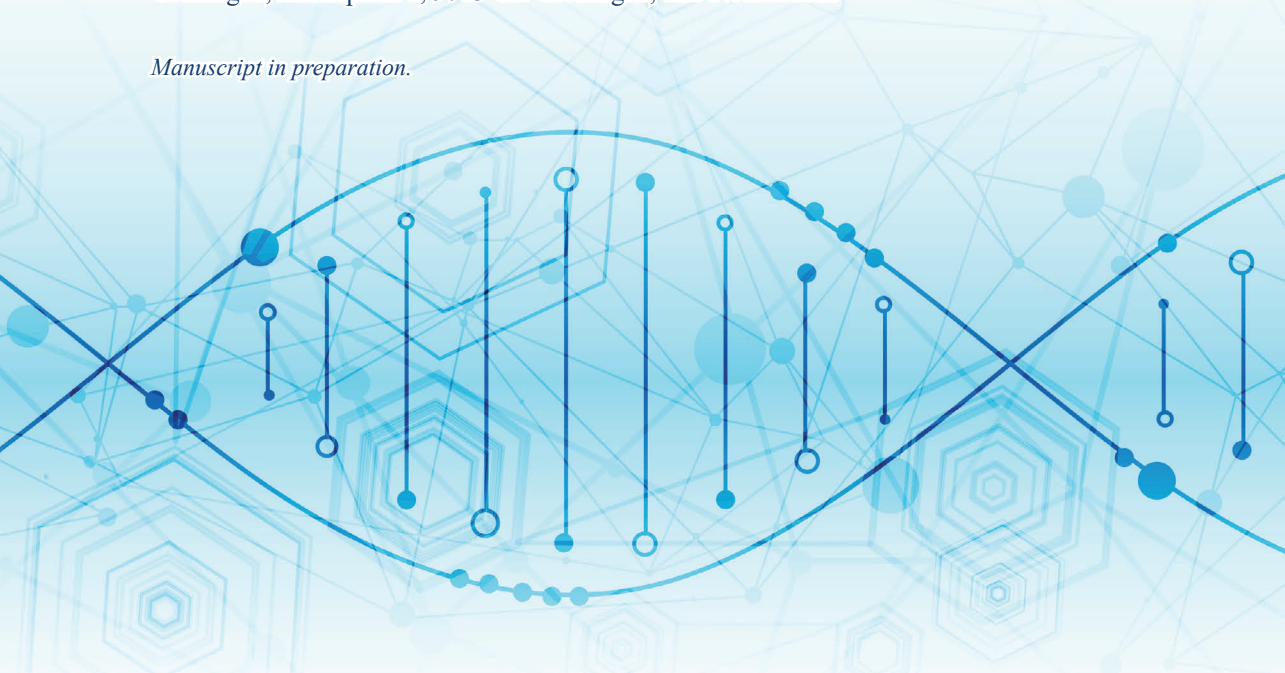
Joyce van Sluis<sup>1</sup>, Ronald Boellaard<sup>1,2</sup>, Rudi A.J.O. Dierckx<sup>1</sup>, Evelien L.M. van Esch<sup>1</sup>, Demi A. Croes<sup>1</sup>, Laura Kist-de Ruijter<sup>3</sup>, Pim P. van der Donk<sup>3</sup>, Elisabeth G.E. de Vries<sup>3</sup>, Walter Noordzij<sup>1</sup>, and Adrienne H. Brouwers<sup>1</sup>

<sup>1</sup>Department of Nuclear Medicine and Molecular Imaging, University of Groningen, University Medical Center Groningen, Hanzeplein 1, 9713 GZ Groningen, The Netherlands

<sup>2</sup>Department of Radiology and Nuclear Medicine, Cancer Center Amsterdam, Amsterdam University Medical Centers, Free University of Amsterdam, De Boelelaan 1117, 1081 HV Amsterdam, The Netherlands

<sup>3</sup>Department of Medical Oncology, University of Groningen, University Medical Center Groningen, Hanzeplein 1, 9713 GZ Groningen, The Netherlands

*Manuscript in preparation.*



## **Abstract**

Antibody-based PET (immunoPET) imaging is important for the characterization of tumor lesions. It may be a valuable tool to determine which patients may benefit from treatment with a specific monoclonal antibody (mAb) and evaluate treatment response. For  $^{89}\text{Zr}$  immunoPET imaging, higher sensitivity of recently introduced PET/CT systems may be beneficial as the low positron abundance of  $^{89}\text{Zr}$  causes a low signal-to-noise level. Moreover, the long physical half-life limits the radiation dose and thus activity that can be administered to the patients. Currently, these factors lead to long scan-times of up to 2 hours at time points  $>6$  days postinjection using conventional analog PET/CT systems.

Here, we investigated the difference in semiquantitative performance between the Biograph mCT and the Biograph Vision PET/CT in  $^{89}\text{Zr}$  immunoPET imaging. Furthermore, the effects of scan duration reduction using the Vision on semiquantitative imaging parameters and its influence on image quality assessment were evaluated.

**Methods** Patients with cancer undergoing  $^{89}\text{Zr}$ -labeled mAb PET/CT imaging were prospectively enrolled. PET/CT data were acquired on day 4 post 37 MBq  $^{89}\text{Zr}$ -labeled mAb injection. Five patients were scanned consecutively on both PET/CT systems. Ten patients were scanned only on the digital Biograph Vision PET/CT. For PET image reconstruction, three protocols were used, i.e., one local clinical protocol and European Association of Nuclear Medicine Research Limited (EARL) standards 1 and 2 compliant protocols. For the acquisitions performed on the Vision, listmode data were reprocessed to obtain images at shorter scan durations.

Volumes of interest were placed in tumor- and healthy tissues to derive semiquantitative PET image biomarkers to assess differences between PET/CT systems and scan durations. Differently reconstructed images obtained using the Biograph Vision PET/CT system were visually scored regarding image quality by two nuclear medicine physicians.

**Results** 15 patients were enrolled. At full scan durations, results obtained from both PET/CT systems were comparable. For all data acquired using the Vision, reconstructions conform to EARL1 standards resulted in comparable semiquantitative measurements at shorter scan-durations (75% and 50%) regarding full scan time on mCT.

**Conclusion** Scan duration of  $^{89}\text{Zr}$  immunoPET imaging using the Vision PET/CT can be decreased up to 50% while maintaining image quality when using the EARL standards 1 compliant reconstruction protocol. For quantitative comparison of tumor lesions across PET/CT systems, it is strongly advised to use  $\text{SUV}_{\text{peak}}$  instead of  $\text{SUV}_{\text{max}}$  because of high noise levels in current  $^{89}\text{Zr}$  immunoPET images.

## **Introduction**

Recently introduced Positron Emission Tomography (PET) integrated with Computed Tomography (CT) systems are equipped with silicon photomultiplier-based detector elements (SiPMs). These systems with improved detection capabilities may contribute to enhanced diagnostic performance, but could also allow a reduction in scan duration (1-7) and/or reduction in administered radioactivity.

Over the past decades, antibody-based PET (immunoPET) imaging has become increasingly important for the characterization of tumor lesions (8). In addition, it may be a valuable tool to determine which patients may benefit from treatment with a specific monoclonal antibody (mAb) and for evaluation of treatment response (9). Numerous advantages of zirconium-89 ( $^{89}\text{Zr}$ ) such as the long half-life of 78.4 h matching the pharmacokinetic behavior of antibodies, its relatively low average positron energy of 395 keV for high-resolution PET imaging, and good *in vivo* stability, make it a suitable candidate for labeling of mAb (8). For  $^{89}\text{Zr}$  immunoPET imaging, the higher sensitivity of SiPM-based PET/CT systems could be particularly beneficial as the low positron abundance causes the acquired PET images to have a low signal-to-noise level. In addition, the high energy gamma emission of 909 keV causes high radiation burden and limits the amount of radiotracer that can be administered to patients (10). Hence long scan durations are required to obtain adequate statistical image quality, especially at later scan time-points.

Currently, total body  $^{89}\text{Zr}$  immunoPET imaging can last up to 2 h acquisition at later time points at 6-7 days postinjection (p.i.), using the conventional PMT-based mCT Biograph PET/CT (from now on referred to as mCT (Siemens Healthineers)). The improved performance characteristics of the SiPM-based Biograph Vision PET/CT (from now on referred to as Vision (Siemens Healthineers) are expected to lead to improved  $^{89}\text{Zr}$  immunoPET image quality, and therefore may allow for a reduction in scan duration to increase patient comfort and throughput, and/or administered amount of activity for reduction of radiation exposure.

This study aimed to investigate the difference in semiquantitative performance between the mCT and the Vision PET/CT systems in  $^{89}\text{Zr}$  immunoPET imaging. In addition, the effects of acquisition time reduction on semiquantitative imaging biomarkers and its influence on image quality assessment were evaluated.

## **Materials and methods**

### **Patient Population**

Patients (n = 15) with cancer with visible  $^{89}\text{Zr}$ -mAb PET tracer uptake in at least one tumor lesion were enrolled in this prospective study between June 2018 and February 2020 in case of a referral for an  $^{89}\text{Zr}$  immunoPET acquisition to solve a clinical dilemma (11) or for research purposes (ClinicalTrials.gov identifiers NCT01832051,

NCT02453984, and NCT04029181). All patients were scanned on the Vision PET/CT system. Patients (n = 5) that underwent the dual acquisition protocol were scanned on both PET/CT systems and gave (additional) written informed consent after being informed on the study aims, procedures, and the additional acquisition of a low dose CT (~1 mSv). For this purpose, the local medical ethics committee exempted approval without additional procedures (waiver number: METc2017/489).

### **Imaging protocol**

Patients received an intravenous injection of 37 MBq  $^{89}\text{Zr}$ -labeled mAb. PET/CT data were acquired on day 4 p.i. On the Vision PET/CT a standard low dose CT scan (an X-ray tube current of 43 mAs, a tube voltage of 100 kV, and a spiral pitch factor of 1) was performed from the vertex to the toes and used for attenuation correction. A consecutive emission PET scan was acquired in listmode at 300 s per bed position (s/bp). In case patients were scanned on the mCT, the acquisition parameters of the low-dose CT were as follows: an X-ray tube current of 99 mAs, a tube voltage of 140 kV, and a spiral pitch factor of 1.5. PET/CT imaging on the mCT was also performed in listmode at 300 s/bp.

Subsequently, PET listmode data acquired on the Vision were reprocessed to produce additional sets of sinograms corresponding to 225, 150, and 75 s/bp (scan durations are hereinafter referred to as 100%, 75%, 50% and 25% of the acquisition time). For reconstruction of Vision PET images, three different protocols were used for each of the four scan durations. We applied the vendor recommended reconstruction protocol currently used to obtain optimal image quality in  $^{18}\text{F}$ -FDG imaging, i.e., an ordinary Poisson ordered-subset expectation maximization (OP-OSEM) 3D-iterative algorithm (12) using 4 iterations, 5 subsets, time-of-flight (ToF) application, resolution modeling, without filtering (hereinafter referred to as the Clinical Vision protocol). In addition, the European Association of Nuclear Medicine (EANM) Research Ltd. (EARL)1 and EARL2 reconstructions (13-15) currently used for quantification of clinically acquired oncological  $^{18}\text{F}$ -FDG images were obtained using 3D OP-OSEM with 4 iterations and 5 subsets, ToF, with resolution modeling and a Gaussian filter of 7 mm and 5 mm, respectively (hereinafter referred to as the EARL1 and EARL2 Vision protocols). The resulting image size of the images obtained on the Vision was 220 x 220 with a voxel size of 3.3 x 3.3 x 1.5 mm.

For PET data acquired on the mCT, also three different reconstruction protocols were used. The clinically preferred multicenter validated  $^{89}\text{Zr}$  PET reconstruction protocol (16,17) using 3D OP-OSEM with 3 iterations, 21 subsets, ToF, resolution modeling, and a Gaussian filter of 8 mm (hereinafter referred to as the  $^{89}\text{Zr}$ -EARL mCT protocol (16)). In addition, images acquired on the mCT were also reconstructed to comply with EARL settings for  $^{18}\text{F}$ -FDG imaging using 3D OP-OSEM with 3 iterations, 21

subsets, ToF, resolution modeling, and a Gaussian filter of 6.5 mm (the EARL1 mCT protocol) and a Gaussian filter of 5 mm (the EARL2 mCT protocol). The resulting image size of the images obtained using the mCT was 256 x 256 with a voxel size of 3.2 x 3.2 x 2.00 mm, thus closely matching those of the Vision PET/CT studies.

### Semiquantitative image analysis

Reconstructed PET/CT data were semiquantitatively analyzed using the quAntitative onCology moleCULAR Analysis suiTE (ACCURATE) version v08072019 (18). Per image, individual tumor lesions were manually delineated to obtain the maximum and the peak standardized uptake value ( $\text{SUV}_{\text{max}}$  and  $\text{SUV}_{\text{peak}}$ ) of the tumor. In addition, 1-cm-diameter spherical volumes of interest (VOIs) were placed in healthy tissues: blood pool, kidney cortex, and spleen. From these VOIs,  $\text{SUV}_{\text{max}}$ ,  $\text{SUV}_{\text{peak}}$  and mean Standardized Uptake Value ( $\text{SUV}_{\text{mean}}$ ) were obtained. A 3-cm-diameter spherical VOI was placed in a homogeneous part of the liver to obtain  $\text{SUV}_{\text{max}}$ ,  $\text{SUV}_{\text{peak}}$ ,  $\text{SUV}_{\text{mean}}$ , and to characterize image noise using the standard deviation of the activity within the VOI with respect to the mean activity.

### Qualitative image analysis

Images obtained on the Vision at the four different reconstructed scan durations using three different reconstruction protocols were evaluated on image quality. Two nuclear medicine physicians (AHB and WN, with 10 and 5 years of experience in  $^{89}\text{Zr}$  immunoPET image reading, respectively) independently assessed the images using a dedicated syngo.via VB30 (Siemens Healthineers) workstation. All images were scored based on a 5-point Likert scale regarding image noise, lesion margin demarcation, and overall image quality (see Supplemental Figure 1 for the used visual image assessment form).

### Statistical analysis

Statistical analyses were performed in SPSS Statistics, version 25.0 (IBM Corp.). To evaluate the difference in semiquantitative performance between systems, non-parametric Wilcoxon Signed Ranks tests were conducted. The difference in lesion  $\text{SUV}_{\text{max}}$  and  $\text{SUV}_{\text{peak}}$ , and the difference in healthy tissue  $\text{SUV}_{\text{max}}$ ,  $\text{SUV}_{\text{peak}}$ , and  $\text{SUV}_{\text{mean}}$  between systems were explored.

For each reconstruction method, lesion  $\text{SUV}_{\text{max}}$  and  $\text{SUV}_{\text{peak}}$  per scan duration, 75%, 50%, and 25%, were compared with the lesion  $\text{SUV}_{\text{max}}$  and  $\text{SUV}_{\text{peak}}$  of images acquired at 100% of the count time using a repeated-measures analysis of variance (ANOVA) with post hoc Bonferroni adjustment for pairwise comparison. A *P* value of less than 0.05 was considered significant. This comparison was also performed for assessing the difference in healthy tissue  $\text{SUV}_{\text{max}}$ ,  $\text{SUV}_{\text{peak}}$ , and  $\text{SUV}_{\text{mean}}$  between



the 100% scan time images and images acquired at shorter scan durations. Furthermore, the standard deviation of the voxel values within the liver VOIs was compared between the 100% scan time images and images acquired at shorter scan durations as well.

Inter-reader agreement concerning image noise, tumor lesion demarcation, and overall image quality was analyzed using  $\kappa$  statistic. To this aim, the original 5-point scores were reassigned to 2-point scores: 1 + 2 + 3 became 1, and 4 + 5 became 2. Here as well, a  $P$  value of less than 0.05 was considered significant.

## **Results**

In total, 15 patients (5 men, 10 women; age 33-79, mean  $\pm$  SD  $58 \pm 13$  years; weight 52-109, mean  $\pm$  SD  $73 \pm 15$  kg) were included in the study. Five of these patients were evaluated for the semiquantitative performance comparison of the mCT versus Vision. All 15 patients were scanned on the Vision and acquired PET/CT data at 4 days p.i. was evaluated regarding image quality at the different simulated acquisition times.

### **Semiquantitative image analysis**

Each acquisition using the mCT resulted in three images (obtained using three different reconstruction protocols), whereas each acquisition using the Vision resulted in 12 images (three reconstruction methods times four scan durations). For illustrative purposes, Figure 1 shows example patient PET/CT images acquired using the three reconstruction protocols at different scan durations ranging from 100% to 25%. For each of the five patients scanned on both the mCT and Vision, a total of 15 images were obtained, whereas 12 images were obtained for each of the 10 patients undergoing acquisition on the Vision only. Overall, 195 images were collected and tumor segmentations were performed on each of the images individually. A total of 5 tumor lesions were found in the double scans, and 17 tumor lesions were included in the single acquisitions obtained using the Vision PET/CT (a total of 2 tumor lesions per tissue type per patient). In total, 279 tumor segmentations were made (a segmentation for each reconstruction method and acquisition time resulted for the acquisitions on the mCT in three segmentations per lesion (i.e.,  $5 \times 3$  tumor segmentations), and for the Vision in 12 segmentations per lesion (i.e.,  $(17 + 5) \times 12$  tumor segmentations).

Concerning the double acquired scans, median lesion  $SUV_{max}$  and  $SUV_{peak}$  derived from the images obtained using the mCT and the EARL standards 1 compliant harmonized reconstruction protocol were 14.1 (range 2.4 - 35.7) and 10.3 (range 1.7 - 14.4). For the dual images obtained with the Vision, median lesion  $SUV_{max}$  and  $SUV_{peak}$  derived from images reconstructed according to the EARL1 standard-

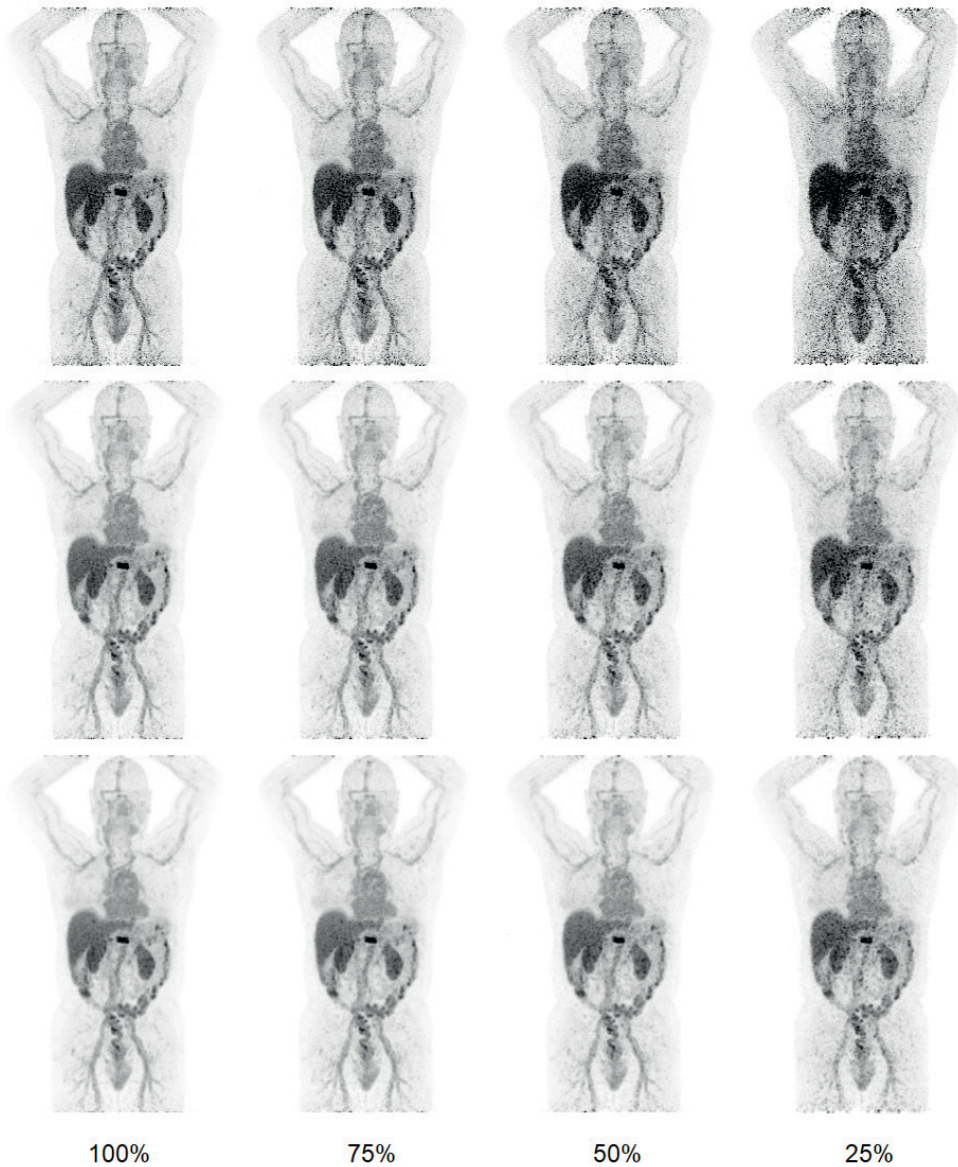


**Figure 1** Clinical example of the segmentation performance of the four standard methods comprising the MV2 delineation method. Clear differences in the segmentation volumes can be observed (in red) for the  $\text{SUV} = 2.5$ ,  $\text{SUV} = 4.0$ , 41MAX, and A50P method (from left to right).

compliant protocol were 17.9 (range 4.1 - 29.7) and 10.1 (range 2.0 - 13.6), respectively. An overview of median lesion  $\text{SUV}_{\text{max}}$  and  $\text{SUV}_{\text{peak}}$  comparison between PET/CT systems obtained using different reconstruction protocols can be found in Table 1. Regarding the included healthy tissues, a comparison of semiquantitative parameters

between PET/CT systems is shown in Table 2. Scatter plots in Figure 2 show the difference in lesion  $SUV_{max}$  and  $SUV_{peak}$  between images derived from both PET/CT systems.

For each of the healthy tissues a similar comparison between systems was performed using  $SUV_{max}$ ,  $SUV_{peak}$ , and  $SUV_{mean}$  (see Figure 3).

**Table 1** Tumor lesion median  $SUV_{max}$  and  $SUV_{peak}$  comparison between both systems (only shown for acquisitions on both PET/CT systems ( $n = 5$ )).

Tissue	Biograph mCT		Biograph Vision	
	$SUV_{max}$ median (range)	$SUV_{peak}$ median (range)	$SUV_{max}$ median (range)	$SUV_{peak}$ median (range)
<u>Tumor lesions</u>				
Reconstruction protocol:				
$^{89}Zr$ -EARL / Clinical	12.7 (2.2 – 27.4)	9.8 (1.8 – 11.9)	25.6 (7.0 – 64.1)	11.9 (2.1 – 14.7)
EARL2	15.5 (2.8 – 48.3)	10.9 (1.8 – 18.2)	17.9 (4.1 – 29.7)	10.7 (1.9 – 13.7)
EARL1	14.1 (2.4 – 35.7)	10.3 (1.7 – 14.4)	15.7 (3.4 – 22.0)	10.1 (2.0 – 13.6)

**Table 2** Healthy tissue median  $SUV_{max}$ ,  $SUV_{peak}$  and  $SUV_{mean}$  comparison between systems (only shown for acquisitions on both PET/CT systems ( $n = 5$ )).

Tissue	Biograph mCT			Biograph Vision		
	$SUV_{max}$ median (range)	$SUV_{peak}$ median (range)	$SUV_{mean}$ median (range)	$SUV_{max}$ median (range)	$SUV_{peak}$ median (range)	$SUV_{mean}$ median (range)
<u>Bloodpool</u>						
Reconstruction protocol:						
$^{89}Zr$ -EARL / Clinical	10.7 (4.3 – 13.7)	7.3 (3.7 – 10.5)	9.11 (3.7 – 9.8)	14.7 (11.1 – 25.4)	7.8 (6.3 – 12.2)	8.6 (6.9 – 15.0)
EARL2	12.8 (7.0 – 18.0)	7.4 (5.3 – 12.1)	9.7 (5.6 – 11.4)	9.7 (8.5 – 18.9)	7.2 (5.8 – 11.7)	8.2 (6.4 – 14.6)
EARL1	11.9 (6.6 – 13.8)	7.1 (5.1 – 11.65)	9.5 (5.5 – 12.0)	9.0 (7.1 – 16.4)	7.0 (5.5 – 11.4)	7.9 (6.4 – 14.1)
<u>Kidney cortex</u>						
Reconstruction protocol:						
$^{89}Zr$ -EARL / Clinical	5.9 (3.1 – 8.7)	5.8 (3.1 – 6.5)	5.6 (3 – 6.9)	5.9 (6.6 – 19.1)	6.9 (4.0 – 7.8)	6.3 (4.2 – 9.3)
EARL2	7.6 (3.6 – 9.7)	5.3 (3.0 – 6.2)	5.0 (3.1 – 7.9)	7.8 (5.9 – 10.2)	6.9 (3.8 – 8.1)	6.4 (3.9 – 8.3)
EARL1	6.9 (4.9 – 9.0)	5.7 (3.9 – 6.5)	5.8 (3.3 – 7.66)	7.4 (5.4 – 13)	6.7 (3.7 – 8.1)	6.4 (3.8 – 7.7)
<u>Spleen</u>						
Reconstruction protocol:						
$^{89}Zr$ -EARL / Clinical	4.3 (3.6 – 7.6)	3.6 (3.3 – 7.5)	3.2 (2.6 – 7.4)	7.7 (6.6 – 17.3)	4.3 (4.0 – 8.6)	4.6 (1.9 – 9.3)
EARL2	5.2 (2.1 – 7.8)	3.6 (2.1 – 7.1)	3.6 (1.8 – 5.6)	6.0 (4.3 – 11.5)	4.7 (3.5 – 8.4)	5.0 (2.4 – 9.1)
EARL1	4.4 (3.4 – 7.6)	3.6 (3.2 – 7.0)	3.3 (3.11 – 6.0)	5.5 (3.7 – 10.5)	4.7 (3.4 – 8.2)	3.3 (3.1 – 5.0)
<u>Liver</u>						
Reconstruction protocol:						
$^{89}Zr$ -EARL / Clinical	8.6 (8.1 – 9.8)	6.8 (6.4 – 8.1)	4.9 (4.3 – 6.0)	11.9 (10.3 – 23.0)	6.0 (4.8 – 8.1)	5.4 (4.0 – 6.1)
EARL2	11.9 (10.2 – 14.0)	6.8 (6.1 – 8.7)	5.2 (4.3 – 6.2)	9.0 (6.5 – 13.4)	6.1 (4.7 – 7.9)	5.3 (4.0 – 6.1)
EARL1	9.5 (8.2 – 11.6)	7.0 (6.6 – 8.8)	4.9 (4.3 – 6.4)	8.4 (5.7 – 11.4)	6.0 (4.9 – 7.8)	5.3 (4.0 – 6.2)

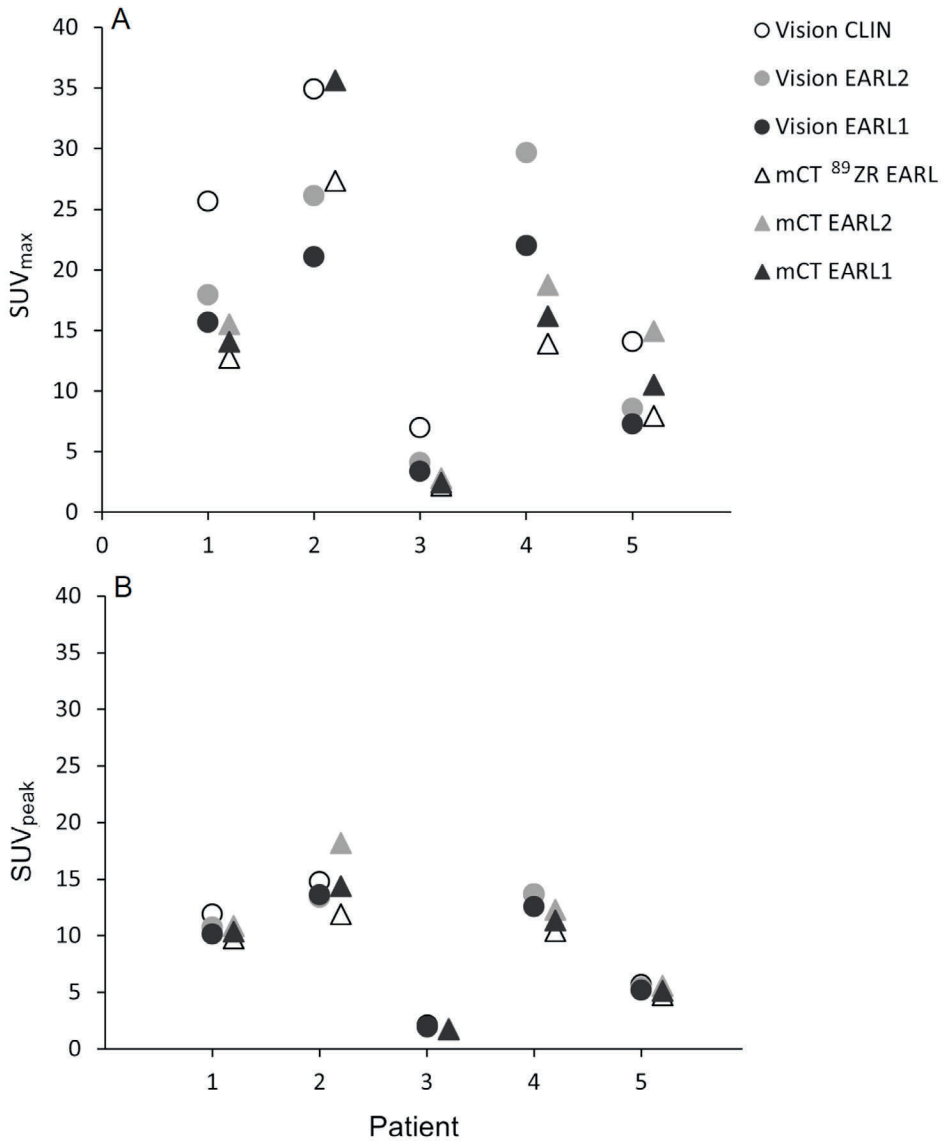


**Figure 2** Semiquantitative tumor lesion comparison between PET/CT systems. For each patient ( $n = 5$ ), the lesion  $\text{SUV}_{\text{max}}$  (A) and  $\text{SUV}_{\text{peak}}$  (B) derived from images obtained with the Vision PET/CT system and using the Clinical Vision (Vision CLIN) (white dot), the EARL2 Vision (gray dot), and the EARL1 Vision reconstruction protocol (black dot) are compared directly with tumor lesion SUVs derived from images using the mCT PET/CT system and  $^{89}\text{Zr}$ -EARL mCT, EARL2 mCT, and EARL1 reconstruction protocols (white, gray, and black triangles, respectively). Please note, for readability reasons, the tumor lesion  $\text{SUV}_{\text{max}}$  outlier found in patient 4 of 64.1 obtained using the Clinical Vision protocol is not shown in subfigure A.



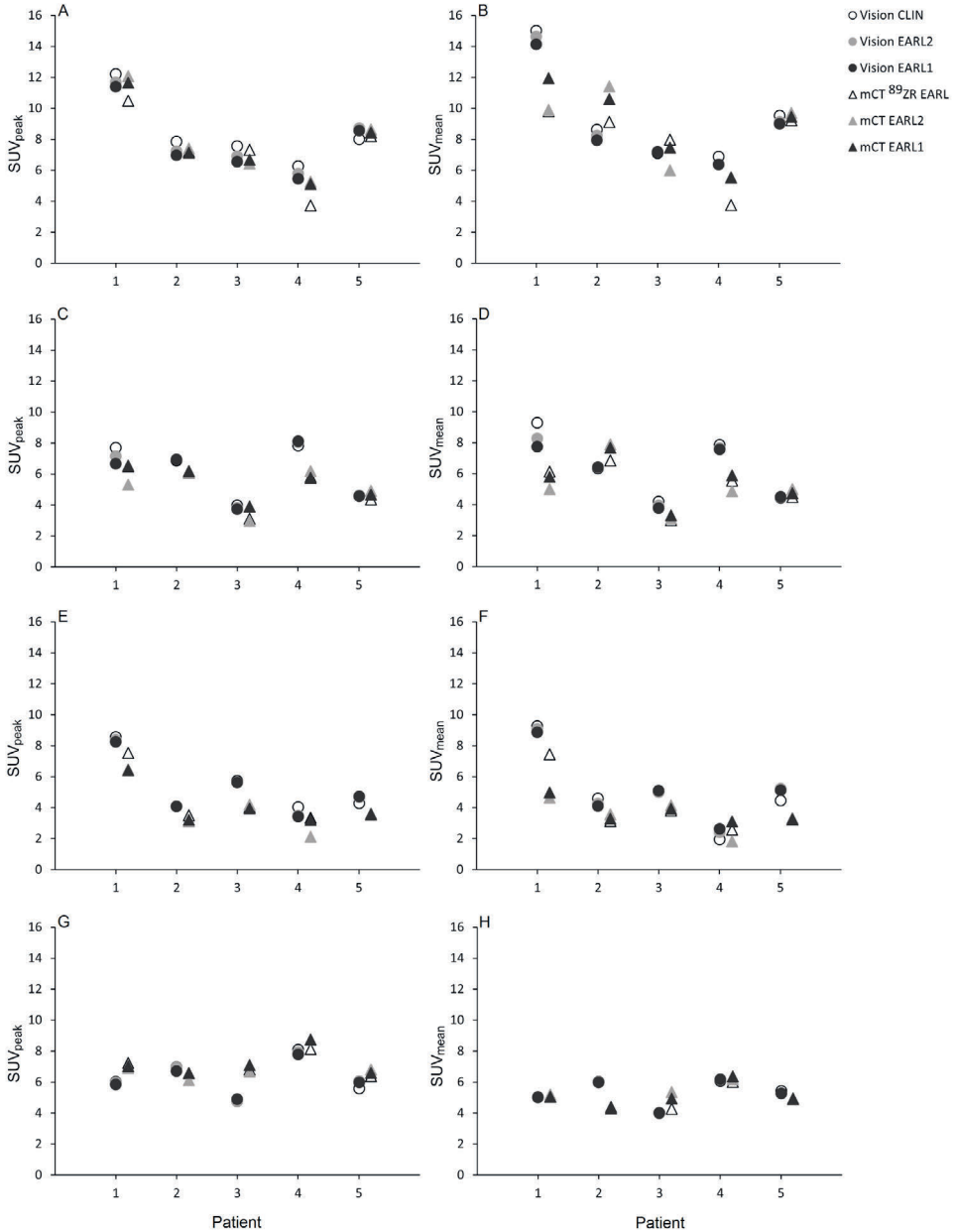


**Figure 3** Semiquantitative healthy tissue comparison between PET/CT systems. For each patient ( $n = 5$ ),  $SUV_{peak}$  (left column) and  $SUV_{mean}$  (right column) of healthy tissues (bloodpool (A and B), kidney cortex (C and D), spleen (E and F), and liver (G and H)) derived from images obtained through use of the Vision PET/CT system and the Clinical Vision (Vision CLIN) reconstruction protocol (white dot), the EARL2 Vision reconstruction protocol (gray dot), and the EARL1 Vision reconstruction protocol (black dot) are compared directly with healthy tissue SUVs derived from images using the mCT PET/CT system and  $^{89}Zr$ -EARL mCT, EARL2 mCT, and EARL1 reconstruction protocols (white, gray, and black triangles, respectively).

The results from the semiquantitative performance comparison in tumor lesions and healthy tissues between PET/CT systems using Wilcoxon Signed Ranks tests are shown in Table 3 and Table 4, respectively; no significant difference is indicated with ‘equivalent’. A significant difference in lesion  $\text{SUV}_{\text{max}}$  and  $\text{SUV}_{\text{peak}}$  was found between systems when comparing the images obtained using the Clinical Vision protocol and the  $^{89}\text{Zr}$ -EARL mCT protocol ( $Z$ -score:  $-2.02$ ,  $P < 0.05$ ); no significant differences in tumor lesion  $\text{SUV}_{\text{max}}$  and  $\text{SUV}_{\text{peak}}$  were found when comparing system semi quantitative performance using the EARL standards compliant settings 1 and 2.

**Table 3** Semiquantitative performance in lesions compared between both PET/CT systems ( $n = 5$ ) using the Wilcoxon Signed Ranks test.

	<b>Z</b>	<b>P value</b>	<b>Equivalence</b>
<b>Tumor lesions</b>			
<i>Reconstruction protocol:</i>			
$^{89}\text{Zr}$ -EARL / Clinical			
SUV <sub>max</sub>	-2.02	0.04	No
SUV <sub>peak</sub>	-2.02	0.04	No
EARL2			
SUV <sub>max</sub>	-0.14	0.89	Yes
SUV <sub>peak</sub>	-0.67	0.50	Yes
EARL1			
SUV <sub>max</sub>	-0.14	0.89	Yes
SUV <sub>peak</sub>	-0.41	0.69	Yes

Concerning the healthy tissues, significantly different  $\text{SUV}_{\text{max}}$  were found between systems in the blood pool, kidney cortex, spleen, and liver when using the Clinical Vision and  $^{89}\text{Zr}$ -EARL mCT reconstruction protocol ( $P < 0.05$ ). Using these reconstruction settings,  $\text{SUV}_{\text{peak}}$  measured in the kidney cortex differed significantly between systems as well ( $Z$ -score:  $-2.02$ ,  $P < 0.05$ ). No significant differences in healthy tissue  $\text{SUV}_{\text{max}}$ ,  $\text{SUV}_{\text{peak}}$ , and  $\text{SUV}_{\text{mean}}$  were found when comparing system semiquantitative performance using the EARL standards compliant settings 1 and 2 for the blood pool, kidney cortex, and liver. However, for the spleen, significant differences between systems regardless of reconstruction settings and semiquantitative parameters were observed ( $P < 0.05$ ). Table 2 shows an overall increase of approximately 25% in median SUV for the spleen, irrespective of reconstruction protocol.

Boxplots in Figure 4 show lesion  $\text{SUV}_{\text{max}}$  and  $\text{SUV}_{\text{peak}}$  comparisons between different scan durations derived from images obtained using the Vision. A significant difference was found in lesion  $\text{SUV}_{\text{max}}$  between images using the Clinical Vision reconstruction protocol obtained at 100% scan duration and 25% ( $P = 0.009$ , 95% CI  $(-18.0 - -2.0)$ ), and between images obtained at 75% scan duration and 25% ( $P =$



**Table 4** Semiquantitative performance in healthy tissues comparison between systems ( $n = 5$ ) using the Wilcoxon Signed Ranks test.

	<b>Z</b>	<b>P value</b>	<b>Equivalence</b>
<b>Healthy tissues</b>			
<u>Bloodpool</u>			
<i>Reconstruction protocol:</i>			
<sup>89</sup> Zr-EARL / Clinical			
SUV <sub>max</sub>	-2.02	0.04	No
SUV <sub>peak</sub>	-1.75	0.08	Yes
SUV <sub>mean</sub>	-0.67	0.50	Yes
EARL2			
SUV <sub>max</sub>	-0.14	0.89	Yes
SUV <sub>peak</sub>	-0.67	0.50	Yes
SUV <sub>mean</sub>	-0.67	0.50	Yes
EARL1			
SUV <sub>max</sub>	-0.67	0.50	Yes
SUV <sub>peak</sub>	-0.41	0.69	Yes
SUV <sub>mean</sub>	-0.14	0.89	Yes
<u>Kidney cortex</u>			
<i>Reconstruction protocol:</i>			
<sup>89</sup> Zr-EARL / Clinical			
SUV <sub>max</sub>	-2.02	0.04	No
SUV <sub>peak</sub>	-2.02	0.04	No
SUV <sub>mean</sub>	-1.21	0.23	Yes
EARL2			
SUV <sub>max</sub>	-1.21	0.23	Yes
SUV <sub>peak</sub>	-1.75	0.08	Yes
SUV <sub>mean</sub>	-0.94	0.35	Yes
EARL1			
SUV <sub>max</sub>	-1.21	0.23	Yes
SUV <sub>peak</sub>	-0.94	0.35	Yes
SUV <sub>mean</sub>	-0.94	0.35	Yes
<u>Spleen</u>			
<i>Reconstruction protocol:</i>			
<sup>89</sup> Zr-EARL / Clinical			
SUV <sub>max</sub>	-2.02	0.04	No
SUV <sub>peak</sub>	-2.02	0.04	No
SUV <sub>mean</sub>	-1.75	0.08	Yes
EARL2			
SUV <sub>max</sub>	-1.48	0.14	Yes
SUV <sub>peak</sub>	-2.02	0.04	No
SUV <sub>mean</sub>	-2.02	0.04	No
EARL1			
SUV <sub>max</sub>	-2.02	0.04	No
SUV <sub>peak</sub>	-2.02	0.04	No
SUV <sub>mean</sub>	-1.75	0.08	Yes
<u>Liver</u>			
<i>Reconstruction protocol:</i>			
<sup>89</sup> Zr-EARL / Clinical			
SUV <sub>max</sub>	-2.02	0.04	No
SUV <sub>peak</sub>	-1.48	0.14	Yes
SUV <sub>mean</sub>	-0.67	0.50	Yes
EARL2			
SUV <sub>max</sub>	-1.21	0.23	Yes
SUV <sub>peak</sub>	-1.21	0.23	Yes
SUV <sub>mean</sub>	-0.14	0.89	Yes
EARL1			
SUV <sub>max</sub>	-0.94	0.35	Yes
SUV <sub>peak</sub>	-1.75	0.08	Yes
SUV <sub>mean</sub>	-0.14	0.89	Yes

0.008, 95% CI (-17.1 - -2.0)). When using the EARL2 Vision reconstruction settings, lesion  $\text{SUV}_{\text{max}}$  differed significantly between 75% and 25% scan duration ( $P = 0.02$ , 95% CI (-5.5 - -0.3)). Images reconstructed using the EARL1 Vision protocol showed significant differences in lesion  $\text{SUV}_{\text{max}}$  between 100% and 25% scan duration ( $P = 0.001$ , 95% CI (-2.3 - -0.5)), and between 75% and 25% ( $P = 0.009$ , 95% CI (-2.5 - -0.3)). No significant differences were found in lesion  $\text{SUV}_{\text{peak}}$  between images obtained at different scan durations.

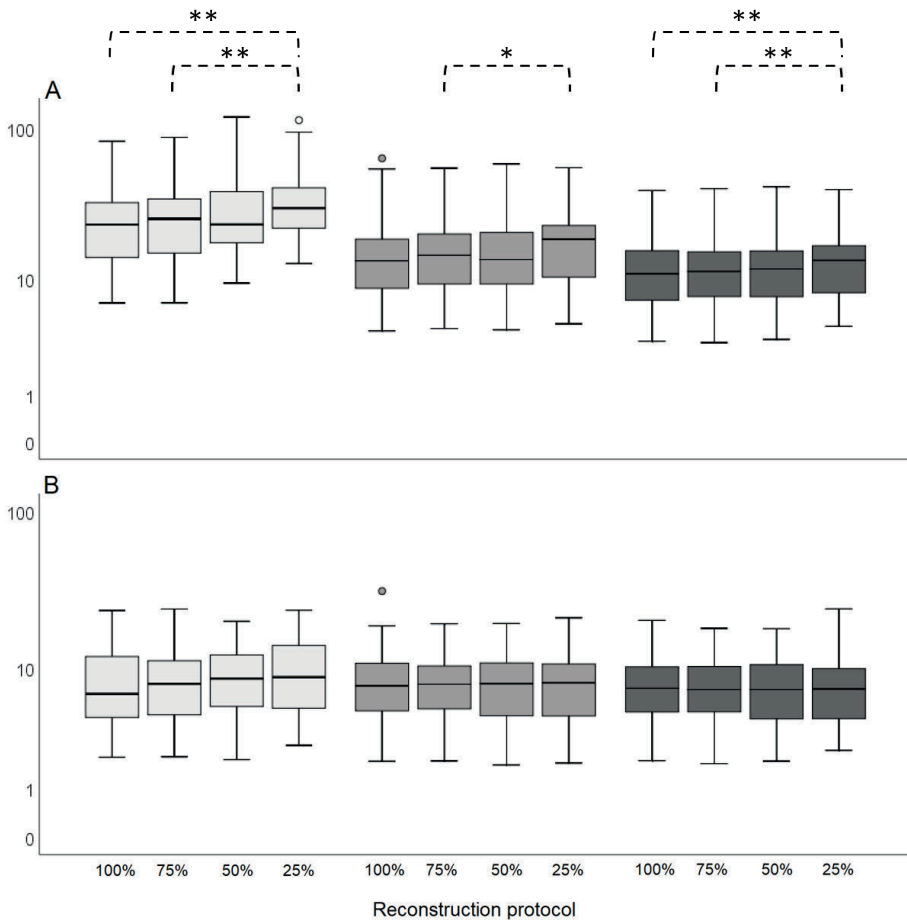


**Figure 4** Vision only semiquantitative tumor lesion comparison between scan durations. For all patients ( $n = 15$ ), the tumor lesion  $\text{SUV}_{\text{max}}$  (A) and  $\text{SUV}_{\text{peak}}$  (B) derived from images obtained using the Vision PET/CT system and the Clinical Vision reconstruction protocol (light gray), the EARL2 Vision reconstruction protocol (grey), and the EARL1 Vision reconstruction protocol (dark gray) are compared at different scan durations (100% to 25%, from left to right for each reconstruction protocol). The boxes illustrate the interquartile range (IQR) divided by the median SUV. The whiskers extend to a maximum of  $1.5 \times \text{IQR}$  beyond the box. \* indicates  $P < 0.05$  and \*\* indicates  $P < 0.01$ . Outliers are represented by dots.

The results of the healthy tissue comparisons between scan durations are shown in Figure 5. No significant differences in healthy tissue  $SUV_{mean}$  and  $SUV_{peak}$  were found between images obtained using the Vision at different scan durations. Because of different  $^{89}\text{Zr}$ -labeled mAbs used in this study, a substantial visual difference was observed in the uptake in the spleen. For clarity, the healthy tissue comparisons per  $^{89}\text{Zr}$ -labeled mAb for the spleen are shown in Supplemental Figure 2.

Noise estimates from calculation of the coefficient of variation (COV) derived from the 3-cm-diameter liver VOIs in each image are shown in Figure 6. A difference in image noise can be observed between reconstruction methods and scan durations. Noise increases with shorter scan times; this effect is more prominent when using the Clinical Vision reconstruction protocol compared to EARL2- and EARL1-compliant reconstruction settings.

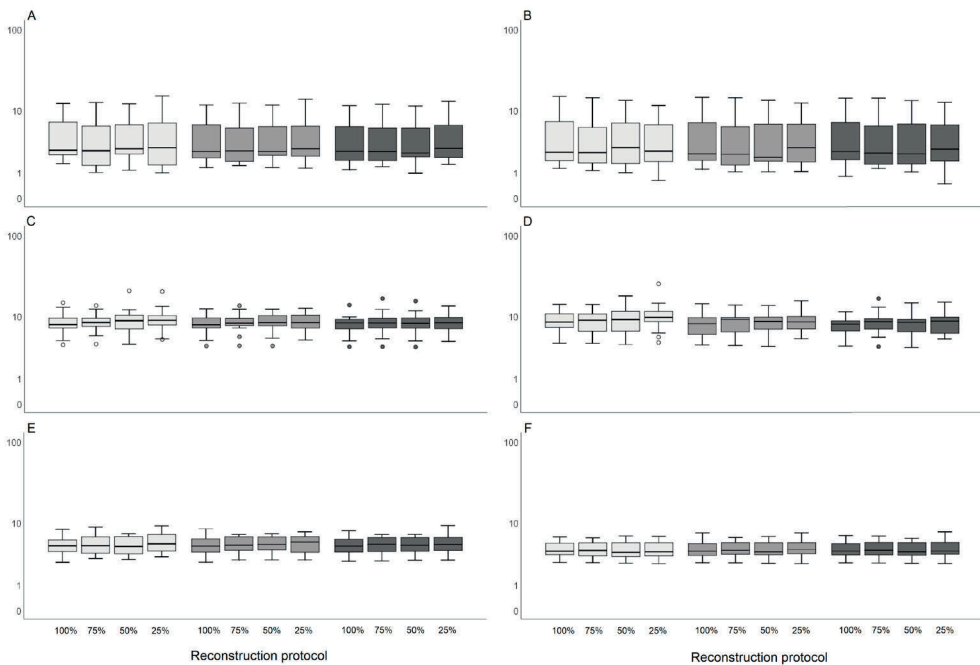


**Figure 5** Vision only semiquantitative healthy tissue comparison between scan durations. For all patients ( $n = 15$ ),  $SUV_{peak}$  (left column) and  $SUV_{mean}$  (right column) of healthy tissues (bloodpool (A and B), kidney cortex (C and D), spleen (E and F), and liver (G and H)) derived from images obtained through use of the Vision PET/CT system and the Clinical Vision reconstruction protocol (light gray), the EARL2 Vision reconstruction protocol (gray), and the EARL1 Vision reconstruction protocol (dark gray) are compared at different scan durations (100% to 25%, from left to right for each reconstruction protocol).

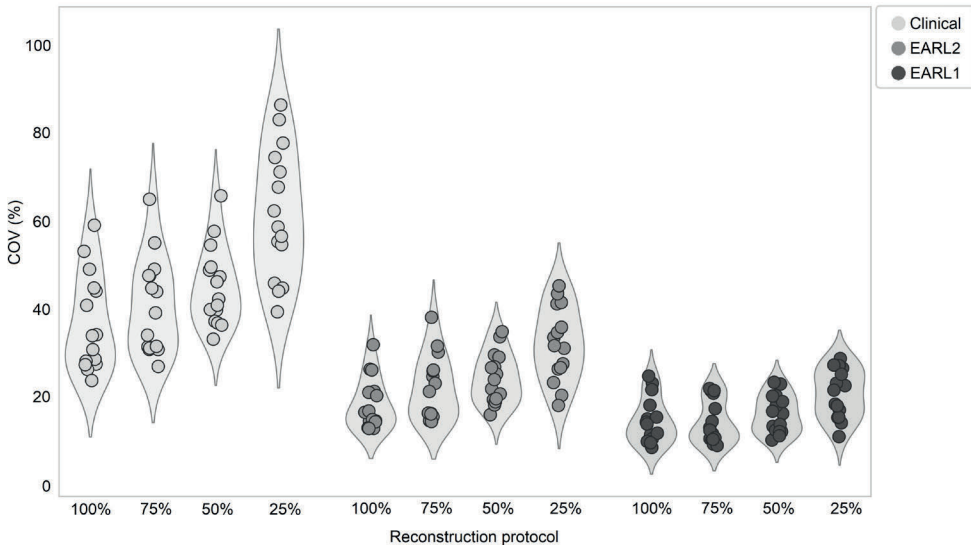


**Figure 6** Liver COV ( $n = 15$ ) obtained from the Clinical Vision (light gray), EARL2 Vision (gray), and EARL1 Vision compliant (dark gray) reconstructed images at 100%, 75%, 50%, and 25% of the scan time (from left to right).

## Qualitative image analysis

With regard to qualitative image evaluation, inter-reader agreement ranged from fair to moderate on noise, lesion demarcation, and overall image quality with  $\kappa = 0.23$  ( $P = 0.000$ , 95% CI (0.12 - 0.34)),  $\kappa = 0.27$  ( $P = 0.000$ , 95% CI (0.13 - 0.41)), and  $\kappa = 0.41$  ( $P = 0.000$ , 95% CI (0.28 - 0.55)), respectively.

## Discussion

In the current study, semiquantitative performance of the Vision with regard to its predecessor, the mCT, was evaluated for  $^{89}\text{Zr}$  immunoPET imaging in oncology patients. In addition, possibilities of reducing scan time while maintaining image quality using the Vision were explored.

This study shows that when using the Vision PET/CT system, a reduction in scan time of 50% is possible while maintaining semiquantitative PET image accuracy, when applying the EARL1 Vision settings for image reconstruction. Significant differences in semiquantitative PET image biomarkers were found for shorter scan durations when using the Clinical Vision reconstruction protocol, especially  $\text{SUV}_{\text{max}}$  increases at shorter scan times (50% and 25%) with regard to full acquisition time. A non-negligible consideration when using  $\text{SUV}_{\text{max}}$  for uptake measurements in PET images is statistical quality. When reducing scan time, variability in  $\text{SUV}_{\text{max}}$  can largely be explained by the associated increase in noise (19) (see Figure 6). The addition of a Gaussian filter (as used in the EARL2 and EARL1 Vision reconstruction

settings (7 mm and 5 mm, respectively)) smooths the image hereby reducing noise and  $SUV_{max}$  variability (20) which results in similar results for lesion quantification at shorter scan times. A more robust alternative, and diminishing the need for a filter at shorter acquisition times, is to use  $SUV_{peak}$  for lesion quantification. Although  $SUV_{peak}$  is expected to be more susceptible to partial volume effect in small lesion segmentation (19), its semiquantitative performance is less affected by scan duration and reconstruction protocol (see Figures 4 and 5). Makris et al. (2014) previously recommended the use of  $SUV_{peak}$  for performing quantitatively accurate  $^{89}Zr$  PET imaging studies. They found very low variability in  $SUV_{peak}$  between various PET/CT systems and imaging sites. Moreover, this recommendation has then been affirmed in an  $^{89}Zr$  PET imaging study by Kaalep et al. (2018) describing a multicenter PET/CT system and reconstruction comparison trial in which  $SUV_{peak}$  was found to be least sensitive to noise and reconstruction differences. As we also found  $SUV_{max}$  to vary between reconstructed images obtained from different PET/CT systems, but also between differently reconstructed images obtained from a single system, our recommendation is (in line with previously reported results described above) to use  $SUV_{peak}$  for quantification of  $^{89}Zr$  PET images. In case EARL standards 1 compliant settings are used (for comparison between systems),  $SUV_{max}$  could be reported as well besides  $SUV_{peak}$  for lesion quantification.

In the current study, the difference between  $SUV_{peak}$  and  $SUV_{mean}$  derived from healthy tissues is minimal due to the small 1-cm-diameter spherical VOI that was used in the bloodpool, kidney cortex, and spleen.  $SUV_{mean}$  was included in the evaluation of semiquantitative performance comparison of healthy tissues between systems as  $SUV_{mean}$  measurement of these organs is used, for example, in whole organ dosimetry analyses. Using  $SUV_{mean}$  for whole organ dosimetry avoids susceptibility to segmentation variability as opposed to using  $SUV_{max}$  or  $SUV_{peak}$  (21). Please note, the significant difference in  $SUV_{max}$  for all healthy tissues found between systems using the Clinical Vision reconstruction protocol versus the  $^{89}Zr$ -EARL mCT protocol (see Table 4). This difference can be explained by the 8 mm Gaussian smoothing filter applied to the images acquired using the mCT, whereas images acquired on the Vision were not smoothed at all. With regard to semiquantitative performance between systems at full acquisition time, no further significant differences between tumor lesions and bloodpool, kidney cortex, and liver measurements were found. For the spleen however, a significant increase in  $SUV$  measured on the images obtained from the Vision PET/CT was observed. As this was only the case for the spleen (and not for the other healthy tissues), a clear explanation for this phenomenon has not yet been found. We suspect the improved tissue demarcation due to improved sensitivity and ToF on the Vision PET/CT system could play a role here. No patient instructions with respect to food and fluid intake

prior to  $^{89}\text{Zr}$  PET acquisition were given, resulting in large cold areas with the size of a filled stomach on the acquired images. These cold spots were more prominently visible on the Vision images with a clearer demarcation of the stomach. Due to the improved ToF, better contrast recovery in the spleen using the Vision PET/CT may have resulted in a better reflection of the true counts originating from the spleen as opposed to some possible larger signal spillover between the cold stomach and the very intense spleen on the mCT images. Future  $^{89}\text{Zr}$  immunoPET studies with a larger homogeneous patient population will have to explore this phenomenon to clarify these findings. Until then, the spleen should not be used as reference tissue in  $^{89}\text{Zr}$  immunoPET imaging studies.

Regarding qualitative image assessment, fair to moderate inter-reader agreement was achieved. As the nuclear medicine physicians were asked to score the images individually without a direct comparison with optimal  $^{89}\text{Zr}$  immunoPET image quality, scoring was considered difficult. Another factor that should be considered when interpreting these results is that the image quality of  $^{18}\text{F}$ -FDG PET scans (compared to  $^{89}\text{Zr}$  immunoPET images) on the Vision is excellent (5). These excellent  $^{18}\text{F}$ -FDG PET images might have been an unintentional reference for visual  $^{89}\text{Zr}$  immunoPET image assessment. Furthermore, previous experience with  $^{89}\text{Zr}$  immunoPET readings, and personal preference of the reading Nuclear Medicine physicians regarding acceptable image quality could have played a role in the observed variation in the image quality assessment.

Previous work also performed by our research group explored the effect of scan time reduction on semiquantitative PET image parameters and image quality in  $^{18}\text{F}$ -FDG PET imaging using the Vision (6). Here, a factor of 3 reduction in scan time was considered possible while maintaining image quality using the clinically preferred Vision reconstruction protocol with additional 2 mm Gaussian filtering. In the current study, possibilities to reduce scan duration in  $^{89}\text{Zr}$  immunoPET imaging were discovered. Using the EARL Vision protocols semiquantitative performance remains reliable when decreasing scan duration up to a factor of 2 (see Figures 4 and 5) at the cost of a slight increase in noise (see Figure 6).

Therefore, for  $^{89}\text{Zr}$  immunoPET imaging in the clinic using a digital PET/CT one may choose to reduce scan duration to improve patient comfort and increase throughput. Also expanding scan time points beyond 6-7 days p.i. may come in reach with acceptable image quality.

## **Conclusion**

In this study we found, when using the Vision for  $^{89}\text{Zr}$  immunoPET imaging and the EARL standards 1 compliant reconstruction settings, semiquantitative PET image biomarkers to remain reliable when using images obtained at reduced scan durations



up to a factor of 2.

Also, as  $SUV_{\max}$  is highly affected by noise and reconstruction settings, and differs considerably in quantification of tumor lesions as well as healthy tissues between various PET/CT systems, we strongly recommend using the EARL standards 1 compliant reconstruction protocol and to report  $SUV_{\text{peak}}$  for reliable, comparable across systems, tumor lesion quantification in  $^{89}\text{Zr}$  immunoPET imaging.

## References

1. Hsu DFC, Ilan E, Peterson WT, Uribe J, Lubberink M, Levin CS. Studies of a next-generation silicon-photomultiplier-based time-of-flight PET/CT system. *J Nucl Med.* 2017;58:1511-1518.
2. van Sluis J, de Jong JR, Schaar J, Noordzij W, van Snick JH, Dierckx RAJO, et al. Performance characteristics of the digital Biograph Vision PET/CT System. *J Nucl Med.* 2019;60:1031-1036.
3. Nguyen NC, Vercher-Conejero JL, Sattar A, Miller MA, Maniawski PJ, Jordan DW, et al. Image quality and diagnostic performance of a digital PET prototype in patients with oncologic diseases: initial experience and comparison with analog PET. *J Nucl Med.* 2015;56:1378-1385.
4. Rausch I, Ruiz A, Valverde-Pascual I, Cal-González J, Beyer T, Carrio I. Performance evaluation of the Philips Vereos PET/CT System according to the NEMA NU2-2012 standard. *J Nucl Med.* 2018;60:561-567.
5. van Sluis J, Boellaard R, Somasundaram A, van Snick JH, Borra RJH, Dierckx RAJO, et al. Image quality and semiquantitative measurements on the biograph vision PET/CT system: initial experiences and comparison with the Biograph mCT. *J Nucl Med.* 2020;61:129-135.
6. van Sluis J, Boellaard R, Dierckx RAJO, Stormezand GN, Glaudemans AWJM, Noordzij W. Image quality and activity optimization in oncologic  $^{18}\text{F}$ -FDG PET using the digital Biograph Vision PET/CT System. *J Nucl Med.* 2020;61:764-771.
7. Salvadori J, Odille F, Verger A, Olivier P, Karcher G, Marie P-Y, et al. Head-to-head comparison between digital and analog PET of human and phantom images when optimized for maximizing the signal-to-noise ratio from small lesions. *EJNMMI Phys.* 2020;7:7:11.
8. Zhang Y, Hong H, Cai W. PET tracers based on Zirconium-89. *Curr Radiopharm.* 2011;4:131-139.
9. Van De Watering FCJ, Rijpkema M, Perk L, Brinkmann U, Oyen WJG, and Boerman OC. Zirconium-89 labeled antibodies: A new tool for molecular imaging in cancer patients. *Biomed Res Int.* 2014;Article ID 203601.
10. Conti M, Eriksson L. Physics of pure and non-pure positron emitters for PET: A review and a discussion. *EJNMMI Phys.* 2016;3:3-8.
11. Bensch F, Brouwers AH, Lub-de Hooge MN, de Jong JR, van der Veegt B, Sleijfer S, et al.  $^{89}\text{Zr}$ -trastuzumab PET supports clinical decision making in breast cancer patients, when HER2 status cannot be determined by standard work up. *Eur J Nucl Med Mol Imaging.* 2018;45:2300-2306.
12. Varrone A, Sjöholm N, Eriksson L, Gulyás B, Halldin C, Farde L. Advancement in PET quantification using 3D-OP-OSEM point spread function reconstruction with the HRRT. *Eur J Nucl Med Mol Imaging.* 2009;36:1639-1650.
13. Boellaard R, Delgado-Bolton R, Oyen WJG, Giammarile F, Tatsch K, Eschner W, et al. FDG PET/CT: EANM procedure guidelines for tumor imaging: version 2.0. *Eur J Nucl Med Mol Imaging.* 2014;42:328-354.
14. Boellaard R. New developments of EANM oncology PET/CT guidelines and update of the EARL accreditation standards presentation. Presented at the: 2018. [https://eanm-earl-wordpress.esh.netkey.at/wp-content/uploads/2021/04/EARL\\_18F\\_stds2\\_PPP\\_Boellaard\\_Oct2018-1.pdf](https://eanm-earl-wordpress.esh.netkey.at/wp-content/uploads/2021/04/EARL_18F_stds2_PPP_Boellaard_Oct2018-1.pdf).
15. Kaalep A, Burggraaff CN, Pieplensbosch S, Verwer EE, Sera T, Zijlstra JM, et al. Quantitative



- implications of the updated EARL 2019 PET-CT performance standards. *EJNMMI Phys.* 2019;6:1-16.
16. Makris NE, Boellaard R, Visser EP, de Jong JR, Vanderlinden B, Wierts R, et al. Multicenter harmonization of  $^{89}\text{Zr}$  PET/CT performance. *J Nucl Med.* 2014;55:264-267.
  17. Kaalep A, Huisman M, Sera T, Vugts D, Boellaard R. Feasibility of PET/CT system performance harmonisation for quantitative multicentre  $^{89}\text{Zr}$  studies. *EJNMMI Phys.* 2018;5:26.
  18. Boellaard R. Quantitative oncology molecular analysis suite: ACCURATE [abstract]. *J Nucl Med.* 2018;59 (supplement 1):1753-1753. [http://jnm.snmjournals.org/cgi/content/short/59/supplement\\_1/1753](http://jnm.snmjournals.org/cgi/content/short/59/supplement_1/1753).
  19. Lodge MA, Chaudhry MA, Wahl RL. Noise considerations for PET quantification using maximum and peak standardized uptake value. *J Nucl Med.* 2012;53:1041-1047.
  20. Boellaard R, Krak NC, Hoekstra OS, Lammertsma AA. Effects of noise, image resolution, and ROI definition on the accuracy of standard uptake values: A simulation study. *J Nucl Med.* 2004;45:1519-1527.
  21. Schwartz J, Humm JL, Gonen M, Kalaigian H, Schoder H, Larson SM, et al. Repeatability of SUV measurements in serial PET. *Med Phys.* 2011;38:2629-2638.

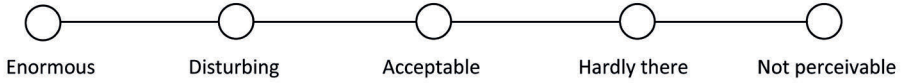
## Supplemental data

# Visual Image Assessment Form

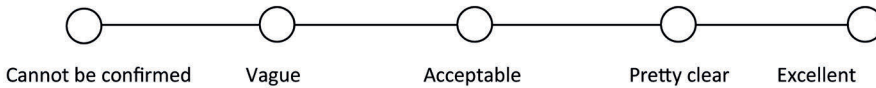
Image code: .....

---

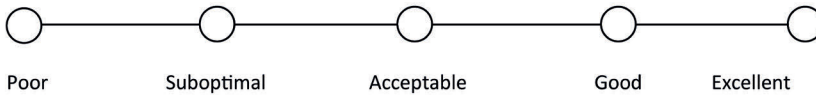
**1. Image noise is:**



**2. The lesion margin delineation:**

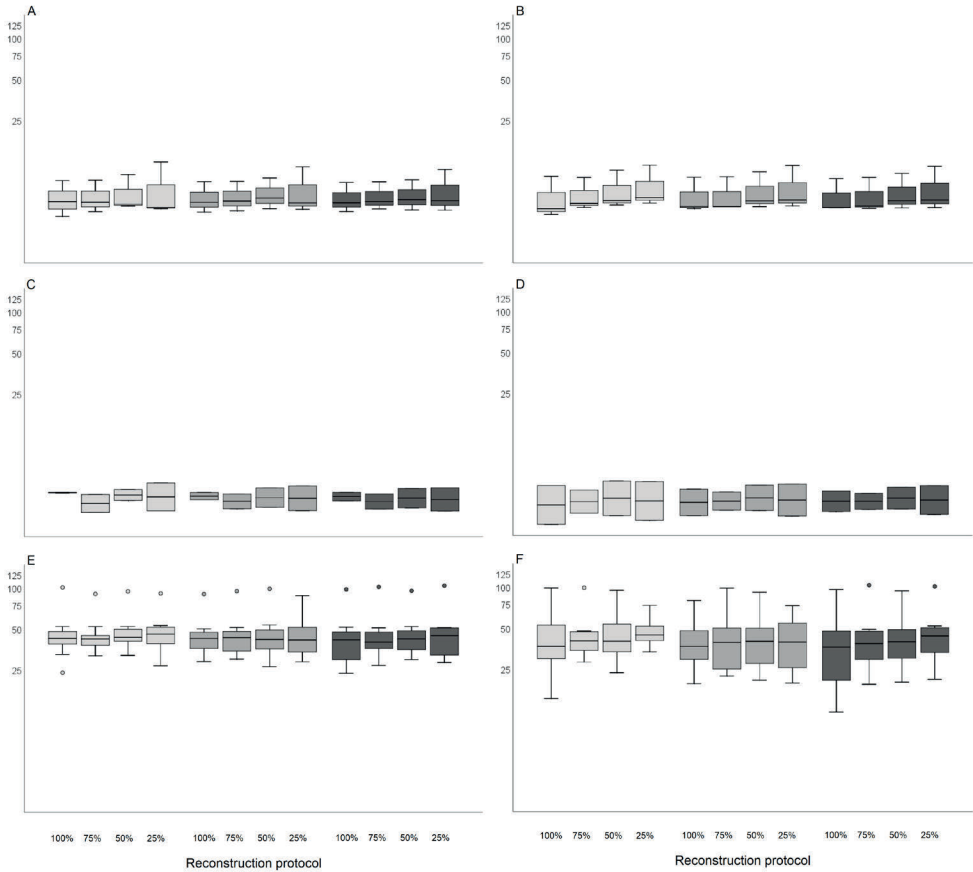


**3. Overall image quality is:**



**Supplemental Figure 1** Image quality assessment form based on a 5-point Likert scale used by two nuclear medicine physicians for visual assessment of image noise, lesion margin demarcation, and overall image quality.





**Supplemental Figure 2** Vision only semiquantitative healthy tissue comparison between scan durations. For all patients ( $n = 15$ ),  $SUV_{peak}$  (left column) and  $SUV_{mean}$  (right column) of the spleen using three different  $^{89}\text{Zr}$ -labeled mAbs (tracer 1 for  $n = 3$  (A and B), tracer 2 for  $n = 2$  (C and D), and tracer 3 for  $n = 10$  (E and F)). PET imaging was performed on the Vision system using the Clinical Vision reconstruction protocol (light gray), the EARL2 Vision reconstruction protocol (gray), and the EARL1 Vision reconstruction protocol (dark gray) are compared at different scan durations (100% to 25%, from left to right for each reconstruction protocol).





# Chapter 7

---

## First-time imaging of $^{89}\text{Zr}$ -trastuzumab in breast cancer using a long axial field-of-view PET/CT scanner

Adrienne H. Brouwers<sup>1</sup>, Joyce van Sluis<sup>1</sup>, Johannes H. van Snick<sup>1</sup>, Carolien P. Schröder<sup>1,2</sup>, Inge O. Baas<sup>3</sup>, Ronald Boellaard<sup>1,4</sup>, Andor W.J.M. Glaudemans<sup>1</sup>, Ronald J.H. Borra<sup>1</sup>, Adriaan A. Lammertsma<sup>1</sup>, Rudi A.J.O. Dierckx<sup>1</sup>, and Charalampos Tsoumpas<sup>1</sup>

<sup>1</sup>Department of Nuclear Medicine and Molecular Imaging, University of Groningen, University Medical Center Groningen, Hanzeplein 1, 9713 GZ Groningen, The Netherlands

<sup>2</sup>Department of Medical Oncology, University of Groningen, University Medical Center Groningen, Hanzeplein 1, 9713 GZ Groningen, The Netherlands

<sup>2</sup>Department of Medical Oncology, University of Utrecht, University Medical Center Utrecht, Heidelberglaan 100, 3584 CX Utrecht, The Netherlands

<sup>4</sup>Department of Radiology and Nuclear Medicine, Cancer Center Amsterdam, Amsterdam University Medical Centers, Free University of Amsterdam, De Boelelaan 1117, 1081 HV Amsterdam, The Netherlands

*Eur J Nucl Med Mol Imaging.* 2022;49:3593-3595.



Long axial field-of-view (LAFOV) PET/CT scanners have been introduced recently (1, 2), which offer numerous advantages (3). One important advantage of using LAFOV PET for imaging  $^{89}\text{Zr}$ -labeled monoclonal antibodies (mAbs), i.e., immunoPET, is the substantial increase in sensitivity compared with standard axial field-of-view (SAFOV) PET/CT systems, which may lead to a remarkable image quality improvement. This first study showcases such improvement in immunoPET imaging with the Biograph Vision Quadra (VQ) LAFOV PET/CT (Siemens Healthineers).

Two patients suffering from metastatic HER2-positive breast cancer were administered with 37 MBq  $^{89}\text{Zr}$ -trastuzumab in order to assist clinical decision-making (4, 5). Patients were scanned 4 days postinjection with a Biograph mCT PET/CT (patient A) (Siemens Healthineers) or a Biograph Vision PET/CT (patient B) (Siemens Healthineers), according to local standard operating procedures with overall scan durations of 45 min and 32 min, for, respectively, mCT and Vision. Following the clinical scans, patients were scanned with the VQ. For the VQ, we chose to apply a long scan duration of 30 min (patient A) and 32 min (patient B) to improve image quality rather than shortening the overall scan duration, as compared to Vision. For SAFOV systems, the acquisition and reconstruction parameters complied with European Association of Nuclear Medicine Research Ltd. (EARL) 1 standard specifications, whilst for LAFOV, we also applied vendor-recommended settings for optimized imaged quality for clinical reading (CLIN) (see Table 1) (6, 7). PET/CT images of patient A are shown in the top two rows (*a-h*), for patient B in the bottom two rows (*i-p*). The same intensity scale, SUV range 0-10, applies for all images, except the fused images (*e*, *m*). Additional reconstructions of the VQ data were obtained, mimicking 3-min (*d*, *h*, *l*, *p*) and 10-min (*c*, *g*, *k*, *o*) acquisitions, illustrating more pragmatic scan durations.

As can be appreciated from these first human immunoPET images on an LAFOV system, the image quality improvement (*f*) is most spectacular when compared with the mCT (*a*). For example, in patient A, an additional small bone lesion was visualized with the VQ in the pelvic area (*f*), which was not visible with the SAFOV system (*a*). Even when compared to the Vision (*i*), the VQ image (*n*) shows improved quality without applying any filter after reconstruction. Moreover, this visual improvement in image quality was even appreciated in the 10 min image compared with the 30-45 min acquisition needed for SAFOV systems.

Thus, this image shows that the large axial FOV system provides substantial improvement in image quality when applying currently preferred total scan durations on SAFOV systems (45 min for mCT, 32 min for Vision). Additionally, with the new LAFOV system, there is room for further reduction of the scan duration with still very acceptable image quality, even for  $^{89}\text{Zr}$ -labeled mAb PET/CT studies.

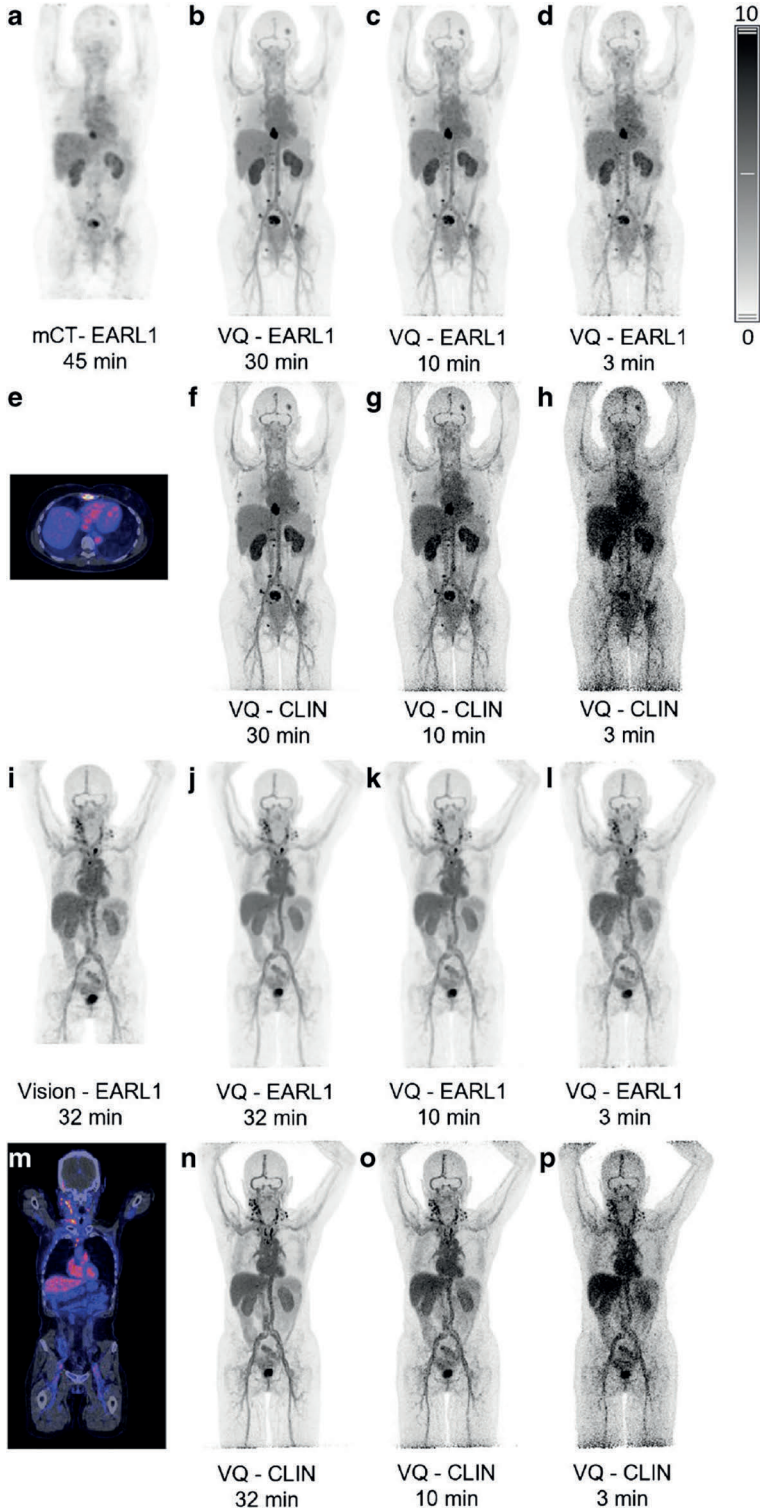


**Table 1** Acquisition and reconstruction parameters for the different systems.

PET/CT system	Acquisition method	Reconstruction protocol name	Reconstruction settings
<u>Biograph mCT</u>	Step-and-shoot: 5 min per bed position (bp), 9 bp in total	EARL1	3D OP-OSEM, 3i21s with ToF + PSF, matrix size 256x256x488 with voxel size 3.2x3.2x2.0 mm <sup>3</sup> , 6.5 mm FWHM Gaussian filter
<u>Biograph Vision</u>	Flow: 8 min per whole body CBM pass, 4 passes	EARL1	3D OP-OSEM, 4i5s with ToF + PSF, matrix size 220x220x706 with voxel size 3.3x3.3x1.5 mm <sup>3</sup> , 7 mm FWHM Gaussian filter
<u>Biograph Vision Quadra</u>	Single bp	EARL1	3D OP-OSEM, 4i5s with ToF + PSF, matrix size 220x220x708 with voxel size 3.3x3.3x1.5 mm <sup>3</sup> , 7 mm FWHM Gaussian filter
	Single bp	CLIN	3D OP-OSEM, 4i5s with ToF + PSF, matrix size 440x440x708 with voxel size 1.6x1.6x1.5 mm <sup>3</sup> , no filtering

EARL = European Association of Nuclear Medicine Research Ltd; 3D OP-OSEM = three dimensional ordinary poisson ordered-subset expectation maximization; i = iterations; s = subsets; ToF = time-of-flight; PSF = point spread function (resolution modeling); FWHM = full width at half maximum; CBM = continuous bed motion

## References

1. Badawi RD, Shi H, Hu P, Chen S, Xu T, Price PM, et al. First human imaging studies with the EXPLORER total-body PET scanner. *J Nucl Med.* 2019;60:299–303.
2. Prenosil GA, Sari H, Fürstner M, Afshar-Oromieh A, Shi K, Rominger A, et al. Performance characteristics of the Biograph Vision Quadra PET/CT system with long axial field of view using the NEMA NU 2–2018 standard. *J Nucl Med.* 2022;63:476–84.
3. Slart RHJA, Tsoumpas C, Glaudemans AWJM, Noordzij W, Willemsen ATM, Borra RJH, et al. Long axial field of view PET scanners: a road map to implementation and new possibilities. *Eur J Nucl Med Mol Imaging.* 2021;48:4236–45.
4. Dijkers EC, Oude Munnink TH, Kosterink JG, Brouwers AH, Jager PL, de Jong JR, et al. Biodistribution of  $^{89}\text{Zr}$ -trastuzumab and PET imaging of HER2-positive lesions in patients with metastatic breast cancer. *Clin Pharmacol Ther.* 2010;87:586–92.
5. Bensch F.  $^{89}\text{Zr}$ -trastuzumab PET supports clinical decision making in breast cancer patients, when HER2 status cannot be determined by standard work up. *Eur J Nucl Med Mol Imaging.* 2018;45:2300–6.
6. Boellaard R, Delgado-Bolton R, Oyen WJG, Giammarile F, Tatsch K, Eschner W, et al. FDG PET/CT: EANM procedure guidelines for tumour imaging: version 2.0. *Eur J Nucl Med Mol Imaging.* 2015;42:328–54.
7. Kaalep A, Huisman M, Sera T, Vugts D, Boellaard R. Feasibility of PET/CT system performance harmonisation for quantitative multicentre  $^{89}\text{Zr}$  studies. *EJNMMI Phys.* 2018;5:26.





# Chapter 8

---

## EARL compliance and imaging optimization on the Biograph Vision Quadra PET/CT using phantom and clinical data

Joyce van Sluis<sup>1</sup>, Johannes H. van Snick<sup>1</sup>, Adrienne H. Brouwers<sup>1</sup>, Walter Noordzij<sup>1</sup>, Rudi A.J.O. Dierckx<sup>1</sup>, Ronald J.H. Borra<sup>1</sup>, Riemer H.J.A. Slart<sup>1</sup>, Adriaan A. Lammertsma<sup>1</sup>, Andor W.J.M. Glaudemans<sup>1</sup>, Ronald Boellaard<sup>1,2</sup>, and Charalampos Tsoumpas<sup>1</sup>

<sup>1</sup>Department of Nuclear Medicine and Molecular Imaging, University of Groningen, University Medical Center Groningen, Hanzeplein 1, 9713 GZ Groningen, The Netherlands

<sup>2</sup>Department of Radiology and Nuclear Medicine, Cancer Center Amsterdam, Amsterdam University Medical Centers, Free University of Amsterdam, De Boelelaan 1117, 1081 HV Amsterdam, The Netherlands

*Eur J Nucl Med Mol Imaging. 2022; Epub ahead of print.*



## **Abstract**

Current European Association of Nuclear Medicine (EANM) Research Ltd. (EARL) guidelines for the standardization of PET imaging developed for conventional systems have not yet been adjusted for long axial field-of-view (LAFOV) systems. In order to use the LAFOV Siemens Biograph Vision Quadra PET/CT (Siemens Healthineers, Knoxville, TN, USA) in multicenter research and harmonized clinical use, compliance to EARL specifications for  $^{18}\text{F}$ -FDG tumor imaging was explored in the current study. Additional tests at various locations throughout the LAFOV and the use of shorter scan durations were included. Furthermore, clinical data were collected to further explore and validate the effects of reducing scan duration on semiquantitative PET image biomarker accuracy and precision when using EARL-compliant reconstruction settings.

**Methods** EARL compliance phantom measurements were performed using the NEMA image quality phantom both in the center and at various locations throughout the LAFOV. PET data (maximum ring difference (MRD) = 85) were reconstructed using various reconstruction parameters and reprocessed to obtain images at shorter scan durations. Maximum, mean and peak activity concentration recovery coefficients (RC) were obtained for each sphere and compared to EARL standards specifications.

Additionally, PET data (MRD = 85) of 10 oncological patients were acquired and reconstructed using various reconstruction settings and reprocessed from 10 min listmode acquisition into shorter scan durations. Per dataset, SUVs were derived from tumor lesions and healthy tissues. ANOVA repeated measures were performed to explore differences in lesion  $\text{SUV}_{\text{max}}$  and  $\text{SUV}_{\text{peak}}$ . Wilcoxon signed-rank tests were performed to evaluate differences in background  $\text{SUV}_{\text{peak}}$  and  $\text{SUV}_{\text{mean}}$  between scan durations. The coefficient of variation (COV) was calculated to characterize noise.

**Results** Phantom measurements showed EARL compliance for all positions throughout the LAFOV for all scan durations. Regarding patient data, EARL-compliant images showed no clinically meaningful significant differences in lesion  $\text{SUV}_{\text{max}}$  and  $\text{SUV}_{\text{peak}}$  or background  $\text{SUV}_{\text{mean}}$  and  $\text{SUV}_{\text{peak}}$  between scan durations. Here, COV only varied slightly.

**Conclusion** Images obtained using the Vision Quadra PET/CT comply with EARL specifications. Scan duration and/or activity administration can be reduced up to a factor of 10 without the interference of increased noise.

## **Introduction**

The non-invasive imaging technique positron emission tomography (PET) integrated with computed tomography (CT) is widely used in oncology (1–3) and many other clinical indications, providing both metabolic and anatomic information (4). In oncology, PET/CT is a rapidly evolving technique which has become part of the daily clinical routine for initial diagnosis, staging, radiation therapy planning, prognosis and treatment response monitoring (3, 5, 6).

The most frequently used PET tracer in oncology is 2-deoxy-2-[fluorine-18] fluoro-D-glucose ( $^{18}\text{F}$ -FDG) (7). Acquired  $^{18}\text{F}$ -FDG images can be interpreted visually, e.g., for staging, or semi-quantitatively, e.g., to determine treatment response, which requires standardized imaging procedures, especially in a multi center setting (8). When procedure guidelines for tumor imaging are followed, PET images can be converted to standardized uptake values (SUV), normalizing the radioactive activity concentration as depicted in the image by body weight and amount of injected tracer activity. Using SUVs as a metric of relative tissue uptake facilitates comparisons between patients (7).

Recently, long axial field-of-view (LAFOV) PET/CT systems have become available with the conceptual idea to increase system sensitivity and reach a larger anatomical coverage (9). Current European Association of Nuclear Medicine (EANM) Research Ltd. (EARL) guidelines (5) to support intersystem standardization of PET imaging, thereby facilitating multicenter studies, have been developed for conventional systems with a 20–25 cm axial field-of-view (FOV). For LAFOV systems, these performance standards have not yet been adjusted or evaluated.

In order to use our newly installed 106-cm LAFOV Siemens Biograph Vision Quadra PET/CT system (Siemens Healthineers) in multicenter research trials and harmonized clinical use together with conventional FOV systems at our PET center, compliance to the EARL guidelines needed to be explored. Therefore, in the current study, compliance of the system to EARL standards 1 and 2 throughout the axial FOV was explored to assess whether this system adheres to the European PET image harmonization guidelines for  $^{18}\text{F}$ -FDG tumor imaging. Scan duration and/or activity optimization has been explored for the Biograph Vision Quadra PET/CT by Alberts et al. (10); however, without the use of standardizing and harmonizing PET image acquisition and reconstruction protocols, they did not focus on maintaining semiquantitative accuracy. Therefore, clinical data were also collected to further explore and validate the effects of reducing scan duration on semiquantitative PET image biomarker accuracy and precision for both EARL1 and EARL2 standard compliant reconstruction protocols as well as for clinically optimized reconstruction settings (for maximum ring difference (MRD) = 85 PET data).

## **Materials and methods**

### **Patient Population**

To test compliance to EARL standards 1 and 2, phantom measurements were performed following EARL standard operating procedures using the NEMA NU2-2001 image quality phantom filled with a sphere-to-background ratio of 10:1 measured in the center of the FOV (11, 12). Subsequently, the phantom was placed and measured at various other positions along the axial FOV: one-eighth, a quarter, three-quarters, and seven-eighths. Listmode PET data were acquired for 7 min at each position. Subsequently, these data were resampled and reconstructed to represent several shorter scan durations: 60 s, 120 s, and 240 s. Images were reconstructed using the three-dimensional (3D) ordered-subset expectation maximization (OSEM) algorithm with 4 iterations, 5 subsets, matrix size of 220 x 220 x 708 with a voxel size of 3.3 x 3.3 x 1.5 mm<sup>3</sup>, with the application of time of flight (ToF), and resolution modeling (PSF). Different Gaussian filters were applied after reconstruction to comply with EARL standards 1 and/or 2. For each image, the maximum, mean and peak activity concentration recovery coefficients (RC) were derived for all spheres and compared to the EARL standards specifications.

Subsequently, a total of 10 clinically referred oncological patients received a standard weight-based (3 MBq/kg) intravenous injection of <sup>18</sup>F-FDG activity, followed by a whole body 10 min listmode PET acquisition. Patients were instructed to fast and avoid exercise at least 4–6 h prior to intravenous <sup>18</sup>F-FDG injection. Plasma glucose levels were <8.3 mmol/L before activity administration. PET data were acquired using a single static bed position covering 106 cm (approximately from skull vertex to mid thigh) at approximately 60 min (± 5%) postinjection. PET data acquired for 10 min were reconstructed, and images at shorter scan times were obtained: 60 s, 120 s, 240 s, and 420 s. Images were reconstructed using the vendor-recommended clinically optimized protocol (hereinafter referred to as CLIN) consisting of 3D OSEM with 4 iterations, 5 subsets, a matrix size of 440 x 440 x 708 with a voxel size of 1.6 x 1.6 x 1.5 mm<sup>3</sup>, ToF, PSF and no filtering. In addition, EARL standards 1 and 2 compliant reconstruction settings were used to obtain images adhering to the European guidelines for multicenter PET image quantification and harmonization which were determined from the phantom measurements described above. For each dataset, tumor lesions were segmented to obtain blood glucose-corrected SUVs using a semi-automated segmentation method (i.e., 50% of SUV<sub>peak</sub> isocontour). In addition, a 3-cm-diameter spherical volume of interest (VOI) was placed in the liver, which served as a reference background uptake VOI and which was used to estimate image noise.

ANOVA repeated measures with post hoc Bonferroni adjustment for pairwise comparisons were performed to explore differences in lesion SUV<sub>max</sub> and SUV<sub>peak</sub>

Between scan durations in the differently reconstructed images. Differences in liver  $SUV_{peak}$  and  $SUV_{mean}$  between scan durations in the differently reconstructed images were evaluated by Wilcoxon signed-rank tests. A  $P$  value of less than 0.05 was considered significant. The coefficient of variation (COV) of the activity concentration (kBq/mL) in the liver VOI was used to characterize noise. Analyses were performed using SPSS Statistics, version 27.0 (IBM corp., Armonk, NY, USA). Both in the phantom measurements as well as in the patient images, data were acquired using a maximum ring difference (MRD) of 322 crystal rings, while at this time, image reconstructions could only be performed with an MRD of 85 crystals rings (13).

## Results

EARL standards 1 compliance was achieved for all positions along the LAFOV using a 7 mm full width at half maximum (FWHM) Gaussian filter for scan durations of 60 s, 120 s, 240 s, and 420 s. However, RCs were close to the specified upper limits. EARL standards 2 compliance was achieved for all positions throughout the LAFOV using a 5 mm FWHM Gaussian filter for all scan durations of 60 s, 120 s, 240 s, and 420 s, and all RCs were in the middle between specified upper and lower limits. Figure 1 shows recovery coefficients obtained from images acquired in the center of the LAFOV for both EARL 1 and 2 standards specifications.

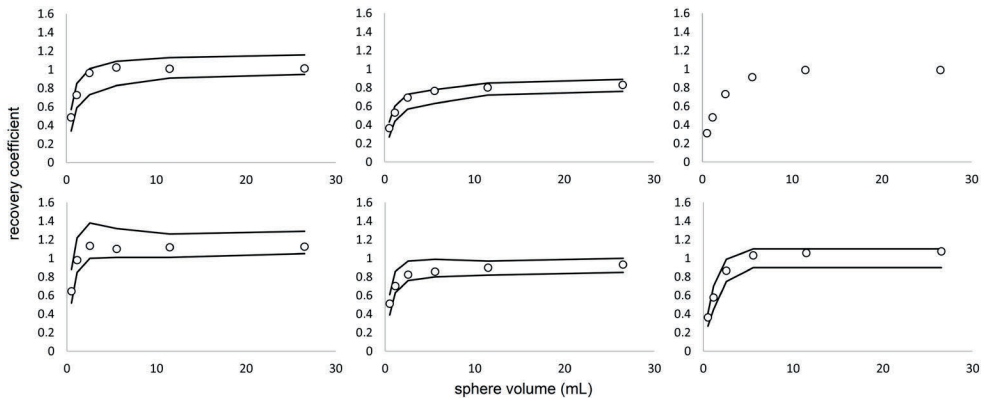


**Figure 1** Max (left), mean (middle) and peak (right) RCs as a function of sphere size obtained from images acquired at the center of the LAFOV reconstructed according to EARL standards 1 (top row) and 2 (bottom row). Solid lines represent the EARL standards acceptability criteria. Please note that EARL 1 standards specifications do not include limits for peak RCs.

For both EARL 1 and 2 standards reconstructions, minimal variability (<7% for  $SUV_{max}$ , and <3% for  $SUV_{peak}$  and  $SUV_{mean}$ ) of RCs was observed between the positions tested along the axial FOV. Figure 2 shows RCs obtained from images acquired at various locations throughout the LAFOV for both EARL 1 and 2 standards specifications. The influence of shorter scan durations on RC measurements regarding EARL standards 1 and 2 specifications in the center of the LAFOV is illustrated in Figure 3.

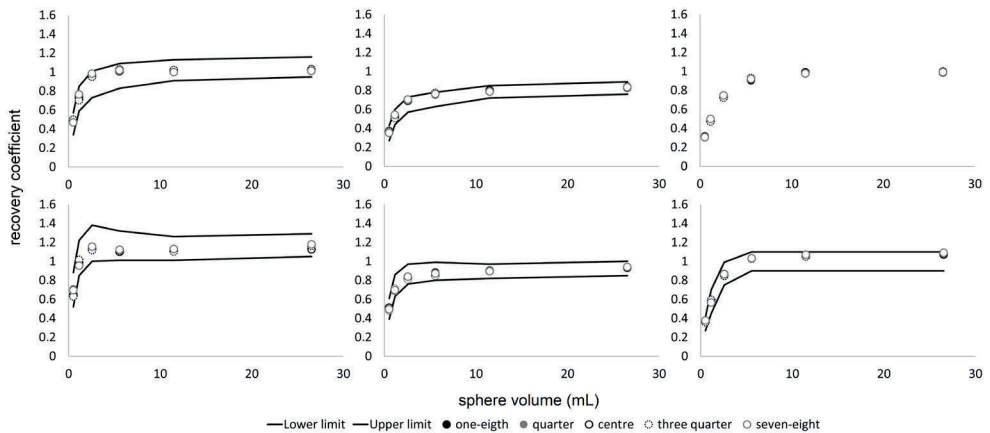


**Figure 2** Max (left), mean (middle) and peak (right) RCs as a function of sphere size obtained from images acquired at various positions throughout the LAFOV reconstructed according to EARL standards 1 (top row) and 2 (bottom row). Solid lines represent the EARL standards acceptability criteria. Please note that EARL 1 standards specifications do not include limits for peak RCs.

Subsequently, a total of 10 oncological patients (6 men, 4 women; age 52–84 years [range],  $71 \pm 9.0$  years [mean  $\pm$  SD]) received a weight-based (3 MBq/kg)  $^{18}\text{F}$ -FDG injected activity (weight: 58–112 kg [range],  $79 \pm 15$  kg [mean  $\pm$  SD]; activity: 174–305 MBq [range],  $238 \pm 36$  MBq [mean  $\pm$  SD]). Examples of patient maximum intensity projection images at different scan durations, reconstructed according to the CLIN protocol and following EARL standards 1 and 2 reconstruction settings are shown in Figure 4. Significant differences in lesion  $SUV_{max}$  ( $n = 16$ ) were found between the 10 min images and the 60 s ( $P < 0.01$ ; 95% CI, 0.91–3.35), and 120 s ( $P < 0.05$ ; 95% CI, 0.10–2.57) images when reconstructed using the CLIN protocol, whereas no differences were found in lesion  $SUV_{peak}$ . EARL standards 1 and 2 compliant images did not show significant differences in lesion  $SUV_{max}$  and  $SUV_{peak}$  between any of the scan durations. An illustration of lesion  $SUV_{max}$  and  $SUV_{peak}$  obtained from images reconstructed following the CLIN and EARL standards 1 and 2 reconstruction settings at different scan durations is shown in the boxplots of

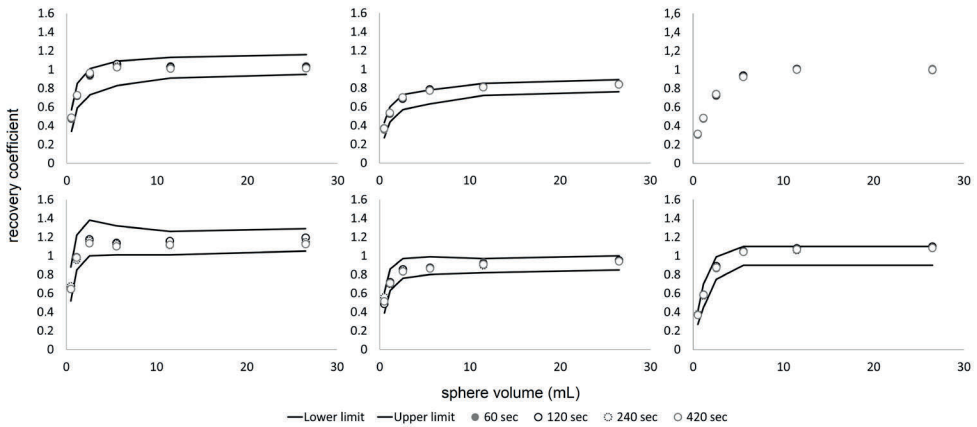


**Figure 3** Max (left), mean (middle) and peak (right) RCs as a function of sphere size obtained from images acquired at the center of the LAFOV reconstructed using various scan durations according to EARL standards 1 (top row) and 2 (bottom row). Solid lines represent the EARL standards acceptability criteria. Please note that EARL 1 standards specifications do not include limits for peak RCs.

Figure 5; for an overview of all the corresponding statistical parameters, please refer to Supplementary Table 1. Concerning  $SUV_{peak}$  in the liver, significant differences were found in the images obtained using the CLIN reconstruction settings between the 600 s scan duration, and the 420 s (Z-score: -2.547;  $P$  value: 0.011), the 240 s (Z-score: -2.701;  $P$  value: 0.007), the 120 s (Z-score: -2.803;  $P$  value: 0.005), and the 60 s (Z-score: -2.803;  $P$  value: 0.005). Furthermore, in the images reconstructed according to EARL standards 1 protocol, a significant difference was found between the 600 s and 240 s images (Z-score: -2.191;  $P$  value: 0.028). Regarding  $SUV_{mean}$  in the liver, the 600 s images differed significantly from the 60 s images reconstructed according to the CLIN (Z-score: -2.191;  $P$  value: 0.028). However, the largest difference in  $SUV_{peak}$  was only 0.11 which is clinically a non-relevant difference. For an illustration of the differences in liver  $SUV_{peak}$  and  $SUV_{mean}$  between scan durations for the differently reconstructed images, see Figure 6; for an overview of all the corresponding statistical parameters, please refer to Supplementary Table 2. Furthermore, the difference in the increase in COV of activity concentration (kBq/mL) in the liver between images obtained using the CLIN and EARL standards 1 and 2 reconstruction settings at different scan durations is illustrated in a violin plot in Figure 7. COV increased substantially from approximately 7% for the 10 min scan up to 25% with decreasing scan duration for images reconstructed with the CLIN protocol. Unlike images reconstructed according to EARL standards protocols in which COV remained constant from the 10 min to the 240 s scan duration and only increased marginally by approximately 5% from 10 min to 60 s (COV increased from 3 to 8% in images reconstructed using EARL 2 settings).

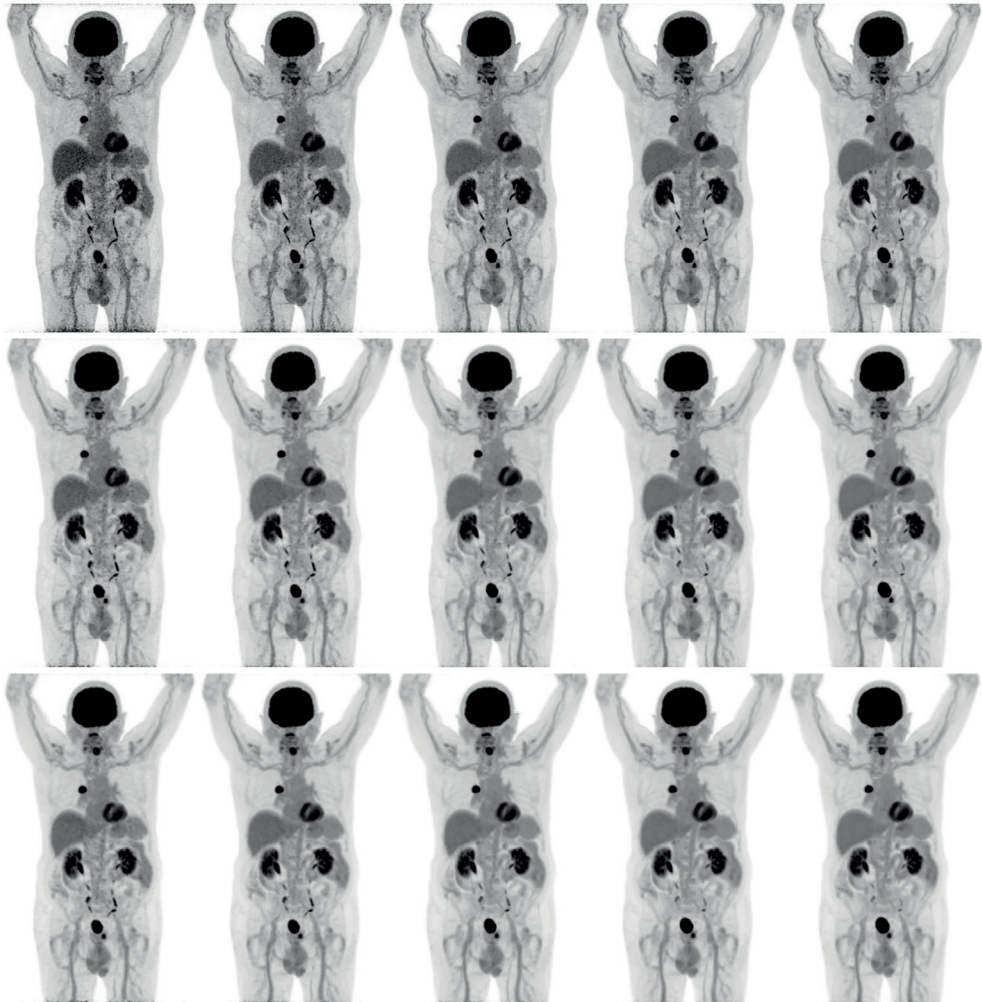


**Figure 4** Maximum intensity projection PET images of an 80-year-old male (weight, 93 kg) with right-sided non-small cell lung carcinoma. The patient received a single injection of 279 MBq  $^{18}\text{F}$ -FDG, and PET images were acquired at 60 min postinjection. Listmode PET data were reconstructed using CLIN (top row), EARL standards 2 (middle row), and EARL standards 1 (bottom row) reconstruction settings for various scan durations: 60 s, 120 s, 240 s, 420 s, and 600 s (from left to right).

## Discussion

In the present study, the ability of the Biograph Vision Quadra PET/CT to adhere to the European PET image harmonization guidelines for  $^{18}\text{F}$ -FDG tumor imaging, EARL standards 1 and 2, was explored. EARL standards 1 compliance was narrowly achieved as RCs were close to the specified EARL standards 1 limits. The EANM guidelines for tumor imaging version 2.0 (5) describe that spatial filters applied during or after reconstruction should not exceed an FWHM of 7 mm; therefore, further optimization for EARL 1 compliance was not performed. With the emergence of so-

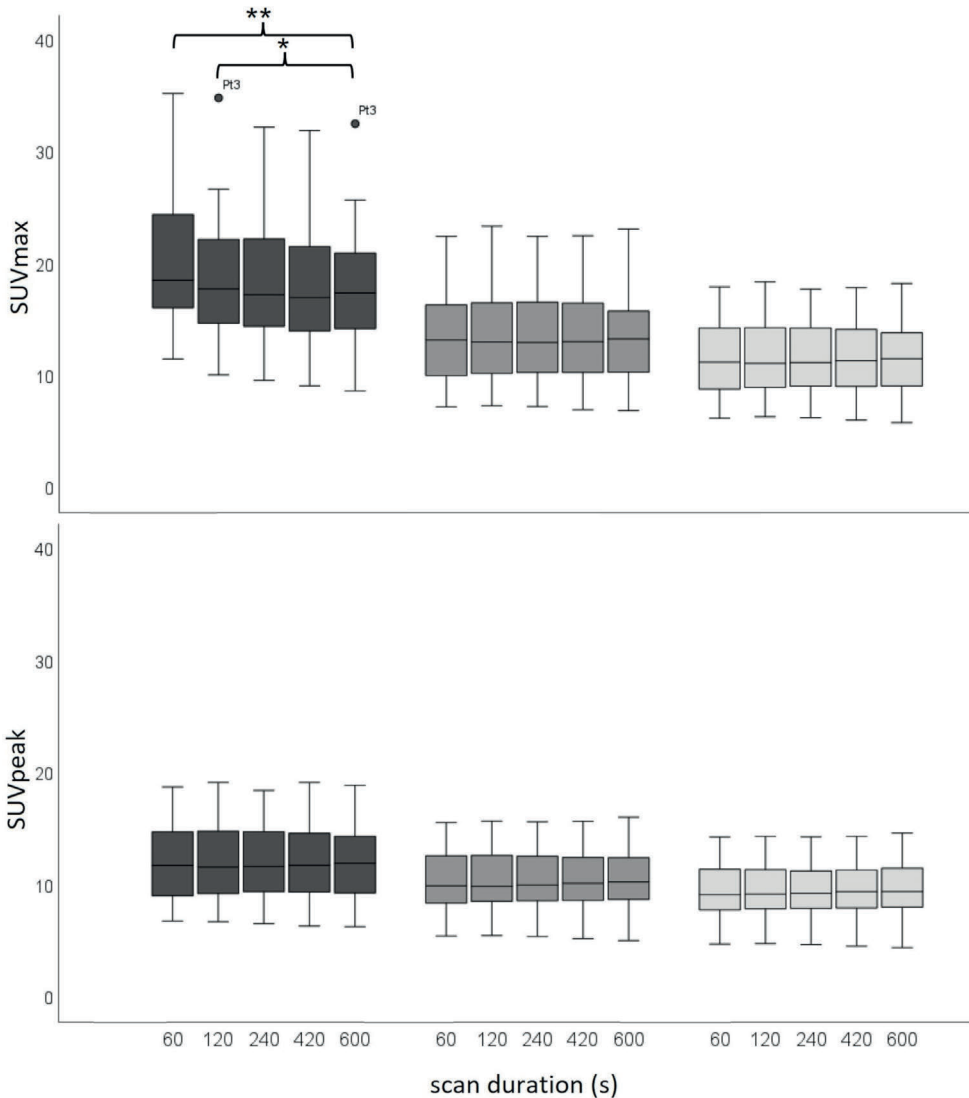


**Figure 5** Boxplots illustrating the spread of lesion  $SUV_{max}$  (top row) and  $SUV_{peak}$  (bottom row) obtained from images reconstructed using the CLIN (dark gray), EARL standards 2 compliant (gray) and EARL standards 1 compliant (light grey) protocol for various scan durations. For a single very  $^{18}\text{F}$ -FDG avid lesion in one patient, occasionally, some data points were seen as an outlier in the boxplot illustrated with circles and labeled with the patient code (Pt<sub>x</sub>). Single asterisks and double asterisks indicate significant differences between scan durations at  $P < 0.05$  and  $P < 0.001$ , respectively.

called digital PET/CT systems equipped with silicon-based photomultiplier (SiPM) detectors, an update of the guideline was introduced, namely the EARL standards 2 (14, 15). The Biograph Vision Quadra PET/CT system essentially consists of four

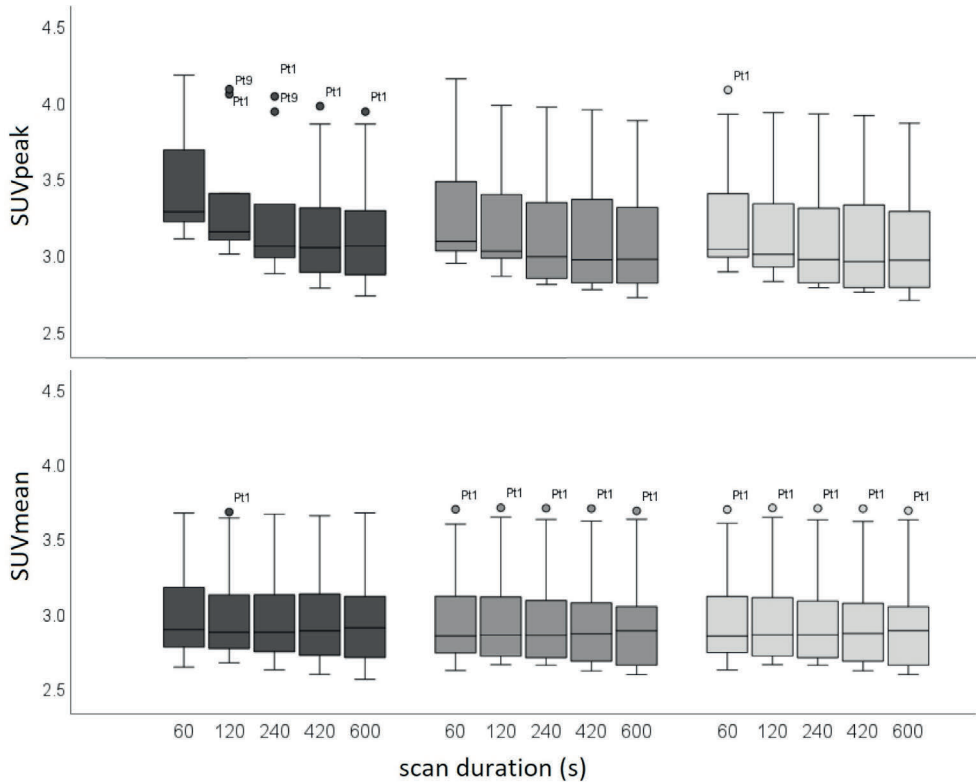


**Figure 6** Boxplots illustrating the spread of liver  $SUV_{peak}$  (top row) and  $SUV_{mean}$  (bottom row) obtained from images reconstructed using the CLIN (dark gray), EARL standards 2 compliant (gray) and EARL standards 1 compliant (light gray) protocol at various scan durations. For one or two subjects with high liver uptake, occasionally, some data points were seen as outliers in the boxplot illustrated with circles and labeled with the patient code (Ptx).

interconnected ‘digital’ Biograph Vision PET systems (16) equipped with SiPM-based photon detectors characterized by superior timing resolution, thereby enabling improved ToF estimation and efficient photon detection, a high spatial resolution and, compared to other commercially available PET/CT systems with shorter axial FOV, a higher sensitivity of 16.4 kcps/MBq. These developments in PET technology over the last five years resulting in improved image quality and, thereby, the possibility to reduce either scan duration or amount of administered activity or optimize both, were already impressive (17, 18). Now, with many more detectors and consequently a substantial increase in sensitivity to 111.5 kcps/MBq (measured using a 140 cm line source in two sets of NEMA sensitivity phantoms (unpublished data, MRD = 85)), the ability of the Biograph Vision Quadra to better adhere to EARL standards 2 than to EARL standards 1 is likely because of improved system performance. As recommended in the literature, the logical next step in clinical practice is to focus solely on EARL 2 standards after finalizing the transition period from EARL 1 to

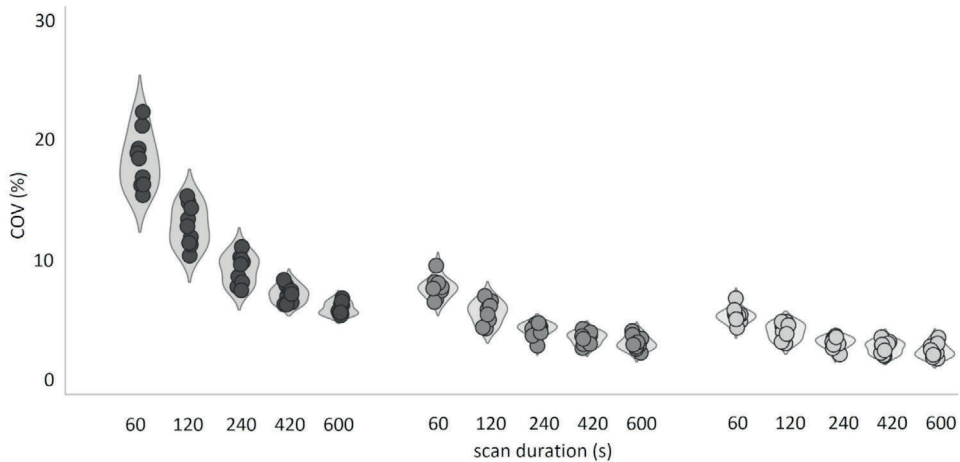


**Figure 7** COV of activity concentration (kBq/mL) obtained from a 3-cm-diameter spherical VOI placed in a homogeneous part of the liver in images reconstructed using the CLIN (dark gray), EARL standards 2 (gray) and EARL standards 1 (light gray) protocol at various scan durations.

EARL 2 (15, 19).

Please note that successive phantom scans were performed at different locations throughout the LAFOV. Data were acquired for 7 min, and no count matching was applied because no impact of increased noise levels was expected. To verify our expectations, the coefficient of variation derived from a 3-mL-spherical VOI placed in the background of the unfiltered phantom PET data was calculated and showed an increase from 9 to 13% between the first and last measurement. The results in the current study show that this difference in noise has no substantial or meaningful impact on the observed RCs as a function of the axial phantom position (variation in recovery was very minimal and would have been even better if count matching would have been applied). Therefore, equivalence has been sufficiently shown as a function of position in the LAFOV.

A portion of the collected clinical data was reconstructed to obtain images at shorter scan durations using different reconstruction protocols, and the effect of scan time reduction on semiquantitative PET image biomarker accuracy and noise was explored. Here, the reduced scan time can also serve as a surrogate for a reduction in injected activity, with an added 10% to compensate for lower noise-equivalent count rates per MBq at higher activity concentrations (6). The current study shows that up to a factor of 10 reduction in scan duration and/or activity administration is possible when  $SUV_{\text{peak}}$  is used for semiquantitative assessment together with EARL-compliant reconstruction settings. This factor of 10 reduction in activity administration or scan duration enables new possibilities for research and in clinical settings. A significant reduction in injected activity results in a proportional reduction

in radiation exposure, which enables new applications for  $^{18}\text{F}$ -FDG PET besides tumor imaging. For example, it may become feasible to screen high-risk populations for abnormal cells that may become cancerous in subjects who have no symptoms (yet). In addition, it facilitates PET/CT imaging of children, who are considerably more sensitive to the carcinogenic effects of ionizing radiation than adults (20). On the other hand, a significant reduction in scan duration may make it possible to scan patients who are unable to lay still for a long time, such as intensive care unit (ICU) patients (21), children (without anesthesia) and patients with severe back pain or claustrophobic patients.

Further research should explore the potential reduction in scan duration and/or activity administration for PET radiotracers with comparatively longer physical half-lives such as  $^{89}\text{Zr}$ -labeled monoclonal antibodies (mAbs). The slow clearance of mAbs, matching the long physical decay half-life of  $^{89}\text{Zr}$ , leads to somewhat higher radiation exposure (22). This limits the amount of activity that can be administered, especially in non-malignant diseases, resulting in poor PET image quality (23). Hence, at present, long scan durations are required when conventional FOV PET/CT systems are used in order to obtain adequate image quality, especially at later scan time-points postinjection. Consequently, reduced radiation risk may justify the use of  $^{89}\text{Zr}$ -labeled mAbs in patients with non-malignant diseases too.

Finally, it is important to note that the data acquired in this study were reconstructed using an MRD of only 85 crystal rings, which translates into a photon acceptance angle of  $18^\circ$  (13). When applying the maximum possible MRD of 322 crystal rings, corresponding to a photon acceptance angle of  $52^\circ$ , the so-called ultra-high sensitivity (UHS) mode becomes available for reconstructing clinical PET data. The sensitivity of the Quadra is rather constant over the LAFOV when using an MRD of 85; when using the UHS mode with an MRD of 322, this is not the case (13; the peak of the sensitivity is located in the center of the LAFOV and degrades towards the edges. Changes in sensitivity may induce changes in noise levels which require repetition of the experiments as reported in the current work with additional noise level characterization using the COV. However, using the MRD of 85 represents the lower limit of the system's potential; the UHS mode will increase image quality even further and will create even more possibilities to reduce scan duration and/or activity administration. Nonetheless, it is expected that the UHS mode will require more careful study due to the fact that the optimal iteration number will need to be explored because of the variant sensitivity and, consequently, noise along the FOV. Furthermore, one may expect a somewhat worse spatial resolution for MRD of 322. These aspects will need to be explored thoroughly in the future, prior to adaptation of the full ring difference for use in clinical routine.

## **Conclusion**

Images obtained using the LAFOV Biograph Vision Quadra PET/CT (MRD = 85) comply with EARL standards specifications when performing reconstructions using 3D ToF OSEM with 4 iterations and 5 subsets, a matrix size of 220 x 220 x 708, resolution modeling and Gaussian filtering of 7 mm and 5 mm FWHM, respectively. Improved performance characteristics of this LAFOV PET/CT system cause RCs to better fall within lower and upper limits of EARL standards 2 specifications than of EARL standards 1 specifications. Therefore, it is recommended to use EARL standards 2 for image quantification and harmonization when using the Biograph Vision Quadra PET/CT.

Furthermore, compared to conventional PET/CT systems, scan duration or  $^{18}\text{F}$ -FDG activity administration could be reduced by a factor of 2.5 when  $\text{SUV}_{\text{max}}$  is used combined with CLIN reconstruction settings compared to conventional PET/CT systems. Serious bias in  $\text{SUV}_{\text{max}}$  is induced at shorter scan durations due to increased noise levels (COV increased up to 25%). When images are reconstructed using the protocol defined by EARL standards 2 and semiquantitative analysis is performed using  $\text{SUV}_{\text{peak}}$ , a factor of 10 reduction is possible, respectively, without the interference of increased noise (COV increased from 3 to 8%).

## References

1. Bastiaannet E, Groen B, Jager PL, Cobben DCP, van der Graaf WTA, Vaalburg W, et al. The value of FDG-PET in the detection, grading and response to therapy of soft tissue and bone sarcomas; a systematic review and meta-analysis. *Cancer Treat Rev.* 2004;30:83-101.
2. Slomka PJ, Pan T, Germano G. Recent advances and future progress in PET instrumentation. *Semin Nucl Med Elsevier.* 2016;46:5-19.
3. Hsu DFC, Ilan E, Peterson WT, Uribe J, Lubberink M, Levin CS. Studies of a next-generation silicon-photomultiplier-based time-of-flight PET/CT system. *J Nucl Med.* 2017;58:1511-8.
4. Townsend DW. Dual-modality imaging: combining anatomy and function. *J Nucl Med.* 2008;49:938-55.
5. Boellaard R, Delgado-Bolton R, Oyen WJG, Giammarile F, Tatsch K, Eschner W, et al. FDG PET/CT EANM procedure guidelines for tumour imaging version 2.0. *Eur J Nucl Med Mol Imaging.* 2014;42:328-54.
6. Boellaard R, Oyen WJG, Hoekstra CJ, Hoekstra OS, Visser EP, Willemsen AT, et al. The Netherlands protocol for standardisation and quantification of FDG whole body PET studies in multi-centre trials. *Eur J Nucl Med Mol Imaging.* 2008;35:2320-33.
7. Kinahan PE, Fletcher JW. PET/CT standardized uptake values (SUVs) in clinical practice and assessing response to therapy. *Semin Ultrasound CT MR.* 2011;31:496-505.
8. Wahl RL, Jacene H, Kasamon Y, Lodge MA. From RECIST to PERCIST: evolving considerations for PET response criteria in solid tumors. *J Nucl Med.* 2009;50:122-51.
9. Vandenberghe S, Moskal P, Karp JS. State of the art in total body PET. *EJNMMI Phys EJNMMI Physics.* 2020;7:35.
10. Alberts I, Hünermund J, Prenosil G, Mingels C, Bohn KP, Viscione M, et al. Clinical performance of long axial field of view PET/CT: a head-to-head intra-individual comparison of the Biograph Vision Quadra with the Biograph Vision PET/CT. *Eur J Nucl Med Mol Imaging.* 2021;48:2395-404.
11. Kaalep A, Sera T, Oyen W, Krause BJ, Chiti A, Liu Y, et al. EANM/EARL FDG-PET/CT accreditation - summary results from the first 200 accredited imaging systems. *Eur J Nucl Med Mol Imaging.* 2018;45:412-22.
12. Boellaard R, Delgado-Bolton R, Oyen WJG, Giammarile F, Tatsch K, Eschner W, et al. FDG PET/CT: EANM procedure guidelines for tumour imaging: version 1.0. *Eur J Nucl Med Mol Imaging.* 2010;37:181-200.
13. Prenosil GA, Sari H, Fürstner M, Afshar-Oromieh A, Shi K, Rominger A, et al. Performance characteristics of the Biograph Vision Quadra PET/CT system with long axial field of view using the NEMA NU 2-2018 Standard. *J Nucl Med.* 2021;63:476-84.
14. Boellaard R. New developments of EANM oncology PET/CT guidelines and update of the EARL accreditation standards presentation [Internet]. 2018. Available from: [https://eanm-earl-wordpress.esh.netkey.at/wp-content/uploads/2021/04/EARL\\_18F\\_stds2\\_PPP\\_Boellaard\\_Oct2018-1.pdf](https://eanm-earl-wordpress.esh.netkey.at/wp-content/uploads/2021/04/EARL_18F_stds2_PPP_Boellaard_Oct2018-1.pdf).
15. Boellaard R, Sera T, Kaalep A, Hoekstra OS, Barrington SF, Zijlstra JM. Updating PET/CT

- performance standards and PET/CT interpretation criteria should go hand in hand. *EJNMMI Res.* 2019;9:5-6.
16. van Sluis J, de Jong JR, Schaar J, Noordzij W, van Snick JH, Dierckx RAJO, et al. Performance characteristics of the Digital Biograph Vision PET/CT System. *J Nucl Med.* 2019;60:1031-6.
  17. van Sluis J, Boellaard R, Somasundaram A, van Snick JH, Borra RJH, Dierckx RAJO, et al. Image quality and semiquantitative measurements on the biograph vision PET/CT system: initial experiences and comparison with the biograph MCT. *J Nucl Med.* 2020;61:129-35.
  18. van Sluis J, Boellaard R, Dierckx RAJO, Stormezand GN, Glaudemans AWJM, Noordzij W. Image quality and activity optimization in oncologic  $^{18}\text{F}$ -FDG PET using the Digital Biograph Vision PET/CT System. *J Nucl Med.* 2020;61:764-71.
  19. Kaalep A, Burggraaff CN, Pieplensbosch S, Verwer EE, Sera T, Zijlstra J, et al. Quantitative implications of the updated EARL 2019 PET-CT performance standards. *EJNMMI Phys.* 2019;6:1-16.
  20. Kleinerman RA. Cancer risks following diagnostic and therapeutic radiation exposure in children. *Pediatr Radiol.* 2006;36:121-5.
  21. Pijl JP, Londema M, Kwee TC, Nijsten MWN, Slart RHJA, Dierckx RAJO, et al. FDG-PET/CT in intensive care patients with bloodstream infection. *Crit Care.* 2021;25:1-12.
  22. Bouleau A, Lebon V, Truillet C. PET imaging of immune checkpoint proteins in oncology. *Pharmacol. Ther.* 2021.
  23. Conti M, Eriksson L. Physics of pure and non-pure positron emitters for PET: a review and a discussion. *EJNMMI Phys* 2016;3:3-8.

## Supplemental data

**Supplemental Table 1** Differences in lesion  $SUV_{max}$  and  $SUV_{peak}$  between scan durations of images reconstructed using various reconstruction settings evaluated using ANOVA repeated measures. Single asterisks and double asterisks indicate significant differences between scan durations at  $P < 0.05$  and  $P < 0.001$ , respectively.

Semiquantitative parameter	Reconstruction settings	Scan duration comparison	Mean difference	P value	95% confidence interval
<u>Lesion <math>SUV_{max}</math></u>	CLIN	600 s – 420 s	-0.168	1.000	-0.792 – 0.456
		600 s – 240 s	-0.594	1.000	-1.755 – 0.568
		600 s – 120 s	-1.334	0.028*	-2.570 – -0.098
		600 s – 60 s	-2.132	0.000**	-3.351 – -0.913
	EARL2	600 s – 420 s	0.076	1.000	-0.243 – 0.394
		600 s – 240 s	0.085	1.000	-0.313 – 0.483
		600 s – 120 s	0.028	1.000	-0.388 – 0.444
		600 s – 60 s	0.168	1.000	-0.416 – 0.752
	EARL1	600 s – 420 s	0.057	1.000	-0.131 – 0.246
		600 s – 240 s	0.107	1.000	-0.207 – 0.421
		600 s – 120 s	0.036	1.000	-0.269 – 0.341
		600 s – 60 s	0.194	1.000	-0.219 – 0.606
<u>Lesion <math>SUV_{peak}</math></u>	CLIN	600 s – 420 s	0.003	1.000	-0.193 – 0.199
		600 s – 240 s	0.074	1.000	-0.224 – 0.372
		600 s – 120 s	0.059	1.000	-0.291 – 0.410
		600 s – 60 s	0.203	1.000	-0.251 – 0.658
	EARL2	600 s – 420 s	0.028	1.000	-0.143 – 0.199
		600 s – 240 s	0.046	1.000	-0.227 – 0.320
		600 s – 120 s	0.053	1.000	-0.223 – 0.329
		600 s – 60 s	0.171	1.000	-0.135 – 0.477
	EARL1	600 s – 420 s	0.036	1.000	-0.103 – 0.175
		600 s – 240 s	0.057	1.000	-0.163 – 0.277
		600 s – 120 s	0.064	1.000	-0.156 – 0.285
		600 s – 60 s	0.140	1.000	-0.118 – 0.398

**Supplemental Table 2** Differences in background  $SUV_{peak}$  and  $SUV_{mean}$  between scan durations of images reconstructed using various reconstruction settings evaluated using Wilcoxon signed-rank tests. Single asterisks and double asterisks indicate significant differences between scan durations at  $P < 0.05$  and  $P < 0.001$ , respectively.

Semiquantitative parameter	Reconstruction settings	Scan duration comparison	Z-score	P value
<u>Background <math>SUV_{peak}</math></u>	CLIN	600 s – 420 s	-2.547	0.011*
		600 s – 240 s	-2.701	0.007*
		600 s – 120 s	-2.803	0.005*
		600 s – 60 s	-2.803	0.005*
	EARL2	600 s – 420 s	-1.580	0.114
		600 s – 240 s	-1.784	0.074
		600 s – 120 s	-1.784	0.074
		600 s – 60 s	-1.784	0.074
	EARL1	600 s – 420 s	-1.478	0.139
		600 s – 240 s	-2.191	0.028*
		600 s – 120 s	-1.784	0.074
		600 s – 60 s	-1.784	0.074
<u>Background <math>SUV_{mean}</math></u>	CLIN	600 s – 420 s	-0.357	0.721
		600 s – 240 s	-1.172	0.241
		600 s – 120 s	-1.478	0.139
		600 s – 60 s	-2.191	0.028*
	EARL2	600 s – 420 s	-1.172	0.241
		600 s – 240 s	-1.274	0.203
		600 s – 120 s	-1.376	0.169
		600 s – 60 s	-0.866	0.386
	EARL1	600 s – 420 s	-1.274	0.203
		600 s – 240 s	-1.274	0.203
		600 s – 120 s	-1.376	0.169
		600 s – 60 s	-1.070	0.285





# Chapter 9

---

## Use of population input functions for reduced scan duration whole body Patlak $^{18}\text{F}$ -FDG PET imaging

Joyce van Sluis<sup>1</sup>, Maqsood Yaqub<sup>1,2</sup>, Adrienne H. Brouwers<sup>1</sup>, Rudi A.J.O. Dierckx<sup>1</sup>, Walter Noordzij<sup>1</sup>, and Ronald Boellaard<sup>1,2</sup>

<sup>1</sup>Department of Nuclear Medicine and Molecular Imaging, University of Groningen, University Medical Center Groningen, Hanzeplein 1, 9713 GZ Groningen, The Netherlands

<sup>2</sup>Department of Radiology and Nuclear Medicine, Cancer Center Amsterdam, Amsterdam University Medical Centers, Free University of Amsterdam, De Boelelaan 1117, 1081 HV Amsterdam, The Netherlands

*EJNMMI Phys.* 2021;8:1-8.



## **Abstract**

Whole body Patlak images can be obtained from an acquisition of first 6 min of dynamic imaging over the heart to obtain the arterial input function (IF), followed by multiple whole body sweeps up to 60 min p.i. The use of a population-averaged IF (PIF) could exclude the first dynamic scan and minimize whole body sweeps to 30-60 min p.i. Here, the effects of (incorrect) PIFs on the accuracy of the proposed Patlak method were assessed. In addition, the extent of mitigating these biases through rescaling of the PIF to image-derived IF values at 30-60 min p.i. was evaluated.

**Methods** Using a representative IF and rate constants from the literature, various tumor time-activity curves (TACs) were simulated. Variations included multiplication of the IF with a positive and negative gradual linear bias over 60 min of 5, 10, 15, 20, and 25% (generating TACs using an IF different from the PIF); use of rate constants ( $K_1$ ,  $k_3$ , and both  $K_1$  and  $k_2$ ) multiplied by 2, 1.5, and 0.75; and addition of noise ( $\mu = 0$  and  $\sigma = 5, 10$  and 15%). Subsequent Patlak analysis using the original IF (representing the PIF) was used to obtain the influx constant ( $K_i$ ) for the differently simulated TACs. Next, the PIF was scaled towards the (simulated) IF value using the 30-60-min p.i. time interval, simulating scaling of the PIF to image-derived values. Influence of variabilities in IF and rate constants, and rescaling the PIF on bias in  $K_i$  was evaluated.

**Results** Percentage bias in  $K_i$  observed using simulated modified IFs varied from -16 to 16% depending on the simulated amplitude and direction of the IF modifications. Subsequent scaling of the PIF reduced these  $K_i$  biases in most cases (287 out of 290) to <5%.

**Conclusion** Simulations suggest that scaling of a (possibly incorrect) PIF to IF values seen in whole body dynamic imaging from 30 to 60 min p.i. can provide accurate  $K_i$  estimates. Consequently, dynamic Patlak imaging protocols may be performed for 30-60 min p.i. making whole body Patlak imaging clinically feasible.

## **Introduction**

Positron emission tomography integrated with computed tomography (PET/CT) imaging using  $^{18}\text{F}$ -2-fluoro-2-deoxy-D-glucose ( $^{18}\text{F}$ -FDG) is widely used in oncology for diagnosis, staging, and treatment response evaluation (1-11). The standardized uptake value (SUV), a semiquantitative metric derived from PET images, is most commonly used as a surrogate of metabolic activity for quantifying  $^{18}\text{F}$ -FDG tumor uptake (1). SUV can be derived from static PET acquisitions, typically initiated 1 h postinjection (p.i.) where every bed position is scanned once for 2-5 min (1, 12). Through standardization methods regarding patient preparation (to avoid, e.g.,

high plasma glucose), PET acquisition settings, image reconstruction, and analysis methods, SUV variability can be limited to a great extent (1, 13, 14). However, quantitative accuracy of SUV can also be influenced by changes in plasma kinetics due to treatment possibly causing inaccurate assessments (15-17).

Dynamic PET imaging allows for spatiotemporal activity concentration distribution measurement which can provide voxel-wise metabolic information when used by tracer pharmacokinetic modeling methods, for example, full kinetic analysis, i.e., Patlak analysis (18-21).

Up to recently, dynamic PET imaging was mainly performed using single-bed/single-axial field-of-view acquisitions. Currently, with state-of-the-art PET/CT systems, whole body dynamic (Patlak) images can be obtained from a combined acquisition of first 6 min of dynamic imaging over the heart to obtain the arterial input function (IF) followed by multiple whole body sweeps up to 60 min p.i. This procedure followed by a standard static whole body PET, however, can take a total examination time to 75 min (22), including the time needed for patient positioning and CT procedure. Initial PET examinations using whole body Patlak imaging showed a high frequency of patients' inability to comply with the long scan duration required for the protocol. The use of a population-averaged input function (PIF) could obviate the need for the first dynamic scan and minimize whole body sweeps to an interval of 30-60 min p.i. (23) making whole body dynamic Patlak imaging clinically feasible. There have been various studies in which using a PIF is explored in oncological whole body dynamic  $^{18}\text{F}$ -FDG imaging (21, 23-26). Promising results were obtained in comparison with using an arterial IF and an image derived IF; however, further evaluation of microparameter estimation (such as  $k_3$  and (if it exists)  $k_4$ ) is recommended before implementation (24). Therefore, given that this approach may introduce some inaccuracy, this study explored the effects of (incorrect) PIFs on the accuracy of the proposed Patlak method using various simulations including variations in rate constants. In addition, the extent of mitigating these biases through rescaling of the PIF to image-derived values at 30-60 min p.i. was evaluated.

## Materials and methods

To explore the effects of (possibly incorrect) PIFs on the accuracy of Patlak analysis based on dynamic whole body PET acquisition from 30 to 60 min p.i., various tumor time-activity curves (TACs) were simulated. To this aim, a representative IF from previously acquired data (acquisition and processing described in (21)) was used as the PIF as well as rate constants based on literature:  $K_1$  was  $0.301 \text{ min}^{-1}$ ,  $k_2$  was  $0.600 \text{ min}^{-1}$ , and  $k_3$  was  $0.047 \text{ min}^{-1}$  (18, 27). TACs were created according to Eq. 1:

$$C_{tissue} = C_{blood} \otimes [k_2 e^{-(k_2+k_3)t} + k_3] \frac{K_1}{k_2+k_3} \quad \text{Eq. 1}$$

Here,  $C_{blood}$  represents the original representative left ventricle arterial IF, and  $C_{tissue}$  is the obtained TAC. The PET TAC was then generated using Eq. 2:

$$C_{PET} = (1 - V_b) * C_{tissue} + V_b * C_{blood} \quad Eq. 2$$

with  $V_b$  equal to the blood volume fraction.

Simulations were performed in the Python programming language using an in-house written code.

Through the multiplication of the IF with a positive and negative gradual linear bias using different slopes over 60 min, variations in IF were simulated. Differences in slope steepness included a positive and negative gradual linear bias from one to 5, 10, 15, 20, and 25% multiplied by the IF, e.g., the IF was multiplied by a positive and negative linear function starting at  $y = 1$  to  $y = 1.25$  and starting at  $y = 1$  to  $y = 0.75$  in the case of 25% bias. These simulations were also reversed, e.g., the IF was multiplied by a positive and negative linear function starting at  $y = 1.25$  to  $y = 1$  and starting at  $y = 0.75$  to  $y = 1$  in the case of 25% bias. Variations in IF accounted for a total number of 35 simulations.

Other variations that were combined with the gradual bias from one to different slope sizes included the use of rate constants ( $K_1$ ,  $k_3$ , and both  $K_1$  and  $k_2$ ) multiplied by 2, 1.5, and 0.75 (fitting the mean and exceeding the range of rate constants observed in clinical data (27)). These rate constant variations combined with IF modifications accounted for a total number of 180 simulations. In addition, noise was added to the IF modifications ( $\mu = 0$  and  $\sigma = 5, 10,$  and  $15\%$  simulating high, medium, and low noise-equivalent count rate (28), respectively) to account for the differences between PET/CT systems and reconstruction settings. The noise additions combined with IF modifications accounted for a total number of 75 simulations. For the simulations described above, the blood volume fraction was fixed at 8.9% (27).

To show the extent to which incorrect PIFs influence the accuracy of Patlak analysis, analyses using the original IF (representing the PIF) were used to obtain the influx constant ( $K_i$ ) for the differently simulated TACs. Subsequently, the incorrect PIFs were scaled towards the correct value using the 30-60-min p.i. time-interval simulating scaling of the PIF to image-derived values. After rescaling,  $K_i$  were obtained using these adjusted PIFs to see the extent to which previously obtained biases in  $K_i$  could be mitigated. A schematic overview regarding the modification and rescaling of the IF is shown in Figure 1.

## Results

In total, 290 variations were simulated (35 gradual in or decrease of the IF and reversed, 180 rate constant variations, and 75 noise simulations). Percentage bias in

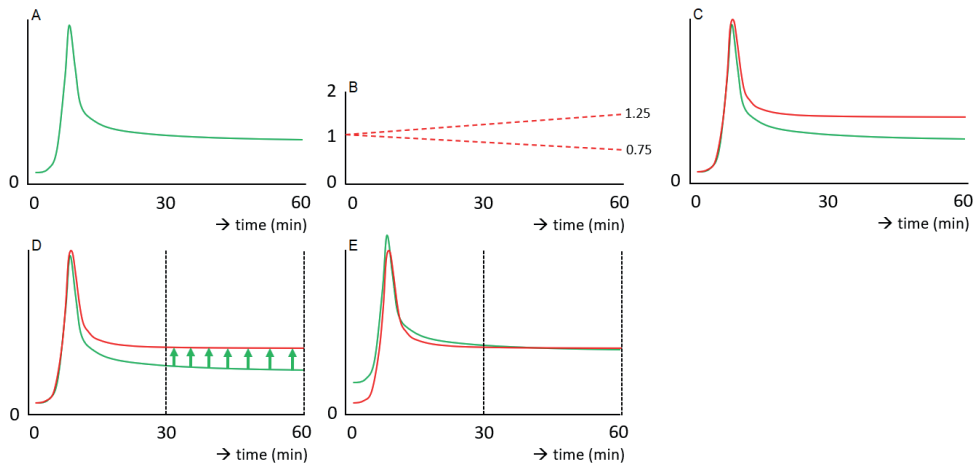


**Figure 1** Schematic overview of PIF (green) with a gradual linear modification (dashed red) towards a variety of (incorrect) IFs (red) (a–c) and subsequent rescaling of the PIF at 30–60 min p.i. (d, e).

$K_i$  using simulated incorrect IFs varied from -16 to 16% depending on the simulation type, amplitude, addition of noise, and direction of the IF modifications. Subsequent scaling of the PIF reduced these  $K_i$  biases in most cases to between -3 and 4% for the gradual in and decrease of the IF and reversed, between -3.7 and 4% for the rate constant variations combined with gradual in and decrease of the IF, and between -2.4 and 3% for the noise addition combined with gradual in and decrease of the IF. Figure 2 shows the influence of positive, negative, and reversed gradual input function modification over 60 min of 5, 10, 15, 20, and 25% on the percentage difference in  $K_i$  before and after rescaling of the PIF. The effect of variations in rate constants combined with a gradual modification of the IF on the percentage difference in  $K_i$  before and after rescaling of the PIF is shown in Figure 3. For the influence of added noise combined with a gradual modification of the IF on the percentage difference in  $K_i$  before and after rescaling of the PIF, see Figure 4.

## Discussion

Tumor quantification using  $SUV_{peak}$  following the PERCIST guidelines describes stable metabolic disease as an increase or decrease in  $SUV_{peak}$  of less than 30% (29). However, SUV can be affected by variations (between subjects or longitudinally) of the plasma kinetics which may cause inaccuracies in clinical assessments. Nevertheless, Patlak analysis also remains an estimate of the tumor's kinetic behavior and may be biased in case of large blood volume fractions for example in cases with bulky tumors (21); this should be taken into account. Based on the reasoning as described above, we determined that an accuracy level of 5% is acceptable, i.e., well

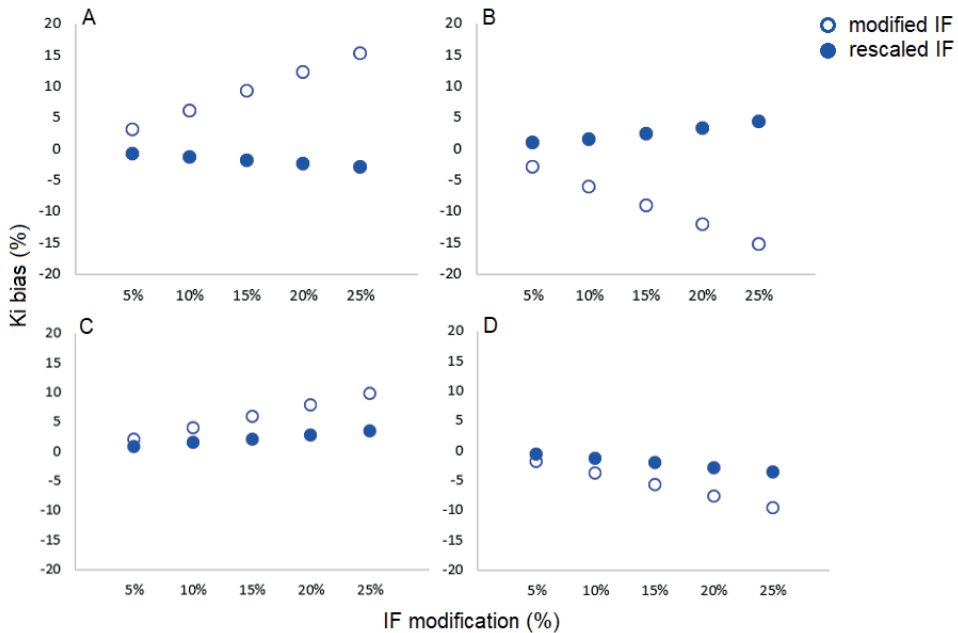


**Figure 2** The effect of positive (a), negative (b), positive reversed (c), and negative reversed (d) gradual input function modification over 60 min of 5, 10, 15, 20, and 25% on the percentage difference in  $K_i$ . The empty markers represent the effect of the modification on  $K_i$ . The filled markers show the remainder of this bias after rescaling of the PIF.

within repeatability levels (which are in the order of 10 to 15% (30-32)).

In most cases, rescaling of the PIF reduced  $K_i$  biases to <5%. However, there were three incidences (out of 290) which resulted in remaining biases >5% after rescaling: the combination of 25% gradual IF modification and  $k_3*2$  resulted in a remaining  $K_i$  bias of 8%, the combination of 25% gradual IF modification and  $k_3*1.5$  resulted in a remaining  $K_i$  bias of 7%, and the combination of 20% gradual IF modification and  $k_3*2$  resulted in a remaining bias in  $K_i$  of 6%. When using PIFs for whole body Patlak imaging in patients with high nuclear grade and/or high proliferation activity tumors (associated with higher  $k_3$  (33)), this should be taken into account.

Please note that when using Patlak analysis, bias may occur even with a perfectly correct IF. Bias in the Patlak analysis may occur as a result of not incorporating the fractional blood volume in the Patlak equations. Blood volume fractions of 0, 8.9, and 20% resulted in a Patlak  $K_i$  bias of -1.2, -10, and -20%, respectively (data not shown). This indicates that the  $K_i$  bias through the use of a (possibly incorrect, but rescaled) PIF is small compared to possible biases in case of large blood volume fractions. With regard to the acceptable accuracy level of 5% when using a PIF for estimating the tumor kinetic behavior, the acceptable total bias would be 25%, which

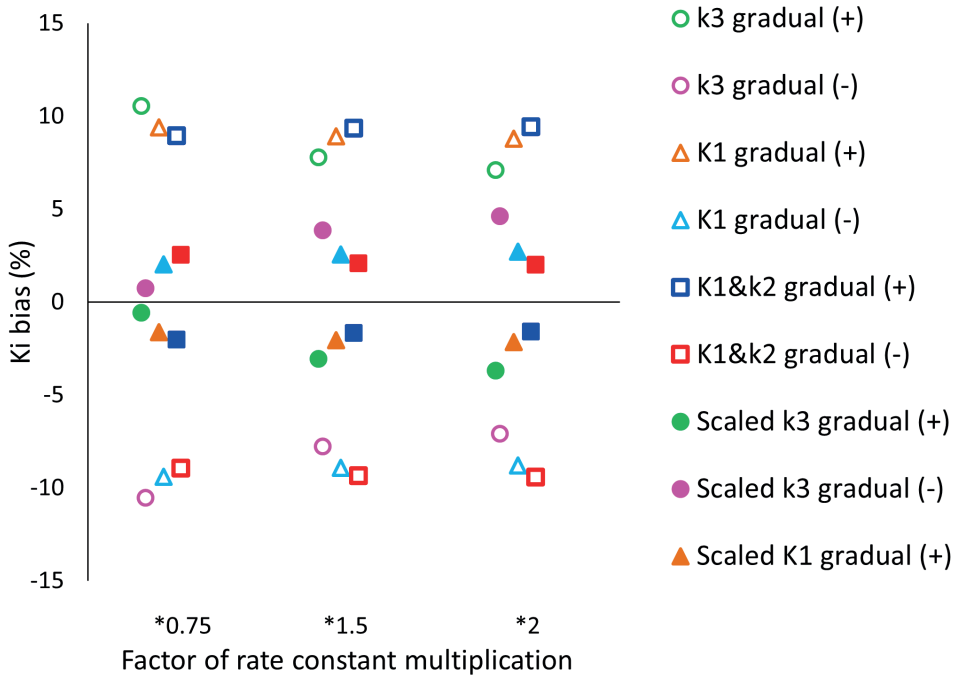


**Figure 3** The effect of variations in rate constants combined with 15% gradual modification of the IF on the percentage difference in  $K_i$ . The empty markers represent the effect of the modification on  $K_i$ . The filled markers show the remainder of this bias after rescaling of the PIF.



is just within the PERCIST recommendations (29). Yet, for most tumors, the blood volume fraction is typically smaller than 10% (27) resulting in a total acceptable bias of 15%, so again, well within the limits of agreement regarding repeatability and PERCIST criteria.

A similar study to develop a simplified Patlak protocol through using PIFs based on clinical data was performed by S. Yao et al. (26). Here, similar biases (from -20 to 20%) were induced to a representative IF to simulate and explore the effect of possible errors in PIFs when applied at 20 min p.i. They concluded that whenever the IF modification remains below 20%, quantitative inaccuracy regarding  $K_i$  would be around 4% (26), which is in line with the results of our simulations.

Another study that explored the alternative of using a PIF instead of arterial blood sampling found a very high correlation between the two methods (23). The addition of variability in rate constants and noise in our study provides a more comprehensive and realistic reflection of the possible range in kinetic parameters seen in tumors.

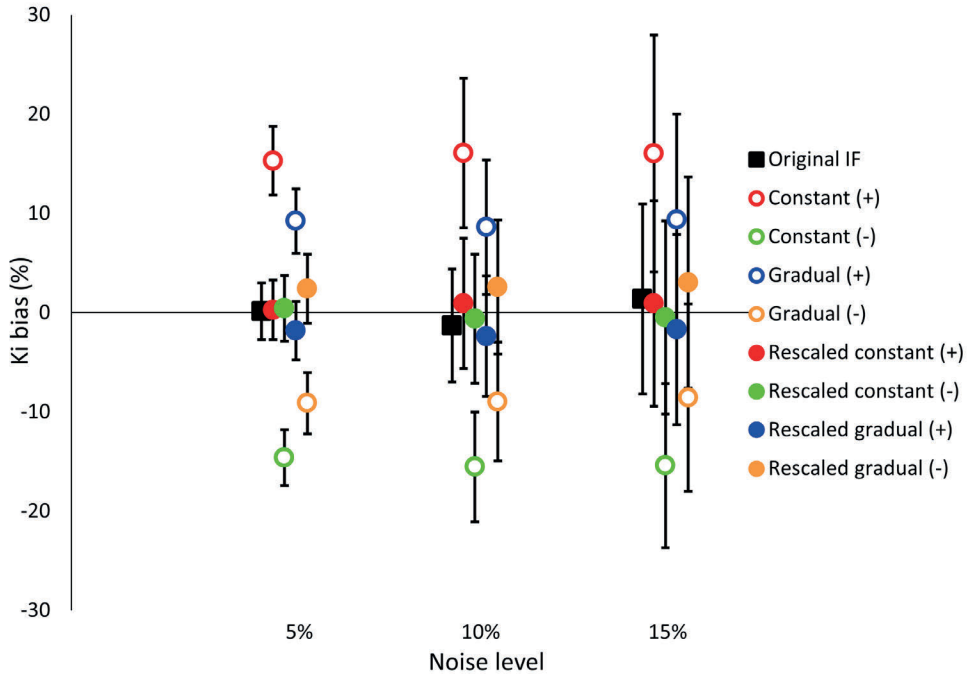


**Figure 4** The effect of added noise combined with 15% gradual modification of the IF on the percentage difference in  $K_i$ . The original input function with added noise is represented by the filled black marker. The empty markers represent the effect of the modification on  $K_i$ . The filled markers show the remainder of this bias after rescaling of the PIF.

## Conclusion

Simulations suggest that scaling of a possibly incorrect PIF to (image derived) IF values seen in whole body dynamic imaging from 30 to 60 min p.i. could be a good strategy to obtain accurate  $K_i$  estimates. Consequently, dynamic Patlak imaging protocols may be performed for 30-60 min p.i. making whole body Patlak imaging clinically feasible.

## References

1. Boellaard R, Delgado-Bolton R, Oyen WJG, Giammarile F, Tatsch K, Eschner W, et al. FDG PET/CT: EANM procedure guidelines for tumour imaging: version 2.0. *Eur J Nucl Med Mol Imaging*. 2014;42:328-54.
2. Avril NE, Weber WA. Monitoring response to treatment in patients utilizing PET. *Radiol Clin N Am*. 2005;43:189-204.
3. Gupta T, Master Z, Kannan S, Agarwal JP, Ghosh-Laskar S, Rangarajan V, et al. Diagnostic performance of post-treatment FDG PET or FDG PET/CT imaging in head and neck cancer: a systematic review and meta-analysis. *Eur J Nucl Med Mol Imaging*. 2011;38:2083-95.
4. Slomka PJ, Pan T, Germano G. Recent advances and future progress in PET instrumentation. *Semin Nucl Med*. Elsevier.2016;46:5-19.
5. Lv YL, Yuan DM, Wang K, Miao XH, Qian Q, Wei SZ, et al. Diagnostic performance of integrated positron emission tomography/computed tomography for mediastinal lymph node staging in non-small cell lung cancer: a bivariate systematic review and meta-analysis. *J Thorac Oncol*. International Association for the Study of Lung Cancer. 2011;6:1350-8.
6. Hsu DFC, Ilan E, Peterson WT, Uribe J, Lubberink M, Levin CS. Studies of a next-generation silicon-photomultiplier-based time-of-flight PET/CT system. *J Nucl Med*. 2017;58:1511-8.
7. Townsend DW. Dual-modality imaging: combining anatomy and function. *J Nucl Med*. 2008;49:938-55.
8. Boellaard R, Oyen WJG, Hoekstra CJ, Hoekstra OS, Visser EP, Willemsen AT, et al. The Netherlands protocol for standardisation and quantification of FDG whole body PET studies in multi-centre trials. *Eur J Nucl Med Mol Imaging*. 2008;35:2320-33.
9. Bastiaannet E, Groen B, Jager PL, Cobben DCP, van der Graaf WTA, Vaalburg W, et al. The value of FDG-PET in the detection, grading and response to therapy of soft tissue and bone sarcomas; a systematic review and meta-analysis. *Cancer Treat Rev*. 2004;30:83-101.
10. Fletcher JW, Djulbegovic B, Soares HP, Siegel BA, Lowe VJ, Lyman GH, et al. Recommendations on the use of  $^{18}\text{F}$ -FDG PET in oncology. *J Nucl Med*. 2008;49:480-508.
11. de Geus-Oei LF, Van Der Heijden HFM, Corstens FHM, Oyen WJG. Predictive and prognostic value of FDG-PET in nonsmall-cell lung cancer. A systematic review. *Cancer*. 2007;110:1654-64.
12. Castell F, Cook GJR. Quantitative techniques in  $^{18}\text{F}$ FDG PET scanning in oncology. *Br J Cancer*. 2008;98:1597-601.
13. Weber WA. Use of PET for monitoring cancer therapy and for predicting outcome. *J Nucl Med*. 2005;46:983-95.
14. Shankar LK, Hoffman JM, Bacharach S, Graham MM, Karp J, Lammertsma AA, et al. Consensus recommendations for the use of  $^{18}\text{F}$ -FDG PET as an indicator of therapeutic response in patients in National Cancer Institute Trials. *J Nucl Med*. 2006;47:1059-66.
15. Freedman NMT, Sundaram SK, Kurdziel K, Carrasquillo JA, Whatley M, Carson JM, et al. Comparison of SUV and Patlak slope for monitoring of cancer therapy using serial PET scans. *Eur J Nucl Med Mol Imaging*. 2003;30:46-53.



16. Huang SC. Anatomy of SUV. *Nucl Med Biol.* 2000;27:643-6.
17. Lammertsma AA, Hoekstra CJ, Giaccone G, Hoekstra OS. How should we analyse FDG PET studies for monitoring tumour response? *Eur J Nucl Med Mol Imaging.* 2006;33:16-21.
18. Karakatsanis NA, Lodge MA, Tahari AK, Zhou Y, Wahl RL, Rahmim A. Dynamic whole body PET parametric imaging: I. Concept, acquisition protocol optimization and clinical application Nicolas. *Phys Med Biol.* 2014;49:1012-6.
19. Patlak CS, Blasberg RG. Graphical evaluation of blood-to-brain transfer constants from multiple-time uptake data. Generalizations. *J Cereb Blood Flow Metab.* 1985;5:584-90.
20. Karakatsanis NA, Zhou Y, Lodge MA, Casey ME, Wahl RL, Zaidi H, et al. Generalized whole-body Patlak parametric imaging for enhanced quantification in clinical PET. *Phys Med Biol.* 2015;60:8643-73.
21. Cheebsumon P, Velasquez LM, Hoekstra CJ, Hayes W, Kloet RW, Hoetjes NJ, et al. Measuring response to therapy using FDG PET: semi-quantitative and full kinetic analysis. *Eur J Nucl Med Mol Imaging.* 2011;38:832-42.
22. Zaidi H, Karakatsanis N. Nuclear medicine: physics special feature review article: towards enhanced pet quantification in clinical oncology. *Br J Radiol.* 2018;91:20170508.
23. Naganawa M, Gallezot J-D, Shah V, Mulnix T, Chen M-K, Smith A, et al. Assessment of population-based input functions for the Patlak plot using whole body  $^{18}\text{F}$ -FDG PET imaging. *EJNMMI Phys.* 2020;7:67.
24. Vriens D, De Geus-Oei LF, Oyen WJG, Visser EP. A curve-fitting approach to estimate the arterial plasma input function for the assessment of glucose metabolic rate and response to treatment. *J Nucl Med.* 2009;50:1933-9.
25. Hunter GJ, Hamberg LM, Alpert NM, Choi NC, Fischman AJ. Simplified measurement of deoxyglucose utilization rate. *J Nucl Med.* 1996;37:950-5.
26. Yao S, Feng T, Zhao Y, Wu R, Wang R, Wu S, et al. Simplified protocol for whole body Patlak parametric imaging with  $^{18}\text{F}$ -FDG PET/CT: feasibility and error analysis. *Med Phys.* 2020. Published 2020 Apr 17.
27. Vriens D, Disselhorst JA, Oyen WJG, De Geus-Oei LF, Visser EP. Quantitative assessment of heterogeneity in tumor metabolism using FDG-PET. *Int J Radiat Oncol Biol Phys.* 2012;82:725-31.
28. Boellaard R, Krak NC, Hoekstra OS, Lammertsma AA. Effects of noise, image resolution, and ROI definition on the accuracy of standard uptake values: a simulation study. *J Nucl Med.* 2004;45:1519-27.
29. Joo Hyun O, Lodge MA, Wahl RL. Practical PERCIST: a simplified guide to PET response criteria in solid tumors 1.0. *Radiology.* 2016;280:576-84.
30. Weber WA, Gatsonis CA, Mozley PD, Hanna LG, Shields AF, Aberle DR, et al. Repeatability of  $^{18}\text{F}$ -FDG PET/CT in advanced non-small cell lung cancer: prospective assessment in 2 multicenter trials. *J Nucl Med.* 2016;56:1137-43.
31. Kramer GM, Frings V, Hoetjes N, Hoekstra OS, Smit EF, De Langen AJ, et al. Repeatability of quantitative whole-body  $^{18}\text{F}$ -FDG PET/CT uptake measures as function of uptake interval and

- lesion selection in non-small cell lung cancer patients. *J Nucl Med.* 2016;57:1343-9.
32. De Langen AJ, Vincent A, Velasquez LM, Van Tinteren H, Boellaard R, Shankar LK, et al. Repeatability of  $^{18}\text{F}$ -FDG uptake measurements in tumors: a metaanalysis. *J Nucl Med.* 2012;53:701-8.
  33. Kajáry K, Lengyel Z, Tókéš AM, Kulka J, Dank M, Tókéš T. Dynamic FDG-PET/CT in the initial staging of primary breast cancer: clinicopathological correlations. *Pathol Oncol Res.* 2020;26:997-1006.





# Chapter 10

---

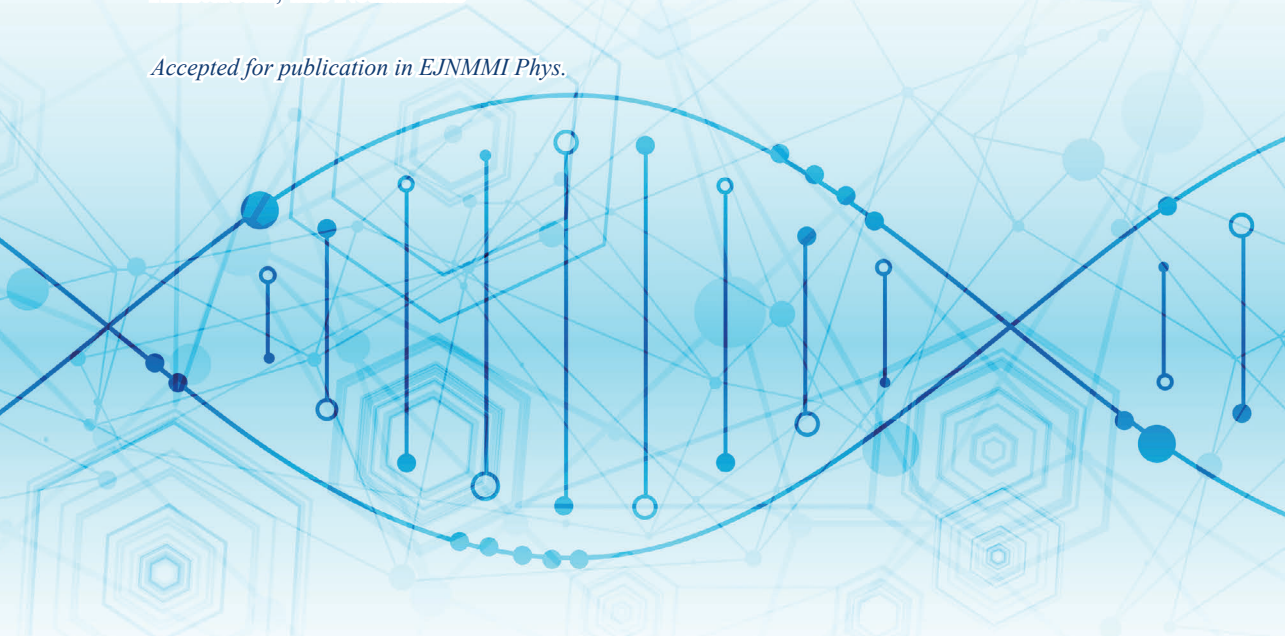
## Shortened duration whole body $^{18}\text{F}$ -FDG PET Patlak imaging on the Biograph Vision Quadra PET/CT using a population-averaged input function

Joyce van Sluis<sup>1</sup>, Johannes H. van Snick<sup>1</sup>, Adrienne H. Brouwers<sup>1</sup>, Walter Noordzij<sup>1</sup>, Rudi A.J.O. Dierckx<sup>1</sup>, Ronald J.H. Borra<sup>1</sup>, Adriaan A. Lammertsma<sup>1</sup>, Andor W.J.M. Glaudemans<sup>1</sup>, Riemer H.J.A. Slart<sup>1</sup>, Maqsood Yaqub<sup>1,2</sup>, Charalampos Tsoumpas<sup>1</sup>, and Ronald Boellaard<sup>1,2</sup>

<sup>1</sup>Department of Nuclear Medicine and Molecular Imaging, University of Groningen, University Medical Center Groningen, Hanzeplein 1, 9713 GZ Groningen, The Netherlands

<sup>2</sup>Department of Radiology and Nuclear Medicine, Cancer Center Amsterdam, Amsterdam University Medical Centers, Free University of Amsterdam, De Boelelaan 1117, 1081 HV Amsterdam, The Netherlands

*Accepted for publication in EJNMMI Phys.*



## **Abstract**

Excellent performance characteristics of the Vision Quadra, e.g., a substantial increase in sensitivity, allow for precise measurements of image derived input functions (IDIF) and tissue time-activity curves. Previously we have proposed a method for a reduced 30 min (as opposed to 60 min) whole body  $^{18}\text{F}$ -FDG Patlak PET imaging procedure using a previously published population-averaged input function (PIF) scaled to IDIF values at 30-60 min post injection (p.i.). The aim of the present study was to apply this method using the Vision Quadra, including the use of a PIF to allow for shortened scan durations.

**Methods** Twelve patients with suspected lung malignancy were included and received a weight-based injection of  $^{18}\text{F}$ -FDG. Patients underwent a 65 min dynamic PET acquisition which were reconstructed using European Association of Nuclear Medicine Research Ltd. (EARL) standards 2 reconstruction settings. Volumes of interest (VOI) were placed in the ascending aorta (AA) and in the left ventricle of the heart (LV) to obtain IDIFs. An external PIF was scaled to AA and LV IDIF values at 30-60, 40-60, and 50-60 min p.i., respectively, and parametric  $^{18}\text{F}$ -FDG influx rate constant ( $K_i$ ) images were generated using a  $t^*$  of 30, 40 or 50 min, respectively. Herein, tumor lesions as well as healthy tissues, i.e. liver, spleen and muscle tissue, were segmented.

**Results**  $K_i$  varied marginally ( $\sim 2\%$ ) between IDIF VOI positioned in the AA versus the LV. Good agreement between the AA IDIF and corresponding PIF scaled to 30-60 min p.i. and 40-60 min p.i. was obtained with  $<8\%$  deviation in  $K_i$ . Bland-Altman plots showed excellent agreement in  $K_i$  obtained using the PIF scaled to the IDIF at 30-60 min p.i. and at 40-60 min p.i. as all datapoints were within the limits of agreement (LOA) (-0.004 - 0.002, bias: -0.001); for the 50-60 min p.i.  $K_i$ , all except one data point fell in between the LOA (-0.021 - 0.012, bias: -0.005).

**Conclusion** Parametric whole body  $^{18}\text{F}$ -FDG Patlak  $K_i$  images can be generated non-invasively on a Vision Quadra system. In addition, using a scaled PIF allows for a substantial (factor 2 to 3) reduction in scan time without substantial loss of accuracy ( $<8\%$ ) and precision (image quality and noise interference).

## **Introduction**

Non-invasive positron emission tomography integrated with computed tomography (PET/CT) imaging using  $^{18}\text{F}$ -2-fluoro-2-deoxy-D-glucose ( $^{18}\text{F}$ -FDG) provides both metabolic and anatomic information (1), and is widely used in oncology (2-4) and many other clinical indications. In oncology, PET/CT has become part of the daily

clinical routine including initial diagnosis, staging, prognosis, radiation therapy planning, and monitoring response to treatment (4-6).

The semiquantitative standardized uptake value (SUV) of  $^{18}\text{F}$ -FDG, derived from static images obtained at 60 minutes post injection (p.i.), is most commonly used as a surrogate of metabolic activity for tumor uptake quantification (5). Following standardization methods such as the European Association of Nuclear Medicine (EANM) procedure guidelines for tumor imaging regarding patient preparation, PET image acquisition and reconstruction settings, and analysis methods can mitigate SUV variability to a great extent (5,7,8). However, these standardization methods are not able to account for changes in plasma kinetics, due to e.g. treatment, and no distinction between specific and nonspecific uptake possibly causing a dissociation between inaccurate SUV measurements and actual tumor metabolic activity (9-11).

In contrast, dynamic PET imaging, both single-bed or whole body dynamic (e.g., via multi-bed or continuous bed motion modes) (12,13) is able to include this information as it allows spatiotemporal activity concentration measurement, providing voxel-wise metabolic information after applying full kinetic- or Patlak analyses (13-15).

Fully quantitative whole body parametric PET imaging for non-invasive quantification of  $^{18}\text{F}$ -FDG kinetics throughout the body is now possible using a long axial field-of-view (LAFOV) Siemens Biograph Vision Quadra PET/CT system (Siemens Healthineers, Knoxville, TN, USA) (hereinafter referred to as Vision Quadra). Its 106 cm long axial coverage captures the heart and all other organs of interest, including possible tumor lesions, simultaneously and continuously within a single bed position. The excellent performance characteristics of the Vision Quadra, such as a substantial increase in sensitivity (16), allows for precise measurements of image derived input functions (IDIF) and tissue time-activity curves (TAC). However, in order to generate whole body parametric PET images, the slow kinetics of  $^{18}\text{F}$ -FDG require scanning for at least 45-60 min (17). This longer scan duration reduces patient throughput and comfort, whereas, improvements in PET technology (3) and the large axial FOV actually enable acquisition of whole body static images at substantially reduced scan durations, thereby providing the potential of increasing patient throughput.

The use of a population-averaged input function (PIF) could obviate the need to acquire  $^{18}\text{F}$ -FDG tracer distribution information immediately following injection, thereby minimizing whole body dynamic imaging to an interval of 30-60 min p.i. (18-22). Moreover, in the case of sufficient increase in signal-to-noise ratio achieved with the Vision Quadra, Patlak analyses could provide accurate voxel-wise metabolic information with fewer dynamic time frames. The feasibility of the current approach has been investigated in (22) for the 2-m LAFOV uEXPLORER PET/CT system (United Imaging Healthcare), but has not yet been explored for the 106-cm Vision

Quadra (Siemens Healthineers). Other described methods for reduced scan duration whole body Patlak imaging, investigated for the uEXPLORER and Vision Quadra, include dual time point dynamic acquisition (23,24). Our proposed method is based on a single time point shortened dynamic scan, which might be a more practical approach regarding patient scheduling in a busy clinic.

Previously, data simulations were performed to evaluate a method for reduced 30 min whole body  $^{18}\text{F}$ -FDG Patlak PET imaging using an external PIF, obtained by arterial blood sampling, scaled to IDIF values at 30-60 min p.i. (25). The aim of the present study was to apply this method using clinically acquired patient data on the Vision Quadra. A secondary aim was to assess whether even shorter scan time intervals could be used given the very high sensitivity of the Vision Quadra system.

## **Materials and methods**

Oncology patients with suspected lung malignancy (lung cancer or lung metastases), referred for clinical diagnosis, were included in this study. The local Medical Ethics Review Committee of the University Medical Center Groningen waived the need for formal ethical review (waiver number METc2020/554). Following the standardized procedure guidelines for tumor imaging, patients were instructed to fast for at least 6 hours prior to  $^{18}\text{F}$ -FDG injection and blood glucose levels were no higher than 11 mmol/L. All patients received a standard weight-based (3 MBq/kg) injection of  $^{18}\text{F}$ -FDG.

Scans were acquired on a Vision Quadra PET/CT (16). Each patient underwent a low dose CT from the top of the head to the mid thighs (X-ray tube current 35 mAs, tube voltage of 100 kV, and spiral pitch factor of 1.1) which was used for both anatomical information and PET attenuation correction. After a delay of 10 seconds following automated  $^{18}\text{F}$ -FDG bolus injection using a MEDRAD Intego PET infusion system (Bayer Pharmaceuticals, Berlin, Germany) and a saline flush of 30 mL, 65 min listmode dynamic PET data were acquired. Data were binned over 31 frames using the following frame durations: 6x10, 3x20, 6x30, 5x60, and 11x300 s. In addition, the last 10 min dynamic frames were summed to obtain a conventional static scan at 60 min p.i.

Dynamic PET images were reconstructed using European Association of Nuclear Medicine Research Ltd. (EARL) standards 2 reconstruction settings to obtain data that complied with European guidelines for multicenter PET image quantification and harmonization (26). These EARL standards 2 reconstruction settings were a three dimensional (3D) ordered-subset expectation maximization (OSEM) algorithm with 4 iterations, 5 subsets and a matrix size of 220 x 220 x 708 with a voxel size of 3.3 x 3.3 x 1.5 mm<sup>3</sup>, time-of-flight (ToF), resolution modeling (PSF), and a 5 mm full width at half maximum Gaussian filter. PET data were corrected for randoms,

scatter, attenuation, and radioactive decay.

For each dynamic PET dataset, volumes of interest (VOI) were placed in the ascending aorta (AA) (27) and in the left ventricle of the heart (LV) to derive IDIFs using in-house developed semi-automated software. The VOI in the AA consisted of 2 x 2 voxels in 6 axial slices in the lumen of the large artery. For the LV, a 3D VOI was drawn manually well within the left ventricle cavity, such to avoid spillover of the signal from the myocardium; the VOI was drawn in 3 axial slices and has a final volume of ~3 mL. To determine  $^{18}\text{F}$ -FDG influx constant ( $K_i$ ) and the total blood distribution volume  $V$ , the measured TAC and input function (IF) serve as input for a voxel-wise Patlak analysis according to Eq. 1 (28):

$$\frac{C(t_n)}{C_P(t_n)} = K_i \frac{\int_0^{t_n} C_P(\tau) d\tau}{C_P(t_n)} + V, t_n > t^*, n = 1 \dots N \quad \text{Eq. 1}$$

Where  $C(t)$  is the measured TAC at each voxel,  $C_P(t)$  the IDIF or PIF, and  $t_n$  with  $n = 1 \dots N$  representing the mid-time points for the  $N$  dynamic PET frames. For the calculations, a  $t^*$  of 30, 40, or 50 minutes was used as the time after which relative kinetic equilibrium between blood and reversible compartment is assumed, i.e., when the Patlak plot becomes linear. Subsequently, a previously published PIF (29), see Supplemental Figure 1, was scaled to AA and LV IDIF values at 30-60, at 40-60, and at 50-60 min p.i., respectively, corresponding with the  $t^*$  values mentioned above. This resulted in 8 IFs per dataset: IDIF\_AA\_30, IDIF\_LV\_30, PIF\_AA\_30, PIF\_LV\_30, PIF\_AA\_40, PIF\_LV\_40, PIF\_AA\_50, and PIF\_LV\_50. For each IF, parametric  $^{18}\text{F}$ -FDG  $K_i$  images were generated. In these  $K_i$  images, tumor lesions were segmented using a semi-automated segmentation method (50% of  $\text{SUV}_{\text{peak}}$  isocontour) using the in-house developed software tool ACCURATE (30). In addition, a 3 cm diameter spherical VOI was placed in the liver and 2-cm-diameter spherical VOIs were placed in the spleen and upper thigh muscle tissue to assess  $K_i$  in healthy organs with clearly different  $K_i$  values.

Scatter and Bland-Altman plots were generated to evaluate variation in lesion  $K_i$  obtained by IDIF VOI positioning (i.e., to compare AA and LV IDIF) and Pearson's correlation analysis was performed to assess the linear relationship between the variables. Agreement between lesion  $K_i$  obtained using the IDIF and corresponding PIF scaled at 30-60, 40-60, and at 50-60 min p.i., respectively, was assessed using Bland-Altman plots. Pearson's correlation analysis was performed to evaluate the linear relationship between the obtained parameters and the coefficient of determination ( $R^2$ ) was obtained to explore the extent to which variability in lesion  $K_i$  obtained using the scaled PIFS can be related to variability in the IDIF. Bland-Altman plots were also used to assess agreement between normal tissue  $K_i$  obtained using the IDIF and the various scaled PIFs.

To assess the effect of scan duration on noise levels, the standard deviation (SD) in  $K_i$  derived from the liver VOI using the IDIF and PIF scaled to the IDIF at 30-60 min p.i. were compared with  $K_i$  obtained using the PIF scaled to the IDIF at various shortened scan time intervals. Moreover, healthy tissue  $K_i$  measured in liver, muscle tissue and spleen obtained using the IDIF versus the corresponding scaled PIF at various shortened scan time intervals p.i. were compared using boxplots and ANOVA repeated measures. These analyses were performed using SPSS Statistics, version 27.0 (IBM corp., Armonk, NY, USA).

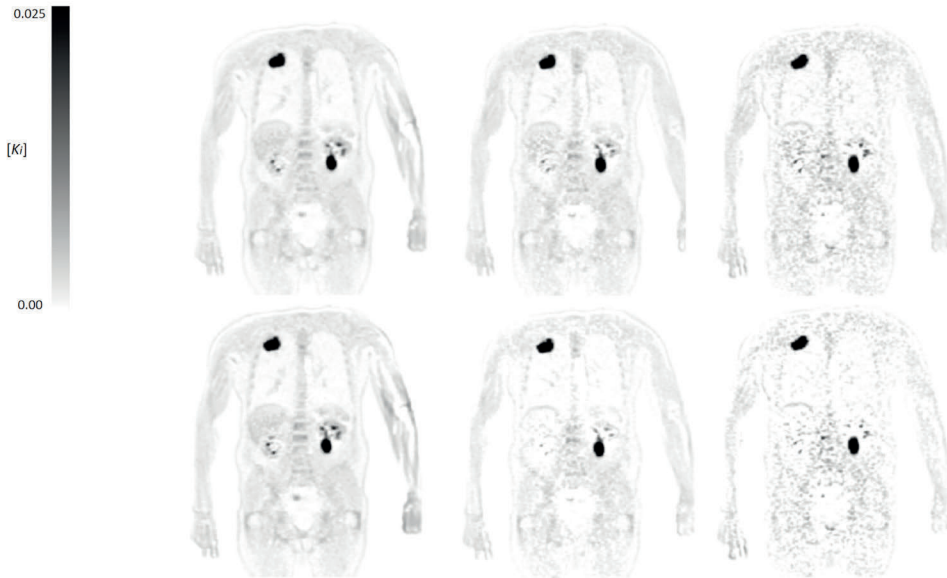
## Results

In total, 12 oncology patients (8 men, 4 women; age 64 - 80 y [range],  $71 \pm 4$  y [mean  $\pm$  SD]) with suspected lung malignancy were included and received a standard weight-based (3 MBq/kg)  $^{18}\text{F}$ -FDG injected activity (weight: 69.0 - 136.5 kg [range],  $90.2 \pm 22.1$  kg [mean  $\pm$  SD]; activity: 206.1 - 443.4 MBq [range],  $272.0 \pm 73.3$  MBq [mean  $\pm$  SD]). A total of 20 tumor lesions were segmented and obtained results are described below. Patient demographics and specific injection parameters can be found in Table 1. Example  $K_i$  images illustrating image quality obtained using both the measured AA IDIF and the scaled PIF at various shortened scan time intervals p.i. are shown in Figure 1.

**Table 1** Patient demographics and activity values.

Pt	Disease	Sexe	Age [y]	Weight [kg]	Activity @ scan start [MBq]	Glucose level [mmol/L]
1	Lung cancer	M	64	134	402.3	6.2
2	Lung cancer	M	76	69	208.6	6.0
3	Lung cancer	F	73	89	268.0	5.3
4	Lung cancer	F	68	69	211.0	6.2
5	Lung cancer	M	70	80	245.5	6.7
6	Lung cancer	M	72	85	241.4	5.8
7	Lung cancer	M	75	74	206.1	6.5
8	Lung cancer	M	68	136	443.4	6.8
9	Diffuse large B cell lymphoma	F	80	89	256.0	6.4
10	Lung cancer	M	69	100	308.0	6.0
11	Diffuse large B cell lymphoma	M	65	70	221.9	4.9
12	Lung cancer	F	72	87	251.9	5.9

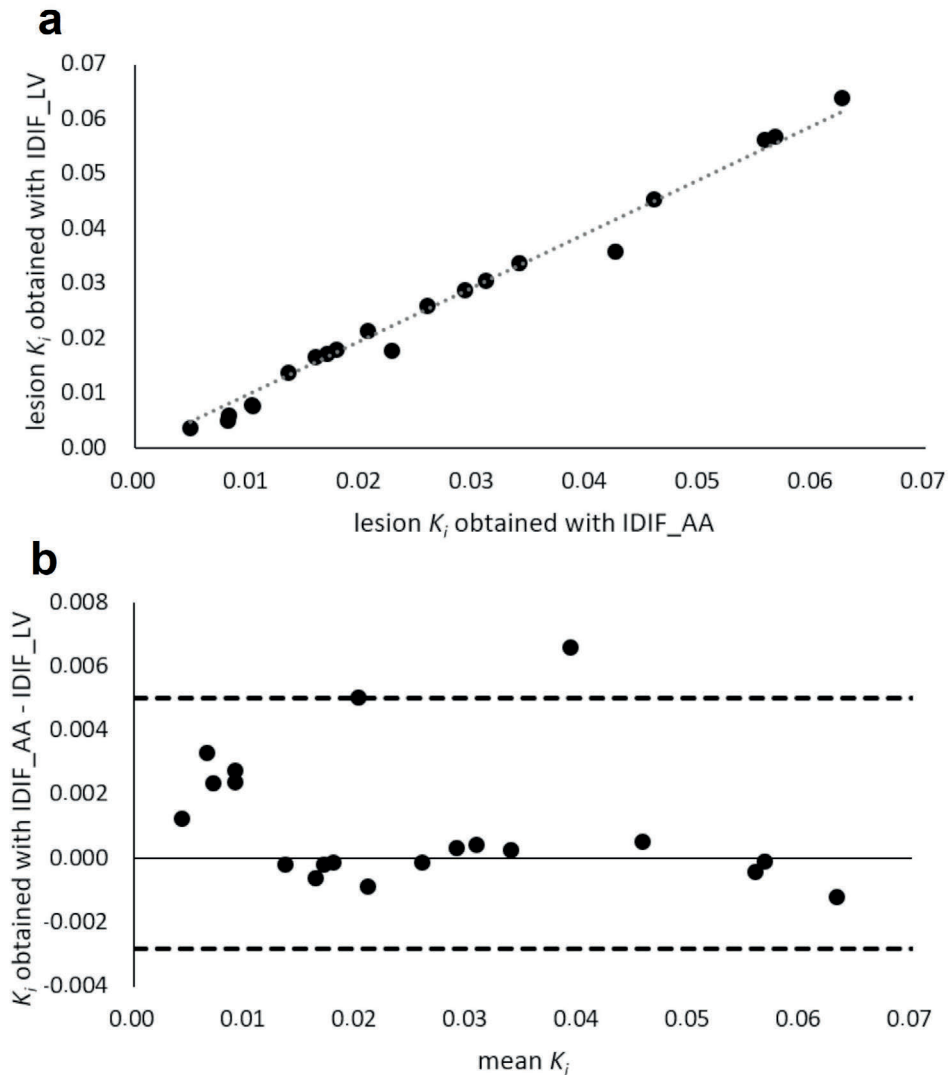
The scatter plot and Bland-Altman plot in Figure 2 show the variation in obtained  $K_i$  due to IDIF VOI placement. The slope of the linear regression line in the scatter plot (Figure 2A), equation  $y = 0.9789x$  with the intercept set to 0.0, shows the IDIF from the LV slightly ( $\sim 2\%$ ) overestimates  $K_i$  with respect to using the IDIF from the AA VOI. Pearson correlation analysis showed a significant positive correlation of  $r$



**Figure 1** Example  $K_i$  images obtained using an IDIF from the AA (top row) and scaled PIF (bottom row). From left to right  $K_i$  images are shown that were generated using 30-60, 40-60, and 50-60 min uptake time intervals p.i., respectively. The same interval was used for scaling the population-averaged curve as to simulate actual shortened PET acquisitions of the same time intervals.

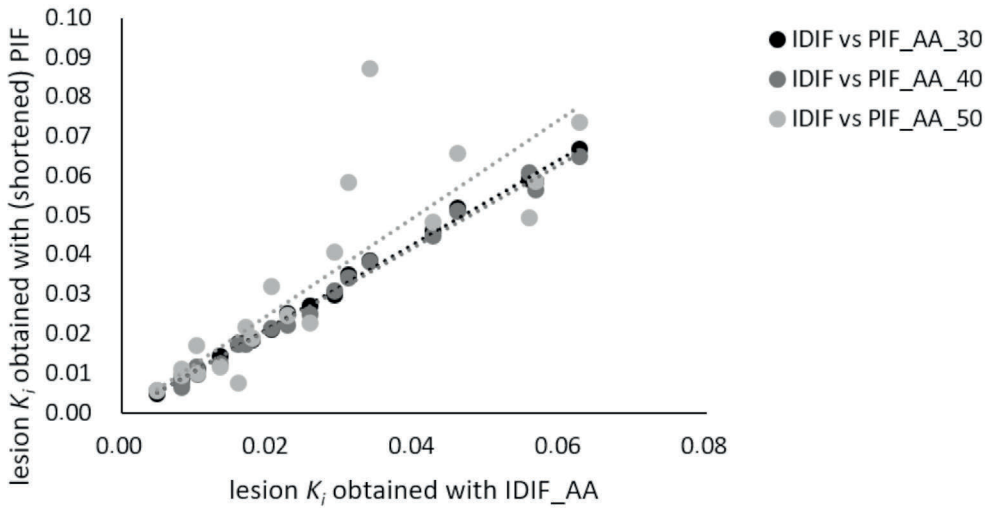
= 0.994,  $P < 0.001$ , and an  $R^2$  of 0.995. Bland-Altman analysis (Figure 2B) showed lower and upper limits of agreement (LOA) of -0.003 - 0.005 and a bias of 0.001. Because of the excellent agreement between  $K_i$  obtained with IDIFs from the AA and the LV, hereafter all further comparisons with respect to  $K_i$  will be performed only using the IDIF from the AA.

Figure 3 illustrates the bias in  $K_i$  that is found when using the PIF scaled to the IDIF at scan time intervals p.i. of 30-60 min, 40-60 min, and 50-60 min. The slopes of the linear regression fits, with intercept set to 0.0, indicate that using a PIF overestimates  $K_i$  in all cases. Linear regression slope equations for scan time intervals p.i. of 30-60 min, 40-60 min, and 50-60 min:  $y = 1.0738x$ ,  $y = 1.0518x$ , and  $y = 1.2405x$ . More specifically, scaling the PIF onto the IDIF at 30-60 min p.i. induces a slight bias in  $K_i$  (<8%). At the shortened scan time interval of 40-60 min p.i., scaling of the PIF onto the IDIF reduces this  $K_i$  bias to ~5%. In cases of scaling the PIF onto the IDIF at the shortest scan time interval of 50-60 min p.i., bias in  $K_i$  increases to >24%. Pearson's correlation analysis showed significant correlation between the AA IDIF and the corresponding scaled PIF at 30-60, at 40-60, and at 50-60 min p.i. with  $r$  values of 0.998, 0.996, and 0.842 ( $P < 0.001$ ), respectively, and  $R^2$  values of 0.999, 0.998, and 0.901, respectively.



**Figure 2** Comparison of lesion  $K_i$  obtained using the IDIF from the VOI placed in the AA versus lesion  $K_i$  obtained using the IDIF from the VOI placed in the LV shown in a scatter plot (A) and a Bland-Altman plot (B). The dashed line in A represents the linear regression fit (intercept set to 0.0).

Bland-Altman plots (see Figure 4) to assess the agreement between  $K_i$  obtained using the IDIF and the PIF scaled to 30-60 min p.i. showed lower and upper LOA of -0.005 - 0.002 and a bias of -0.002. For the agreement between  $K_i$  obtained using the IDIF and the PIF scaled to 40-60 min p.i., upper and lower LOA were -0.004 - 0.002 and the bias was -0.001. When scaling the PIF to the IDIF at the shortest scan time interval of 50-60 min p.i., upper and lower LOA were -0.021 - 0.012 and the bias was

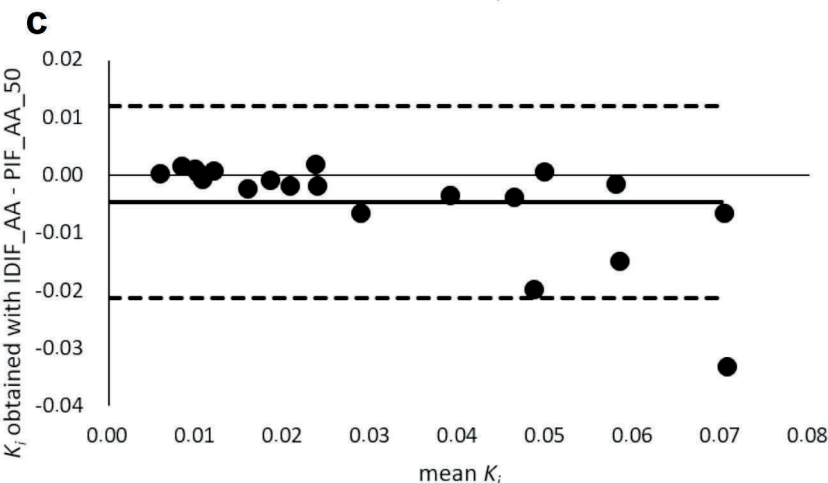
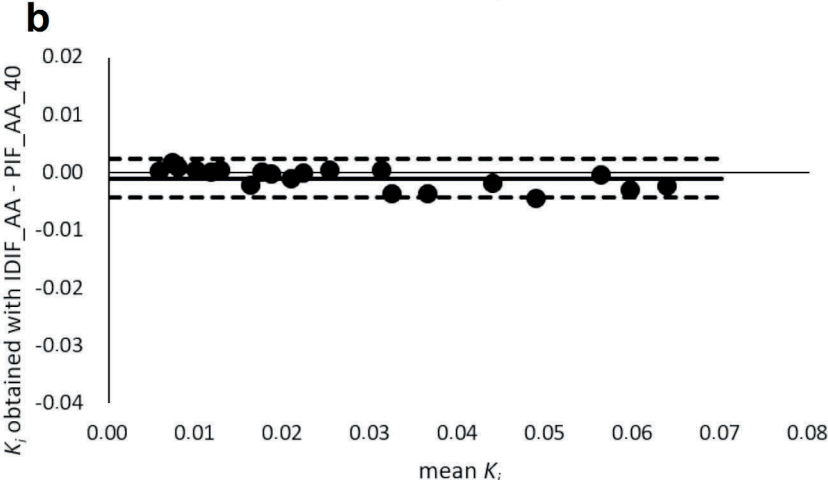
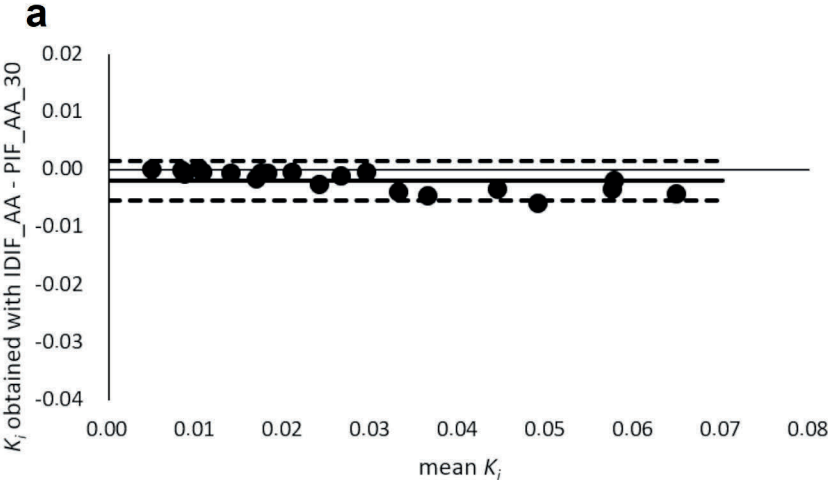


**Figure 3** Scatter plots of lesion  $K_i$  obtained using the IDIF from the AA versus lesion  $K_i$  obtained using the PIF scaled to the IDIF\_AA at 30-60 min p.i. (PIF\_AA\_30) and the PIF scaled to the IDIF at shortened scan time intervals p.i. (PIF\_AA\_40 and PIF\_AA\_50). Dashed lines represent linear regression fits (with intercept set to (0,0)).

-0.005. When scaling the PIF to the IDIF at 30-60 min p.i. as well as 40-60 min p.i., all 20 lesion datapoints were located in between the LOAs. With regard to scaling of the PIF towards IDIF at the 50-60 min p.i. scan time interval, all but one datapoint were located in between the LOAs. With regard to assessment of agreement between obtained healthy tissue  $K_i$  using the IDIF and PIF scaled to various shortened scan time intervals p.i., Bland-Altman analysis results are summarized in Table 2.

In Figure 5, SD in  $K_i$  derived from the liver VOI generated using the IDIF obtained in the AA and scaled PIF at various shorter scan time intervals p.i. are shown to indicate the increase in noise levels as scan time is reduced.

Comparison of healthy tissue  $K_i$  of liver, muscle tissue, and spleen obtained using the IDIF from the AA versus the corresponding scaled PIF at various shortened scan time intervals p.i. are shown in Figure 6. ANOVA repeated measures show significant differences in liver  $K_i$  obtained using the AA IDIF and the PIF at 40-60 min (confidence interval (CI) (0.002 - 0.004),  $P < 0.001$ ) and at 50-60 min scan time interval p.i. (CI (0.003 - 0.004),  $P < 0.001$ ). Significant differences were also found between liver  $K_i$  obtained using the PIF at 30-60 min p.i. scan time interval and the PIF at shortened time intervals of 40-60 min (CI (0.002 - 0.003),  $P < 0.001$ ) and 50-60 min (CI (0.003 - 0.005),  $P < 0.001$ ). For muscle tissue, ANOVA repeated measures showed significant differences in  $K_i$  obtained using AA IDIF and the PIF scaled to the IDIF at 40-60 min p.i. (CI (0.000 - 0.001),  $P < 0.001$ ) and between  $K_i$  obtained using the PIF at 30-60 min versus 40-60 min (CI (0.000 - 0.001),  $P < 0.001$ ).



← **Figure 4** Bland-Altman plot of lesion  $K_i$  differences obtained with the IDIF minus the PIF scaled to the scan time interval at 30-60 min p.i. (PIF\_AA\_30) (A), and the PIF scaled to the IDIF at shorter scan time intervals p.i. (PIF\_AA\_40 and PIF\_AA\_50) (B and C). To illustrate differences between the comparisons, the scales on the vertical axes are matched in the subfigures.

**Table 2** Healthy tissue  $K_i$  Bland-Altman analysis results.

Tissue	Comparison	Lower LOA	Upper LOA	Bias	Datapoints between LOAs (N = 12)
Liver	IDIF_AA_30 – PIF_AA_30	-0.0014	0.0020	0.0003	11
	IDIF_AA_40 – PIF_AA_40	0.0006	0.0048	0.0027	11
	IDIF_AA_50 – PIF_AA_50	0.0021	0.0065	0.0043	12
Muscle	IDIF_AA_30 – PIF_AA_30	-0.0005	0.0005	-0.0000	11
	IDIF_AA_40 – PIF_AA_40	-0.0001	0.0001	0.0005	12
	IDIF_AA_50 – PIF_AA_50	-0.0004	0.0018	0.0007	12
Spleen	IDIF_AA_30 – PIF_AA_30	-0.0008	0.0010	0.0001	11
	IDIF_AA_40 – PIF_AA_40	0.0004	0.0034	0.0019	12
	IDIF_AA_50 – PIF_AA_50	0.0011	0.0044	0.0028	12

LOA = limit of agreement

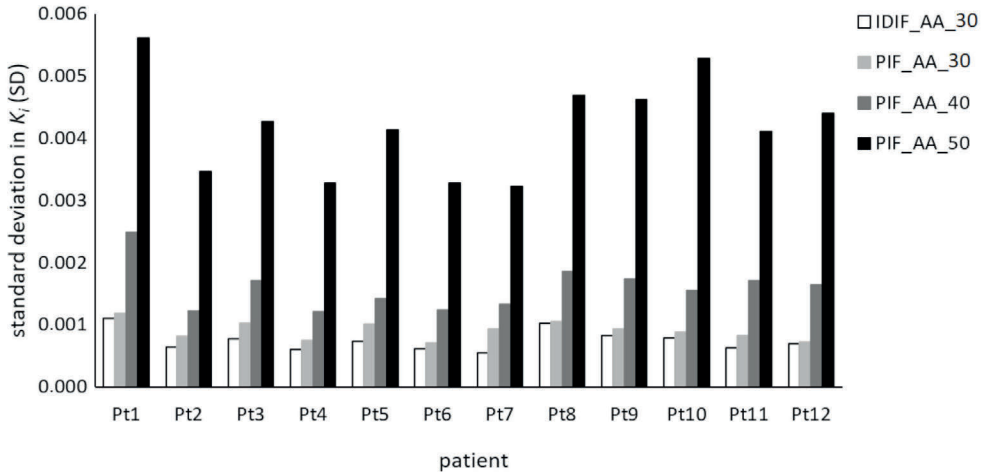


**Figure 5** Barplot of  $K_i$  SD obtained from the liver VOI (as indication for Patlak image noise) generated with IDIF and various PIF at shorter scan time intervals p.i.

With regard to the spleen, significant differences were found in  $K_i$  obtained using the AA IDIF and the corresponding shortened PIF scaled to 40-60 min p.i. (CI (0.001 - 0.003),  $P < 0.001$ ) and scaled to 50-60 min p.i. (CI (0.001 - 0.004),  $P < 0.001$ ).

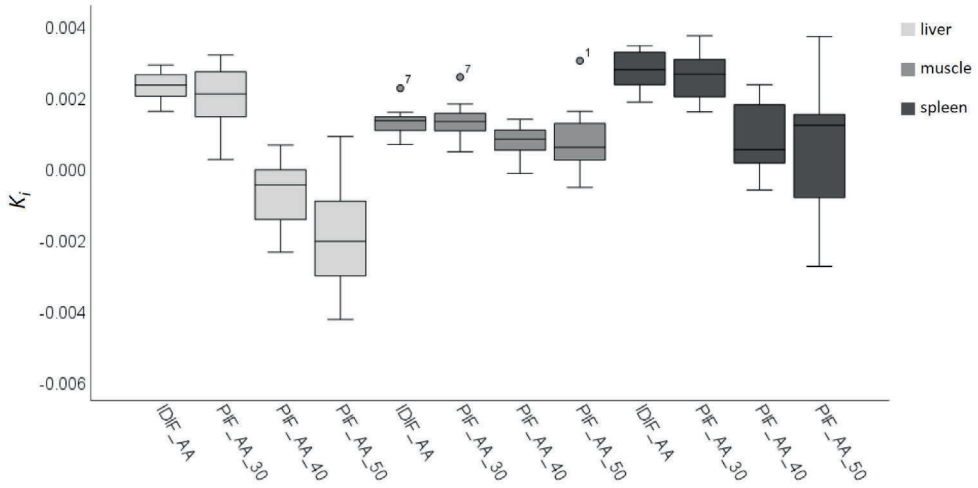


**Figure 6** Healthy tissue  $K_i$  obtained using the IDIF from the AA compared with  $K_i$  obtained with the PIF scaled to the IDIF at scan time interval 30-60 min p.i. (PIF\_AA\_30), 40-60 min p.i. (PIF\_AA\_40), and 50-60 min p.i. (PIF\_AA\_50). Mild outliers are marked with a circle and are data points that fall outside quartile 1( $Q1$ )- $1.5 \times$ interquartile range (IQR) or  $Q3 + 1.5 \times$  IQR. Extreme outliers are marked with an asterisk and fall outside  $Q1 - 3 \times$  IQR or  $Q3 + 3 \times$  IQR.

## Discussion

Over the last decade, improvements in detector technology (3,31) and higher demands for clinical application have led to the development and recent introduction of LAFOV PET systems (31,32). Apart from the Vision Quadra PET/CT, other LAFOV PET systems that have been introduced recently are the uEXPLORER (United Imaging Healthcare, Houston, TX, USA) with an LAFOV of 194 cm (33,34) and the PennPET Explorer (University of Pennsylvania) with an LAFOV of 64 cm (35,36). Using these systems, access to arteries for arterial sampling to obtain the arterial IF to allow full quantitative kinetic analysis is challenging. Because of the substantial increase in sensitivity with regard to conventional PET systems (with a more limited axial FOV) and the corresponding lower noise levels, LAFOV systems allow for non-invasive whole body dynamic  $^{18}\text{F}$ -FDG Patlak imaging methods using an IDIF (validated against the gold standard arterial blood sampling in (37)). However, whereas improvements in PET technology allow whole body parametric imaging, these also enable acquisition of whole body static images at substantially reduced scan durations for increased patient throughput. Hence, the assessment of non-invasive whole body  $^{18}\text{F}$ -FDG Patlak imaging using a PIF for acquisition at shortened scan time intervals to reduce scan time for whole body parametric imaging as conducted in this study, will be a useful and compatible method to apply with these LAFOV PET systems.

The current study shows that non-invasive whole body  $^{18}\text{F}$ -FDG Patlak imaging to be feasible using a representative PIF scaled to the IDIF obtained from the AA or LV at 30-60 min p.i. An even shorter scan time interval of 40-60 min p.i. may also be a good compromise between overall scan duration and quantitative robustness of tumor  $K_i$  values, although it is associated with an increase in noise and a slight deterioration in image quality. In the present study,  $K_i$  estimates deviated marginally (<8%) when using the PIF scaled to the IDIF at 30-60 min p.i. with respect to using the IDIF itself. The observed deviation agrees well with those as published before (25). An accuracy level of 8% is well within the tumor SUV quantification repeatability levels of 10-15% (38-40). Although Viswanath et al. also studied an abbreviated whole body dynamic  $^{18}\text{F}$ -FDG imaging protocol for the Vision Quadra, they recommend 20 min total scan time subdivided into 10-15 min p.i. and 5 min at 60 min p.i., which could be less pragmatic for routine clinical implementation. For example, the dual time point approach would require each subject to be positioned on the system twice, which may add to dead time in the use of the system, requires additional patient handling, and consequently hamper a busy clinical workflow. In addition, a second CT acquisition is required which increases total radiation exposure. Finally, both image datasets need to be coregistered carefully, possibly requiring non-rigid transformations.

When using the PIF scaled to the IDIF at 40-60 min,  $K_i$  bias decreased, but the SD in  $K_i$  obtained from the liver increased, indicating a trade off between image quality (Figure 1) and shorter scan duration at the expense of increased noise.  $K_i$  bias increases to >24% when using even shorter scan duration, i.e., 50-60 min. In addition, this shorter scan interval was associated with substantial increase in noise. Moreover, for some organs  $^{18}\text{F}$ -FDG may show reversible kinetics, such as liver and spleen. The latter explains the change or decrease in  $K_i$  with later  $t^*$  values and for these organs, generalized Patlak analysis or spectral analysis may be more appropriate (12,17). For tumors this phenomenon was not seen and use of Patlak with  $t^* = 30$  or 40 min, thus analysis time intervals of 30 to 60 min or 40 to 60 min, did not introduce bias while maintaining sufficient precision (Figures 3 and 4).

Benefits of incorporating shorter scan times are not only patient throughput, but also patient comfort. A short 20 to 30 min (dynamic) scan protocol at the interval of 40-60 or 30-60 min p.i. is more likely to be tolerated with respect to the standard (at least) 65 min that is necessary for a full whole body dynamic Patlak acquisition. In addition, parametric images obtained using 20 or 30 min scan duration are less prone to motion artifacts (41,42).

The effect of VOI placement on IDIF measurement has been included in the current study as well. Literature describes that the advantage of using the AA over the LV is the possibility of defining larger VOIs, hereby obtaining data with better statistical

properties. Furthermore, the larger diameter of the lumen of the AA reduces partial volume effects. In addition, the IDIF from the AA will result in less spillover from myocardial high uptake tissue with respect to the IDIF obtained from the LV which has increased vulnerability to cardiac motion (37,42,43).

With regard to clinical advantages of whole body dynamic Patlak imaging over conventional static scans, parametric images can provide complementary information to standard SUV images, or rather filter information by deleting intravascular contributions to the PET signal, enabling easier detection and classification of small  $^{18}\text{F}$ -FDG avid lesions, particularly in high background uptake regions, such as the liver (41,44). However, even with the possibility to reduce scan duration to 20 min, including the low dose CT and patient positioning, examination time will increase up to 30 min. LAFOV systems allow standard whole body static scan durations of less than 2 min (36,45,46), including patient positioning and CT this could lead to a total examination time of ~10 to 15 min, which is a factor 3 to 2 less with respect to the shortest feasible whole body Patlak acquisition procedure. Based on these findings and the specific aims regarding patient throughput at different PET centers, dynamic whole body Patlak imaging may not be suitable for all patient studies; for diagnostics and staging, a simple static scan would do. However, for select patient groups, additional information to more accurately monitor treatment response may be required, especially when comparing to a baseline scan. In those cases  $^{18}\text{F}$ -FDG blood clearance changes may affect SUV-based quantification (9,29,44,47,48).

## **Conclusion**

Our study shows that parametric whole body  $^{18}\text{F}$ -FDG Patlak  $K_i$  images can be obtained non-invasively using a Vision Quadra system. In addition, using a PIF scaled to the IDIF allows for a factor 2 to 3 reduction in scan time, from 65 min to a scan time interval of 30-60 or 40-60 min p.i., without substantial loss of accuracy (less than 8%) and precision (image quality and noise interference).

## References

1. Townsend DW. Dual-modality imaging: combining anatomy and function. *J Nucl Med.* 2008;49:938-55.
2. Bastiaannet E, Groen B, Jager PL, Cobben DCP, van der Graaf WTA, Vaalburg W, et al. The value of FDG-PET in the detection, grading and response to therapy of soft tissue and bone sarcomas; a systematic review and meta-analysis. *Cancer Treat Rev.* 2004;30:83-101.
3. Slomka PJ, Pan T, Germano G. Recent advances and future progress in PET instrumentation. *Semin Nucl Med.* 2016;46:5-19.
4. Hsu DFC, Ilan E, Peterson WT, Uribe J, Lubberink M, Levin CS. Studies of a next-generation silicon-photomultiplier-based time-of-flight PET/CT System. *J Nucl Med.* 2017;58:1511-8.
5. Boellaard R, Delgado-Bolton R, Oyen WJG, Giammarile F, Tatsch K, Eschner W, et al. FDG PET/CT: EANM procedure guidelines for tumour imaging: version 2.0. *Eur J Nucl Med Mol Imaging.* 2014;42:328-54.
6. Boellaard R, Oyen WJG, Hoekstra CJ, Hoekstra OS, Visser EP, Willemsen AT, et al. The Netherlands protocol for standardisation and quantification of FDG whole body PET studies in multi-centre trials. *Eur J Nucl Med Mol Imaging.* 2008;35:2320-33.
7. Weber WA. Use of PET for monitoring cancer therapy and for predicting outcome. *J Nucl Med.* 2005;46:983-95.
8. Shankar LK, Hoffman JM, Bacharach S, Graham MM, Karp J, Lammertsma AA, et al. Consensus recommendations for the use of  $^{18}\text{F}$ -FDG PET as an indicator of therapeutic response in patients in National Cancer Institute Trials. *J Nucl Med.* 2006;47:1059-66.
9. Freedman NMT, Sundaram SK, Kurdziel K, Carrasquillo JA, Whatley M, Carson JM, et al. Comparison of SUV and Patlak slope for monitoring of cancer therapy using serial PET scans. *Eur J Nucl Med Mol Imaging.* 2003;30:46-53.
10. Huang SC. Anatomy of SUV. *Nucl Med Biol.* 2000;27:643-6.
11. Lammertsma AA, Hoekstra CJ, Giaccone G, Hoekstra OS. How should we analyse FDG PET studies for monitoring tumour response? *Eur J Nucl Med Mol Imaging.* 2006;33:S16-21.
12. Zaidi H, Karakatsanis N. Towards enhanced pet quantification in clinical oncology. *Br J Radiol.* 2018;91:20170508.
13. Karakatsanis NA, Zhou Y, Lodge MA, Casey ME, Wahl RL, Zaidi H, et al. Generalized whole-body patlak parametric imaging for enhanced quantification in clinical PET. *Phys Med Biol.* 2015;60:8643-73.
14. Karakatsanis NA, Lodge MA, Tahari AK, Zhou Y, Wahl RL, Rahmim A. Dynamic whole body PET parametric imaging: I. Concept, acquisition protocol optimization and clinical application Nicolas. *Phys Med Biol.* 2014;49:1012-6.
15. Patlak CS, Blasberg RG. Graphical evaluation of blood-to-brain transfer constants from multiple-time uptake data. Generalizations. *J Cereb Blood Flow Metab.* 1985;5:584-90.
16. Prenosil GA, Sari H, Fürstner M, Afshar-Oromieh A, Shi K, Rominger A, et al. Performance characteristics of the Biograph Vision Quadra PET/CT system with long axial field of view using

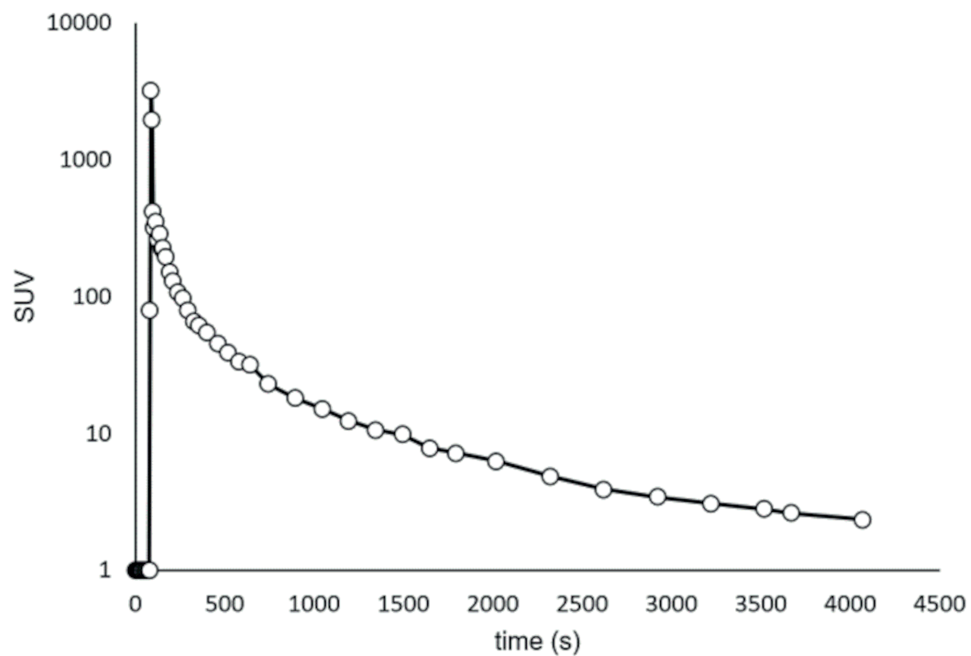


- the NEMA NU 2-2018 Standard. *J Nucl Med.* 2021;63:476-84.
17. Karakatsanis NA, Casey ME, Lodge MA, Rahmim A, Zaidi H. Whole-body direct 4D parametric PET imaging employing nested generalized Patlak expectation-maximization reconstruction. *Phys Med Biol.* 2016;61:5456-85.
  18. Naganawa M, Gallezot J-D, Shah V, Mulnix T, Chen M-K, Smith A, et al. Assessment of population-based input functions for the Patlak plot using whole body  $^{18}\text{F}$ -FDG PET imaging. *EJNMMI Phys.* 2020;7:67.
  19. Karakatsanis N, Zhou Y, Lodge M, Casey M, Wahl R, Subramaniam R, et al. Clinical Whole-body PET Patlak imaging 60-90min post-injection employing a population-based input function. *J Nucl Med.* 2015;56(suppl 3):1786.
  20. Karakatsanis N, Lodge M, Casey M, Wahl R, Subramaniam R, Zaidi H, et al. Novel multi-parametric SUV/Patlak FDG-PET whole-body imaging framework for routine application to clinical oncology. *J Nucl Med.* 2015;56(suppl 3):625.
  21. Yao S, Feng T, Zhao Y, Wu R, Wang R, Wu W, et al. Simplified protocol for whole-body Patlak parametric imaging with  $^{18}\text{F}$ -FDG PET/CT : Feasibility and error analysis. *Med Phys.* 2021;48:2160-9.
  22. Wu Y, Feng T, Shen Y, Fu F, Meng N, Li X, et al. Total-body parametric imaging using the Patlak model: Feasibility of reduced scan time. *Med Phys.* 2022;1-11.
  23. Wu J, Liu H, Ye Q, Gallezot JD, Naganawa M, Miao T, et al. Generation of parametric Ki images for FDG PET using two 5-min scans. *Med Phys.* 2021;48:5219-31.
  24. Viswanath V, Sari H, Pantel AR, Conti M, Daube-Witherspoon ME, Mingels C, et al. Abbreviated scan protocols to capture  $^{18}\text{F}$ -FDG kinetics for long axial FOV PET scanners. *Eur J Nucl Med Mol Imaging.* 2022;49:3215-3225.
  25. van Sluis J, Yaqub M, Brouwers AH, Dierckx RAJO, Noordzij W, Boellaard R. Use of population input functions for reduced scan duration whole-body Patlak  $^{18}\text{F}$ -FDG PET imaging. *EJNMMI Phys.* 2021;8:11.
  26. Boellaard R. New developments of EANM oncology PET/CT guidelines and update of the EARL accreditation standards presentation. 2018. Available from: [https://eanm-earl-wordpress.esh.netkey.at/wp-content/uploads/2021/04/EARL\\_18F\\_stds2\\_PPP\\_Boellaard\\_Oct2018-1.pdf](https://eanm-earl-wordpress.esh.netkey.at/wp-content/uploads/2021/04/EARL_18F_stds2_PPP_Boellaard_Oct2018-1.pdf). Accessed June 5th 2022.
  27. Weerdt AP Van Der, Klein LJ, Boellaard R, Visser CA, Visser FC, Lammertsma AA. Image-derived input functions for determination of MRGlu in cardiac  $^{18}\text{F}$ -FDG PET Scans. *J Nucl Med.* 2001;42:1622-9.
  28. Patlak CS, Blasberg RG. Graphical evaluation of blood-to-brain transfer constants from multiple-time uptake data. *J Cereb Blood Flow Metab.* 1983;5:584-90.
  29. Cheebsumon P, Velasquez LM, Hoekstra CJ, Hayes W, Kloet RW, Hoetjes NJ, et al. Measuring response to therapy using FDG PET: semi-quantitative and full kinetic analysis. *Eur J Nucl Med Mol Imaging.* 2011;38:832-42.
  30. Boellaard R. Quantitative oncology molecular analysis suite: ACCURATE [abstract]. *J Nucl Med.* 2018;59(suppl 1):1753-1753.

31. Vandenberghe S, Moskal P, Karp JS. State of the art in total body PET. *EJNMMI Phys.* 2020;7:35.
32. Surti S, Pantel AR, Karp JS. Total body PET: Why, how, what for? *IEEE Trans Radiat Plasma Med Sci.* 2021;4:283-92.
33. Badawi RD, Shi H, Hu P, Chen S, Xu T, Price PM, et al. First human imaging studies with the Explorer total-body PET scanner. *J Nucl Med.* 2019;60:299-303.
34. Spencer BA, Berg E, Schmall JP, Omidvari N, Leung EK, Abdelhafez YG, et al. Performance evaluation of the uEXPLORER total-body PET/CT scanner based on NEMA NU 2-2018 with additional tests to characterize PET scanners with a long axial field of view. *J Nucl Med.* 2021;62:861-70.
35. Karp JS, Viswanath V, Geagan MJ, Muehllhner G, Pantel AR, Parma MJ, et al. PennPET explorer: design and preliminary performance of a whole-body imager. *J Nucl Med.* 2020;61:136-43.
36. Pantel AR, Viswanath V, Daube-witherspoon ME, Dubroff JG, Muehllhner G, Parma MJ, et al. PennPET Explorer: human Imaging on a whole-body imager. *J Nucl Med.* 2020;61:144-51.
37. de Geus-Oei LF, Visser EP, Krabbe PFM, Van Hoorn BA, Koenders EB, Willemsen AT, et al. Comparison of image-derived and arterial input functions for estimating the rate of glucose metabolism in therapy-monitoring  $^{18}\text{F}$ -FDG PET studies. *J Nucl Med.* 2006;47:945-9.
38. de Langen AJ, Vincent A, Velasquez LM, Van Tinteren H, Boellaard R, Shankar LK, et al. Repeatability of  $^{18}\text{F}$ -FDG uptake measurements in tumors: A metaanalysis. *J Nucl Med.* 2012;53:701-8.
39. Weber WA, Gatsonis CA, Mozley PD, Hanna LG, Shields AF, Aberle DR, et al. Repeatability of  $^{18}\text{F}$ -FDG PET/CT in advanced non-small cell lung cancer: prospective assessment in 2 multicenter trials. 2016;56:1137-43.
40. Kramer GM, Frings V, Hoetjes N, Hoekstra OS, Smit EF, De Langen AJ, et al. Repeatability of quantitative whole-body  $^{18}\text{F}$ -FDG PET/CT uptake measures as function of uptake interval and lesion selection in non-small cell lung cancer patients. *J Nucl Med.* 2016;57:1343-9.
41. Dias AH, Pedersen MF, Danielsen H, Munk OL, Gormsen LC. Clinical feasibility and impact of fully automated multiparametric PET imaging using direct Patlak reconstruction: evaluation of 103 dynamic whole-body  $^{18}\text{F}$ -FDG PET/CT scans. *Eur J Nucl Med Mol Imaging.* 2021;48:837-50.
42. Hoekstra CJ, Hoekstra OS, Stroobants SG, Vansteenkiste J, Nuyts J, Smit EF, et al. Methods to monitor response to chemotherapy in non-small cell lung cancer with  $^{18}\text{F}$ -FDG. 2015;43:1304-10.
43. Sari H, Mingels C, Alberts I, Hu J, Buesser D, Shah V, et al. First results on kinetic modelling and parametric imaging of dynamic  $^{18}\text{F}$ -FDG datasets from a long axial FOV PET scanner in oncological patients. *Eur J Nucl Med Mol Imaging.* 2022; 49:1997-2009.
44. Hoekstra CJ, Hoekstra OS, Stroobants SG, Vansteenkiste J, Nuyts J, Smit EF, et al. Methods to monitor response to chemotherapy in non-small cell lung cancer with  $^{18}\text{F}$ -FDG PET. *J Nucl Med.* 2002;43:1304-9.
45. Alberts I, Hünermund J, Prenosil G, Mingels C, Bohn KP, Viscione M, et al. Clinical performance of long axial field of view PET/CT: a head-to-head intra-individual comparison of the Biograph Vision Quadra with the Biograph Vision PET / CT. *Eur J Nucl Med Mol Imaging.* 2021;48:2395-

- 404.
46. Hu P, Zhang Y, Yu H, Chen S, Tan H, Qi C, et al. Total-body  $^{18}\text{F}$ -FDG PET / CT scan in oncology patients: how fast could it be? *Eur J Nucl Med Mol Imaging*. 2021;48:2384-94.
  47. Doot RK, Pierce LA, Byrd D, Elston B, Allberg KC, Kinahan PE. Biases in multicenter longitudinal PET standardized uptake value measurements. *Transl Oncol*. 2014;7:48-54.
  48. Lammertsma AA. Forward to the past: the case for quantitative PET imaging. *J Nucl Med*. 2017;58:1019-24.

## Supplemental data



Supplemental Figure 1 Plot of population-averaged input function. The y-axis is in logarithmic scale.



# Chapter 11

---

Future perspectives and concluding  
remarks



Since the 1970's, when the first PET systems were built, there has been a significant evolution in PET system technology. Progress in development of detector technology from photomultiplier tubes (PMTs) to silicon-based photomultiplier (SiPM) detector elements has led to the development of digital PET/CT scanners. Performance, image quality, and implications for clinical practice of this major step in PET technology development have been described in **Chapters 2-6** in this thesis. The latest improvement in PET system technology is the development of long axial field-of-view (LAFOV), or so-called total body, PET/CT systems resulting in a larger simultaneous coverage of the human body and a greatly increased sensitivity (a factor of 10 to 40 depending on the length of the scanner) compared with conventional PET scanners (1,2), illustrated in **Chapter 7** with improved image quality and increased signal-to-noise ratio (SNR) in  $^{89}\text{Zr}$  ImmunoPET imaging. **Chapter 8** continues with LAFOV PET imaging and touches upon the first benefits in terms of reduced scan duration or injected radiotracer activity, or both, when using  $^{18}\text{F}$ -FDG for oncological applications. Moreover, the large coverage of an LAFOV PET system enables simultaneous dynamic imaging of all internal organs and (possible) tumor lesions (3,4). The current chapter will more elaborately focus on future possibilities using LAFOV PET for clinical and research applications. In addition, possible future hardware developments in PET detectors, new photon detection technologies, and the associated expected benefits in both research and clinical settings will be described.

### **PET imaging optimization**

The ability to determine the position of single annihilation events along the line of response (LOR) with precise timing information (time-of-flight (ToF)) is the strength of state of the art PET systems. With the introduction of digital PET technology, ToF improved to 210-400 picoseconds (ps) thereby providing images with improved quality (5). Moreover, on analog systems the sensitivity was one of the limiting factors in both temporal and spatial image resolution; long acquisition times were applied and image filtering was often used to reduce image noise. The improved sensitivity in state of the art PET systems results in a substantial increase in counts, i.e., detected annihilation photons, which results in improved statistics and thus substantially increased SNR as well (4).

Increased sensitivity of LAFOV PET systems now results in images with low noise and improved underlying anatomic details not easily appreciated on conventional PET systems, including activities related to brain substructures (e.g., basal ganglia subregions (6)) and vessel walls. This improvement in image quality may have direct effect on clinical applications resulting in a better understanding of disease burden and residual disease evaluation (3). Higher system sensitivity and improved ToF mean that diagnostic image quality can be obtained at shorter scan durations or with

less injected activity than is typically used in current clinical practice (3,7).

### **Imaging with lower radiation exposure**

A significant reduction in injected activity results in a proportional reduction in radiation exposure, which enables new applications for  $^{18}\text{F}$ -FDG PET. For example, it may become feasible to screen high-risk populations for early detection of malignancies in subjects who have no symptoms (yet), e.g., based on abnormally altered blood biomarkers and/or genetic risk factors.

In oncology, many patients undergo repeat imaging, especially when evaluating treatment response. More frequent response monitoring assessments, and consequently the possibility to swiftly switch to another, more effective treatment is possible with reduction in administered radioactive dose (2,4). In the case of monoclonal antibody (mAb) treatment, lowering the administered radioactive  $^{89}\text{Zr}$  dose allows for repeat immunoPET scans.

At present, immunoPET is used almost exclusively in a research setting concerning oncological patients with a relatively shorter life expectancy. High mean effective doses are obtained using  $^{89}\text{Zr}$ -labeled mAbs ranging from 0.36-0.66 mSv/MBq (8). Administering a standard 37 MBq of  $^{89}\text{Zr}$  activity results in a radiation exposure of up to 25 mSv. Lowering the amount of administered radioactive  $^{89}\text{Zr}$  activity could reduce radiation exposure to below 10 mSv which opens up the possibility to use labeled mAbs for other indications, for example, younger patients with inflammatory diseases, first in a research setting, in the future maybe also in a routine clinical setting.

In addition, lower radiation exposure facilitates PET imaging in children, who are considerably more sensitive to the carcinogenic effects of ionizing radiation than adults (9). Pediatric patients, often diagnosed with malignant diseases such as lymphoma, require frequent repeat imaging during treatment (10). What's more is the potential of LAFOV PET to facilitate and improve efficacy of drug development, a process that is known to be cumbersome and expensive (11). A major limitation here, often limiting the number of scans performed during a trial, is the maximum permissible radiation dose (12). LAFOV enables imaging with lower doses, consequently there are less restrictions in the number of scans which provides more flexibility to look at different biological processes with a combination of different tracers (2,4). Such a substantial reduction in radiation exposure even opens up inclusion of healthy volunteers (undergoing repeat PET scans) in clinical drug development trials.

For example, in the cases described above, radiation exposure with serial PET imaging using a LAFOV system can be reduced to such an extent, that CT will be the dose limiting factor. (Serial) low dose CT scans merely used for the purpose of PET attenuation and scatter correction, do not provide additional clinical information.

Hence, more emphasis is placed on developing reconstruction algorithms that do not require a CT for attenuation correction, such as maximum likelihood reconstruction of attenuation and activity (MLAA) (13,14). CT-based PET attenuation correction is the current clinical standard where the attenuation of x-rays transmitted through the patient directly relates to electron density; CT Hounsfield Units undergo (bi-) linear transformation to PET linear attenuation coefficient values resulting in an attenuation map, or  $\mu$ -map (15). Image quality and quantitative accuracy rely heavily on correction of absorption and scatter caused by photon-tissue interaction of the detected photons; varying electron density and tissue thickness influence photon attenuation which, in some regions, can result in a 90% signal reduction (15,16). MLAA methods for attenuation correction rely primarily on emission data to estimate attenuation information through iterative joint estimation based on maximum likelihood and are promising reconstruction approaches to enhance quantitative accuracy of CT-free PET studies (15,17,18). Other possibilities for ultralow-dose CT acquisition are for example the application of a tin filter (19,20) or a split-filter consisting of a gold and a tin part (21) achieving radiation doses as low as 0.06 mSv for a thoracic CT scan (22). However, the suitability of these filtered CT for accurate PET attenuation correction has not been demonstrated yet.

Low-dose imaging may also enable dual isotope imaging or multiple studies (with different radioactive tracers) in a single patient examination. For example, dual isotope imaging to study two physiological functions with two radioactive tracers simultaneously in a single acquisition, such as simultaneous imaging of tumor hypoxia and metabolism using  $^{60}\text{Cu}$ -diacetyl-di( $\text{N}^4$ -methylthiosemicarbazone) co-injected with  $^{18}\text{F}$ -FDG (23). Simultaneous study during one acquisition, instead of two separate sessions, will be more comfortable for the patient, will reduce radiation exposure to the patient by requiring only one CT, will reduce the cost, and will avoid inaccuracy due to possible metabolic changes between two separate acquisitions (23).

### **Faster static PET imaging procedures**

Reprocessing of acquired listmode data has shown that diagnostic image quality scans can be obtained using 1-2 min scan duration, or less (1,6,7). Fast PET imaging allows a higher patient throughput, limited by patient positioning time, rather than scan duration. Consequently, more patients could be scanned within a certain time window so that these patients can be studied with the same tracer production batch leading to a reduction in overall costs (please note, in case of faster examination times without lowering the amount of injected activity, a larger tracer production batch is required). Furthermore, a significant reduction in scan duration may make it possible to scan patients who are unable to lay still for a long time, children

(without anesthesia) or elderly patients, and patients, e.g., with severe back pain or claustrophobic patients (4). In the case of Intensive Care Unit patients, in which PET/CT imaging is currently not often performed due to logistical issues and the need for continuous monitoring in unstable patients (24), an ultra-fast scan protocol may be beneficial adding to the anatomical CT in a one-stop shop metabolic information, for example on possible sources and locations of frequently occurring infections.

Other applications of faster PET acquisition procedures can be for example indeterminate pulmonary nodule quantification of  $^{18}\text{F}$ -FDG uptake to distinguish benign (i.e., inflammatory processes) from malignant disease. Particularly imaging and quantification of small nodules (<1 cm) (25) at the lung bases is erroneous due to partial volume effects and respiratory motion artifacts (3). Breath-hold  $^{18}\text{F}$ -FDG PET, acquiring images in 15-30 seconds, may be achieved with a LAFOV scanner which can mitigate these issues (26) and obviate the necessity to apply sophisticated motion-correction algorithms (27).

### Delayed imaging

Equivalent to imaging with lesser injected radioactive tracer, the increased sensitivity of a LAFOV scanner could be used for delayed imaging, with acquisition times post injection (p.i.) far beyond the possibilities of conventional PET systems; for  $^{18}\text{F}$ -FDG, e.g., 2-18 hours (10 half-lives) (6,7). This prolonged uptake time ensures increased trapping of the tracer via the hexokinase enzyme in metabolically active tissues. Tumor contrast increases over time and nearly full washout of free (i.e., non-metabolized)  $^{18}\text{F}$ -FDG (background) occurs, resulting in a higher lesion-to-background ratio; the signal's specificity increases. Delayed imaging is particularly promising in detecting metastases in tissues with high physiological uptake such as the liver which decreases over time (28). The acquired standardized uptake value (SUV) image at 2-18 hours p.i. could resemble the parametric image of  $^{18}\text{F}$ -FDG influx rate ( $K_i$ ) using simple and easy static imaging and reconstruction without the need for time consuming whole body dynamic image acquisition, reconstruction, and analysis. However, this needs to be explored in future studies.

A prolonged uptake time with long-lived radionuclides, e.g.,  $^{89}\text{Zr}$  immunoPET imaging, e.g., beyond 7 days, is expected to similarly result in an improved lesion-to-background ratio. Furthermore, combining delayed imaging with novel radioactive agents, including new  $^{89}\text{Zr}$  immunotracers, allows extended study of *in vivo* biology (29).

### Opportunities in dynamic imaging

The aforementioned semiquantitative SUV of  $^{18}\text{F}$ -FDG, derived from static images obtained at 60 minutes p.i., is most commonly used as a surrogate of metabolic

activity for tumor uptake quantification (30). Following standardization methods can mitigate SUV variability to a great extent (30-32), however, cannot account for changes in plasma kinetics and cannot distinguish between specific and nonspecific uptake. This may lead to a dissociation between inaccurate SUV measurements and actual tumor metabolic activity (33-35). Conversely, dynamic PET imaging is able to include this information as it allows spatiotemporal activity concentration measurement, providing voxel-wise metabolic information after applying full kinetic- or Patlak analyses (36-38). **Chapters 9 and 10** in this thesis described a method to reduce the total examination time of dynamic  $^{18}\text{F}$ -FDG whole body (Patlak) imaging from up to 75 min to 30-60 min p.i. and 40-60 min p.i., respectively, using a population-averaged input function, making full kinetic- or Patlak analyses more suitable for application in the clinic. The otherwise occupied camera time can, in the case of shortened whole body Patlak imaging, be used for another or maybe two routine clinical static PET examinations.

### **Non-invasive full quantitative imaging**

The higher sensitivity and larger axial coverage of the body allow LAFOV PET to capture time-activity in multiple organs and lesions relatively noise free, which enhances our ability to study the pharmacokinetic behavior of radiotracers. Using conventional PET systems, an image derived input function (IDIF) can only be obtained for studies where the heart or a large blood pool structure is in the (restricted) axial field-of-view (FOV). As LAFOV PET imaging captures the heart together with all other main organs of interest, it ensures the FOV always contains a large vascular structure for an IDIF. Moreover, dynamic total body scans make it possible to derive quantitative biological information for multiple lesions within a single FOV. This is important in those cases where interlesional heterogeneity exists and where static images are non-informative or misleading, such as was seen for  $^{11}\text{C}$ -erlotinib (39). Given known associations of tumoral heterogeneity and resistance to targeted therapy, capturing all lesions simultaneously and dynamically is important for response monitoring (40), as overall response depends on the response of the least responsive lesion (4).

For other tracers than, for example  $^{18}\text{F}$ -FDG, that are not ‘metabolically trapped’ inside the cell and undergo metabolism, kinetic modeling requires a more complex approach than Patlak analyses taking into account reversible kinetics and/or tracer metabolism. Studying the dynamic tracer uptake in the liver may provide a means to non-invasively estimate tracer metabolism and derive a metabolite corrected plasma input function, although this is yet to be explored.

## Human connectome

Unique about a LAFOV system is capturing all relevant organs in one FOV with enhanced pharmacokinetic modeling possibilities which provides a unique means to quantitatively and non-invasively study the physiological or pathophysiological interactions between organs, the human connectome, including brain-body interactions (3).

There is increasing evidence that many diseases, traditionally thought to be limited to a single organ, are involved in complex interplays with other organs or organ systems (41). For example, the brain-gut axis: bacteria in the gut might be linked to a whole family of neurological disorders (41-44). Furthermore, more evidence shows gut-lung crosstalk and herewith the influence of the gut microbiome and gastrointestinal disorders on chronic inflammatory reactions in the airways (45) and treatment response in advanced non-small cell lung cancer (46). Also, the importance of the gut-lung axis in managing Covid-19 diseases has been described, e.g. targeting gut microbiota can avoid progression of Covid-19 (47-50). Here, labeling of immune cells of the gut to follow interactions with distant organ systems could be captured with LAFOV.

It has also become apparent that cardiovascular function, neurochemical asymmetries and depression are interconnected (51). Furthermore, recently, a tight inflammatory interaction has been revealed between the myocardium and the kidneys as secondary affected organs following acute myocardial infarction (52), i.e., the heart-kidney axis. Moreover, the so-called brain-heart axis is for example implicated in cardiovascular complications after acute ischemic stroke known as the stroke-heart syndrome (53).

## Future PET developments

Apart from improving detector efficiency and increasing the geometrical acceptance through extension of the axial length of the PET system, there is another way to increase photon detection sensitivity: pushing ToF performance. Improving ToF performance can be combined with enhancement of detector efficiency and extending the axial FOV to further increase PET effective sensitivity (54). Improving ToF PET from the current 200 ps to 10 ps would ultimately allow reconstruction-free imaging, i.e., PET imaging without the need for reconstruction because of the improved spatial resolution along the LOR of less than 1.5 mm (54). The benefits and opportunities of improved sensitivity using LAFOV PET as described above in this chapter would be even more extensive in combination with 10 ps ToF. Cherenkov light detection, a phenomenon described later in this chapter, could also play a role in pushing ToF performance.

Another application of interest could be translating the use of 10 ps ToF PET in the design of LAFOV PET systems, without increasing the cost, using PET sparse-

ring detector configurations (54-56). Previous research demonstrated feasibility of reducing the number of detectors by 50% without compromising image quality compared to a standard conventional FOV PET system (57). With the expected improved spatial resolution along the LOR, the same number of detectors used in conventional PET systems could be used for larger axial coverage (1 - 2 m). The main advantages of such an extended coverage include simultaneous dynamic imaging of all internal organs and (possible) tumor lesions, as described above, however without the relative high cost associated with an LAFOV PET system, at present (54,57).

Furthermore, one focus of PET development is detector technology. Current detector technology incorporates pixelated scintillation crystals which form the dominant factor determining system spatial resolution. Instead of pixelated scintillating crystals, monolithic ones, consisting of a continuous scintillation crystal coupled to an array of SiPMs, which can provide depth-of-interaction (DOI) information, could overcome this limitation in spatial resolution, improve system resolution also at off-center positions using DOI measurement, and maintain high sensitivity (58). Inside the crystal, the incoming scintillation light spreads and the light distribution can be sampled by the SiPM array. From the shape of the light distribution, the 2D position and DOI can be derived. This is especially relevant for LAFOV PET systems, where DOI is of interest to correct for parallax effects and degradation of spatial resolution in the axial direction (58). However, where pixelated crystals are one-to-one coupled to a single photosensor element with no involvement of neighbor photosensors allowing the collection of high amounts of photons in a short time frame, the wide light spread in the monolithic block activating multiple photosensors prohibits the collection of a high number of photons per photosensor element in a short time, which is essential for a good ToF performance (59). For digital SiPM arrays introduced by Philips Digital Photon Counting, the use of multiple time stamps for each scintillation event can overcome this issue and sub-200 ps timing resolution can be achieved (60). For analog SiPM arrays, multichannel application-specific integrated circuit (ASIC)-based readout using the TOFPET2 ASIC (PETsys, Lisbon, Portugal) comes into play (61). This ASIC was designed to operate in different PET light collection schemes such as one-to-one coupling or light-sharing among several SiPM pixels. This is ongoing research and timing resolution for a thick monolithic scintillation block is now down to 580 ps (62).

Continuing on this concept of a continuous scintillation medium, the PETALO (Positron Electron ToF Apparatus using Liquid xenOn) is a prototype PET scanner which uses liquid xenon as the active scintillating material, coupled to UV-sensitive vacuum ultraviolet (VUV)-SiPMs (63), incorporating the TOFPET2 ASIC general

architecture for scintillation readout (61). A promising development in PET detector technology which could play an important role in reducing costs for LAFOV PET systems (64) with liquid xenon costs of around 3 \$/cc (65) compared to 22-30 \$/cc for lutetium oxyorthosilicate (LSO)/lutetium-yttrium oxyorthosilicate (LYSO) crystals (66). As liquid xenon is a continuous medium with uniform response which can be incorporated in a single compact, full-body, and highly efficient detector, the localization of annihilation events is expected to be improved resulting in improved image quality. Monte Carlo characterization shows that this setup can currently achieve a timing resolution of approximately 350 ps and a spatial resolution of 1-2 mm at FWHM (64).

Another development providing a cost-effective solution for LAFOV PET systems is the plastic scintillator alternative for LSO crystals (67). Axially arranged scintillators reduce the costs of readout electronics and SiPMs as well (67). A plastic-based LAFOV PET system is expected to cost about five times less than the crystal-based LAFOV PET system (68). With respect to conventional FOV LSO systems, the plastic-based LAFOV PET system with 200 cm axial coverage results in a 27-fold gain in sensitivity as compared to 46-fold for the 200 cm crystal-based LAFOV PET (68); thus a slight compromise on sensitivity with the benefit of LAFOV opportunities at reduced cost. Furthermore, where in current PET imaging procedures, prompt gammas are generally a source of unwanted background, since the plastic-based PET is not restricted to standard double annihilation photon coincidences, it allows capturing events originating from various isotopes simultaneously (one with a prompt gamma and one without a prompt gamma); i.e., information can be obtained from two tracers (one with a prompt gamma and one without) simultaneously during a single PET examination (68,69).

Moreover, positronium imaging incorporates a detection alternative which is a promising new imaging approach to assess tissue pathology *in vivo* (68). Detection in conventional PET is based on the annihilation of a positron with one of the electrons in the surrounding tissue. The emitted positron can also form the metastable state of an electron and positron called a positronium (70), which may be trapped inside free volumes between and within molecules *in vivo*. Imaging the properties of positronium such as the average lifetime, which depends on the size of free volumes between atoms, correlates with the stage of the development of metabolic disorders and may provide new diagnostic information (70,71). Approximately 40% of annihilations proceed via formation of positronium, whereof 0.5% decay in three photons. Even though the rate of three photon producing annihilations is low, imaging may be feasible with highly sensitive (plastic-based) LAFOV PET systems (70).

Alternatively, Cherenkov light detection is another approach which has been under

development for over a decade (72,73). This phenomenon can be exploited and re-introduce bismuth germanate oxide (BGO) scintillators, towards a more cost-effective ToF-PET detector alternative to LSO/LYSO (4-5-fold lower scintillation material cost) (74). Extraction of improved timing information from the relatively few emitted Cherenkov photons is now feasible because of recent developments in near-ultraviolet high-density (NUV-HD) SiPM technology (75,76). Cherenkov light is produced when an electron travels with enough kinetic energy through scintillating material, faster than the speed of light. When detected, this promptly emitted form of light can be used to estimate 511 keV photon interaction time with improved accuracy than achievable with the overall luminescence yield, hence improving timing resolution (74); the fast rise of the Cherenkov signal can be distinguished from the slower overall luminescence yield with rise time correction signal processing methods. BGO is favored over LSO because of its higher refractive index, producing more Cherenkov light. In addition, BGO allows better transmission of UV light. The study by Gonzalez-Montoro et al. (2022) demonstrates ToF performance values of  $163 \pm 8$ ,  $224 \pm 8$ ,  $266 \pm 9$ , and  $428 \pm 8$  ps for  $3 \times 3 \times 3 \text{ mm}^3$ ,  $3 \times 3 \times 5 \text{ mm}^3$ ,  $3 \times 3 \times 10 \text{ mm}^3$ , and  $3 \times 3 \times 15 \text{ mm}^3$  BGO crystals, respectively, which is equivalent to the ToF performance of state-of-the art LSO PET/CT systems (77,78).

Because of these upcoming developments, many new designs and applications for LAFOV systems will be introduced. Some developments may result in more affordable LAFOV PET system designs and potentially support a more widespread use.

### **Concluding remarks**

LAFOV PET is a new player in the nuclear medicine and molecular imaging field with many clinical workflows to optimize for patient care and new clinical and (advanced) research possibilities to explore. Future technological developments to optimize PET image quality, new detection approaches involving the formation of positronium and the detection of Cherenkov light, and alternative detector materials to make LAFOV PET systems more affordable have been described in this chapter. But first and foremost, this chapter aimed to provide an overview of the opportunities and hypotheses of what LAFOV PET imaging could bring to the field, and to all other medical fields including various patient populations and conditions for which (low dose) PET/CT imaging could be a gamechanger.

## References

1. Alberts I, Hünermund J, Prenosil G, Mingels C, Bohn KP, Viscione M, et al. Clinical performance of long axial field of view PET / CT: a head-to-head intra-individual comparison of the Biograph Vision Quadra with the Biograph Vision PET / CT. *Eur J Nucl Med Mol Imaging*. 2021;48:2395-404.
2. Nadig V, Herrmann K, Mottaghy FM, Schulz V. Hybrid total-body pet scanners - current status and future perspectives. *Eur J Nucl Med Mol Imaging*. 2022;49:445-59.
3. Surti S, Pantel AR, Karp JS. Total Body PET: Why, How, What for? *IEEE Trans Radiat Plasma Med Sci*. 2021;4:283-92.
4. Slart RHJA, Tsoumpas C, Glaudemans AWJM, Noordzij W, Willemsen ATM, Borra RJH, et al. Long axial field of view PET scanners: a road map to implementation and new possibilities. *Eur J Nucl Med Mol Imaging*. 2021;48:4236-45.
5. Surti S, Viswanath V, Daube-Witherspoon ME, Conti M, Casey ME, Karp JS. Benefit of improved performance with state-of-the art digital PET/CT for lesion detection in oncology. *J Nucl Med*. 2020;61:1684-90.
6. Pantel AR, Viswanath V, Daube-witherspoon ME, Dubroff JG, Muehllhner G, Parma MJ, et al. PennPET Explorer : Human imaging on a whole-Body imager. *J Nucl Med*. 2020;61:144-51.
7. Badawi RD, Shi H, Hu P, Chen S, Xu T, Price PM, et al. First human imaging studies with the explorer total-body PET scanner. *J Nucl Med*. 2019;60:299-303.
8. Merckx RIJ, Lobeek D, Konijnenberg M, Jiménez-Franco LD, Kluge A, Oosterwijk E, et al. Phase I study to assess safety, biodistribution and radiation dosimetry for <sup>89</sup>Zr-girentuximab in patients with renal cell carcinoma. *Eur J Nucl Med Mol Imaging*. 2021;48:3277-85.
9. Kleinerman RA. Cancer risks following diagnostic and therapeutic radiation exposure in children. *Pediatr Radiol*. 2006;36:121-5.
10. Spijkers S. Imaging features of extranodal involvement in paediatric Hodgkin lymphoma. *Pediatr Radiol*. 2019;49:266-76.
11. Matthews PM, Rabiner EA, Passchier J, Gunn RN. Positron emission tomography molecular imaging for drug development. *Br J Clin Pharmacol*. 2011;73:175-86.
12. Publication of the Netherlands Commission on Radiation Dosimetry (Nederlandse Commissie Voor Stralingsdosimetrie NCS). Human exposure to ionising radiation for clinical and research purposes: radiation dose & risk estimates. 2016.
13. Li Y, Matej S, Karp JS. Practical joint reconstruction of activity and attenuation with autonomous scaling for time-of-flight PET. 2021;65:235037.
14. Teimoorisichani M, Panin V, Rothfuss H, Sari H, Rominger A, Conti M. A CT-less approach to quantitative PET imaging using the LSO intrinsic radiation for long-axial FOV PET scanners. *Med Phys*. 2021;49:309-23.
15. Chen Y, An H. Attenuation correction of PET/MR imaging. *Magn Reson Imaging Clin N Am*. 2017;25:245-55.
16. Zaidi H, Hasegawa B. Determination of the attenuation map in emission tomography. *J Nucl Med*.

- 2003;44:291-315.
17. Boellaard R, Hofman MBM, Hoekstra OS, Lammertsma AA. Accurate PET/MR quantification using time of flight MLLAA image reconstruction. *Mol Imaging Biol.* 2014;16:469-77.
  18. Rezaei A, Defrise M, Bal G, Michel C, Conti M, Watson C, et al. Simultaneous reconstruction of activity and attenuation in time-of-flight PET. *IEEE Trans Med Imaging.* 2012;31:2224-33.
  19. Greffier J, Pereira F, Hamard A, Addala T, Beregi JP, Frandon J. Effect of tin filter-based spectral shaping CT on image quality and radiation dose for routine use on ultralow-dose CT protocols : a phantom study. *Diagn Interv Imaging.* 2020;101:373-81.
  20. Prieto E, Garcia-Velloso MJ, Damaso JA, Rosales JJ, Bastidas JF, Soriano I, et al. Ultra-low dose whole-body CT for attenuation correction in a dual tracer PET/CT protocol for multiple myeloma. *Phys Medica.* 2021;84:1-9.
  21. Petritsch B, Pannenbecker P, Weng AM, Grunz J, Veldhoen S, Bley TA, et al. Split-filter dual-energy CT pulmonary angiography for the diagnosis of acute pulmonary embolism: a study on image quality and radiation dose. *Quant Imaging Med Surg.* 2021;11:1817-27.
  22. Gordic S, Morsbach F, Schmidt B, Allmendinger T, Flohr T, Husarik D, et al. Ultralow-dose chest computed tomography for pulmonary nodule detection: first performance evaluation of single energy scanning with spectral shaping. *Radiology.* 2014;49:465-73.
  23. Walrand S, Hesse M, Jamar F. Nuclear medicine: Physics and instrumentation special feature review article update on novel trends in PET/CT technology and its clinical applications. *Br J Radiol.* 2018;89:20160534.
  24. Pijl JP, Londema M, Kwee TC, Nijsten MWN, Slart RHJA, Dierckx RAJO, et al. FDG-PET/CT in intensive care patients with bloodstream infection. *Crit Care.* 2021;25:1-12.
  25. Maiga AW, Deppen SA, Mercaldo SF, Blume JD, Montgomery C, Vaszar LT, et al. Assessment of fluorodeoxyglucose F18-Labeled positron emission tomography for diagnosis of high-Risk lung nodules. *JAMA Surg.* 2018;153:329-34.
  26. Torizuka T, Tanizaki Y, Kanno T, Futatsubashi M, Yoshikawa E, Okada H. Single 20-second acquisition of clinical feasibility for lung cancer. *J Nucl Med.* 2009;50:1579-84.
  27. Lu Y, Fontaine K, Mulnix T, Onofrey JA, Ren S, Panin V, et al. Respiratory motion compensation for PET/CT with motion gated PET data. *J Nucl Med.* 2018;59:1480-6.
  28. Lee JW, Kim S, Lee SM, Moon SH, Kim T. Detection of hepatic metastases using dual-time-point FDG PET/CT scans in patients with colorectal cancer. *Mol Imaging Biol.* 2011;13:565-72.
  29. Berg E, Gill H, Marik J, Ogasawara A, Williams S, van Dongen G, et al. Total-body PET and highly stable chelators together enable meaningful <sup>89</sup>Zr-antibody PET studies up to 30 days after injection. *J Nucl Med.* 2020;61:453-60.
  30. Boellaard R, Delgado-Bolton R, Oyen WJG, Giammarile F, Tatsch K, Eschner W, et al. FDG PET/CT: EANM procedure guidelines for tumour imaging: version 2.0. *Eur J Nucl Med Mol Imaging.* 2014;42:328-54.
  31. Weber WA. Use of PET for monitoring cancer therapy and for predicting outcome. *J Nucl Med.* 2005;46:983-95.
  32. Shankar LK, Hoffman JM, Bacharach S, Graham MM, Karp J, Lammertsma AA, et al. Consensus

- recommendations for the use of  $^{18}\text{F}$ -FDG PET as an indicator of therapeutic response in patients in National Cancer Institute Trials. *J Nucl Med.* 2006;47:1059-66.
33. Freedman NMT, Sundaram SK, Kurdziel K, Carrasquillo JA, Whatley M, Carson JM, et al. Comparison of SUV and Patlak slope for monitoring of cancer therapy using serial PET scans. *Eur J Nucl Med Mol Imaging.* 2003;30:46-53.
  34. Huang SC. Anatomy of SUV. *Nucl Med Biol.* 2000;27:643-6.
  35. Lammertsma AA, Hoekstra CJ, Giaccone G, Hoekstra OS. How should we analyse FDG PET studies for monitoring tumour response? *Eur J Nucl Med Mol Imaging.* 2006;33:S16-21.
  36. Karakatsanis NA, Lodge MA, Tahari AK, Zhou Y, Wahl RL, Rahmim A. Dynamic whole body PET parametric imaging: I. Concept, acquisition protocol optimization and clinical application Nicolas. *Phys Med Biol.* 2014;49:1012-6.
  37. Karakatsanis NA, Zhou Y, Lodge MA, Casey ME, Wahl RL, Zaidi H, et al. Generalized whole-body patlak parametric imaging for enhanced quantification in clinical PET. *Phys Med Biol.* 2015;60:8643-73.
  38. Patlak CS, Blasberg RG. Graphical evaluation of blood-to-brain transfer constants from multiple-time uptake data. Generalizations. *J Cereb Blood Flow Metab.* 1985;5:584-90.
  39. Yaqub M, Bahce I, Voorhoeve C, Schuit RC, Windhorst AD, Hoekstra OS, et al. Quantitative and simplified analysis of  $^{11}\text{C}$ -erlotinib studies. *J Nucl Med.* 2016;57:861-6.
  40. Dagogo-jack I, Shaw AT. Tumour heterogeneity and resistance to cancer therapies. *Nat Publ Gr.* 2017;15:81-94.
  41. Borghammer P, van den Berge N. Brain-first versus gut-first Parkinson's disease: a hypothesis. *J Parkinsons Dis.* 2019;9:S281-95.
  42. Willyard BC. How gut bacteria alter the brain. *Nature.* 2006;590:22-5.
  43. Zhu S, Jiang Y, Xu K, Cui M, Ye W, Zhao G, et al. The progress of gut microbiome research related to brain disorders. *J Neuroinflammation.* 2020;17:1-20.
  44. Klingelhoef L, Reichmann H. Pathogenesis of Parkinson disease - the gut - brain axis and environmental factors. *Nat Publ Gr.* 2015;11:625-36.
  45. Wang H, Liu JS, Peng SH, Deng XY, Zhu DM, Javidiparsijani S, et al. Gut-lung crosstalk in pulmonary involvement with inflammatory bowel diseases. *World J Gastroenterol.* 2013;19:6794-804.
  46. Cvetkovic L, Régis C, Richard C, Derosa L, Leblond A, Malo J, et al. Physiologic colonic uptake of  $^{18}\text{F}$ -FDG on PET/CT is associated with clinical response and gut microbiome composition in patients with advanced non-small cell lung cancer treated with immune checkpoint inhibitors. *Eur J Nucl Med Mol Imaging.* 2021;48:1550-9.
  47. d'Ettorre G, Ceccarelli G, Marazzato M, Campagna G, Pinacchio C, Alessandri F, et al. Challenges in the management of SARS-CoV2 Infection: the role of oral bacteriotherapy as complementary therapeutic strategy to avoid the progression of COVID-19. *Front Med.* 2020;7:1-7.
  48. Di Renzo L, Gualtieri P, Pivari F, Soldati L, Attinà A, Leggeri C, et al. COVID-19: is there a role for immunonutrition in obese patient? *J Transl Med.* 2020;18:1-22.
  49. Crawford MS, Nordgren TM, McCole DF. Every breath you take: impacts of environmental

- dust exposure on intestinal barrier function-from the gut-lung axis to COVID-19. *Am J Physiol - Gastrointest Liver Physiol.* 2021;320:G586-600.
50. Dang AT, Marsland BJ. Microbes, metabolites, and the gut-lung axis. *Mucosal Immunol.* 2019;12:843-50.
  51. Segarra AB, Prieto I, Ramírez-Sánchez M. Is there a link between depression, neurochemical asymmetry and cardiovascular function? *AIMS Neurosci.* 2020;7:360-72.
  52. Werner RA, Hess A, Koenig T, Diekmann J, Derlin T, Melk A, et al. Theranostics Molecular imaging of inflammation crosstalk along the cardio-renal axis following acute myocardial infarction. *Theranostics.* 2021;11:7984-94.
  53. Battaglini D, Robba C, Lopes A, Samary S, Silva PL, Pizzol FD, et al. Brain-heart interaction after acute ischemic stroke. *Crit Care.* 2020;24:1-12.
  54. Lecoq P, Morel C, Prior JO, Visvikis D, Gundacker S, Auffray E, et al. Roadmap toward the 10 ps time-of-flight PET challenge. *Phys Med Biol.* 2021;65:1-94.
  55. Daube-witherspoon, Margaret E Viswanath V, Werner ME, Karp JS. Performance characteristics of long axial field-of-view scanners with axial gaps. *IEEE Trans Radiat Plasma Med Sci.* 2022;5:322-30.
  56. Conti M. Why is TOF PET reconstruction a more robust method in the presence of inconsistent data? *Phys Med Biol.* 2011;56:155-68.
  57. Zhang J, Knopp MI, Knopp M V. Sparse Detector Configuration in SiPM Digital Photon Counting PET: a Feasibility Study. *Mol Imaging Biol.* 2019;21:447-53.
  58. Stockhoff M, Decuyper M, Van Holen R, Vandenberghe S. High-resolution monolithic LYSO detector with 6-layer depth-of-interaction for clinical PET. *Phys Med Biol.* 2021;66: 155014.
  59. Lamprou E, Gonzalez AJ, Sanchez F, Benlloch JM. Exploring TOF capabilities of PET detector blocks based on large monolithic crystals and analog SiPMs. *Phys Medica.* 2020;70:10-8.
  60. Van Dam HT, Borghi G, Seifert S, Schaart DR. Sub-200 ps CRT in monolithic scintillator PET detectors using digital SiPM arrays and maximum likelihood interaction time estimation. *Phys Med Biol.* 2013;58:3243-57.
  61. Di Francesco A, Bugalho R, Oliveira L, Pacher L, Rivetti A, Rolo M, et al. TOFPET2: a high-performance ASIC for time and amplitude measurements of SiPM signals in time-of-flight applications. *J Instrum.* 2016;11:C03042.
  62. Lamprou E, Gonzalez-Montoro A, Canizares G, Ilisie V, Barrio J, Sanchez F, et al. Characterization of TOF-PET detectors based on monolithic blocks and ASIC-readout. *arXiv:1806.08715.* 2018;3-6.
  63. Jamil A, Ziegler T, Hufschmidt P, Li G, Michel T, Ostrovskiy I, et al. VUV-sensitive silicon photomultipliers for xenon scintillation light detection in nEXO. *IEEE Trans Nucl Sci.* 2018;65:2823-33.
  64. Renner J, Romo-Luque C, Aliaga RJ, Álvarez V, Ballester F, Benlloch-Rodríguez JM, et al. Monte Carlo characterization of PETALO, a full-body liquid xenon-based PET detector. *J Instrum.* 2022;17:P05044.
  65. Gomez-Cadenas JJ, Benlloch-Rodríguez JM, Ferrario P, Monrabal F, Rodríguez J, Toledo JF.

- Investigation of the coincidence resolving time performance of a PET scanner based on liquid xenon: a Monte Carlo study. arXiv:1604.04106. 2016;11.
66. Zhu R-Y. Presentation on CEPC Crystal Calorimetry. Topical workshop on the CEPC Calorimetry, Beijing, China. 2019. Available from: [http://www.hep.caltech.edu/~zhu/talks/ryz\\_190314\\_CEPC\\_summary.pdf](http://www.hep.caltech.edu/~zhu/talks/ryz_190314_CEPC_summary.pdf)
  67. Moskal P, Kowalski P, Shopa RY, Raczyński L, Baran J, Chug N, et al. Simulating NEMA characteristics of the modular total-body J-PET scanner - An economic total-body PET from plastic scintillators. *Phys Med Biol.* 2021;66:175015
  68. Moskal P, Stępień E. Prospects and clinical perspectives of total-body PET imaging using plastic scintillators. *PET Clin.* 2020;15:439-52.
  69. Gajos A, Kaminska D, Moskal P, Czerwiński E. Method for reconstructing multi-tracer metabolic and morpho-metric images and tomography system for multi-tracer metabolic and morphometric imaging. Patent number: US 10339676, 2017.
  70. Moskal P, Kisielewska D, Curceanu C, Czerwiński E, Dulski K, Gajos A, et al. Feasibility study of the positronium imaging with the J-PET tomograph. *Phys Med Biol.* 2019;64:055017.
  71. Moskal P, Moskal I, Moskal G. A TOF-PET tomograph and a method of imaging using a TOF-PET tomograph, based on a probability of production and lifetime of a positronium. Patent number: WO 2015/028604 A1. 2015.
  72. Miyata M, Tomita H, Watanabe K, Kawarabayashi J, Iguchi T. Development of TOF-PET using Cherenkov Radiation. *Journal of Nuclear Science and Technology.* 206;43:339-343.
  73. Ooba T, Fukushima T, Kawai H, Konishi M. Proposal of Cherenkov TOFPET with Silica Aerogel. *IEEE* 2004;6:3781-3784.
  74. Gonzalez-Montoro A, Pourashraf S, Cates JW, Levin CS. Cherenkov radiation-based coincidence time resolution measurements in BGO scintillators. *Front Phys.* 2022;10:1-12.
  75. AFBR-S4N33C013 NUV-HD Single silicon photomultiplier data sheet. Available from: <https://www.broadcom.com/products/optical-sensors/silicon-photomultiplier-sipm/afbr-s4n33c013>
  76. Gola A, Acerbi F, Capasso M, Marcante M, Mazzi A, Paternoster G, et al. NUV-sensitive silicon photomultiplier technologies developed at fondazione Bruno Kessler. *Sensors.* 2019;9:308.
  77. van Sluis J, de Jong JR, Schaar J, Noordzij W, van Snick JH, Dierckx RAJO, et al. Performance characteristics of the digital Biograph Vision PET/CT system. *J Nucl Med.* 2019;60:1031-6.
  78. Rausch I, Ruiz A, Valverde-Pascual I, Cal-González J, Beyer T, Carrio I. Performance evaluation of the Philips Vereos PET/CT System according to the NEMA NU2-2012 standard. *J Nucl Med.* 2018;60:561-7.



# Chapter 12

---

## Summary



The most specific and sensitive imaging modality for visualizing and measuring human (patho)physiology *in vivo* is Positron Emission Tomography (PET). PET is a firmly established biomedical imaging modality with applications in routine clinical diagnostic imaging, but also in research, including clinical trials. Over the past few years, decades of PET technology development brought new innovative PET systems to the commercial market: silicon photomultiplier (SiPM)-based or ‘digital’ PET/CT systems and long axial field-of-view (LAFOV) or ‘total body’ PET/CT systems. This thesis describes the recent innovations which, in the (near) future, can further realize the full potential of PET. A summary of the thesis is provided in the current chapter.

Continuing on the introduction, the technical principles regarding digital PET/CT systems, a summary of the performance characteristics of the three different commercially available systems, and the resulting image quality, lesion detectability, and possibilities to reduce scan duration and/or lower the amount of radiotracer administration are described in **Chapter 2**. Over the past decades, the main development in PET technology has been detector design, specifically the adoption of solid-state technology. This led to the replacement of conventional photomultiplier tubes (PMTs) with compact detector elements commonly referred to as SiPMs. At present, three PET/CT systems equipped with SiPM-based detectors have been introduced onto the commercial market. These so-called digital PET/CT systems are the Philips Vereos PET/CT (Philips Healthcare), the Siemens Biograph Vision PET/CT (Siemens Healthineers), and the GE Discovery MI PET/CT (General Electric Healthcare). With their improved performance characteristics, better image quality is obtained with respect to conventional PMT equipped systems. Enhanced image quality leads to improved lesion detectability and possibilities to reduce scan duration for a higher patient throughput and/or lower the amount of injected radiotracer to reduce radiation exposure.

Taking a step back to the start of introducing a new PET/CT system to the clinics and the technical and clinical validation this process requires, **Chapter 3** focuses on the technical validation of the, worldwide first, installation of the digital SiPM-based Biograph Vision PET/CT at the University Medical Center Groningen in 2018. PET/CT system performance conform the NEMA NU 2-2012 standard with additional measurements described in the (at the time of study still unpublished) NEMA NU 2-2018 standard was explored. Results from phantom measurements were directly compared to results from its analog predecessor, the PMT-based Biograph mCT PET/CT (Siemens Healthineers), found in existing literature. Spatial resolution, sensitivity, count rate performance, accuracy of attenuation and scatter correction, time-of-flight (ToF) performance, image quality, and coregistration accuracy were

determined. Moreover, feasibility to comply with the European Association of Nuclear Medicine (EANM) Research Ltd (EARL) criteria was evaluated and some illustrative first patient PET images were shown. The main results reported in this chapter were a transverse (respectively axial) spatial resolution at full width half maximum (FWHM) of 3.6 mm (respectively 3.5 mm) at 1 cm offset of the center of the field-of-view (FOV) (measured with a  $^{22}\text{Na}$  0.25 mm diameter point-source), a sensitivity of 16.4 kcps/MBq, and a NEMA peak noise-equivalent count rate (NECR) of 306 kcps at 32.6 kBq/mL. ToF resolution varied from 210 to 215 as count rate increased up to the peak NECR. The overall image contrast seen with the NEMA image quality phantom ranged from 77.2% to 89.8%. Furthermore, the system was able to comply with EARL standards 1 and 2 performance criteria. From comparison with performance characteristics of its analog predecessor reported in literature, it was concluded that the Biograph Vision PET/CT outperforms the Biograph mCT PET/CT and the new system is able to meet European harmonizing performance standards.

Following technical validation of a newly installed PET/CT system with phantom measurements comes clinical validation and first experiences of the reading nuclear medicine physicians required to work with the new system in daily clinical routine. Therefore, **Chapter 4** evaluates initial clinical experiences with the digital Biograph Vision PET/CT in terms of perceived image quality and semiquantitative analysis in comparison with the Biograph mCT PET/CT. To this aim, 20 oncological patients received a single  $^{18}\text{F}$ -FDG injection and underwent a dual PET/CT imaging protocol, including a scan with equal scan duration and similar reconstruction settings, on both systems. Various reconstruction settings were used to obtain differently reconstructed images: one with optimized image quality for image reading and one compliant to EARL standards 1 for PET image harmonization. The clinically optimized images were blindly reviewed by three nuclear medicine physicians regarding tumor lesion demarcation, overall image quality, and image noise. In addition, these clinically optimized images were used for semiquantitative analysis; measurement of standardized uptake values (SUVs) in tumor lesions. Images compliant to EARL standards 1 specifications were also used for measurements of SUVs in tumor lesions and healthy tissues for comparison between systems. This study showed a significantly higher appreciation of tumor lesion demarcation, overall image quality, and image noise in images acquired on the Biograph Vision in comparison with images acquired on the Biograph mCT. The overall inter-reader agreement was substantial with a Fleiss  $\kappa$  of 0.61. Furthermore, the measured SUVs in tumor lesions and healthy tissues were comparable between PET/CT systems, in particular when using EARL-compliant reconstructions on both systems. The initial clinical

experiences comparing the new Biograph Vision PET/CT with the conventional Biograph mCT system showed higher appreciation of lesion demarcation, overall image quality and signal-to-noise ratio when using the digital Biograph Vision PET/CT. Moreover, regarding semiquantitative performance, we showed that the two systems were comparable for assessing quantitative PET imaging biomarkers in tumor lesions and healthy tissues.

Now that the newly introduced system was validated and declared ready for clinical use, possibilities of reducing scan duration and/or reducing the amount of injected activity were explored in **Chapter 5**. Previous chapters showed improved technical performance and increased visually assessed image quality with the new system while keeping scan duration equal to settings that are used on the conventional Biograph mCT. The improved performance of the Biograph Vision PET/CT could allow for a reduction in activity administration and/or scan duration. Therefore, this study aimed to evaluate the effects of reduced scan duration in  $^{18}\text{F}$ -FDG PET imaging on semiquantitative and subjective imaging parameters and its influence on clinical image reading. Therefore, 30 patients referred for a clinical PET/CT scan were enrolled in this study, received a weight-based  $^{18}\text{F}$ -FDG injected activity, and underwent a 180 seconds per bed position (s/bp) listmode PET acquisition. The acquired PET data were reconstructed using various reconstruction settings including the clinically optimized settings for image reading, the clinically optimized reconstruction protocol with additional 2 mm FWHM Gaussian filtering, as well as using EARL standards 1 and 2 compliant reconstruction settings. Additionally, PET data were reprocessed to obtain various shorter scan durations: 120, 60, 30, and 10 s/bp. The obtained images were semiquantitatively assessed for comparison of SUVs and noise, and clinically optimized images were qualitatively evaluated by three nuclear medicine physicians. The main results of this study included significant differences in lesion  $\text{SUV}_{\text{max}}$  between the 180 s/bp images and the 30 and 10 s/bp images reconstructed with clinically optimized settings, whereas no differences were found in lesion  $\text{SUV}_{\text{peak}}$ . EARL-compliant images did not show differences in lesion  $\text{SUV}_{\text{max}}$  or  $\text{SUV}_{\text{peak}}$  between scan durations. Because semiquantitative parameters deviated only marginally ( $\sim 5\%$ ) in the 60 s/bp images reconstructed according to the clinically optimized protocol, further subjective image quality assessment was conducted using the 60 s/bp images. Qualitative assessment revealed the influence of personal preference on physicians' willingness to adopt the 60 s/bp images in clinical practice. Although quantitative PET parameters differed minimally, an increase in noise was observed. From these findings it was concluded that using the Biograph Vision PET/CT for  $^{18}\text{F}$ -FDG imaging, scan duration and/or activity administration could be reduced by a factor of 3 or more when using the clinically optimized

---

reconstruction settings with additional 2 mm FWHM Gaussian filtering or EARL-compliant reconstruction protocols, respectively.

Up to now, the tracer used in the studies throughout this thesis has been  $^{18}\text{F}$ -FDG. The next two chapters will focus on PET imaging using the long-lived isotope  $^{89}\text{Zr}$ , labeled with monoclonal antibodies (mAb), i.e., immunoPET. **Chapter 6** compares image quality between images obtained using the new Biograph Vision PET/CT and the conventional Biograph mCT PET/CT using different  $^{89}\text{Zr}$ -labeled mAb PET tracers. Because the long half-life of these tracers results in high radiation exposure, the amount of injected  $^{89}\text{Zr}$  activity is relatively low compared to  $^{18}\text{F}$ -FDG. Coupled with the low positron abundance, poor count statistics are associated with  $^{89}\text{Zr}$  immunoPET imaging. In addition, scan duration optimization was explored using the new digital PET system. For the initial comparison between systems, semiquantitative performance was investigated including patient data of 5 patients who underwent immunoPET imaging on both systems with equal scan duration and similar reconstruction settings; one clinically optimized reconstruction protocol was used for both systems as well as EARL standards 1 and 2 reconstruction settings. Obtained images were semiquantitatively analyzed through segmentation of tumor lesions and healthy tissues. Furthermore, PET data of 10 additional patients solely obtained on the Biograph Vision PET/CT to study the effects of reducing scan duration on semiquantitative imaging parameters and its influence on visual image quality assessment was evaluated. To this aim, listmode PET data were reprocessed to obtain images at shorter scan durations, tumor lesions and healthy tissues were semiquantitatively analyzed per dataset, and image quality was visually evaluated by three nuclear medicine physicians. Results included comparable semiquantitative performance between systems at full scan duration; results remained comparable even when reducing scan duration on the Biograph Vision system to 75% and 50% when applying EARL standards 1 reconstruction settings. Hence, the conclusion of this study was that scan duration of  $^{89}\text{Zr}$  immunoPET can be reduced up to 50% whilst maintaining adequate image quality for diagnostic image reading and semiquantitative performance using EARL standards 1 compliant reconstruction settings.

In 2021, the University Medical Center Groningen, having a strong interest in imaging technology innovations, installed one of the first LAFOV Biograph Vision Quadra PET/CT systems. To provide the nuclear medicine field with a first impression of the improved image quality such a high-sensitivity system can provide when using long-lived radiotracers with poor count statistics, **Chapter 7** illustrates  $^{89}\text{Zr}$  immunoPET images of two patients obtained with the Biograph Vision Quadra PET/CT. For a

complete overview, and a direct comparison of image quality, these two patients underwent a dual imaging protocol including one scan on the LAFOV Biograph Vision Quadra and the other scan on either the conventional analog Biograph mCT or the digital Biograph Vision PET/CT system. Patients were scanned 4 days postinjection (p.i.) according to local clinical standard operating procedures with overall scan durations of 45 min and approximately 30 min, for, respectively, the Biograph mCT and Biograph Vision. Following the standard clinical scans, additional imaging was performed on the LAFOV Biograph Vision Quadra system. A scan duration of approximately 30 min, equal to the procedure on the Biograph Vision system, was used to showcase improved image quality. Image reconstruction settings were EARL 1 standard compliant, but for the LAFOV system, also clinically optimized reconstruction settings for optimal image quality were applied. Furthermore, LAFOV listmode PET data were reprocessed to obtain additional images with shorter scan durations (10 min and 3 min) to illustrate image quality at more clinically pragmatic scan durations. The images show that the LAFOV system provides substantial improvement in visually assessed image quality and, a first impression of, still very acceptable image quality with reduced scan durations.

To facilitate multicenter research and harmonized clinical use of the LAFOV Biograph Vision Quadra PET/CT system together with other conventional systems, compliance of the system to current EARL specifications for  $^{18}\text{F}$ -FDG tumor imaging (specified for conventional 20-25 cm axial FOV PET systems) was explored in **Chapter 8**. Here, EARL phantom measurements were performed, with additional tests at various locations throughout the LAFOV, and the use of shorter scan durations. EARL compliance phantom measurements were performed using the NEMA image quality phantom, both in the center and at various locations throughout the LAFOV. PET data were reconstructed using various reconstruction settings and reprocessed to obtain images at different scan durations: 60, 120, 240, and 420 s. Maximum, mean, and peak activity concentration recovery coefficients were obtained for each sphere and compared with the EARL standards specifications. Furthermore, clinical PET data of 10 oncological patients were collected to further explore and validate the effects of reducing scan duration on semiquantitative PET image biomarker accuracy and precision when using EARL-compliant reconstruction settings. Clinical PET data were acquired using 10 min total scan duration, reconstructed using the EARL standards 1 and 2 compliant reconstruction settings, resulting from the phantom data analysis, as well as using clinically optimized reconstruction settings for optimal image quality. A portion of these data were also reprocessed to obtain additional images with shorter scan durations: 60, 120, 240, and 420 s. For each clinical dataset, healthy tissue and tumor lesions were semiquantitatively analyzed and noise levels

were characterized. This study showed EARL compliance of the Biograph Vision Quadra PET/CT for all positions throughout the LAFOV for all scan durations. Regarding patient data, EARL-compliant images showed no significant differences in healthy tissue or lesion SUV, and noise levels only varied slightly. From these findings it was concluded that while adhering to EARL specifications, scan duration and/or activity administration in  $^{18}\text{F}$ -FDG PET imaging can be reduced up to a factor of 10 without interference of increased noise using the LAFOV Biograph Vision Quadra PET/CT.

So far, this thesis mainly included static imaging and semiquantification using the simplified SUV metric; very pragmatic and directly applicable in clinical practice. SUV derived from static images obtained at 60 minutes p.i., is most commonly used as a surrogate of metabolic activity for tumor uptake quantification. Following standardization methods such as the EANM procedure guidelines for tumor imaging regarding patient preparation, PET image acquisition and reconstruction settings, and analysis methods can mitigate SUV variability to a great extent. However, these standardization methods are not able to account for changes in plasma kinetics, due to e.g., treatment, and there is no distinction between specific and nonspecific uptake possibly causing a dissociation between inaccurate SUV measurements and actual tumor metabolic activity. These issues can be overcome by dynamic  $^{18}\text{F}$ -FDG whole body (Patlak) imaging, therefore **Chapter 9** focuses on this full quantitative imaging method. This procedure, however, can take a total examination time of up to 75 min including the time needed for patient positioning and CT scanning. Hence, this study aims to reduce the total examination time of dynamic  $^{18}\text{F}$ -FDG whole body (Patlak) imaging, with data simulations, from up to 75 min to 30-60 min p.i. using a population-averaged input function (PIF). A representative input function (IF) from previously acquired data was used as the PIF, and rate constants  $K_1$ ,  $k_2$ , and  $k_3$  were based on existing literature. Various time-activity curves (TACs) were simulated. Variations included multiplication of the IF with a positive and negative gradual linear bias over 60 min of 5, 10, 15, 20, and 25% (generating TACs using an IF different from the PIF); use of rate constants ( $K_1$ ,  $k_3$ , and both  $K_1$  and  $k_2$ ) multiplied by 2, 1.5, and 0.75; and addition of noise ( $\mu = 0$  and  $\sigma = 5, 10$  and 15%). Subsequent Patlak analysis using the original IF (representing the PIF) was used to obtain the net influx constant ( $K_i$ ) for the differently simulated TACs. Next, the PIF was scaled towards the (simulated) IF value using the 30-60-min p.i. time interval, simulating scaling of the PIF to image-derived values. Influence of variabilities in IF and rate constants, and rescaling the PIF on bias in  $K_i$  were evaluated. Percentage bias in  $K_i$  observed using simulated modified IFs varied from -16 to 16% depending on the simulated amplitude and direction of the IF modifications. Subsequent scaling of the

PIF reduced these  $K_i$  biases in most cases (287 out of 290) to <5%. From these results it was concluded that the conducted simulations in this study suggest that scaling of a (possibly incorrect) PIF to IF values seen in whole body dynamic imaging from 30 to 60 min p.i. can provide accurate  $K_i$  estimates. This indicates that dynamic Patlak imaging protocols may be performed for 30-60 min p.i. making whole body Patlak imaging more clinically feasible.

**Chapter 10** continues on the previous chapter by validating the use of a PIF to reduce examination time of the dynamic  $^{18}\text{F}$ -FDG whole body (Patlak) imaging procedure with dynamic whole body  $^{18}\text{F}$ -FDG PET data obtained using the LAFOV Biograph Vision Quadra PET/CT system. To this aim, 12 patients with suspected lung malignancy were included and underwent a 65-min dynamic PET acquisition. Full quantitative Patlak analysis was performed on both the entire 65 min scans, as well as on various shortened scan duration intervals p.i. using a PIF for scaling; analysis results from the full 65 min were compared to the results obtained using shorter scan duration intervals p.i. Included shortened scan durations were 30-60, 40-60, and 50-60 min p.i. Volumes of interest were placed in the ascending aorta and in the left ventricle of the heart to obtain image derived IFs (IDIFs). Subsequently, the PIF was scaled to AA and LV IDIF values at 30-60, 40-60, and 50-60 min p.i., respectively, and parametric  $^{18}\text{F}$ -FDG  $K_i$  images were generated. In the obtained  $K_i$  images, tumor lesions as well as healthy tissues were segmented. Results showed that  $K_i$  only varied marginally (~2%) between the IDIF obtained from the ascending aorta versus the left ventricle of the heart. Further analyses were therefore continued with only the IDIF obtained from the ascending aorta. Good agreement between the IDIF and corresponding PIF scaled to 30-60 min p.i. and 40-60 min p.i. was obtained with less than 8% deviation in  $K_i$ . Bland-Altman analyses confirmed the good agreement in  $K_i$  between the IDIF and corresponding PIF scaled to various shortened scan time intervals p.i. The conclusion of this study was that parametric whole body  $^{18}\text{F}$ -FDG Patlak  $K_i$  images can be generated non-invasively on a Biograph Vision Quadra system. In addition, using a scaled PIF allows for a substantial (factor 2 to 3) reduction in scan time without loss of accuracy (<8%) and precision (image quality and noise interference).

To conclude the summary of the work described in this thesis, **Chapter 11** discusses potential future clinical and research directions, potential developments in photon detection technology, and (more cost-effective) hardware developments in PET detectors.

LAFOV PET is the newest technological development in (molecular) imaging

instrumentation. Its improved sensitivity provides many unique opportunities that were not available before, e.g., improved image quality, opportunities to substantially reduce dose and/or scan duration, improved accuracy in monitoring and predicting treatment response, and a means to study molecular interactions between organs. It is expected that this generation of scanners will significantly advance the field of nuclear medicine and molecular imaging in the near future.



# Chapter 13

---

Nederlandse samenvatting



De meest specifieke en gevoelige beeldvormende techniek voor het *in vivo* visualiseren en meten van (patho)fysiologische processen is Positron Emissie Tomografie (PET). PET is een erkende biomedische beeldvormende techniek met toepassingen in routinematige klinische diagnostische beeldvorming, maar ook in onderzoek, inclusief klinische trials. Tientallen jaren van PET technologie ontwikkeling hebben zich de laatste jaren vertaald in de introductie van nieuwe innovatieve PET systemen op de commerciële markt: op silicon photomultipliers (SiPM) gebaseerde ofwel 'digitale' PET/CT systemen en long axial field-of-view (LAFOV) ofwel 'total body' PET/CT-systemen. Dit proefschrift beschrijft de recente innovaties die in de (nabije) toekomst het volledige potentieel van PET verder kunnen realiseren. Een samenvatting van het proefschrift is te vinden in het huidige hoofdstuk.

Voortbordurend op de inleiding worden in **Hoofdstuk 2** de technische principes met betrekking tot digitale PET/CT systemen beschreven, tevens bevat het hoofdstuk een samenvatting van de prestatiekenmerken van de drie verschillende commercieel verkrijgbare systemen en de resulterende beeldkwaliteit, laesiedetectie prestaties en mogelijkheden om de scanduur te verkorten en/of de hoeveelheid toegediende radiotracer te verlagen. In de afgelopen decennia was de belangrijkste ontwikkeling in PET technologie het detector ontwerp, met name de toepassing van solid-state technologie. Dit leidde tot de vervanging van conventionele photomultiplier tubes (PMTs) door compacte detectorelementen, SiPMs welteverstaan. Op dit moment zijn er drie PET/CT systemen uitgerust met op SiPMs gebaseerde detectoren commercieel verkrijgbaar. Deze zogenaamde digitale PET/CT systemen zijn de Philips Vereos PET/CT (Philips Healthcare), de Siemens Biograph Vision PET/CT (Siemens Healthineers) en de GE Discovery MI PET/CT (General Electric Healthcare). Met hun verbeterde prestaties wordt een betere beeldkwaliteit verkregen in vergelijking met conventionele met PMTs uitgeruste systemen. Verbeterde beeldkwaliteit leidt tot verbeterde detecteerbaarheid van laesies. Tevens bieden verbeteringen in prestaties mogelijkheden om de scanduur te verkorten, voor een hogere patiëntdoorvoer, en/of om de hoeveelheid geïnjecteerde radiotracer te verlagen, om de blootstelling aan radioactieve straling te verminderen.

Wanneer we een stap terug nemen naar het begin van de introductie van een nieuw PET/CT systeem in de kliniek en de bijbehorende technische en klinische validatie die dit proces vereist, richt **Hoofdstuk 3** zich op de technische validatie van de wereldwijd allereerste installatie van de digitale op SiPMs gebaseerde Biograph Vision PET/CT in het Universitair Medisch Centrum Groningen in 2018. De prestaties van het PET/CT systeem zijn getest en beschreven conform de NEMA NU 2-2012 standaard met aanvullende metingen beschreven in de (op het moment van

uitvoering van het onderzoek nog niet gepubliceerde) NEMA NU 2-2018 standaard. Resultaten van fantoomproeven werden direct vergeleken met resultaten van zijn analoge voorganger, de op PMTs gebaseerde Biograph mCT PET/CT (Siemens Healthineers), verkregen uit bestaande literatuur. Spatiële resolutie, gevoeligheid, count rate prestaties, nauwkeurigheid van attenuatie en scatter correctie, time-of-flight (ToF) prestaties, beeldkwaliteit en nauwkeurigheid van co-registratie werden bepaald. Bovendien werden mogelijkheden om te voldoen aan PET standaardisatie en harmonisatie criteria van de European Association of Nuclear Medicine (EANM) Research Ltd (EARL) geëvalueerd en werden enkele illustratieve PET beelden van de eerste patiënten getoond. De belangrijkste resultaten die in dit hoofdstuk worden gerapporteerd zijn een transversale (respectievelijk axiale) spatiële resolutie at full width half maximum (FWHM) van 3,6 mm (respectievelijk 3,5 mm) op 1 cm offset van het midden van het field-of-view (FOV) (gemeten met een  $^{22}\text{Na}$  puntbron van 0,25 mm diameter), een gevoeligheid van 16,4 kcps/MBq en een NEMA peak noise-equivalent count rate (NECR) van 306 kcps bij 32,6 kBq/ml. De ToF resolutie varieerde van 210 tot 215 naarmate de count rate toenam tot de peak NECR. Het algehele beeldcontrast dat werd waargenomen met het NEMA IQ fantoom varieerde van 77,2% tot 89,8%. Bovendien kon het systeem voldoen aan de prestatiecriteria van de EARL 1 en 2 normen. Vergeleken met de prestaties van de analoge voorganger PET/CT systeem, gerapporteerd in de literatuur, werd geconcludeerd dat de Biograph Vision PET/CT beter presteert dan de Biograph mCT PET/CT en dat het nieuwe systeem kan voldoen aan Europese standaardisatie en harmonisatie normen.

Na de technische validatie met fantoomproeven van een nieuw geïnstalleerd PET/CT systeem volgt de klinische validatie en onderzoek naar de eerste ervaringen van de beeld beoordelende nucleair geneeskundigen die in de dagelijkse klinische routine met de verkregen beelden moeten werken. Daarom evalueert **Hoofdstuk 4** de eerste klinische ervaringen met de digitale Biograph Vision PET/CT in termen van waargenomen beeldkwaliteit en semikwantitatieve analyse in vergelijking met de Biograph mCT PET/CT. Hiertoe kregen 20 oncologische patiënten een enkele injectie met  $^{18}\text{F}$ -FDG en ondergingen ze een dubbel PET/CT beeldvormingsprotocol; twee scans met gelijke scanduur en vergelijkbare reconstructie-instellingen, één op beide systemen. Er werden verschillende reconstructie-instellingen gebruikt om verschillend gereconstrueerde beelden te verkrijgen: één met geoptimaliseerde beeldkwaliteit voor het visueel beoordelen van de beelden (klinisch geoptimaliseerd) en één welke voldoet aan de EARL 1 norm voor geharmoniseerde PET beelden. De klinisch geoptimaliseerde beelden werden blind beoordeeld door drie nucleair geneeskundigen met betrekking tot de afgrenzing van tumorlaesies, de algehele beeldkwaliteit en beeldruis. Daarnaast werden deze klinisch geoptimaliseerde beelden

gebruikt voor semikwantitatieve analyse; meting van standardized uptake values (SUVs) in tumorlaesies. Beelden die voldoen aan EARL 1 specificaties werden ook gebruikt voor SUV metingen in tumorlaesies en gezonde weefsels voor vergelijking tussen systemen. Deze studie toonde een significant hogere waardering aan voor de afgrenzing van tumorlaesies, de algehele beeldkwaliteit en beeldruis van beelden verkregen met de Biograph Vision PET/CT in vergelijking met beelden verkregen met de Biograph mCT PET/CT. De overeenstemming tussen beeldbeoordelaars was voldoende tot goed met een Fleiss  $\kappa$  van 0,61. Bovendien waren de gemeten SUVs in tumorlaesies en gezonde weefsels vergelijkbaar tussen PET/CT systemen, met name bij gebruik van EARL 1 gereconstrueerde beelden van beide systemen. De eerste klinische ervaringen bij het vergelijken van de nieuwe Biograph Vision PET/CT met het conventionele Biograph mCT systeem toonden een hogere waardering van tumorlaesie afgrenzing, algehele beeldkwaliteit en visueel geïnterpreteerde signaalruisverhouding bij gebruik van de digitale Biograph Vision PET/CT. Bovendien toonden we met betrekking tot semikwantitatieve prestaties aan dat de twee systemen vergelijkbaar zijn in het verkrijgen van semikwantitatieve PET beeld biomarkers in tumorlaesies en gezonde weefsels.

Nu het nieuwe systeem zowel technisch gevalideerd is als gereed is verklaard voor klinisch gebruik, gaat **Hoofdstuk 5** verder met het onderzoek naar mogelijkheden om scanduur te verkorten en/of de hoeveelheid geïnjecteerde activiteit te verlagen. Eerdere hoofdstukken toonden verbeterde technische prestaties en verbeterde visueel beoordeelde beeldkwaliteit aan met de nieuwe digitale Biograph Vision PET/CT, terwijl de scanduur gelijk bleef aan de instellingen die worden gebruikt op de conventionele Biograph mCT PET/CT. De verbeterde prestaties van de Biograph Vision PET/CT kunnen een vermindering van de toediening van radioactieve tracer en/of scanduur mogelijk maken. Daarom was deze studie gericht op het evalueren van de effecten van verminderde scanduur bij PET beeldvorming met  $^{18}\text{F}$ -FDG op semikwantitatieve en subjectieve beeldparameters en de invloed ervan op klinische beeldbeoordeling. Hiertoe werden 30 patiënten, verwezen voor een klinische PET/CT scan, geïnccludeerd in deze studie. Zij kregen een op lichaamsgewicht gebaseerde injectie met  $^{18}\text{F}$ -FDG activiteit en ondergingen een listmode PET acquisitie van 180 seconden per bed positie (s/bp). De verkregen PET data werden gereconstrueerd met behulp van verschillende reconstructie-instellingen, waaronder instellingen voor geoptimaliseerde beeldkwaliteit ten behoeve van de klinische beeldbeoordeling (klinisch geoptimaliseerd), het klinisch geoptimaliseerde reconstructieprotocol met extra 2 mm FWHM Gauss-filter, evenals met reconstructie-instellingen conform de EARL 1 en 2 normen. Daarnaast werden verkregen PET data opnieuw verwerkt en gereconstrueerd om beelden met verschillende kortere scanduren te verkrijgen: 120,

60, 30 en 10 s/bp. De verkregen beelden werden semikwantitatief geanalyseerd voor vergelijking van SUVs en ruisniveau. De klinisch geoptimaliseerde beelden werden kwalitatief beoordeeld door drie nucleair geneeskundigen. De belangrijkste resultaten van deze studie waren significante verschillen in de  $SUV_{max}$  van tumor laesies tussen de 180 s/bp beelden en de 30 en 10 s/bp beelden gereconstrueerd met het klinisch geoptimaliseerde protocol, terwijl er geen verschillen werden gevonden in de tumor laesie  $SUV_{peak}$ . EARL-compatibele beelden lieten geen verschillen zien tussen scanduren in de  $SUV_{max}$  of  $SUV_{peak}$  van tumor laesies. Omdat semikwantitatieve parameters slechts marginaal (~5%) afweken in de 60 s/bp beelden ten opzichte van de 180 s/bp beelden gereconstrueerd volgens het klinisch geoptimaliseerde protocol, werd verdere subjectieve beoordeling van de beeldkwaliteit uitgevoerd tussen de 180 s/bp beelden in vergelijking met de 60 s/bp beelden. Kwalitatieve beoordeling liet invloed van persoonlijke voorkeur van de nucleair geneeskundigen zien op hun bereidwilligheid om de 60 s/bp beelden standaard in de klinische praktijk te gebruiken. Hoewel semikwantitatieve PET parameters minimaal verschilden, werd een toename in ruisniveau waargenomen. Uit deze bevindingen werd geconcludeerd dat bij gebruik van de Biograph Vision PET/CT, de scanduur en/of hoeveelheid toegediend radioactief  $^{18}F$ -FDG met een factor 3 of meer kan worden verminderd bij gebruik van de klinisch geoptimaliseerde reconstructie-instellingen met extra 2 mm Gauss-filter of de reconstructie-instellingen conform EARL.

Tot dusverre was  $^{18}F$ -FDG de radioactieve tracer gebruikt in de studies beschreven in dit proefschrift. De volgende twee hoofdstukken zullen zich richten op PET beeldvorming met behulp van de langlevende isotoop  $^{89}Zr$ , gelabeld met monoklonale antilichamen (mAb), ofwel immunoPET. **Hoofdstuk 6** vergelijkt de beeldkwaliteit tussen beelden verkregen met de nieuwe digitale Biograph Vision PET/CT en de conventionele Biograph mCT PET/CT, gebruikmakend van verschillende  $^{89}Zr$ -gelabelde mAb PET tracers. Omdat de lange halfwaardetijd van deze tracers resulteert in een hoge blootstelling aan radioactieve straling, is de hoeveelheid geïnjecteerde  $^{89}Zr$  activiteit relatief laag in vergelijking met  $^{18}F$ -FDG. In combinatie met de lage hoeveelheid aanwezige positronen, worden slechte count statistieken geassocieerd met  $^{89}Zr$  immunoPET beeldvorming. Naast de vergelijking in beeldkwaliteit tussen de twee genoemde scan systemen, werd scanduuroptimalisatie onderzocht bij gebruik van het nieuwe digitale PET systeem. Voor de eerste vergelijking tussen systemen werden semikwantitatieve prestaties onderzocht, hiertoe ondergingen 5 patiënten immunoPET beeldvorming op beide systemen met gelijke scanduur en vergelijkbare reconstructie-instellingen; één klinisch geoptimaliseerd reconstructieprotocol werd gebruikt evenals reconstructie-instellingen conform EARL 1 en 2 normen. De verkregen beelden werden semikwantitatief geanalyseerd door middel van

segmentatie van tumorlaesies en gezonde weefsels. Verder werden PET data geïncorporeerd van 10 extra patiënten, uitsluitend verkregen met de Biograph Vision PET/CT, om de effecten van het verkorten van de scanduur op semikwantitatieve beeldvormingsparameters en de invloed ervan op visueel geïnterpreteerde beeldkwaliteit te bestuderen. Hiertoe werden PET data in listmode opnieuw verwerkt en gereconstrueerd om extra beelden te verkrijgen met kortere scanduren, werden per dataset tumorlaesies en gezonde weefsels semikwantitatief geanalyseerd, en werd de beeldkwaliteit visueel beoordeeld door drie nucleair geneeskundigen. Resultaten omvatten vergelijkbare semikwantitatieve prestaties tussen systemen bij volledige scanduur. De resultaten bleven vergelijkbaar, zelfs wanneer de scanduur op de Biograph Vision werd teruggebracht tot 75% en 50% bij toepassing van de EARL 1 reconstructie-instellingen. De conclusie van dit onderzoek was dan ook dat de scanduur van  $^{89}\text{Zr}$  immunoPET met een factor 2 kan worden verminderd met behoud van voldoende beeldkwaliteit voor diagnostische beeldbeoordeling en semikwantitatieve analyses bij toepassing van reconstructie-instellingen die aan de EARL 1 normen voldoen.

In 2021 installeerde het Universitair Medisch Centrum Groningen, met een sterke interesse in innovaties op het gebied van beeldvormende technologie, één van de eerste LAFOV Biograph Vision Quadra PET/CT-systemen. Om het vakgebied van de nucleaire geneeskunde een eerste indruk te geven van de verbeterde beeldkwaliteit wat dit ultra-gevoelige systeem kan bieden bij gebruik van langlevende radiotracers met slechte count statistieken, worden illustratieve voorbeeld PET patiëntbeelden in **Hoofdstuk 7** weergegeven;  $^{89}\text{Zr}$  immunoPET beelden van twee patiënten verkregen met de Biograph Vision Quadra PET/CT. Voor een volledig overzicht en een directe vergelijking van de beeldkwaliteit in vergelijking met conventionele PET systemen ondergingen deze twee patiënten een dubbel PET/CT beeldvormingsprotocol, waaronder één scan op de LAFOV Biograph Vision Quadra en één andere scan op óf de conventionele analoge Biograph mCT óf de digitale Biograph Vision PET/CT. De patiënten werden 4 dagen na injectie (p.i.) gescand volgens lokale klinische standaard scanprocedures met een totale scanduur van 45 min en ongeveer 30 min, voor respectievelijk de Biograph mCT PET/CT en de Biograph Vision PET/CT. Na de standaard klinische scans werd aanvullende beeldvorming uitgevoerd op het LAFOV Biograph Vision Quadra systeem. Een scanduur van ongeveer 30 min, gelijk aan de procedure op de Biograph Vision, werd aangehouden om de verbeterde beeldkwaliteit te demonstreren. Beeld reconstructie-instellingen voldeden aan de EARL 1 norm, maar voor het LAFOV-systeem werden ook klinisch geoptimaliseerde reconstructie-instellingen voor optimale beeldkwaliteit toegepast. Daarnaast werden LAFOV listmode PET data opnieuw verwerkt en gereconstrueerd om extra beelden

te verkrijgen met kortere scanduren (10 min en 3 min); ter illustratie van de verkregen beeldkwaliteit bij meer pragmatische scanduren voor de dagelijkse kliniek. De beelden laten zien dat het LAFOV systeem voor een aanzienlijke verbetering van de visueel geïnterpreteerde beeldkwaliteit zorgt en daarnaast wordt er een eerste indruk gegeven van een zeer acceptabele beeldkwaliteit bij kortere scanduren.

Om multicenteronderzoek en geharmoniseerd klinisch gebruik van het LAFOV Biograph Vision Quadra PET/CT systeem samen met andere conventionele systemen mogelijk te maken, werd getest of de Biograph Vision Quadra aan huidige EARL criteria voor  $^{18}\text{F}$ -FDG tumorbeeldvorming (gespecificeerd voor conventionele 'korte' FOV PET-systemen) kan voldoen in **Hoofdstuk 8**. Hierin werden EARL fantoomproeven uitgevoerd met aanvullende proeven op verschillende locaties in het LAFOV en het gebruik van kortere scanduren. EARL fantoomproeven werden uitgevoerd met behulp van het NEMA IQ fantoom, zowel in het midden als op verschillende locaties in het LAFOV. PET data werden gereconstrueerd met behulp van verschillende reconstructie-instellingen en opnieuw verwerkt om extra beelden te verkrijgen met verschillende kortere scanduren: 60, 120, 240 en 420 s. Max, peak en mean recoverycoëfficiënten voor de activiteit per bol in het fantoom werden verkregen en vergeleken met de specificaties van de EARL 1 en 2 normen. Verder werden klinische PET data van 10 oncologische patiënten verzameld om de effecten van verkorte scanduur en/of verlaagde hoeveelheid toegediende activiteit op de nauwkeurigheid en precisie van semikwantitatieve PET beeldbiomarkers verder te onderzoeken en te valideren bij gebruik van EARL reconstructie-instellingen. Klinische PET patiënten data werden verkregen met een totale scanduur van 10 minuten, gereconstrueerd met reconstructie-instellingen die aan EARL 1 en 2 criteria voldoen, vastgesteld met behulp van de eerdere fantoomproeven, evenals met klinisch geoptimaliseerde reconstructie-instellingen voor optimale beeldkwaliteit. Deze data werden ook opnieuw verwerkt om extra beelden te verkrijgen met kortere scanduren: 60, 120, 240 en 420 s. Voor elke klinische dataset werden gezonde weefsels en tumorlaesies semikwantitatief geanalyseerd en werden de ruisniveaus gekarakteriseerd. Deze studie toonde dat het nieuwe systeem kan voldoen aan Europese harmoniserende prestatienormen voor alle posities in het LAFOV voor alle scanduren. Met betrekking tot de patiënten data toonden EARL-compatibele beelden geen significante verschillen in gezond weefsel of tumorlaesie SUVs en de ruisniveaus varieerden slechts gering. Uit deze bevindingen werd geconcludeerd dat door gebruik te maken van de EARL reconstructie-instellingen, de scanduur en/of hoeveelheid toegediende  $^{18}\text{F}$ -FDG activiteit met een factor 10 kan worden verlaagd zonder invloed van verhoogde ruis met behulp van het LAFOV Biograph Vision Quadra PET/CT systeem.

Tot dusverre omvatte dit proefschrift voornamelijk eenvoudige statische beeldvorming en semikwantificering met behulp van de vereenvoudigde SUV methode; zeer pragmatisch en direct toepasbaar in de klinische praktijk. SUV afgeleid van statische beelden verkregen bij 60 minuten p.i., wordt gebruikt als een surrogaat van metabole activiteit voor kwantificering van tumoropname. Het volgen van standaardisatiemethoden zoals de EANM procedurerichtlijnen voor tumorbeeldvorming met betrekking tot patiëntvoorbereiding, PET beeldacquisitie en reconstructie-instellingen, en analysemethoden kunnen SUV variabiliteit in grote mate verminderen. Deze standaardisatiemethoden houden echter geen rekening met veranderingen in de plasmakinetiek, bijvoorbeeld door behandeling met cytostatica, en er is geen onderscheid tussen specifieke en niet-specifieke opname, wat mogelijk een dissociatie veroorzaakt tussen onnauwkeurige SUV metingen en werkelijke metabolische activiteit van de tumor. Deze problemen kunnen mogelijk worden overkomen door dynamische  $^{18}\text{F}$ -FDG beeldvorming van het hele lichaam (Patlak), daarom concentreert **Hoofdstuk 9** zich op deze volledige kwantitatieve beeldvormingsmethode. Deze procedure kan echter een totale onderzoekstijd van maximaal 75 minuten in beslag nemen, inclusief de tijd die nodig is voor patiëntpositionering en CT acquisitie. Vandaar dat het doel van het onderzoek beschreven in dit hoofdstuk is om met behulp van datasimulaties de totale onderzoekstijd van dynamische  $^{18}\text{F}$ -FDG beeldvorming van het hele lichaam (Patlak) te verlagen van maximaal 75 min tot 30 min gedurende het scantijdsinterval van 30-60 min p.i. met behulp van een populatie-gemiddelde inputfunctie (PIF). Een representatieve eerder verkregen inputfunctie (IF) werd gebruikt als de PIF, en de rateconstants  $K_1$ ,  $k_2$  en  $k_3$  werden gebaseerd op bestaande literatuur. Er werden verschillende tijdsactiviteitscurves (TACs) gesimuleerd. Variaties omvatten vermenigvuldiging van de IF met een positief en negatief geleidelijk lineair verloop gedurende 60 minuten van 5, 10, 15, 20 en 25% (voor het genereren van TACs met behulp van een IF die verschilt van de PIF); gebruik van rateconstants ( $K_1$ ,  $k_3$ , en zowel  $K_1$  als  $k_2$ ) vermenigvuldigd met 2, 1,5 en 0,75; en toevoeging van ruis ( $\mu = 0$  en  $\sigma = 5, 10$  en 15%). Daarop volgde Patlak analyse gebruikmakend van de oorspronkelijke IF (die de PIF voorstelt) om de netto-influxrate ( $K_i$ ) voor de verschillende gesimuleerde TACs te verkrijgen. Vervolgens werd de PIF geschaald naar de (gesimuleerde) IF waarden op het p.i. tijdsinterval van 30-60 minuten, waarbij het schalen van de PIF naar van parameterische beelden afgeleide waarden werd gesimuleerd. De invloed van variaties in IF en rateconstants, en het herschalen van de PIF op afwijkingen in  $K_i$  werden geëvalueerd. Procentuele afwijkingen in  $K_i$  waargenomen met behulp van gesimuleerde gemodificeerde IFs varieerde van -16 tot 16%, afhankelijk van de gesimuleerde amplitude en richting van de IF modificaties. Daaropvolgende schaling van de PIF verminderde deze  $K_i$  afwijking in

de meeste gevallen (287 van de 290) tot <5%. Uit de resultaten werd geconcludeerd dat simulaties in deze studie suggereren dat het schalen van een (mogelijk incorrecte) PIF naar IF waarden, verkregen met dynamische beeldvorming van het hele lichaam van 30 tot 60 min p.i. nauwkeurige  $K_i$  schattingen kan opleveren. Dit geeft aan dat dynamische Patlak beeldvormingsprotocollen kunnen worden uitgevoerd gedurende 30-60 min p.i., waardoor Patlak dynamische beeldvorming van het hele lichaam klinisch meer haalbaar wordt.

**Hoofdstuk 10** borduurt verder op het vorige hoofdstuk door het gebruik van een PIF, om de onderzoekstijd van de dynamische  $^{18}\text{F}$ -FDG beeldvormingsprocedure voor het hele lichaam (Patlak) te verminderen, te valideren met dynamische  $^{18}\text{F}$ -FDG PET data verkregen met behulp van de LAFOV Biograph Vision Quadra PET/CT. Hiertoe werden 12 patiënten met een verdenking op longmaligniteit geïncludeerd en ondergingen ze een dynamische PET acquisitie van 65 minuten. Volledige kwantitatieve Patlak analyse werd uitgevoerd op zowel de volledige scans van 65 minuten als op verschillende kortere scantijdsintervallen p.i. met behulp van een PIF voor schaling; analysesresultaten van de volledige 65 min werden vergeleken met de resultaten verkregen met kortere scantijdsintervallen p.i. Gebruikte kortere scantijdsintervallen waren 30-60, 40-60 en 50-60 min p.i. Volumes of interest om image-derived IFs (IDIFs) te verkrijgen werden in de opstijgende aorta (AA) en in de linkerventrikel van het hart (LV) geplaatst. Vervolgens werd de PIF geschaald naar AA en LV IDIF waarden op respectievelijk 30-60, 40-60 en 50-60 min p.i., en werden parametrische  $^{18}\text{F}$ -FDG  $K_i$  beelden gegenereerd. In de verkregen  $K_i$  beelden werden zowel tumorlaesies als gezonde weefsels gesegmenteerd. De resultaten toonden dat  $K_i$  slechts marginaal varieerde (~2%) tussen de IDIF verkregen uit de AA versus de LV van het hart. Verdere analyses werden daarom voortgezet met alleen de IDIF verkregen uit de AA. Een goede overeenkomst tussen de IDIF en de overeenkomstige PIF, geschaald naar 30-60 min p.i. en 40-60 min p.i., werd verkregen met een afwijking van minder dan 8% in  $K_i$ . Bland-Altman analyses bevestigden de goede overeenkomst in  $K_i$  tussen de IDIF en de bijbehorende PIF geschaald naar verschillende verkorte scantijdsintervallen p.i. De conclusie van dit onderzoek was dat parametrische  $^{18}\text{F}$ -FDG Patlak  $K_i$  beelden van het hele lichaam noninvasief kunnen worden gegenereerd met een Biograph Vision Quadra systeem. Bovendien zorgt het gebruik van een geschaalde PIF voor een aanzienlijke (factor 2 tot 3) vermindering in scantijd zonder verlies van nauwkeurigheid (<8%) en precisie (beeldkwaliteit en ruisinterferentie).

Om de samenvatting van het werk beschreven in dit proefschrift af te sluiten, bespreekt **Hoofdstuk 11** mogelijke toekomstige klinische- en onderzoeksrichtingen,

mogelijke ontwikkelingen in fotondetectietechnologie en (meer kosteneffectieve) hardware ontwikkelingen in PET detectoren.

Tot slot, LAFOV PET is de nieuwste technologische ontwikkeling in (moleculaire) beeldvormingsinstrumentatie. De verbeterde gevoeligheid biedt vele unieke mogelijkheden die voorheen niet beschikbaar waren, bijvoorbeeld verbeterde beeldkwaliteit, mogelijkheden om de dosis en/of scanduur aanzienlijk te verminderen, verbeterde nauwkeurigheid bij het bewaken en voorspellen van de behandelingsrespons, en een middel om moleculaire interacties tussen organen te bestuderen. Verwacht wordt dat deze generatie scanners het veld van de nucleaire geneeskunde en moleculaire beeldvorming in de nabije toekomst aanzienlijk zal verbeteren.





# Appendices

---

List of publications  
Dankwoord  
Curriculum Vitae



## **List of publications** (until 20 October 2022)

**Joyce van Sluis**, Johan R. de Jong, Jenny Schaar, Walter Noordzij, Johannes H. van Snick, Rudi A.J.O. Dierckx, Ronald J.H. Borra, Antoon T.M. Willemsen, and Ronald Boellaard. Performance characteristics of the digital Biograph Vision PET/CT system. *J Nucl Med.* 2019;60:1031-1036.

**Joyce van Sluis**, Ronald Boellaard, Ananthi Somasundaram, Johannes H. van Snick, Ronald J.H. Borra, Rudi A.J.O. Dierckx, Gilles N. Stormezand, Andor W.J.M. Glaudemans, and Walter Noordzij. Image quality and semi-quantitative measurements of the Siemens Biograph Vision PET/CT: initial experiences and comparison with Siemens Biograph mCT PET/CT. *J Nucl Med.* 2020;61:129-135.

Elisabeth Pfaehler, **Joyce van Sluis**, Bram B.J. Merema, Peter van Ooijen, Ralph C.M. Berendsen, Floris H.P. van Velden, and Ronald Boellaard. Experimental multicenter and multivendor evaluation of the performance of PET radiomic features using 3-dimensionally printed phantom inserts. *J Nucl Med.* 2020;61:469-476.

**Joyce van Sluis**, Ronald Boellaard, Rudi A.J.O. Dierckx, Gilles N. Stormezand, Andor W.J.M. Glaudemans, and Walter Noordzij. Image quality and activity optimization in oncological  $^{18}\text{F}$ -FDG PET using the digital Biograph Vision PET/CT. *J Nucl Med.* 2020;61:764-771.

**Joyce van Sluis**, Maqsood Yaqub, Adrienne H. Brouwers, Rudi A.J.O. Dierckx, Walter Noordzij, and Ronald Boellaard. Use of population input functions for reduced scan duration whole-body Patlak  $^{18}\text{F}$ -FDG PET imaging. *EJNMMI Phys.* 2021;8:11.

**Joyce van Sluis**, Ellen C. de Heer, Mayke Boellaard, Mathilde Jalving, Adrienne H. Brouwers, and Ronald Boellaard. Clinically feasible semi-automatic workflows for measuring metabolically active tumour volume in metastatic melanoma. *Eur J Nucl Med Mol Imaging.* 2021;41:1498-1510.

**Joyce van Sluis**, Adrienne H. Brouwers, Ronald Boellaard, and Walter Noordzij. Book chapter 'Digital PET systems' in Encyclopaedia of Nuclear Medicine. Volume 1. Basic concepts, radiopharmacy, and instrumentation. Editor-in-Chief: Alberto Signore. *Elsevier.* 2022;408-415.

---

Adrienne H. Brouwers, **Joyce van Sluis**, Johannes H. van Snick, Carolina P. Schröder, Inge O. Baas, Ronald Boellaard, Andor W.J.M. Glaudemans, Ronald J.H. Borra, Adriaan A. Lammertsma, Rudi A.J.O. Dierckx, and Charalampos Tsoumpas. First-time imaging of  $^{89}\text{Zr}$ -trastuzumab in breast cancer using a long axial field-of-view PET/CT scanner. *Eur J Nucl Med Mol Imaging*. 2022;49:3593-3595.

**Joyce van Sluis**, Johannes H. van Snick, Walter Noordzij, Adrienne H. Brouwers, Ronald Boellaard, Rudi A.J.O. Dierckx, Andor W.J.M. Glaudemans, Adriaan A. Lammertsma, Charalampos Tsoumpas, and Riemer H.J.A. Slart..First experience in UMCG with LAFOV PET: opportunities and challenges. *TvNG*. 2022-02:2893-2901.

**Joyce van Sluis**, Johannes H. van Snick, Adrienne H. Brouwers, Walter Noordzij, Rudi A.J.O. Dierckx, Ronald J.H. Borra, Riemer H.J.A. Slart, Adriaan A. Lammertsma, Andor W.J.M. Glaudemans, Ronald Boellaard, and Charalampos Tsoumpas. EARL compliance and imaging optimisation on the Biograph Vision Quadra PET/CT using phantom and clinical data. *Eur J Nucl Med Mol Imaging*. 2022;Epub ahead of print.

Ananthi Somasundaram, David Vázquez García, Elisabeth Pfaehler, **Joyce van Sluis**, Rudi A.J.O. Dierckx, Elisabeth G.E. de Vries, and Ronald Boellaard. Mitigation of noise-induced bias of PET radiomic features. *PLoS ONE*. 2022;17:e0272643.

**Joyce van Sluis**, Walter Noordzij, Elisabeth G.E. de Vries, Iris C. Kok, Derk Jan A. de Groot, Mathilde Jalving, Marjolijn N. Lub-de Hooge, Adrienne H. Brouwers, and Ronald Boellaard. Manual versus artificial intelligence-based segmentations as a pre-processing step in whole-body PET dosimetry calculations. *Mol Imaging Biol*. 2022;Epub ahead of print.

**Joyce van Sluis**, Johannes H. van Snick, Adrienne H. Brouwers, Walter Noordzij, Rudi A.J.O. Dierckx, Ronald J.H. Borra, Adriaan A. Lammertsma, Andor W.J.M. Glaudemans, Riemer H.J.A. Slart, Maqsood Yaqub, Charalampos Tsoumpas, and Ronald Boellaard. Shortened duration whole body  $^{18}\text{F}$ -FDG Patlak imaging on the Biograph Vision Quadra PET/CT using a population-averaged input function. *EJNMMI Phys*. 2022; In press.

## Dankwoord

Zo aan het einde van mijn promotieperiode, wat toch wel voelt als het einde van een tijdperk, moet ik toegeven erg trots te zijn op het eindresultaat en de weg die ik bewandeld heb de afgelopen jaren. Zonder hulp van mijn eerste promotor, copromotores en vele anderen had ik dit niet waar kunnen maken. In deze appendix van het proefschrift zal ik dan ook de gelegenheid nemen om hierbij stil te staan en de betreffende personen te bedanken voor hun hulp, steun, vertrouwen in mij, of simpelweg gezelligheid de afgelopen jaren.

### **Binnen de werkomgeving**

Allereerst, mijn eerste promotor **prof. dr. Ronald Boellaard**. Beste **Ronald**, als de dag van gisteren voel ik nog de vreugde bij het lezen van de mail waarin mij de positie van promovenda werd aangeboden, "YES!" Na een periode van werken in een vakgebied waar ik mij toch niet helemaal op mijn plek voelde, was ik meer dan klaar om het roer om te gooien en nieuwe uitdagingen aan te gaan. Ik deins niet snel terug voor een sprong in het diepe en met jouw ondersteunende kennis en gestructureerde begeleiding had ik het gevoel dat ik overal klaar voor was. Waren er periodes van onzekerheid en twijfel of het wel zou lukken? Absoluut, vallen en weer opstaan, dat hoort bij de leercurve van een promotieonderzoek. Maar van de fouten die ik heb gemaakt die vervolgens van duidelijke feedback werden voorzien door jou, heb ik het meest geleerd. Je gaf mij het vertrouwen dat het 'oké' was in deze promotieperiode om fouten te maken, want waarom zou je anders promoveren als je alles al weet. Ik wil je bedanken voor de tijd die je voor mij genomen hebt. Onze wekelijkse afspraken boden structuur en waren voor mij een stok achter de deur om telkens nieuwe resultaten te presenteren voor een zo hoog mogelijke productiviteit. Menig keer zaten we samen, met of zonder andere collegae, in het lab en bij de PET/CT in de late avonduren voor fantoomexperimenten of extra PET reconstructies. Vooral in de beginperiode heeft mij dit geholpen om zeer snel, zeer zelfstandig te werk te kunnen gaan op de afdeling. Verhalen over eerste promotores die hun promovendi soms eens per jaar zien doen mij realiseren dat ik zeer bevoorrecht ben geweest met de intensieve begeleiding die ik heb mogen ervaren. Ondanks dat je in verband met je dubbele affiliatie slechts één dag per week fysiek aanwezig was op de afdeling, heb ik dit nooit als een belemmering ervaren en kon ik ook tussendoor bij je terecht via de mail of, toen covid insloeg, via Teams.

Uiteraard waren het niet jaren van non-stop zwoegen en serieuze praat, bij elke afspraak die we hebben gehad was je eerste vraag: "zo, hoe is het leven?". En waarschijnlijk naar aanleiding van mijn voorspoedige start waren sommige afspraken samen met Walter meer grappen en grollen dan werkbesprekingen. Agenda entries

die je opmerkte, waarin ik weer eens een sportgerelateerde auditie in de planning had staan, werden niet vergeten en hier kwam je nadien heel attent weer op terug. Tot slot vond ik de gezamenlijke eet/drinkgelegenheden tijdens verblijf in het buitenland voor congressen, al dan niet met medecollegae, zeer aangenaam.

Bedankt voor alles Ronald, ik hoop dat dit niet het einde hoeft te zijn van onze samenwerkingen. Als ik weet dat je langskomt zorg ik dat de doos met vezelrijke voedzame graanrepen aangevuld op ons kantoor staat :)

Dan mijn copromotor **dr. Walter Noordzij. Walter**, bedankt dat je mijn copromotor wilde zijn en dat je deur altijd open stond. Hoe vaak ik wel niet onaangekondigd je kantoor binnen ben gevallen met een klinische vraag of een andere dagelijkse of persoonlijke kwestie. Vooral tijdens en na de installatie van de Vision was jij als aangestelde zogenaamde Vision arts de eerste persoon waarmee ik intensief dagelijks contact had op de afdeling, uiteraard droeg je toepasselijk een op de Vision afgestemd blauw pak met oranje stopdas; toendertijd nog niet eens officieel mijn copromotor, maar altijd open en behulpzaam. Bedankt voor de prettige samenwerking en hopelijk kunnen we dit voortzetten in de toekomst. Voor de toekomst moet ik wellicht een serieuze kledingkast upgrade overwegen, want rondom jou voelt iedereen zich 'underdressed'.

Mijn andere copromotor, **dr. Adrienne H. Brouwers**. Bedankt **Adrienne** dat je mijn copromotor wilde zijn en dat ik ook altijd bij jou terecht kon met vragen. Ik heb grote bewondering voor je eindeloze geduld bijvoorbeeld bij het nakijken en aanpassen van mijn <sup>89</sup>Zr tumor segmentaties. Elke laesie zorgvuldig bij langsgaand was je het soms met me eens, maar soms moesten we toch nog eens beter kijken, al heen en weer scrollend. Ditzelfde geduld is ook nodig bij het stap voor stap opzetten van klinische studies heb je me geleerd. Naargelang het proces vorderde en er geen einde aan de opmerkingen van- en de discussies met de ethische commissie leken te komen zag ik dat zélf bij jou het geduld een keer kan opraken; gelukkig was ik niet de enige hierin. De aanhouder wint en we gaan nog even door met onze studies! Bedankt voor de samenwerking, je inzet en je bijdrage aan de totstandkoming van dit proefschrift.

Ons afdelingshoofd **prof. dr. Rudi A.J.O Dierckx**. Beste **Rudi**, ondanks dat je officieel niet als promotor aangesteld was voor mijn promotieonderzoek, maakte je dit niet minder betrokken bij de verschillende projecten. Zo hadden we bijvoorbeeld eens per drie maanden een overleg, zodat je de voortgang kon bewaken, en deze gelegenheid werd ook gebruikt om een overvloed aan nieuwe ideeën te delen. Zo snel als ik kon schrijven probeerde ik het bij te houden, al Vlaams ontcijferend,

om naderhand niets te vergeten. Samen met Andor hebben jullie gezorgd dat ik in samenwerking met de afdeling medische oncologie tenminste nog een aantal jaren kan aanblijven in de rol van postdoc. Bedankt voor je vertrouwen, de kansen die je me gegund hebt de afgelopen jaren en de (hopelijk vele) jaren die nog zullen komen.

Over naar **prof. dr. Andor W.J.M. Glaudemans**. Beste **Andor**, ik weet nog goed dat je op een dag (toen ik precies één jaar en één dag in dienst was) langskwam in de kelder van het Triadegebouw om één van je nieuwe promovendi te introduceren. Je vroeg hoe lang ik nog moest en toen ik antwoordde dat ik nét een jaar in dienst was, zei jij: "Goh, echt? Ik heb het gevoel dat je hier al jaren rondloopt!" Op dat moment vroeg ik me af of dit een goed of slecht gevoel was. Inmiddels heb je samen met Rudi mij aanbevolen bij de afdeling Medische Oncologie voor een deeltijd postdoc in samenwerking met de afdeling Nucleaire Geneeskunde zodat ik tenminste nog een aantal jaren kan blijven, en hebben we samen projecten afgerond en nieuwe studies in de pijplijn. Ook bij jou loop ik de deur plat, want langsgelopen praat vaak net wat makkelijker dan via een email. Ondanks je drukke agenda heb ik me nog nooit onwelkom gevoeld. Bedankt voor je vertrouwen en steun, en dat je daarnaast ook nog in de oppositie plaats wilde nemen.

Niet te vergeten, **prof. dr. Riemer H.J.A. Slart**. Beste **Riemer**, onlangs hebben we een groepje van vier Technische Geneeskunde bachelor studenten succesvol begeleid in hun afstudeeropdracht en in de nabije toekomst zullen we hier hopelijk meerdere masterstudenten aan toevoegen. Daarnaast heb je mij samen met Andor recentelijk een rol van assistant editor bezorgd, weer iets nieuws voor mij! Bedankt voor de fijne samenwerking en ik kijk uit naar meerdere nieuwe, spannende projecten in de toekomst.

Dear **prof. dr. Charalampos Tsoumpas**, dear **Harry**, not too long ago you joined the UMCG. Only just in, but eager to help/provide input/brainstorm/initiate new projects right from the start. Together with Andor and you, I am now supervising a PhD student for the first time. Thus far, we have been quite busy with a lot of startup technicalities regarding optimal use of our brand new PET system, and now that it is finally up and running for the most part I believe there are exciting opportunities ahead. Thank you for our intriguing conversations over the last year, and for your time and feedback that helped to improve this thesis. I look forward to initiate more new exciting research projects in the near future together.

Mijn 'nieuwe baas' **prof. dr. Elisabeth G.E. de Vries**, beste **Liesbeth**, bedankt voor de kans die je me hebt gegeven als deeltijd postdoc. We kenden elkaar alleen van

naam tot je gesprek met Andor en Rudi, die dachten (zoals vaker) dat ik ongeveer aan het einde van mijn PhD was aangekomen en klaar was voor de volgende stap. Dat duurde toch nog iets langer (anderhalf jaar), maar gelukkig was er de mogelijkheid om toch alvast te starten; dan maar in deeltijd. De afgelopen maanden hebben vooral in het teken gestaan van studies opzetten in samenwerking met de farmaceutische industrie en ik hoop dat ik hier mijn steentje voldoende aan bij heb kunnen dragen. Nu de tijdrovende afronding van mijn promotietraject achter de rug is hoop ik dat we onze kennis en krachten nog beter kunnen bundelen en een veelbelovende toekomst tegemoet gaan.

**Physician assistant** en PET/CT specialist **Johannes H. van Snick**, of makkelijker gezegd, **Paul**. Wat hebben we al vaak avonden samen gezeten bij de PET systemen. Tevens heb je zo vaak geholpen met data import/export/reconstructies onder klinische werkuren wat me vele avonden en weekenden werk heeft gescheeld. Niet te vergeten, je inzet bij het vullen en scannen van fantomen, de inclusies van patiënten en voorbereiding van presentaties. Er zijn teveel aspecten om op te noemen, daarom in het algemeen, duizendmaal dank voor je ondersteuning bij alles wat met de PET op de werkvloer te maken heeft. Daarnaast bedankt voor de gezelligheid en de theetjes, daar moeten we weer eens tijd voor maken (en dan trakteer ik).

**De medisch nucleair werkers:** vanaf het begin van mijn aanstelling kwam ik te pas en te onpas langs voor extra scans/reconstructies en andere vragen. Veel dank voor jullie bereidheid om extra scans te verrichten en mee te denken over de aanpak van onderzoek.

Voor alle **co-auteurs** die niet apart worden benoemd elders in dit dankwoord, een speciale 'Bedankt!'. In het bijzonder **Antoon T.M. Willemsen** en **Adriaan A. Lammertsma**, hartelijk dank voor jullie altijd kritische blik en de hieruit voortkomende verbeteringen in presentaties, artikelen en dit proefschrift. Verder **Johan R. de Jong**, **Jenny Schaar**, **Ronald J.H. Borra**, **Gilles N. Stormezand**, **Maqsood Yaqub**, **Evelien L.M. van Esch**, **Demi A. Croes**, **Pim P. van der Donk**, en **Laura Kist-de Ruijter**. Bedankt voor de tijd en energie die jullie in de totstandkoming van dit proefschrift hebben gestoken.

Dan de leden van de beoordelingscommissie: **prof. dr. Jan Pruijm**, **prof. dr. Josée M. Zijlstra** en **prof. dr. H.W.A.M. de Jong**. Bedankt voor uw bereidheid deel uit te maken van de beoordelingscommissie en uw ideeën en mening met betrekking tot dit proefschrift met mij te delen.

Mijn paranimfen **Sabine L. Collette** en **Ananthi Somasundaram**. Bedankt dat jullie mijn paranimfen wilden zijn. Lieve **Sabine**, ik was al een jaartje bezig toen jij bij ons in de kelder van het triade gebouw ook aan je PhD kwam werken. Vanaf dag één hadden wij een klik: dezelfde mindset, dezelfde drive, dezelfde perfectionistische trekjes ;), maar toch ook gezelligheid in korte mini-pauzes onder werktijd. Wat vond ik het jammer dat je uiteindelijk besloot naar de afdeling Neurologie te verhuizen zodat je met neurologische vragen direct daar terecht kon of met collegae kon sparren. Gelukkig verwaterde ons contact niet, alleen moesten we het iets beter plannen, bijvoorbeeld bijkletsen tijdens een 8-10 km wandeling in de lockdown periode, of beter, onder het genot van een grote kom ramen noodle soep of iets anders lekkers. Later gestart en eerder klaar, op naar Leeuwarden voor je volgende stap als ANIOS Interne Geneeskunde. Ik gun je een zeer succesvolle carrière en hoop dat je in je drukke werkrooster af en toe nog tijd hebt voor een gezellige dinner-date met mij. Dear **Ananthi**, should I write this in English or Dutch? I remember the times we worked together in one office during autumn or winter, always cold and always battling our colleagues for turning up the heater; you already with three pants, two sweaters, gloves, and a hat on though ;). I cannot keep up with your knowledge on radiomics and coding skills. But luckily, just like me, you are not leaving the UMCG soon so perhaps I can ask you for some favors and explanations in the future. Off late, we made a habit out of having regular lunch or tea breaks once a week to keep each other up to date on work, hobbies, and other stuff. I look forward to continuing this in the future and wish you all the best with your goals in academia.

**Elisabeth Pfaehler**, dear **Elli**, you were my PhD buddy when this whole journey started. Thank you for taking the time to get me settled at the department and the graduate school of medical sciences at the university, to teach me how to perform phantom experiments, and get me acquainted with Ronald's tools. Apart from that I enjoyed our lunches, baking experiences, and our walks. Big hugs to you and your wonderful girls from me.

**Danique Giesen**, lieve **Danique**, mijn huidige kantoorgenoot. Wat een geluk dat we samen de voorbereidingen voor onze promotie doorliepen. We hebben elkaar stap voor stap geholpen (misschien jij mij iets meer dan andersom). Je kennis van de  $^{89}\text{Zr}$  tracersbereidingen en immuuntherapie hebben mij wijzer gemaakt en ik hoop dat ik ook nog wat nuttige kennis met jou heb kunnen delen over PET technologie en kwantificatie. Op naar meer productieve jaren in kamer G.2.16!

Er zijn natuurlijk veel medewerkers die achter de schermen zorgen dat de dagelijkse gang van zaken soepel verloopt. Vandaar bedank ik de **afdeling Nucleaire**

**Geneeskunde en Moleculaire Beeldvorming** en alle logistieke, administratieve en andere medewerkers die de dagelijkse kliniek en alles wat hierbij komt kijken draaiende houden. In het bijzonder **Gerda L. Bakker** dankjewel, omdat je erom vroeg ;), en **Sarita I. Evers**. Zonder jullie hadden wij PhD studenten geen contract, geen kamer, geen bureau, geen computer, geen sleutels en vooral geen idee waar we moesten beginnen. Ook **Klaas Willem Sietsma**, bedankt voor je hulp bij computerproblemen, maar ook bij EARL gerelateerde zaken en fantoomproeven. Tevens **Joyce M. Wieringa**, we kennen elkaar nog niet zo lang, maar we hebben wat gemeen; ik heb al een speciale 'forward' knop voor verwarrende mails die waarschijnlijk fout geadresseerd zijn. Bedankt voor je vriendelijkheid, openheid en hulp de afgelopen periode.

De dames en heren van het lab, want zonder tracers bestaat er geen afdeling Nucleaire Geneeskunde. In het speciaal **Bram Maas**, bedankt voor het regelen van (soms belachelijk hoge hoeveelheden) radioactieve tracer voor fantoomproeven, bijvoorbeeld voor de NEMA testen. Maar soms ook last-minute aanvragen doordeeweeks waar je gelukkig altijd een oplossing voor vind.

To all current and past **PhDs and postdocs** with whom I have enjoyed my time working in the basement of the Triade building, in the Meditech building, and now continue to enjoy collaborations with in separate offices, thank you for your company, friendliness, and cooperation.

### **Mijn familie**

Lieve **mama**, al bel ik midden in de nacht, je bent er altijd voor mij met een luisterend oor. Bedankt voor alles wat je voor me hebt gedaan en nog steeds doet; ik weet je zou me de hele wereld geven als je die in handen had. Bedankt voor je eindeloze liefde, ik heb geluk met een moeder zoals jij.

Lieve **Tim**, mijn grote broer(tje), ookal zijn we op sommige vlakken heel verschillend, hebben we veel lol samen met spelletjes doen, films en de Formule 1 kijken. Door de jaren heen heb je altijd oprecht interesse getoond in mijn studie, werk en belangrijke gebeurtenissen zoals congressen of bijvoorbeeld deze promotie, dankjewel.

Lieve **papa**, bij jou kan ik te allen tijde terecht voor advies ongeacht waarover. Je hebt me altijd gestimuleerd volgende stappen te nemen en na te denken over de toekomst. Bedankt voor je onaflatende vertrouwen in mij en je onvoorwaardelijke steun al deze jaren. Dankzij jouw steun ben ik gekomen tot waar ik nu ben. Ik kan mij geen betere vader wensen.

Daarbij hoort lieve **Willie**, mijn bonusmoeder, bedankt voor je vrolijkheid, steun en liefde door de jaren heen.

**Marjan**, lieve schoonmoeder, ondanks dat het soms lastig is om uit te leggen wat mijn werk precies inhoudt, was je altijd zeer geïnteresseerd. Bedankt dat je me altijd met open armen hebt ontvangen en bedankt voor Pat.

En tot slot natuurlijk **Pat**, mijn dagelijkse steun en toeverlaat. Jij was de enige aan wie ik mijn twijfels en onzekerheden op elk moment suprême ook echt (lichtelijk in paniek) uitsprak. Maar jij, wel van mij gewend dat ik goed kan overdrijven zoals je vaker zegt, hebt altijd onbetwist het volste vertrouwen gehad dat ik heus wel een oplossing zou vinden of heus wel goed voorbereid was op de volgende uitdaging. Hierin probeerde je mij, zover als lukte, gerust te stellen. De rust zelf, mijn nonchalante 'blok beton'. Ontelbare keren kon ik je kort nadien dan vertellen dat alles toch goed was gekomen en dat het uiteindelijk best meeviel, waar jij dan totaal niet verrast door was.

Bedankt voor het doorstaan van mijn presentatievoorbereidingen, vooral in het begin van het promotietraject, waar je keer op keer aandachtig naar luisterde. Eenmaal aangekomen op de dag van de presentatie kon jij hem ook dromen.

Daarnaast hebben we de grootste lol samen, delen we dezelfde interesses en zijn we beide druk aan het werk. Samen trainen in de sportschool, samen lessen en samen nog een uurtje 's avonds op de bank zitten na de drukte van de dag, daar geniet ik van. 's Weekends halen we de gemiste avond eetmomenten weer in, lekker thuis tijdens een film of bij onze favoriete restaurantjes.

Bedankt voor je goede zorgen en bemoediging, ik weet dat ik altijd op je terug kan vallen en dat geeft me de rust en zekerheid die ik nodig heb om dagelijks met volle focus goed te kunnen presteren. Jij maakt het verschil en betekent alles voor mij.

A handwritten signature in black ink, appearing to read 'Joyce'.





---

## Curriculum Vitae

Joyce van Sluis werd geboren in Groningen op 5 juni 1990. Na het behalen van het VWO diploma begon zij in 2009 met de studie Technische Geneeskunde aan de Universiteit Twente in Enschede. In 2015 studeerde zij af als Master of Science in Technical Medicine - track Medical Sensing and Stimulation.

Vervolgens startte Joyce aan een gecombineerde praktisch georiënteerde postmaster (PDEng) Qualified Medical Engineering aan de Technische Universiteit Eindhoven en Kempenhaeghe Epilepsiecentrum. De tweejarige postmaster zou overlopen in een PhD traject; een vijfjarig project in totaal. In verband met conflicten tussen de organisaties binnen het onderzoeksconsortium ging de overloop naar een PhD traject niet door en rondde Joyce begin 2018 de postmaster af.

Er deed zich een nieuwe kans voor. Een PhD in een ander werkgebied, beeldvorming in plaats van signalen, en een andere werkplek: het Universitair Medisch Centrum Groningen. Sinds 2018 werkt Joyce op de afdeling Nucleaire Geneeskunde en Moleculaire Beeldvorming met als aandachtsgebieden PET technologie en methodologie, beeldverwerking, biomarkers, en (farmacokinetische) kwantitatieve analyse. Deze aandachtsgebieden hebben zich met name geconcentreerd op de tracers  $^{18}\text{F}$ -FDG en  $^{89}\text{Zr}$  in de oncologische setting (dit proefschrift). Sinds 2021 werkt Joyce ook als deeltijd (0.5 fte) postdoc bij de afdeling Medische Oncologie om de samenwerking tussen beide afdelingen te bevorderen, nieuwe gezamenlijke studies op te zetten, en technologische en methodologische ondersteuning te bieden betreffende PET.

Na haar promotie zal de afdeling Nucleaire Geneeskunde en Moleculaire Beeldvorming met 0.5 fte de postdoc aanstelling aanvullen tot 1 fte en zal zij werkzaam blijven bij beide afdelingen.





